Doctoral Dissertation
Doctoral Program in Civil and Environmental Engineering (39th Cycle)

# Seismic precursor identification method integrating acoustic emission physical models and multi-source data

**Zihan Jiang**
* * * * * *

**Supervisors**
Prof. Giuseppe Lacidogna, Politecnico di Torino, Supervisor
Prof. Zhiwen Zhu, Shantou University, Co-Supervisor

Politecnico di Torino & Shantou University
May 10, 2026

I hereby declare that, the contents and organisation of this dissertation constitute my own original work and does not compromise in any way the rights of third parties, including those relating to the security of personal data.

……...

Zihan Jiang

Turin, May 10, 2026

# Abstract

Earthquakes are among the most devastating natural hazards worldwide. Accurate earthquake prediction can significantly reduce disaster losses, yet seismic precursor identification remains one of the most challenging scientific problems of our time. Earthquakes result from macroscopic rock fracture in the Earth's crust, and their preparation process shares profound physical homology with the cross-scale damage evolution in materials, from microcrack initiation and propagation to macroscopic instability. Acoustic emission (AE), as stress waves generated by the release of strain energy during rock microfracturing, offers the potential to capture direct physical effects of earthquake preparation and to explore physics-based earthquake precursor identification. However, existing research faces challenges such as unclear precursor mechanisms, high false-alarm rates of single methods, and difficulties in unifying laboratory and field observation scales. Addressing these issues, this study takes fracture mechanics as the theoretical foundation, adopts the novel Method of Critical Fluctuations-Based (MCF-B) analysis as the core approach, and leverages AE technique to conduct cross-scale precursor identification research spanning laboratory experiments and field measurements, while integrating multi-source data and deep learning techniques to construct an intelligent precursor warning framework. The main research work and conclusions are as follows:

(1) An AE signal analysis method based on the critical fluctuation (MCF-B) approach is proposed. Traditional *b*-value analysis has limitations in describing nonlinear amplitude distributions. Grounded in critical fluctuation theory, the MCF-B method is introduced, incorporating a power-law decay exponent ($p_2$) and an exponential decay exponent ($p_3$). Its potential for cross-scale application, from material fracture to earthquake preparation, is demonstrated. It quantifies deviations of amplitude distributions from ideal power-law behavior and captures crossover

phenomena ($p_2$ decrease, $p_3$ increase) as systems approach instability, providing a more physically meaningful and sensitive statistical criterion for precursor identification.

(2) A series of experiments were conducted, including compression tests on steel fiber-reinforced concrete (SFRC), size effect tests on ultra-high performance concrete (UHPC), flexural tests on UHPC-strengthened beams, field monitoring of cracks in steel-UHPC composite decks, and flexural tests on glass fiber-reinforced polymer (GFRP) bar-reinforced concrete beams. Results indicate: AE parameters (*b*-value, RA-AF, etc.) effectively characterize damage evolution and cracking mode transitions; AE energy follows a fractal scaling law, with fiber toughening increasing the fractal dimension of the damage domain; Natural time (NT) analysis can serve as an earlier warning indicator than the *b*-value method. In the GFRP beam tests, the MCF-B method, through the synergistic evolution of its parameters, tracked the entire process from critical state to instability more robustly and persistently than the traditional *b*-value method. Its identification results were consistent with NT analysis and AE information entropy analysis, validating the effectiveness and superiority of the MCF-B method in identifying failure precursors across scales.

(3) Synchronous monitoring of AE and seismicity was conducted in a granite mountain tunnel. Significant correlations were found between intense AE bursts and regional earthquakes. AE characteristic parameters, *b*-value, and NT analysis effectively identified pre-seismic anomalies. Multimodal statistical analysis showed that temporal variations in AE distribution precede those of seismicity, serving as earthquake precursors capable of identifying seismic events approximately 17 hours in advance. The MCF-B method was applied to field AE data, revealing significant synergistic anomalies in $p_2$ and $p_3$ parameters before earthquakes. Simultaneous electromagnetic emission (EME) monitoring cross-validated the reliability of AE precursors, revealing a strict temporal sequence of "EME precursor first, AE precursor second" before earthquakes, with signal strength positively correlated with subsequent magnitude.

(4) A physics-data driven deep learning model for earthquake precursor identification was constructed, achieving real-time warning with high accuracy. Based

on fundamental features (AE count, count rate, frequency, amplitude), a deep neural network model was designed. Through cross-validation and hyperparameter optimization, the baseline model achieved 97.6% accuracy on the test set, significantly outperforming traditional machine learning methods. Validation using 180-day long-term time-series data showed an average warning lead time of 20.5 hours for four major seismic events, with 97.1% accuracy and 97.8% recall, indicating good generalization ability and stability in long-term practical applications. By further incorporating higher-order physical features, namely MCF-B parameters ($p_2$, $p_3$) and NT variance ($\kappa_1$), into the model, a physics-data hybrid-driven framework was constructed, improving accuracy and extending warning lead time. SHAP analysis confirmed the key contribution of these physical feature parameters ($p_2$, $p_3$, $\kappa_1$) to model decisions, demonstrating the effectiveness of the physics-data synergistic-driven approach.

In summary, through theoretical innovation, methodological development, and multi-scale empirical validation, this study establishes a set of theories and methods for cross-scale precursor identification, from microfracture to macro-earthquake. The research findings can provide new scientific basis and technical pathways for earthquake early warning.

**Keywords:** Earthquake precursor; Acoustic emission (AE); Fracture mechanics; Method of critical fluctuations-based (MCF-B); Natural time (NT) analysis; Cross-scale; Deep learning; Physics-data synergistic driving.

# Acknowledgment

As I reach this point in my writing, my journey as a student is drawing to a close. Looking back on my doctoral years, from the dawn at Shantou University to the sunset at Politecnico di Torino, the successful completion of my research would not have been possible without the unwavering support of my supervisors, family, and friends. I wish to express my sincere gratitude to all who have helped and supported me.

First and foremost, I would like to thank my supervisor, Professor Zhiwen Zhu. His rigorous and pragmatic approach to research, his dedication to scholarly excellence, and his keen insight into scientific problems have profoundly influenced me. During the writing of my first academic paper, his painstaking, line-by-line revisions taught me the true meaning of precision and conciseness in academic writing. I am also grateful to Professor Zhu for providing me with the freedom to explore my research interests and for supporting my participation in international conferences and applications for overseas study funding, thereby broadening my horizons on a larger stage. I thank my fellow lab members; working alongside you in the laboratory has been a cherished memory of my academic journey. I am thankful to Professor Alberto Carpinteri and Professor Federico Accornero for their theoretical guidance and advice, and to Dr. Chuanlin Wang for his assistance with material experiments. I also extend special thanks to the Department of Civil Engineering and Smart Cities at Shantou University for providing excellent conditions and a stimulating academic environment for my experiments and research.

I acknowledge the China Scholarship Council (CSC) for funding my joint doctoral training at Politecnico di Torino. I am deeply grateful to my supervisor in Turin, Professor Giuseppe Lacidogna, who not only provided meticulous guidance on my academic research but also offered me thoughtful care in my daily life. I thank Professors Stefano Invernizzi, Ignacio Iturrioz, and Leandro Friedrich for their

invaluable help. I am also thankful to Drs. Ediblu Silva Cezar, Pedro Marin Montanari, and Qinghua Ou from the Fracture Mechanics Laboratory; the time we spent dining together and discussing problems represents my warmest memories of Turin.

Finally, and most importantly, I wish to thank my parents and family. Your understanding and support have afforded me the opportunity to dedicate myself to my studies without worry. The completion of my doctorate is not an end, but a new beginning. I will carry this gratitude and these achievements forward as I continue my journey.

# Contents

# Chapter 1

# 1 Introduction

## 1.1 Research background and significance

### 1.1.1 Earthquake disasters

Earthquakes are extremely destructive and have caused immense suffering to human societies. In 2001, the magnitude 7.6 earthquake in Gujarat, India, resulted in 35,000 deaths, 67,000 injuries, and economic losses exceeding USD 10 billion. On December 26, 2003, the magnitude 6.6 earthquake in Bam, Iran, killed 31,000 people and injured 30,000, destroying the ancient city of Bam. On December 26, 2004, the magnitude 9.1 Sumatra-Andaman earthquake and the ensuing Indian Ocean tsunami led to 283,000 deaths and disappearances. On October 8, 2005, a magnitude 7.6 earthquake in Pakistan caused 86,000 deaths, over 10,000 injuries, and more than 9,000 disappearances. According to statistics, earthquake-related deaths account for 54% of the total deaths from all natural disasters worldwide, making earthquakes the deadliest of all natural hazards.

China, located at the intersection of the Circum-Pacific and Eurasian seismic belts, is one of the countries most severely affected by earthquake disasters worldwide. On March 8, 1966, a magnitude 6.7 earthquake in Xingtai killed over 8,000 people. On July 28, 1976, the magnitude 7.8 Tangshan earthquake caused over 240,000 deaths, severely affecting Beijing and Tianjin and causing widespread destruction of residential and public infrastructure. On May 12, 2008, the magnitude 8.0 Wenchuan earthquake, which is the most destructive, widest-reaching, and most disastrous earthquake in

China's history, resulted in 69,227 deaths, 17,923 disappearances, 46.255 million people affected, and direct economic losses of CNY 845.14 billion. The magnitude 7.1 earthquake in Yushu, Qinghai, in 2014 and the magnitude 6.5 earthquake in Ludian, Yunnan, in August of the same year also caused significant casualties and substantial property damage. According to the 2022 China Statistical Yearbook, a total of 230 earthquake disasters occurred in China between 2000 and 2021, resulting in 489,000 casualties and direct economic losses of CNY 1,158.259 billion.

Guangdong Province is located in the coastal seismic belt of southeastern China and has experienced multiple moderate-to-strong earthquakes throughout history, with particularly notable seismic activity in the eastern region (eastern Guangdong). In 1600, a magnitude 7.0 earthquake struck Nan'ao, Shantou, causing severe damage to coastal areas. In 1918, a magnitude 7.3 earthquake in Nan'ao, Shantou, the largest and most destructive earthquake in Guangdong's history, with an epicentral intensity of X, killed over 1,000 people. Although its epicenter was at sea, the 1994 magnitude 7.3 earthquake in the Taiwan Strait still caused significant ground shaking and social panic in the coastal areas of eastern Guangdong. In recent years, seismic activity in eastern Guangdong has remained relatively active. For example, a magnitude 5.0 earthquake occurred in the Nan'ao sea area in 2023, indicating that this region still possesses the tectonic setting capable of generating moderate-to-strong earthquakes. These historical events fully demonstrate that the earthquake disaster risk in Guangdong Province, especially in its eastern region, cannot be ignored. Conducting region-specific research on seismic precursor identification is therefore of great practical significance and urgency.

According to the Seismic Ground Motion Parameters Zonation Map of China (GB 18306-2015), approximately 57% of China's population, 51% of its cities, and 58% of its land area are located in regions with a seismic fortification intensity of VII or above. About 10% of the population and more than 14% of the value of fixed assets are located in regions with a fortification intensity of VIII or above. It should be noted that earthquakes are characterized by high frequency, high intensity, wide distribution, severe losses, profound social impacts, and great difficulty in prediction and mitigation.

Moreover, due to population and wealth concentration driven by social development, the risk of catastrophic earthquakes is increasing. Earthquakes also trigger various secondary disasters, particularly geological hazards such as rockfalls, landslides, and debris flows in mountainous areas, which exacerbate the impact of the earthquake. Furthermore, earthquakes not only cause severe casualties and economic losses but also damage infrastructure, leading to long-term social and economic consequences. Therefore, the ability to predict earthquakes would enable the timely implementation of appropriate preventive measures, thereby minimizing their adverse effects.

Conducting scientific observation and research on seismic precursors and exploring precursor identification methods have long been a practical societal need. The prevention and mitigation of earthquake disasters is not only a scientific problem but also a major political, social, and economic issue. Accurate earthquake prediction is extremely challenging. The successful and timely identification of seismic precursors would significantly reduce property damage and casualties, yielding substantial economic and social benefits, and has thus motivated continued exploration into the causes and prediction of earthquakes. Since the founding of modern seismology in the 1870s, earthquake prediction has been one of its principal research questions. Especially since the 1950s, it has been a major scientific focus of governments and seismologists worldwide. Through the efforts of several generations of seismologists, meaningful progress has been made, particularly in medium- to long-term earthquake prediction. However, the overall level of prediction capability remains low, and the current state of short-term and imminent prediction falls far short of societal needs.

The core of earthquake forecasting is the early identification of the time, location, and intensity of an impending earthquake, thereby providing early warning for disaster prevention and mitigation. Current earthquake prediction relies on the observation and analysis of seismic precursors, namely various signs that precede an earthquake, such as anomalous animal behavior, ground deformation, changes in groundwater levels, crustal stress variations, geoelectric changes, gravity anomalies, geoacoustic and geomagnetic field variations, and environmental radioactivity changes. These precursor signals are often subject to significant uncertainty in complex geological environments,

leading to poor accuracy and timeliness in predictions. For many years, seismologists have been dedicated to the search for "deterministic seismic precursors", anomalies that are invariably observed before every large earthquake and whose appearance invariably signals an imminent large earthquake. Clearly, once a deterministic seismic precursor is identified, the credibility of earthquake prediction would be significantly enhanced. In June 1978, the Japanese government passed a major earthquake countermeasure bill based on earthquake prediction and aimed at preventing and mitigating earthquake disasters. This bill established detailed emergency response plans and short-term forecast issuance procedures. A key provision is that, within one hour of a monitoring network detecting an anomaly, an expert committee must convene and reach a determination within 30 minutes as to whether the anomaly constitutes a precursor to a predicted earthquake. If so, the finding is compiled into an earthquake prediction report, submitted via the Director-General of the Japan Meteorological Agency to the Prime Minister, who then immediately issues a "warning declaration" in a cabinet meeting and initiates the emergency response plan [1].

### 1.1.2 Acoustic emission (AE) technique

An earthquake is the result of macroscopic fracture of crustal rocks. During the fracturing process under stress, rocks release various physical signals, including acoustic and electromagnetic emissions. Therefore, monitoring these signals essentially captures the direct physical effects of the earthquake preparation process, offering the potential for physics based seismic precursor identification.

Before an earthquake, stress accumulates within rocks. When the stress reaches the rock's strength limit, fracture occurs, and the enormous accumulated strain energy is released, generating an earthquake. Notably, during the pre earthquake preparation period, large volumes of crustal rock are compressed, storing substantial strain energy. In highly compressed zones, local rock fractures occur, producing concentrated and intense acoustic emission (AE) phenomena. In fracture mechanics, AE represents a

portion of the strain energy released during material failure (see Fig. 1.1(a)), which is emitted in the form of stress waves (see Fig. 1.1(b)). Rock AE is a seismic precursor directly linked to the earthquake process. Since AE inevitably occurs before rock failure, this provides a clue to deterministic earthquake precursors. The frequency range of stress waves is extremely broad, spanning from stress waves in the 1 THz band released by nm scale fractures to those in the 1 Hz band released by km scale fractures. The latter corresponds to the typical frequencies of seismic waves (see Fig. 1.2) and can be detected by deploying sensors. Before an earthquake, under the influence of tectonic stress, fractured rocks near the source region become more active and gradually approach a critical state. When brittle fracture occurs in these fractured rocks, stress waves are generated and propagate at velocities on the order of $1\times10^3$ m/s [2]. For example, in intact rock, assuming a constant stress wave velocity, the correlation between the wavelength (which governs crack dimensions) and frequency is illustrated in Fig. 1.2. Figure 1.3 presents an evolution model of the earthquake preparation zone [3]. In Fig. 1.3(a) to Fig. 1.3(d), each circle represents the boundary of the preparation zone, within which the equivalent crack lengths are sequentially: $10^{-9}$ to $10^{-6}$ m, $10^{-6}$ to $10^{-3}$ m, and $10^{-3}$ to $10^{0}$ m. The black dot marks the epicenter of an impending earthquake. In early Stage I, the preparation zone expands to its maximum radius, characterized primarily by nm scale microcracks. Subsequently, in Stages II and III, tectonic stress becomes concentrated towards the epicenter, the radius of the preparation zone further decreases, and crack sizes grow from the mm scale to the meter scale. In the final Stage IV, macroscopic cracks along the earthquake fault coalesce, the earthquake occurs, and seismic waves begin to propagate.

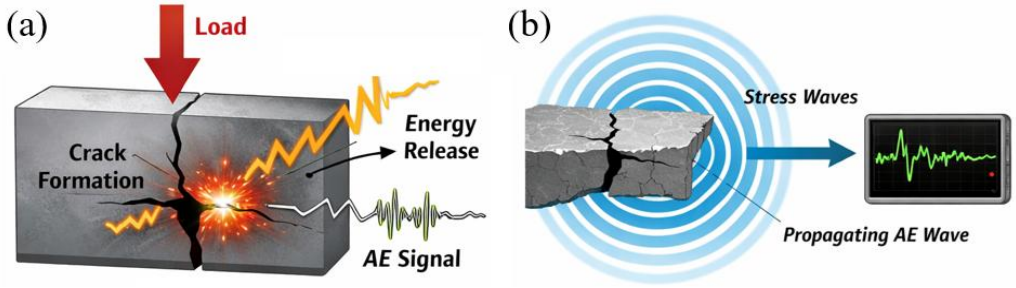


**Figure 1.1** Schematic diagram of AE during material fracture: (a) strain energy release; (b) stress wave propagation.

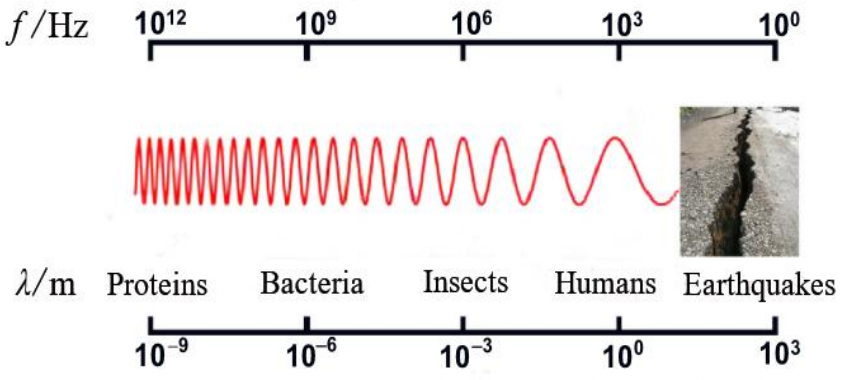


**Figure 1.2** Correlation between wavelength scale and frequency scale [2].

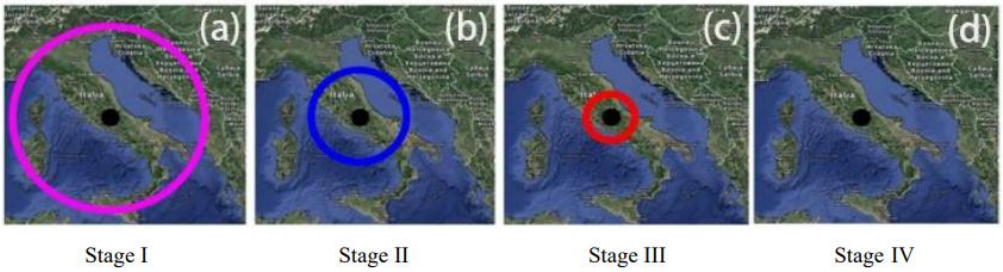


**Figure 1.3** Evolution of earthquake preparation zone [3].

Rock AE monitoring technology based on fracture mechanics (see Fig. 1.4) is an advanced diagnostic tool in geophysics and has demonstrated significant potential in structural monitoring and seismic precursor identification [2,3]. An earthquake is the result of macroscopic fracture of crustal rock under tectonic stress. From a microscopic perspective, rock fracture is essentially a cross-scale damage accumulation process involving microcrack initiation, propagation, coalescence, and eventual formation of a macroscopic fault. AE is the direct physical signal of strain energy released in the form of stress waves when rock fractures at the micro to meso scale. Therefore, an earthquake can be regarded as a "macro acoustic emission" at the crustal scale, while AE monitored in the laboratory represents "micro seismicity" at scales ranging from micrometers to meters. The two phenomena share the same physical origin and both obey the fundamental laws of fracture mechanics. On this basis, monitoring AE activity in crustal rocks essentially captures the "microfracturing" activity that occurs during earthquake preparation before macroscopic rupture. These pre-seismic microfracturing events and

the abundant AE signals they generate may reveal critical state information regarding the transition of source rocks from steady state damage to unstable fracture, thereby providing the most direct physical precursor for detecting pre-earthquake anomalies.

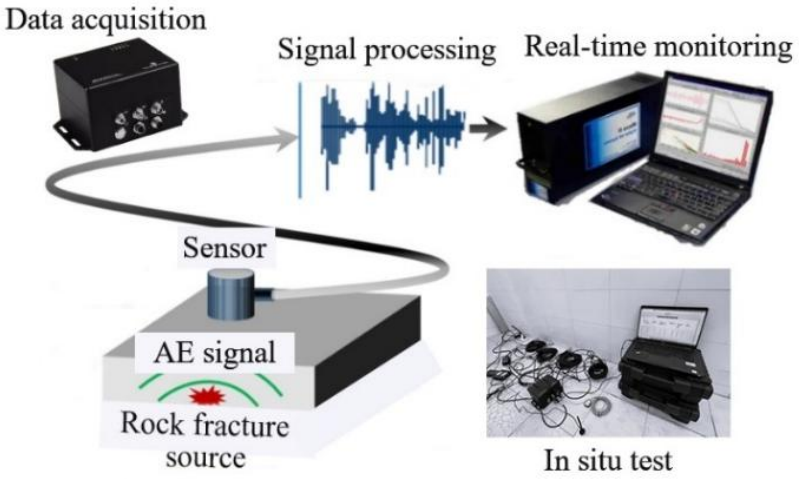


**Figure 1.4** Schematic diagram of rock AE detection technique.

### 1.1.3 Artificial intelligence (AI) technology

Artificial Intelligence (AI) is a scientific discipline that simulates intelligent human behavior through computer systems. Its core objective is to equip machines with capabilities such as perception, reasoning, learning, and decision making. Since the concept of AI was formally introduced at the Dartmouth Conference in 1956, AI has undergone multiple technological evolutions, from symbolism and expert systems to statistical learning and deep learning [4]. In recent years, driven by advances in computational power, the emergence of large scale datasets, and breakthroughs in deep learning algorithms, AI has been widely applied in various fields, including image recognition, natural language processing, autonomous driving, medical diagnosis, and financial risk control, demonstrating powerful data processing and pattern recognition capabilities [5]. From a capability perspective, AI can be categorized into three levels: Narrow AI, General AI, and Superintelligence. Current mainstream applications remain at the Narrow AI stage, where machines exhibit superhuman performance in specific tasks, such as convolutional neural networks (CNNs) in image classification and long short term memory (LSTM) networks in time series prediction [6]. Deep learning, as

the core technology driving current AI development, constructs multi-layer nonlinear neural networks that can automatically extract high dimensional features from massive data, overcoming the reliance of traditional methods on manual feature engineering [7].

In the field of seismology, the application of AI is expanding from phase picking and seismic event detection to seismic precursor analysis and prediction. For example, Reynen et al. [8] used machine learning methods to classify seismic waveforms, achieving high precision seismic event detection. Mousavi et al. [9] developed a deep learning based phase picking model that maintains high accuracy even under low signal to noise ratio conditions. These studies demonstrate that AI technology has significant advantages in processing complex, noisy, and nonlinear seismic data. Looking forward, the development of AI exhibits several trends. First, the continuous improvement in model scale and capability, with large models represented by Transformers, will further push the boundaries of general intelligence. Second, the enhancement of multimodal fusion capabilities will enable AI to simultaneously process various data types, including text, images, and signals, achieving more comprehensive environmental perception and understanding. Third, the introduction of physical interpretability and causal inference will gradually transform AI from a "black box" model into a physics aware "grey box" or "white box" model, enabling deeper mechanistic modeling and prediction in geophysics and other scientific fields [10]. Therefore, deeply integrating AI with fracture mechanics and AE physical models to construct an intelligent seismic precursor identification system with physical interpretability holds significant theoretical value and application prospects.

In seismic activity monitoring, multi-system AE monitoring records massive amounts of multi-source noisy data. Manual sequence analysis struggles to extract useful seismic precursor information quickly and efficiently, potentially reducing the timeliness of earthquake prediction. Therefore, leveraging the powerful data processing and pattern recognition capabilities of deep learning to train and analyze rock AE signals and seismic datasets, and to construct an intelligent seismic precursor identification model, holds promise for real-time remote earthquake monitoring. By incorporating large training datasets and algorithm optimization, deep learning models

can automatically analyze and process vast amounts of AE data, uncover hidden seismic precursor features, improve the generalization ability and robustness of the identification model, and achieve efficient recognition of seismic precursor signals. Notably, deep learning models can be applied to real-time data streams after training, continuously monitoring AE signal variations and instantly identifying precursor anomalies, offering the potential for imminent earthquake precursor identification.

Furthermore, the reliability and effectiveness of AE based precursor identification need to be validated by other methods to enhance the credibility of seismic precursor detection. To this end, this study will integrate observation methods of other precursor parameters. In seismic precursor research, electromagnetic emission (EME) is often associated with crustal movement and stress changes. When crustal rocks are subjected to compressive stress and fracture, they release electromagnetic waves. These electromagnetic waves can also serve as seismic precursors, providing cross validation for earthquake precursor identification and revealing the imminent earthquake monitoring and prediction capabilities of different methods.

It should be noted that seismic precursor identification is a complex and challenging topic. By introducing advanced AE technique and deep learning methods, this study will provide a new technical approach for seismic precursor identification. Through the analysis and modeling of large volumes of AE signal data, and by integrating AE and EME precursor observation methods, this study will overcome the limitations of traditional earthquake observation methods, construct a reliable seismic precursor identification model, and achieve imminent earthquake precursor identification. This research integrates knowledge from multiple disciplines, including geophysics, fracture mechanics, statistics, and computer science, to conduct cross disciplinary research. The study will be based on actual field seismic monitoring, and through long-term observation and analysis, validate the practicality and stability of the proposed model. This research provides a methodological and scientific basis for developing reliable earthquake early warning systems, and offers important guidance for disaster prevention and mitigation efforts.

## 1.2 Literature review

### 1.2.1 History and development of earthquake prediction

In the early to mid 20th century, countries such as China, the Soviet Union, and Japan launched their respective national earthquake prediction research programs and compiled seismic distribution and zonation maps. These efforts not only provided a research basis for medium and long-term earthquake prediction but also promoted the development of seismology and geology. Short-term and imminent prediction are considered the most effective methods for mitigating earthquake disasters, yet they also represent the most challenging research directions. Since the 1966 Xingtai earthquake in Hebei Province, China has begun exploring various monitoring methods for seismic precursor anomalies. The goals of earthquake prediction typically include the time, location, and magnitude of an impending earthquake, referred to as the "three elements of earthquake prediction." In long-term prediction, the focus is often on the probability of earthquake occurrence. Although there have been several successful prediction cases in history, accurately predicting the magnitude and occurrence time remains very difficult; therefore, such methods have not yet been widely adopted. In medium term prediction, research on earthquake sequences based on the stress shadow pattern has become quite common. However, due to the difficulty in determining stress distribution patterns, related methods have not yet been practically applied to earthquake forecasting. Short-term and imminent prediction initially employed geophysical and geochemical methods to capture precursor anomalies. Examples include in situ stress observation, borehole strain measurement, and GPS monitoring, all of which attempt to predict the three elements of an earthquake by observing stress changes and strain accumulation combined with numerical simulation.

Although earthquake prediction has a history of nearly a century, research in this field experienced a period of decline following the failure of the Parkfield prediction experiment [11]. Scholars began to recognize that many problems concerning the earthquake preparation process remained unsolved. In recent decades, with the

acquisition of large scale seismic data, various earthquake precursors have been successively identified, including fault tilting, strain, electromagnetic signals, and groundwater anomalies. At the same time, computational techniques such as time series analysis have also advanced, injecting new momentum into earthquake prediction research. Anomalies in neutron emission, radon, and carbon dioxide levels have been identified by multiple studies as common physical phenomena for predicting seismic activity [12,13]. Currently, researchers have discovered various types of precursory anomaly information and are conducting prediction studies based on these precursors. For example, Hashemi et al. [14] proposed an earthquake prediction algorithm based on radon concentration changes to forecast the epicenter location and magnitude. Although this method provides a new approach for gas based prediction, radon concentration is influenced by factors such as climate change and geological conditions, and its generalizability across different regions and environments has not been fully validated. Chien et al. [15] studied the relationship between ground temperature precursor anomalies and the locations of future earthquakes in a specific region of China. However, the study was limited to a single area, and ground temperature variations may be disturbed by seasonal fluctuations and surface activities. Eliminating these interferences remains a challenge. Singh et al. [16] investigated the relationship between hydrogen peroxide concentration in hot spring boreholes within active fault zones and earthquakes. Although changes in hydrogen peroxide concentration may be related to seismic activity, the study had a small sample size and did not fully account for differences among fault types and seismic activities, limiting the generalizability of the results. Li et al. [17] developed a short-term and imminent earthquake prediction technique based on continuous GPS signal anomalies. Although this technique enables real-time monitoring of seismic precursors, GPS signals can be affected by atmospheric conditions and crustal movements. Improving signal accuracy and eliminating interfering factors require further investigation. Yusof et al. [18] attempted to identify key features of earthquake precursors through signal processing and validated the correlation between these features and earthquake attributes, achieving a precursor anomaly recognition rate of 58.8%. Although this study improved recognition accuracy,

the recognition rate still needs significant enhancement, and maintaining high efficiency under complex environmental conditions remains a major challenge.

Despite the numerous prediction methods proposed by the seismological community, existing research still faces common problems due to factors such as instrument instability, limited data volume, and noise interference. These problems include unclear precursor mechanisms (the physical link between anomalies and earthquake occurrence is not well understood), high false alarm rates (due to a lack of quantitative criteria), and difficulties in cross-scale data fusion (scale discrepancies between laboratory and field observations). Consequently, research progress has been slow. To date, understanding of the mechanisms of earthquake preparation and occurrence, as well as the evolution of earthquake disasters, remains very limited.

### 1.2.2 AE and seismic precursor research

Fracture of crustal rocks spans a continuous scale spectrum. Rock AE at the laboratory scale (>1 kHz), microseismicity recorded in the field (10-100 Hz), and earthquakes (<10 Hz) represent manifestations of the same fracture process at different spatial scales and frequency ranges [19]. Research on predicting large earthquakes based on microseismic activity (e.g., *b*-value parameters) has been ongoing for several decades in seismology. "Macro AE" can be regarded as microseismic activity at higher frequencies, with the advantage of potentially being more sensitive to smaller and faster physical changes immediately prior to rock failure.

Advanced rock AE monitoring technology offers new possibilities for seismic precursor identification. Today, AE technique is not only widely used in civil engineering but has also gradually become an important diagnostic tool in geophysics. The earthquake preparation period is typically accompanied by crustal stress changes [20], and an increase in AE activity may reflect the redistribution of crustal stress in the preparation zone [21,22]. However, existing studies have not thoroughly investigated the specific physical mechanisms linking AE activity to crustal stress changes. In

laboratory studies, AE technique has been used to develop earthquake precursor tools [23], but differences between experimental environments and actual earthquake conditions limit the extrapolation of these findings. Lukovenkova et al. [24] identified frequency distribution differences in pre-seismic AE signals compared to background signals during non-seismic periods for the Zhupanov earthquake. Spivak et al. [25] studied AE signals from earthquakes of magnitudes 5.1 to 6.9 in Albania, Greece, Iran, and Turkey, exploring the propagation and perturbation of infrasound signals in the atmosphere and estimating earthquake energy based on signal spectral characteristics. Research over many years on the correlation between AE and seismic activity suggests that AE signals can be considered earthquake precursors. For example, before the Assisi earthquake, a significant increase in the number of AE signals was observed approximately 400 km from the epicenter [26], validating the potential of AE as a precursor identification tool. Using AE technique, Carpinteri et al. [27] studied the correlation between AE in masonry structures and regional earthquakes. Lacidogna et al. [28] proposed a regional earthquake risk assessment method based on AE technique and developed a statistical method for the spatiotemporal correlation between AE and earthquakes. Zimatore et al. [29] studied AE time series obtained from two monitoring stations 300 km apart in Italy and found that AE signals could reflect anomalies in crustal stress trends. Carpinteri et al. [2,3] conducted experimental observations in a gypsum mine in northern Italy and found a strong correlation between AE signals and earthquake sequences occurring in the surrounding area. However, this study was limited to a single mine site and was not extended to other seismically active regions.

The *b*-value and natural time (NT) variance derived from AE time series can serve as characteristic indicators of seismic precursors. In several studies, changes in the *b*-value have been identified as precursor anomalies and are widely recognized as important for quantifying seismic activity and identifying precursors. Sammonds et al. [30] found that the *b*-value exhibits a V-shaped trend before an earthquake, typically increasing in the medium term and then decreasing significantly before the earthquake, with most seismic activity occurring near the minimum *b*-value. Han et al. [31] proposed a robust *b*-value estimation method that, compared to traditional methods,

provides stable and reliable *b*-values and is highly sensitive to large magnitude earthquakes. However, the broad applicability of this method across different regions and earthquake types requires further verification. Recently, NT analysis has been applied in seismic precursor identification research. Varotsos et al. [32] found that when a mainshock occurs, seismic activity in regions within the same tectonic belt enters a critical state, and the NT variance $\kappa_1$ rapidly decreases to zero at the time of the mainshock. Sarlis et al. [33] performed NT analysis on all earthquake sequences with $M \geq 3.5$ in Japan from 1984 to 2011 and found that for earthquakes with $M \geq 7.6$, $\kappa_1$ exhibited a significant minimum before the mainshock. More recently, Sarlis et al. [34] applied NT analysis to the 2023 magnitude 7.8 doublet earthquake sequence in Turkey and found that approximately three and a half months before the earthquake, the fluctuation of the seismic order parameter exhibited a significant minimum; about two weeks before the mainshock, the normalized power spectrum of seismic activity closely matched the theoretical critical spectrum, validating the effectiveness of the NT method in identifying precursors to strong earthquakes. Regarding AE time series research, although some studies have achieved preliminary results, they still lack in-depth investigation of the underlying physical mechanisms and suffer from poor generalizability, requiring further improvement and validation.

**A**lthough AE technique shows considerable potential in seismic precursor identification, it still faces several limitations. First, AE signal data are voluminous and can be contaminated by environmental noise. Effectively distinguishing precursor signals from background noise in massive datasets remains a challenge. Second, insufficient monitoring network coverage may lead to missed potential warning signals, especially in regions with low seismic activity. Furthermore, AE as a precursor identification tool is relatively new and lacks long-term historical data and case studies. Therefore, its reliability and stability in practical applications require further validation, supported by more cross regional and cross geological field data.

### 1.2.3 Electromagnetic emission and seismic precursor research

Observable electromagnetic anomalies often appear before earthquakes [35]. The seismo electromagnetic method plays an important role in observing seismic precursor anomalies and is considered one of the geophysical methods most likely to achieve a breakthrough in short-term and imminent earthquake prediction [36]. However, due to the limited number of seismic events, physical simulations and numerical models have become key components in studying seismo electromagnetic anomalies and their mechanisms.

Researchers in China have also conducted relevant experiments and physical mathematical simulations [37,38], but existing simulation results have not effectively accounted for the influence of complex geological conditions on electromagnetic signals. Rock failure can generate observable electromagnetic signals, and in depth investigation of the characteristics and mechanisms of these signals is crucial for short-term and imminent earthquake prediction. Although scholars worldwide have achieved many results in laboratory experiments, theoretical modeling, and field applications [39,40], significant discrepancies remain between laboratory studies and actual seismo electromagnetic signals due to limitations in experimental conditions, rock sample sizes, and observation frequency bands. Furthermore, systematic reproducibility validation has been lacking for nearly a decade.

In recent years, progress has been made in electromagnetic signal research. For example, Varotsos et al. [41] investigated earthquakes in western Greece from 1983 to 1994 and proposed a correlation between electromagnetic signal characteristics and seismic activity. Hayakawa et al. [42] found that ultra low frequency electromagnetic disturbance signals are important seismic precursors. Before the 2009 L'Aquila earthquake in Italy, electromagnetic anomalies in the kHz and MHz ranges were also recorded [43,44]. Potirakis et al. [45] applied critical analysis to identify ultra low frequency electromagnetic signal anomalies before the 2017 Lesvos earthquake. Despite these important advances, signal identification remains difficult due to attenuation and propagation differences of electromagnetic signals, noise interference

in monitoring data, and environmental effects on instruments. To date, the seismological community has not proposed a mature electromagnetic based method for seismic precursor identification. Further accumulation of experimental and field data, as well as cross regional validation, are essential.

In addition to electromagnetic emission, neutron emission has also attracted attention in seismic precursor research. Neutron emission is typically generated by the de excitation of excited atomic nuclei. Carpinteri et al. [46] conducted mechanical experiments on non radioactive rocks such as granite and basalt and found that mechanical instability can induce high-frequency pressure waves (up to $10^{12}$ Hz), which in turn trigger low-energy fission reactions and produce neutron or alpha particle emissions [47]. Russian scholars Volodichev and Sobolev et al. [48,49] detected neutron flux exceeding background values before earthquakes in the Pamir region, correlated with earthquakes of $M \geq 4$. Sigaeva et al. [50] observed changes in neutron flux in Crimea and other locations several days before the 2004 Sumatra earthquake. Carpinteri et al. [2] further confirmed a significant increase in neutron radiation one week before an earthquake. However, neutron emission research still faces several challenges. These include discrepancies between experimental conditions and natural environments, susceptibility of neutron signals to natural radiation interference, and a lack of long-term field data. The reliability and effectiveness of neutron emission as an earthquake precursor currently require further validation.

### 1.2.4 AI and seismic precursor research

With the rapid development of AI technology, the introduction of deep learning has brought new technical breakthroughs to the field of seismic precursor identification. In recent years, an increasing number of researchers have attempted to use deep learning methods to address seismic precursor identification problems [51]. Although some progress has been made, existing research still faces many challenges and limitations. For example, Maya et al. [52] adopted a time series prediction perspective, using

historical data from the Italian national database and transfer learning to predict earthquake magnitude as well as the relative distance and time between two consecutive seismic events. Berhich et al. [53] used seismic activity data from the Morocco region and applied LSTM networks to predict magnitude, latitude, longitude, and year. Banna et al. [54] collected historical earthquake data from the area surrounding Bangladesh and constructed an LSTM model to predict seismic events within the following month. Jozinović et al. [55] employed CNNs to predict peak ground motion intensity for distant earthquakes and used transfer learning to improve prediction capability in data sparse regions. Kail et al. [56] proposed a hybrid model combining CNN and LSTM to predict the probability of earthquakes exceeding a certain magnitude threshold in a typical seismically active region of Japan. Fuentes et al. [57] developed a CNN LSTM based model to predict the daily average number of seismic events above a given magnitude in central Chile, achieving some predictive success. However, the model still suffers from poor generalizability and insufficient real-time prediction capability. Although these studies have made preliminary progress in seismic precursor identification, they generally overlook the complexity and challenges of real-time data integration. Real-time data processing requires efficient algorithms and substantial computational power. Effectively processing and integrating massive and diverse seismic precursor data remains an urgent problem. Further optimization of data integration methods, enhancement of model adaptability, and improvement of input data quality are key to advancing the application of deep learning in seismic precursor identification.

The introduction of AI technology to earthquake disaster mitigation has demonstrated its strong potential to enhance big data analysis in seismology. If deep learning can be combined with existing seismic precursor data, such as AE and EME, it may reveal underlying patterns within these data. By improving the efficiency and accuracy of short-term seismic precursor identification, deep learning can not only issue early warnings and reduce social losses but also advance the development of seismic precursor identification technology and promote the synergistic evolution of deep learning and seismology.

### 1.2.5 Summary of the current research status

At present, seismic precursor identification, especially for short-term and imminent precursors, remains in the early stages of scientific exploration. Due to the extreme complexity of the physical mechanisms underlying earthquakes and their precursors, which are not yet fully understood, existing research still lacks a representative model that can comprehensively address the problem of seismic precursor identification. On one hand, the seismic data currently accessible to humanity remain limited, constraining the conduct of in depth and systematic research. On the other hand, the high complexity of the earthquake physical process itself makes it difficult for existing models to fully characterize the regularities of earthquake occurrence. Furthermore, the causal relationship between seismic precursors and earthquake occurrence has not yet been clearly established by the academic community. However, with the continuous development of monitoring technologies such as AE and EME, as well as deep learning algorithms, research on seismic precursor identification is encountering new opportunities and is expected to respond to the urgent public demand for accurate earthquake prediction.

It should be pointed out that understanding seismic precursors must be built upon a cross-scale unified framework of fracture mechanics, linking microscopic material damage to large scale seismic events. In this process, AE technique has significant potential as a key link connecting different scales and identifying precursor events. However, comprehensive studies that systematically integrate theoretical analysis, laboratory experiments, and field measurements are still lacking. Currently, the application of AE technique to field seismic monitoring remains in an exploratory stage. As a precursor identification tool, it still lacks long-term historical data and case study support, and its reliability in practical applications requires further validation through more cross regional field observation data.

Rock can more directly reflect stress changes in the deep crust, is sensitive to microseismic activity, and exhibits slower signal attenuation for stress waves propagating through it. By monitoring AE signals in rock, more accurate seismic precursor information can be captured with reduced noise interference. Existing research faces problems such as background noise interference, difficulty in identifying precursor signals, high false alarm rates, and challenges in integrating real-time data. There is an urgent need to develop accurate and efficient methods for seismic precursor identification.

## 1.3 Research content and technical roadmap

This research integrates a novel signal processing method (MCF-B), laboratory fracture monitoring tests on concrete structures, field measurement of rock AE, and deep learning based intelligent identification technology. It establishes a cross-scale, multimodal precursor identification system spanning from microscopic material fracture to macroscopic seismic events, and systematically investigates methods for seismic precursor identification. The aim is to improve the reliability and timeliness of seismic precursor identification and to advance the transition from empirical methods to real time, intelligent, physics based precursor identification.

Based on the above research objectives, the main research contents of this thesis are organized as follows:

Chapter 1 is the introduction. This chapter systematically elaborates the background and significance of seismic precursor identification, reviews the current applications of AE technique, electromagnetic emission, and AI in seismic precursor identification, identifies the limitations of existing research, and clarifies the research content and technical roadmap of this thesis.

Chapter 2 presents fracture mechanics and the MCF-B signal analysis theory for AE. Starting from fracture mechanics theory, this chapter introduces AE signal processing and analysis methods, with a focus on the theoretical basis of the novel

MCF-B method and its potential for cross-scale application in material fracture and earthquake faulting, thereby laying the theoretical foundation for subsequent research.

Chapter 3 elaborates on the application of fracture monitoring in concrete structures and the validation of the MCF-B method. Through multiple AE monitoring tests on concrete specimens and structural components, this chapter systematically analyzes the evolution of AE signals under different sizes, materials, and loading conditions, and validates the precursor identification capability of the MCF-B method at the laboratory scale. The study further reveals the fractal scaling law of energy emission, the crack mode transition mechanism, and the robustness and superiority of the MCF-B method over the traditional *b*-value method in critical precursor identification.

Chapter 4 presents seismic precursor identification research based on field measurement of rock AE. Relying on monitoring stations located in a mountain tunnel in eastern Guangdong, rock AE and earthquake catalog data were synchronously collected. The correlation between AE activity and regional seismicity is analyzed, and multi-precursor cross validation is performed by incorporating electromagnetic emission (EME) signals. The MCF-B method is applied to field AE data to explore the anomalous evolution characteristics of its parameters before actual earthquakes.

Chapter 5 conducts research on intelligent identification of AE-based seismic precursors using deep learning. A deep learning based AE precursor identification model is constructed. Field monitoring data are used to train and optimize the network structure to achieve real-time identification and early warning of seismic events. The model is compared with traditional methods to demonstrate its advantages in high dimensional feature extraction and generalization capability. Furthermore, MCF-B parameters and NT variance are introduced as higher order physical features to construct a physics-data hybrid driven model, which significantly improves early warning accuracy and timeliness.

Chapter 6 presents the conclusions and future work. The research findings are summarized, the effectiveness and applicability of the proposed method in cross-scale precursor identification are clarified, research limitations are identified, and suggestions for future research and engineering applications are provided.

Figure 1.5 shows the technical roadmap of this thesis. Starting from theoretical and improved methods, this research adopts a dual validation approach through "laboratory experiments and field measurements" to progressively enhance the reliability of the methods. Finally, AI technology is integrated to form a complete methodology for seismic precursor identification that integrates AE physical models and multi-source data, spanning from microfracture activity to macroscopic earthquakes.

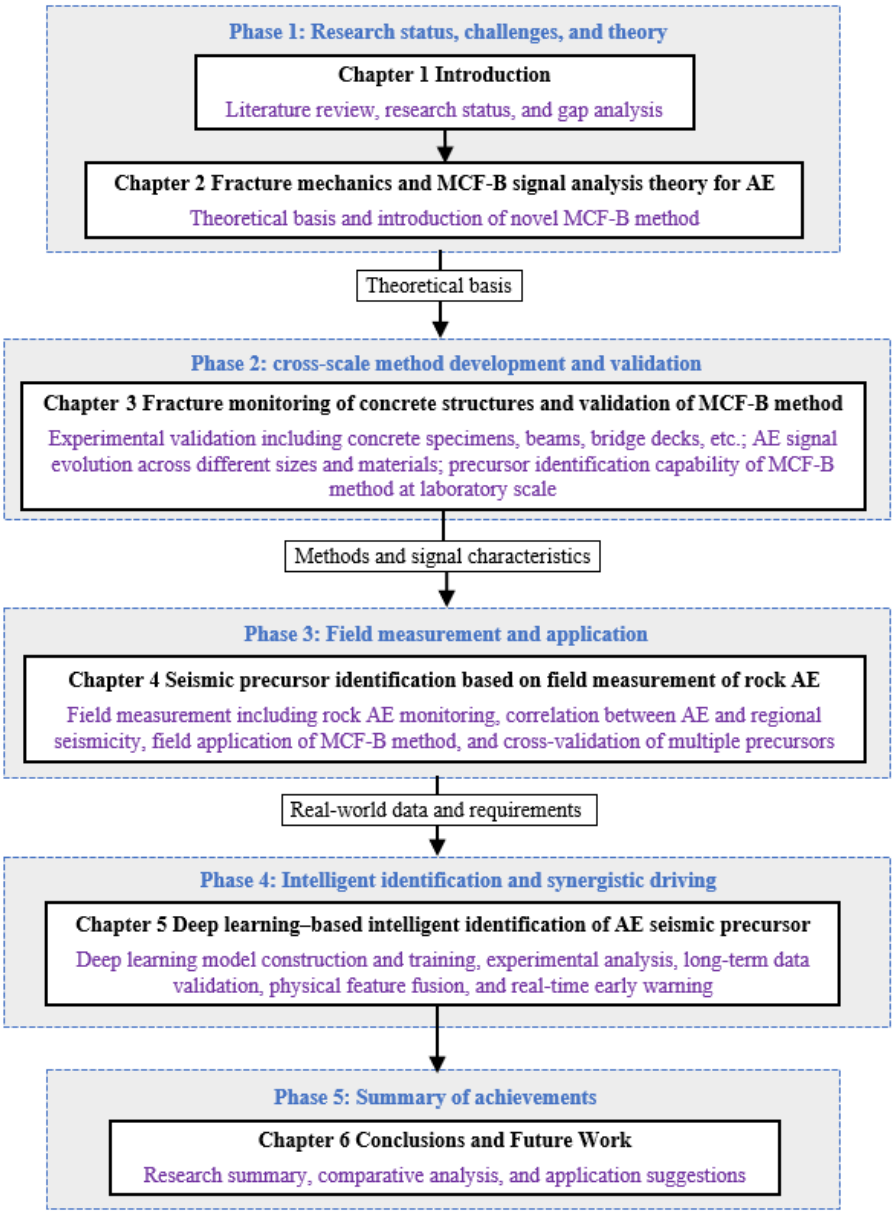


**Figure 1.5** Schematic diagram of the technical approach.

# Chapter 2

# 2 Fracture mechanics and MCF-B signal analysis theory for AE

## 2.1 Introduction

An earthquake is a natural phenomenon characterized by sudden unstable fracture of crustal rocks under long-term tectonic stress. Its physical essence shares profound mechanical homology with the macroscopic fracture of materials [58]. Traditional seismology, based on the elastic rebound theory and continuum mechanics, has successfully described the generation and propagation of macroscopic seismic waves. However, a unified physical model for quantitatively characterizing the micro and meso scale mechanisms controlling rupture initiation and nucleation, particularly the microfracturing activity with precursor significance during earthquake preparation, is still lacking.

Fracture mechanics provides a universal theoretical framework for understanding this complex process. By introducing the "crack" as the core research object, this theory links the macroscopic mechanical properties of materials to the evolution of their internal defects. Consequently, it can reasonably describe the energy transformation and stress redistribution throughout the entire process from microcrack initiation and propagation to macroscopic unstable failure of materials. From this theoretical perspective, faults in the Earth's crust can be viewed as macroscopic cracks, while the surrounding microcrack clustering and nucleation zone evolution correspond to damage accumulation and localization within the crack tip process zone.

AE technique, as a key means of detecting transient stress waves released by internal microfracturing in materials, provides indispensable data support for studying fracture physics at the laboratory scale and linking it to field observations. AE events are the direct physical responses of microfracturing activity, and their characteristic parameters, such as waveform, energy, and frequency, carry rich information about the fracture source mechanism.

This chapter aims to construct a systematic theoretical system that bridges fracture physics and seismic precursor signals. First, the fundamental theories of fracture mechanics are systematically elaborated to establish a mechanical description of crack behavior. Subsequently, AE theory and the novel MCF-B signal analysis technique are introduced to build a bridge from fracture physics to observed signals, thereby establishing the theoretical foundation for the research paradigm of this thesis, which is "integrating AE physical models with multi-source data."

## 2.2 Fundamental theory of fracture mechanics

Fracture mechanics is the science that studies the initiation and propagation of cracks in solid materials containing defects. It provides a solid foundation for understanding the failure mechanisms of quasi brittle materials such as rock. Unlike traditional strength theory, which focuses only on the stress level within a continuum, fracture mechanics introduces crack size as a key variable and reveals that macroscopic fracture originates from the evolution and coalescence of microscopic defects. This section elaborates the basic framework of fracture mechanics, discusses the connection between brittle fracture and damage mechanics, and analyzes the inherent cross-scale characteristics of the fracture process, thereby building a theoretical bridge linking AE signals to the physical process of rock fracture.

### 2.2.1 Linear elastic fracture mechanics

Linear Elastic Fracture Mechanics (LEFM) is the most fundamental and mature branch of fracture mechanics. It assumes that the material fully obeys Hooke's law (i.e., stress is proportional to strain) before crack propagation, and that the size of the plastic zone at the crack tip is much smaller than the crack length and other characteristic geometric dimensions (small scale yielding condition). Its core concept is that the fracture behavior of a cracked component can be characterized by a single parameter, such as the stress intensity factor or the energy release rate. The LEFM theoretical system mainly consists of the interrelated energy criterion and stress field theory.

From an energy perspective, Griffith [59] pioneered the energy criterion for unstable crack propagation. This criterion states that for an infinite thin plate containing a center crack of length 2a subjected to remote uniform tension, the system reaches a critical state when the elastic strain energy released by crack propagation, $\frac{dW_e}{da}$, is greater than or equal to the surface energy required to form the new crack surface, $\frac{dW_s}{da}$. The critical condition can be expressed as:

$$\sigma = \sqrt{\frac{2\gamma E}{\pi a}} \tag{2.1}$$

where σ is the remote tensile stress, $\gamma$ is the surface energy density of the material, and E is the elastic modulus. Irwin [60] subsequently generalized the concept of energy release rate to the strain energy release rate $G_{\mathrm{I}}$ and defined $G_{\mathrm{IC}}$ as the critical strain energy release rate, which represents the material's resistance to brittle fracture propagation. When the applied strain energy release rate reaches the critical value of the material, the crack propagates unstably. Accordingly, the Griffith criterion can be universally expressed as:

$$G_I \geq G_{IC} \tag{2.2}$$

From the perspective of stress field, analytical analysis of the crack tip stress field reveals that each stress component exhibits an $r^{-1/2}$ singularity in the vicinity of the crack tip, where r is the distance from the crack tip. Taking the Mode I (opening mode) crack as an example, its crack tip stress field can be expressed as:

$$\sigma_{ij}^{(I)}(r,\theta) = \frac{K_I}{\sqrt{2\pi r}} f_{ij}^{(I)}(\theta) + \cdots \tag{2.3}$$

where $f_{ij}^{(I)}(\theta)$ is a known function characterizing the angular distribution of stresses. The dominant term, $K_I$, is the stress intensity factor. $K_I$ is a function of the far field load, crack geometry, and dimensions. For an infinite plate containing a center crack of length 2a, $K_I = \sigma\sqrt{\pi a}$. The corresponding fracture criterion is:

$$K_I \geq K_{IC} \tag{2.4}$$

where $K_{IC}$ is the plane strain fracture toughness of the material, another material constant. The energy criterion and the stress criterion are unified through the following relationship:

$$K_{IC}^2 = E' G_{IC} \tag{2.5}$$

where $E' = E$ (for plane stress) or $E' = E / (1-\nu^2)$ (for plane strain), and $\nu$ is Poisson's ratio. This relationship profoundly reveals the intrinsic connection between macroscopic fracture toughness and energy dissipation during the microfracturing process.

## 2.2.2 Brittle fracture and damage mechanics

Although LEFM has achieved great success, the stress singularity at the crack tip it predicts does not exist in real materials. In actual materials, especially quasi brittle

materials such as rock and concrete, a process zone forms near the crack tip, within which the material undergoes nonlinear deformation and damage due to microcrack nucleation and coalescence.

To describe this physical process, Irwin introduced a plastic correction to LEFM and proposed a first order estimate of the plastic zone size $r_p$:

$$r_p \approx \frac{1}{2\pi}\left(\frac{K_I}{\sigma_y}\right)^2 \tag{2.6}$$

where $\sigma_y$ is the yield strength of the material. This equation indicates that the ratio $K_I/\sigma_y$ is a key parameter for measuring the size of the nonlinear region at the crack tip. The existence of the plastic zone consumes additional energy and is the microscopic source of macroscopic material toughness.

To more universally describe the progressive degradation of materials under load, damage mechanics has been introduced. It continuously characterizes the degradation of material stiffness and strength by introducing internal variables, such as the damage variable $D$. From the perspective of damage mechanics, the formation of a macroscopic crack is the result of the localization of distributed damage. In this process, the initiation and propagation of each microcrack constitute a microscopic damage event and also serve as a source event for an AE signal.

For quasi brittle materials, the cohesive crack model provides a theoretical framework linking microscopic damage to macroscopic fracture [61]. This model assumes the existence of a process zone ahead of the macroscopic crack tip, where the material is not completely separated but is connected by cohesive stress $\sigma$ that decays with increasing crack opening displacement $w$. The relationship $\sigma = f(w)$ is called the cohesive law, which is a constitutive relationship of the material defining its softening behavior and fracture energy $G_f = \int_0^{w_c} \sigma(w)dw$. This model physically describes the existence of the fracture process zone, which is precisely the region where AE activity is most intense during rock fracture.

### 2.2.3 Cross-scale characteristics of the fracture process

Rock fracture is an evolutionary process spanning the micro, meso, and macro scales. The preparation of an earthquake is the ultimate manifestation of this cross-scale damage evolution.

Fracture mechanics itself inherently exhibits a strong size effect. The Griffith criterion $\sigma_c \propto 1/\sqrt{a}$ indicates that the nominal strength of a structure decreases as the size of the initial defect increases. This characteristic can be quantified by the brittleness number $S$:

$$S = \frac{K_{IC}}{\sigma_y \sqrt{L}} \tag{2.7}$$

where $L$ is the characteristic dimension of the structure. The smaller the $S$ value, the more brittle the structural behavior. This explains why large rock masses (with large $L$) are more prone to sudden unstable fracture when subjected to stress. By analogy, at the crustal scale, the brittleness number of large-scale rock masses is extremely small. Once the elastic strain energy accumulated under tectonic stress reaches a critical value, it is released suddenly and violently in the form of an earthquake. Therefore, from the perspective of the size effect in fracture mechanics, an earthquake can be regarded as a "sudden unstable fracture" phenomenon at the crustal scale.

The cross-scale evolution of fracture follows certain regularities. At the microscopic scale, stress concentration leads to mineral grain boundary sliding and microcrack initiation. This stage corresponds to low-energy, high-frequency AE signals. At the meso scale, microcracks interact and coalesce into dominant cracks. The amplitude and energy of AE signals increase significantly, and the $b$-value may decrease. At the macro scale, the dominant crack propagates unstably, penetrating through to form the main fault and releasing enormous energy. Fracture mechanics, particularly meso scale damage mechanics combined with statistical methods, provides quantitative tools for describing the correlation and evolution of damage events across these different scales. The macroscopic fracture toughness $K_{IC}$ and fracture energy $G_f$

are essentially the macroscopic manifestations of all micro and meso scale energy dissipation mechanisms. Therefore, by monitoring physical signals such as AE that reflect cross-scale damage evolution, it is possible to observe the critical process of rock transitioning from stable damage accumulation to unstable fracture.

## 2.3 AE monitoring technology

AE is a phenomenon in which transient stress waves are generated due to the rapid release of local internal strain energy during deformation, crack initiation, and crack propagation in materials or structures [62,63]. As a passive and dynamic non destructive testing technique, the core of AE monitoring lies in capturing and analyzing these stress wave signals directly excited by damage events, thereby achieving real time, online assessment of the internal damage evolution process in materials [64,65]. Its physical essence is highly similar to the process of seismic wave generation from crustal rupture in seismology, as both involve energy radiation caused by local instability in an elastic medium. This similarity not only enables the widespread application of AE technique in materials science and structural engineering [66,67] but also makes it an important tool for studying the physical mechanisms of crustal rupture and exploring earthquake precursors [2, 3, 68].

### 2.3.1 Generation and propagation mechanisms of AE signals

The generation of AE signals originates from the rapid dynamic adjustment of the stress field at microscopic or macroscopic defects within a material. For quasi-brittle heterogeneous materials such as concrete and rock, pre existing microscopic weak regions such as microcracks, pores, and interfaces become stress concentration points under external loading. As shown in Fig. 2.1, a microfracture event typically consists of three consecutive physical processes:

a) At the weakest point where stress concentration is most significant, atomic or molecular bonds break, leading to microcrack nucleation. This corresponds to initial instability at the microscopic scale.

b) Once nucleated, the microcrack begins to open, and the stress field ahead of its tip undergoes a drastic redistribution. The load carried by the failed bonds is suddenly released, and this stress is instantaneously redistributed to the surrounding material matrix through propagating stress waves. This process is a key step in converting elastic strain energy into wave energy.

c) When the stress redistribution reaches a new local mechanical equilibrium, crack propagation stops. At this point, a complete AE source event is completed.

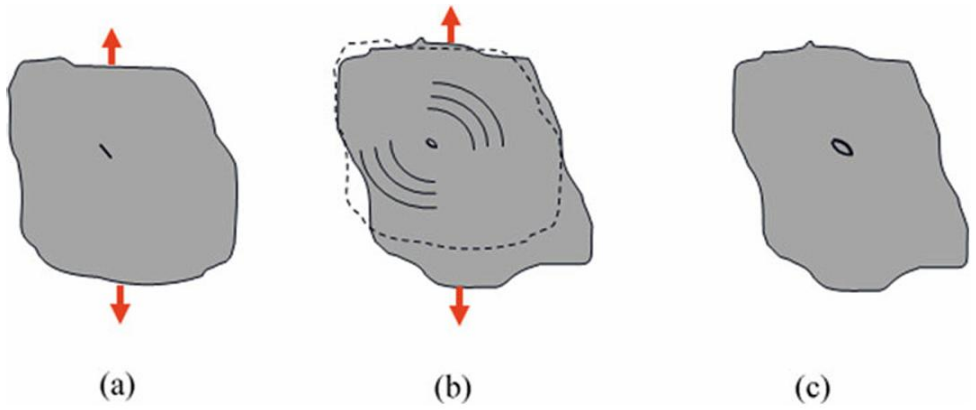


**Figure 2.1** Schematic diagram of the three stages of AE generation during microcrack formation: (a) Stage I; (b) Stage II; (c) Stage III.

From the perspective of energy conservation, the formation of microcracks causes a portion of the elastic strain energy stored within the material to be emitted in the form of stress waves, which is known as AE energy. These stress waves propagate within the material in multiple modes, including longitudinal waves (P waves, or compressional waves), where the particle vibration direction is parallel to the wave propagation direction; transverse waves (S waves, or shear waves), where the particle vibration direction is perpendicular to the wave propagation direction; and Rayleigh waves (surface waves), which propagate along the material surface, as shown in Fig. 2.2. P waves have the fastest velocity, followed by S waves, while Rayleigh waves are the

slowest but often exhibit the largest amplitude. These differences in velocity and amplitude arise from the distinct physical mechanisms of the wave propagation modes. P waves involve volume compression and expansion of the medium; the medium has a strong resistance to volume deformation, resulting in the fastest propagation velocity. S waves involve shear deformation of the medium; the medium typically has a weaker resistance to shear deformation than to volume deformation, resulting in a slower velocity. Rayleigh waves propagate along the medium surface, with energy confined to a near surface two dimensional plane. Their geometric attenuation ($\propto 1/\sqrt{r}$) is much slower than the three dimensional attenuation of body waves ($\propto 1/r$). Additionally, they tend to form elliptical particle trajectories near the surface (see Fig. 2.2), leading to the largest amplitude and slowest attenuation.

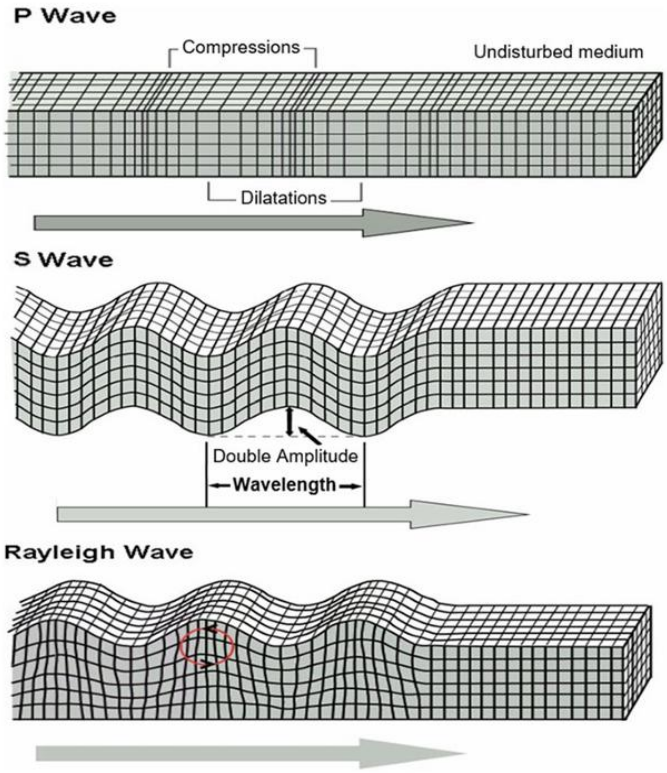


**Figure 2.2** Wave propagation modes of AE in an elastic medium.

During propagation, AE waves are attenuated and distorted by factors such as material heterogeneity, internal friction, scattering, and geometric spreading. For heterogeneous materials like concrete, the attenuation characteristics can be approximately described by Eq. (2.8):

$$A(f) = e^{-\frac{\pi f r}{vQ}} \tag{2.8}$$

where $A$(f) is the amplitude of the frequency component $f$, $r$ is the propagation distance, $v$ is the wave velocity, and $Q$ is a parameter representing the attenuation characteristics of the material. For example, for ordinary concrete ($Q \approx 100$, $v \approx 4000$ m/s), the amplitude of a 100 kHz AE component will attenuate to about half after propagating 1 m [62]. This strong attenuation characteristic dictates that in practical monitoring, sensor placement must be optimized according to material properties and the frequency range of the monitoring target to ensure effective signal detection.

### 2.3.2 Typical AE waveform signals

The voltage time signal received by a sensor is jointly influenced by the AE source signal, propagation path effects, and the frequency response of the sensor. AE data analysis mainly employs a parameter based analysis method. The core of this method is that upon detection of an AE signal, a set of characteristic parameters is extracted and stored in real time, while the raw complete waveform data are discarded. These parameters are sufficient to describe the basic statistical characteristics of damage activity in most cases. A typical AE signal waveform and the definitions of its key parameters are shown in Fig. 2.3 [69].

Commonly used core parameters include (see Fig. 2.3):

1）Threshold voltage: a preset threshold used to discriminate between valid signals and background noise;

2）Event count: the entire cluster of signal oscillations associated with a single independent damage source (e.g., a single microcrack event) is counted as one event, reflecting the frequency of damage events.

3）Ringing count: the number of times the oscillation amplitude of a single AE event exceeds the preset threshold.

4）Arrival time: the moment when the signal first exceeds the threshold, serving as key information for source localization.

5）Amplitude: the maximum peak voltage of the signal waveform, which is a direct measure of event intensity.

6）Duration: the time interval between the first and last threshold crossings of the signal.

7）Rise time: the time from the first threshold crossing to the attainment of the maximum signal amplitude.

8）Energy: the area under the signal envelope, which is related to the elastic strain energy released by the event.

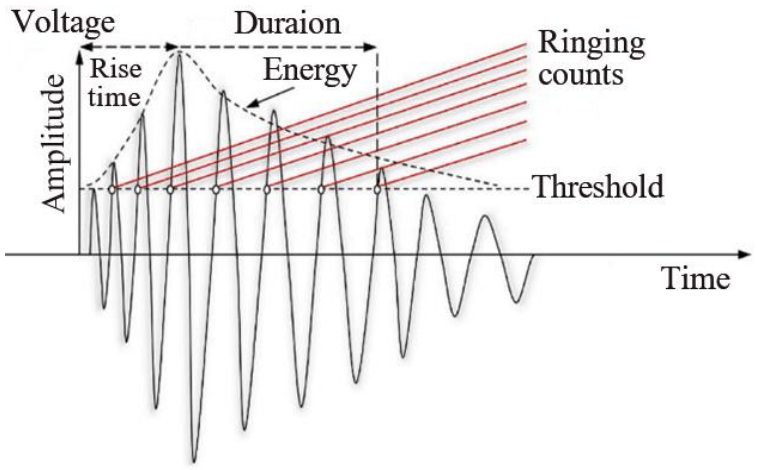


**Figure 2.3** Example of typical AE waveform parameters.

By analyzing the trends of these parameters over time or with increasing load, the activity level, accumulation, and evolution stage of damage can be assessed. For example, during the linear stage of a load-displacement curve, AE activity is typically low. As the peak load is approached, the event rate, cumulative event count, and energy often exhibit an accelerating growth trend, signaling the approach of macroscopic fracture instability.

### 2.3.3 Crack mode identification and RA-AF analysis

To gain a deeper understanding of the physical mechanisms of damage, the morphology of AE signals needs to be analyzed to identify crack modes. The morphological characteristics of AE waveforms are closely related to their generation mechanisms (crack modes) [70, 71].

The Average Frequency (AF) is defined as the ratio of the ringing count of an AE event to its duration (see Eq. 2.9), expressed in kHz. It reflects the dominant frequency component of the signal. The Rise Angle (RA) is the ratio of the rise time (RT) to the amplitude (A) (Eq. 2.10), expressed in ms/V.

$$AF = \frac{RC(Ringing\ Count)}{DT(Duration\ Time)} \tag{2.9}$$

$$RA = \frac{RT(Rise\ Time)}{A_{\max}\ (Amplitude)} \tag{2.10}$$

As shown in Fig. 2.4(a), during tensile (Mode I) crack opening, energy release is relatively concentrated, resulting in a high proportion of P wave components. Due to the fast propagation of P waves, the signal exhibits a short RT and a small RA. Conversely, during shear (Mode II) crack sliding, the radiation efficiency of S waves is higher, causing a slight delay in the arrival of the main signal energy, which results in a longer RT and a larger RA. Therefore, waveform parameters, especially RA and AF values, can serve as empirical criteria for distinguishing crack modes [72]. According to the RILEM recommendation, tensile cracks are characterized by high AF values and low RA values, while shear cracks are characterized by relatively low AF values and high RA values [73], as illustrated in Fig. 2.4(b).

By plotting a scatter plot of RA versus AF for all AE events, an empirical threshold can be set based on the clustering pattern of the data to classify events as predominantly tensile or predominantly shear. This method can evaluate specific types of damage, such as bond-slip between steel reinforcement and concrete in reinforced concrete structures,

sliding mechanisms of faults in rock, and fiber debonding in composite materials [74, 75].

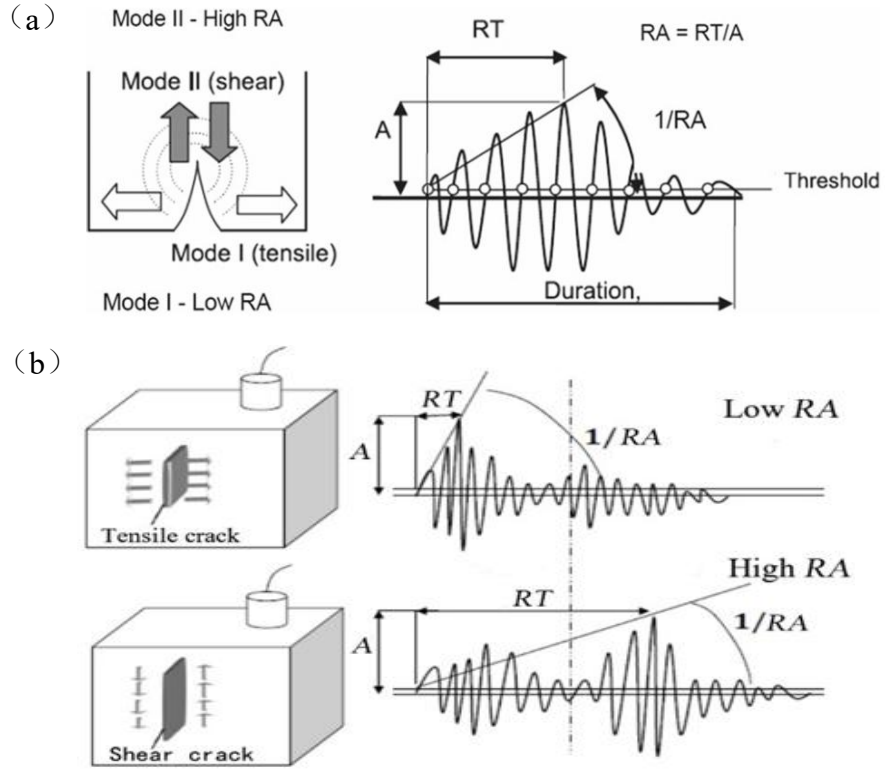


**Figure 2.4** Crack modes and typical AE signals: (a) AE signal waveform parameters; (b) crack types and waveform characteristics.

## 2.3.4 AE source localization

AE source localization is a core technique for determining the spatial location of damage. Its mathematical model originates from source localization methods in seismology. The basic assumptions are that the material is a homogeneous, isotropic elastic medium with constant wave velocity and that waves propagate in straight lines.

Based on the above assumptions, in a one dimensional case (such as a beam or rod), if an AE source S is located between two sensors $S_1$ and $S_2$ (Fig. 2.5), its coordinate x can be accurately determined by Eq. (2.11):

$$x = \frac{1}{2}(x_2 + x_1) - \frac{1}{2}v(t_2 - t_1) \tag{2.11}$$

where $x_1$ and $x_2$ are the sensor coordinates, $t_1$ and $t_2$ are the signal arrival times, and $v$ is the wave velocity. If the source is located outside the sensor array, additional information (such as the emission time) is required to uniquely determine its position.

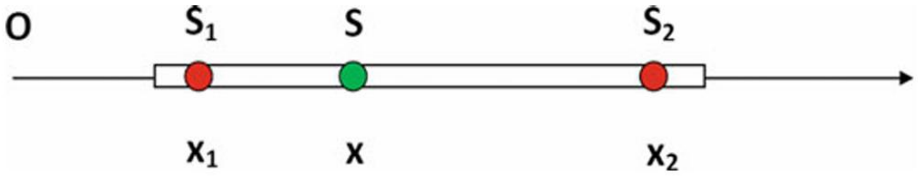


**Figure 2.5** One-dimensional AE source localization ($S_i$: AE sensor; S: AE source).

In two dimensional localization, a minimum of three sensors is required. Determining a point requires two coordinates, and each sensor pair provides an equation based on the difference in arrival times. As shown in Fig. 2.6, for sensor pair $S_1$ and $S_2$, the time difference $\Delta t_{21} = t_2 - t_1$ defines the locus of points where the difference in distances to the two points is constant, which is a hyperbola with foci at $S_1$ and $S_2$. Similarly, sensor pair $S_1$ and $S_3$ defines another hyperbola. The intersection of the two hyperbolas is the potential AE source location. Its mathematical expression involves solving a system of nonlinear equations, as shown in Equations (2.12) and (2.13).

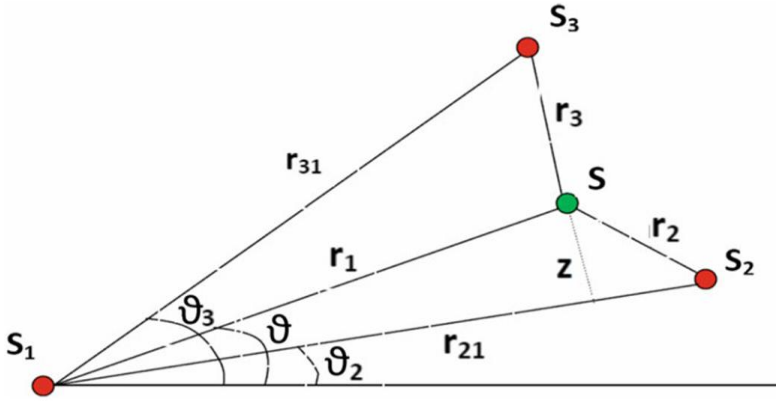


**Figure 2.6** Two-dimensional AE source localization (polar coordinates).

$$r_1 = \frac{r_{21}^2 - \Delta t_{21}^2 v^2}{2(\Delta t_{21} v + r_{21} \cos(\vartheta - \vartheta_2))} \tag{2.12}$$

$$r_1 = \frac{r_{31}^2 - \Delta t_{31}^2 v^2}{2(\Delta t_{31} v + r_{31} \cos(\vartheta_3 - \vartheta))} \tag{2.13}$$

For more general three dimensional localization, at least four non coplanar sensors are required. Assuming an AE signal occurs at point S at time $t_0$ and is received by four sensors ($\Delta t_i = t_i - t_0$), a system of linear equations, as shown in Eq. (2.14), can be formulated and solved to simultaneously invert for the spatial coordinates ($x, y, z$) of the source and the emission time $t_0$. The coefficient matrix of this system is composed of the sensor coordinates and the differences in arrival times.

$$\begin{bmatrix} 2(x_2-x_1)2(y_2-y_1)2v^2(t_2-t_1) \\ 2(x_3-x_1)2(y_3-y_1)2v^2(t_3-t_1) \\ 2(x_4-x_1)2(y_4-y_1)2v^2(t_4-t_1) \end{bmatrix} \begin{bmatrix} x \\ y \\ \Delta t_1 \end{bmatrix} = \begin{bmatrix} (x_2^2+y_2^2)-(x_1^2+y_1^2)-v^2(t_2-t_1)^2 \\ (x_3^2+y_3^2)-(x_1^2+y_1^2)-v^2(t_3-t_1)^2 \\ (x_4^2+y_4^2)-(x_1^2+y_1^2)-v^2(t_4-t_1)^2 \end{bmatrix} \quad (2.14)$$

However, the heterogeneity and anisotropy of actual materials, especially concrete and rock, make the assumptions of constant wave velocity and straight line propagation overly idealized. As shown in Fig. 2.7, the actual wave propagation path $\Gamma_i$ may be curved, and the wave velocity $v(\vec{r})$ is a function of spatial position. This leads to discrepancies between the theoretical travel time $r_i/v$ calculated using a homogeneous model and the actual travel time $\int_{\Gamma_i} ds/v(\vec{r})$ (Eq. 2.15), thereby introducing localization errors $m_i$. To improve accuracy, the least squares method can be used for optimization, or correction parameters characterizing the degree of material heterogeneity can be introduced [76].

$$\Delta t_i = t_i - t_0 = \int_{\Gamma_i} \frac{\mathrm{d}s}{v(\vec{r})} + m_i = \frac{r_i}{v} \quad (2.15)$$

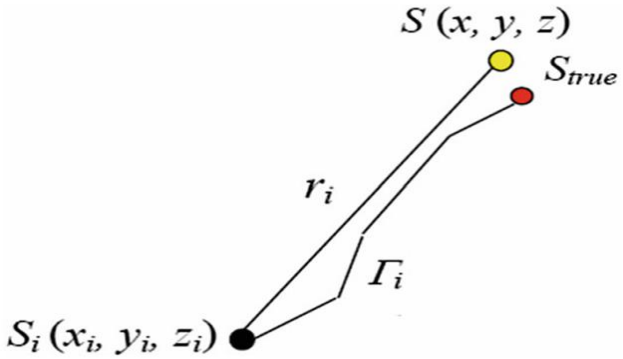


**Figure 2.7** AE wave propagation path model.

### 2.3.5 Damage domain and fractal energy density

Numerous experimental observations have shown that during the failure process of quasi brittle materials, the distribution and evolution of microcracks and the associated AE activity exhibit significant scale invariance and fractal characteristics [77].

According to fractal fragmentation theory, the energy $E$ emitted by microcrack propagation is not uniformly distributed throughout the entire specimen volume V, but is instead confined to a damage domain with a fractal dimension $D$ ($2 < D < 3$) [77]. This leads to a scaling law for energy emission:

$$E \propto V^{D/3} \tag{2.16}$$

This equation indicates that the emitted energy increases more slowly with specimen size than the volume does (if $D < 3$). The traditional energy density $\Psi = E/V$ exhibits a size effect, satisfying $\Psi \propto V^{(D-3)/3}$, and is therefore not a material constant.

To eliminate the size effect, a fractal energy density with a non integer physical dimension is introduced [78]:

$$\Gamma = \frac{E}{V^{D/3}} \tag{2.17}$$

$\Gamma$ is a parameter independent of specimen size and characterizes the inherent damage energy emission property of the material.

Since the cumulative number of AE events $N$ is proportional to the emitted energy $E$ ($E \propto N$), the above scaling law can be directly applied to AE data [78]:

$$N \propto V^{D/3} \tag{2.18}$$

Therefore, the fractal density of AE events can be defined as:

$$\Gamma_{AE} = \frac{N}{V^{D/3}} \tag{2.19}$$

$\Gamma_{AE}$ is another size independent damage indicator. Experimental validation was conducted through uniaxial compression tests on concrete and rock cylinders of different sizes. For the tested concrete and rock, the fractal dimensions D were approximately 2.29 and 2.33, respectively, values that lie between 2 (two dimensional plane) and 3 (three dimensional volume) [79, 80]. This confirms that damage evolution occurs within a fractal domain, and that the fractal energy density or fractal AE density is a reliable and size independent physical quantity for assessing the damage state of materials.

## 2.4 AE signal processing and analysis methods

### 2.4.1 Amplitude-frequency statistics and *b*-value

Inspired by the Gutenberg-Richter law describing the magnitude frequency distribution of earthquakes in seismology, AE research has introduced a completely analogous analytical framework to characterize the statistical distribution of AE amplitudes. The original form of the G-R law is [81]:

$$\log_{10} N(\geq M) = a - bM \tag{2.20}$$

where $N$ is the cumulative number of earthquakes with magnitude not less than $M$, a is a constant, and the $b$-value is a key parameter describing the magnitude distribution of earthquakes. Studies have found that the G-R law is equivalent to a power law relationship between the number of earthquakes $N$ and the rupture area $A$ [82]:

$$N(\geq A) \propto A^{-b} \tag{2.21}$$

where $A \propto L^2$, and $L$ is the characteristic rupture length. This indicates that the $b$-value also describes the power law distribution characteristics of rupture scales. When $b \approx 1$, for every tenfold decrease in rupture area, the number of earthquakes increases approximately tenfold. Extensive observations over the past 50 years have shown that $b$-values are generally close to 0.9 and are often approximately taken as 1 [83], implying that seismic activity exhibits significant scale invariance.

The G-R law can be extended and applied to the statistical analysis of AE signals. By analogy, in Eq. (2.20), $M = log_{10}A$ is the logarithm of the AE event amplitude (analogous to magnitude $M$). $N$ is the cumulative number of AE events with amplitude exceeding $A$, and a and $b$ are positive coefficients determined by statistical analysis of the collected AE data. The parameter $b$ is commonly referred to as the $b$-value of AE signals. It represents the negative slope of the linear portion of the G-R law and is obtained by least squares fitting. The calculation process is illustrated in Fig. 2.8 [84]. The amplitude of each signal is collected and organized into a histogram. Subsequently, a log-log plot is constructed to display the cumulative number $N$ of signals with amplitude exceeding $A$. Accordingly, the $b$-value is the slope of the fitted straight line connecting the signal amplitudes and the cumulative event numbers. As shown in Fig. 2.9, experimental tests and numerical results have shown that the $b$-value gradually decreases as a structure approaches failure [85].

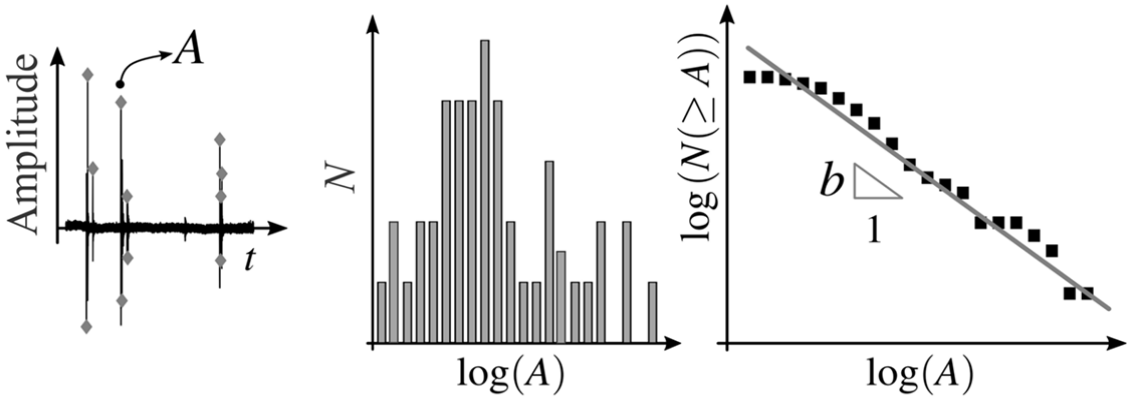


**Figure 2.8** Schematic diagram of $b$-value calculation for AE.

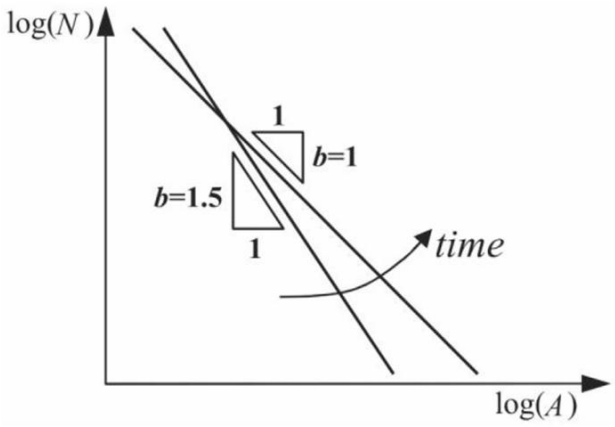


**Figure 2.9** Evolution of *b*-value obtained from experimental fitting.

The power law distribution reflected by the *b*-value is consistent in form with other scaling laws in fracture mechanics, such as the variation of material strength and fracture energy with structural size [86]:

$$\sigma_{\mathrm{u}}(h) \propto h^{-d_\sigma}, \quad G_{\mathrm{f}}(h) \propto h^{d_G} \tag{2.22}$$

Eq. (2.22) reveals the size effect on the strength and fracture energy of quasi brittle materials: as the characteristic structural dimension h increases, the nominal strength $\sigma_{\mathrm{u}}$ decays as a power law, while the fracture energy $G_f$ increases as a power law. This phenomenon originates from the cross-scale characteristics of the damage evolution process, namely that microcrack distribution and energy emission are not uniformly distributed throughout the entire volume but are instead confined to a damage domain with a fractal dimension between 2 and 3. The fractal scaling exponents $d\sigma$ and $dG$ are quantitative descriptions of this fractal behavior and are closely related to the microstructural characteristics of the material.

These relationships collectively reveal the similarity of the fracture process across different scales. The *b*-value, as a statistical scaling exponent, serves as an important bridge connecting earthquake rupture and microscopic fracture behavior of materials.

### 2.4.2 Temporal scaling law and $\beta_t$ analysis

AE monitoring not only captures the spatial distribution and evolution of damage (fractal dimension $D$ and $b$-value) but also characterizes the dynamic behavior of damage in the temporal domain. To quantify the temporal evolution characteristics of the damage process, particularly its accelerating or decelerating trends, researchers have introduced a temporal scaling law based on a power law relationship and the corresponding temporal scaling exponent $\beta_t$ analysis [80]. This method analyzes the evolution of cumulative AE event counts over time, providing a quantitative tool for assessing the stability of structures under constant or varying loads, predicting their remaining lifespan, and understanding earthquake like "foreshock-mainshock-aftershock" sequences.

Inspired by Omori's law [81] (describing aftershock decay) in seismology and power law acceleration phenomena in damage mechanics, the cumulative released energy $W$ (proportional to the cumulative number of AE events $N$) during damage evolution of materials or structures under loading follows a power law relationship with time $t$ [87, 88]:

$$W \propto N \propto t^{\beta_t}, \quad \text{where } 0 \leq \beta_t \leq 3 \tag{2.23}$$

Here, $N$ represents the total cumulative number of AE events up to time $t$, and $\beta_t$ is termed the temporal scaling exponent. This exponent is a key parameter characterizing the rate of temporal evolution of the damage process. Since the total duration and cumulative event count vary across different monitoring periods, directly comparing the original dimensions of $N$ and $t$ cannot effectively reveal the intrinsic laws of damage evolution. Therefore, the above relationship is typically normalized. Let $N_d$ be the cumulative number of AE events recorded at the end of the entire monitoring period, and $t_d$ be the total monitoring time. The normalized power law relationship can be expressed as:

$$\frac{N}{N_d} = \left(\frac{t}{t_d}\right)^{\beta_t} \tag{2.24}$$

It is worth noting that $N_d$ and $t_d$ do not necessarily correspond to the final failure of the structure; they are merely observed values within a specific monitoring window. By applying a logarithmic transformation $log_{10}(N/N_d)$ versus $log_{10}(t/t_d)$ to the $N$-$t$ data obtained during monitoring and performing linear regression, the slope provides an estimate of the temporal scaling exponent $\beta_t$. The magnitude of $\beta_t$ directly reflects whether the damage evolution process is stable or not, providing a dynamic criterion for structural health status. When $\beta_t < 1$, the cumulative number of AE events grows slower than linearly with time, indicating that the energy dissipation rate is slowing down and the damage process is tending toward stability. When $\beta_t > 1$, the cumulative number of AE events accelerates with time, which is a clear signal of imminent damage instability and macroscopic failure. This acceleration implies that the interaction, nucleation, propagation, and coalescence of microcracks are intensifying, and the elastic strain energy within the structure is being rapidly released through an increasing number of AE events.

$\beta_t$ analysis complements the $b$-value analysis and fractal analysis described earlier, collectively forming a multi-dimensional damage assessment system. $b$-value analysis focuses on the evolution of amplitude distribution to reveal the transition of damage mechanisms from microscopic to macroscopic fracture. $\beta_t$ analysis directly quantifies the dynamic stability of the damage process from the perspective of temporal evolution rate. Fractal energy density addresses the size effect of damage parameters, while $\beta_t$ and $b$-value analyses provide information on temporal evolution and event intensity distribution. In practical applications, the combined use of these methods, namely monitoring the decrease of the $b$-value (indicating damage localization) and the increase of the $\beta_t$ value (indicating damage acceleration), can more reliably capture the complete evolutionary path of a structure from stable damage accumulation to unstable failure, greatly improving the accuracy and timeliness of early warnings.

### 2.4.3 Natural time (NT) analysis

Natural time (NT) is a time series analysis method used to identify the critical state of a system. It was first proposed by Varotsos et al. [89, 90] for analyzing seismic electric signals. This method transforms a time series into the "NT" domain and extracts statistical features of event order and energy distribution to identify whether the system is approaching a critical point [91, 92]. In the process of material fracture, AE events can be regarded as a series of discrete energy emission processes, and their time series can be reconstructed through NT analysis. A schematic diagram of the NT analysis method is shown in Fig. 2.10.

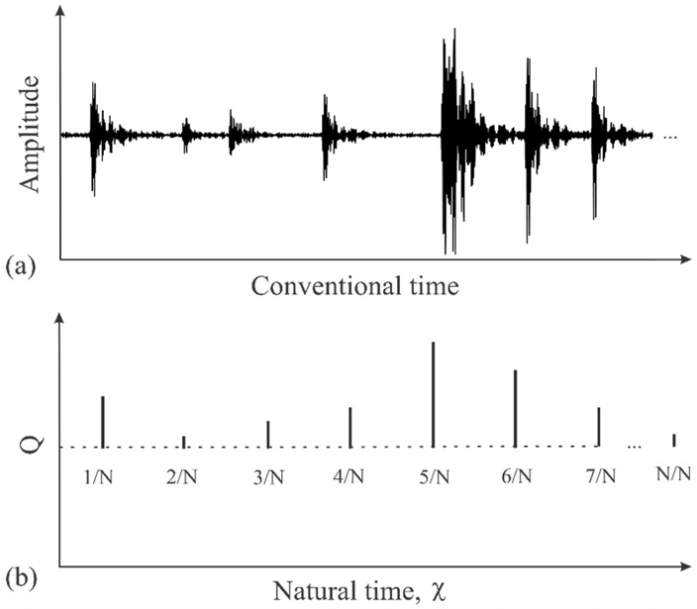


**Figure 2.10** NT analysis method: (a) typical AE time series; (b) corresponding NT sequence

Consider an AE event sequence containing $N$ events, each corresponding to a physical quantity $Q_k$, such as energy, rise angle, or amplitude [93, 94]. The natural time $\chi_k$ and the normalized probability $p_k$ are defined as:

$$\chi_k = \frac{k}{N} \ , \quad p_k = \frac{Q_k}{\sum_{i=1}^{N} Q_i} \tag{2.25}$$

where $k$ = 1, 2, ..., $N$ is the event index. For AE signals, $Q_k$ can be taken as the signal amplitude or energy ($Q_k \propto A_k^{1.5}$). For earthquakes, $Q_k = 10^{1.5M_k}$, where $M_k$ is the magnitude.

Based on sequence ($\chi_k$, $p_k$), NT variance $\kappa_1$ of the system is calculated as follows:

$$\kappa_1 = \sum_{k=1}^{N} p_k \chi_k^2 - \left(\sum_{k=1}^{N} p_k \chi_k\right)^2 \tag{2.26}$$

When the system approaches a critical point, $\kappa_1$ gradually decreases to the critical value of 0.07 [95]. Furthermore, the entropy $S$ and the time reversed entropy $S_{rev}$ are other key parameters. The entropy $S$ is defined as:

$$s = \langle \chi\, ln\, \chi \rangle - \langle \chi \rangle\, ln\langle \chi \rangle, \text{ where } \langle \chi\, ln\, \chi \rangle = \sum_{k=1}^{N} p_k \chi_k\, ln\, \chi_k \tag{2.27}$$

where $\langle \cdot \rangle$ denotes the weighted average. The entropy $S_{rev}$ is calculated by reversing the probability sequence ($T_{PK} = P_{N-K+1}$). The entropy $S$ and the time reversed entropy $S_{rev}$ should satisfy the condition of being below the uniform noise entropy $S_u$ = 0.0966 to further confirm criticality [96].

In addition, the average distance $\langle D \rangle$ is used to compare the normalized power spectrum $\Pi(\omega)$ with the ideal critical power spectrum $\Pi(\omega)_{\text{ideal}}$. In NT, the normalized power spectrum is defined as:

$$\Pi(\omega) = |\Phi(\omega)|^2, \text{ where } \Phi(\omega) = \sum_{k=1}^{N} p_k e^{i\omega\frac{k}{N}} \tag{2.28}$$

where $\omega$ is the angular frequency, and $\Pi(\omega)_{\text{ideal}} \approx 1 - 0.07\omega^2 (\omega \to 0)$. When the average distance $\langle D \rangle$ between the normalized power spectrum $\Pi(\omega)$ curve and the theoretically estimated $\Pi(\omega)_{\text{ideal}}$ curve is less than $10^{-2}$, the system is considered to be approaching criticality, i.e., $\langle D \rangle = \langle |\Pi(\omega) - \Pi(\omega)_{\text{ideal}}| \rangle < 10^{-2}$.

When the above parameters simultaneously satisfy their respective critical conditions, the structure is considered to have entered a critical state. NT analysis is

updated iteratively on an event by event basis, recalculating all parameters with each new event.

NT analysis has been successfully applied to the study of fracture processes in brittle materials such as concrete and rock, demonstrating its potential for identifying failure precursors [97-99].

### 2.4.4 AE information entropy analysis

Compared with other traditional AE parameters, AE information entropy exhibits higher analytical efficiency because it is unaffected by threshold settings and is more sensitive to changes in AE signal irregularity [100-102]. In previous studies, traditional AE parameters such as amplitude, energy, duration, rise time, and peak count have been widely used in concrete fracture research, but each of these parameters has its own limitations [103].

The concept of information entropy was first introduced by Shannon in 1948 [104] and appears capable of overcoming the aforementioned limitations. The calculation formula for information entropy is as follows:

$$H = -\frac{1}{\log_{10} 2}\sum_{i=1}^{n} p(x_i)\log_{10} p(x_i) \tag{2.29}$$

where $x_1$, $x_2$, $x_3$, …. $x_n$ are a given random sequence, $p(x_i)$ is the corresponding probability distribution, and $H$ is the non negative Shannon entropy value.

Santo et al. [105] found that as the threshold increases, parameters such as AE energy, count, duration, and rise time all decrease. Only AE information entropy and amplitude were found to be independent of the threshold. However, unlike amplitude, AE information entropy carries the necessary information for predicting waveform characteristics. The study also found that changes in arrival time affect all AE parameters except entropy. For example, during material loading, AE waves generated by crack initiation and propagation exhibit unique waveform disorder characteristics.

These characteristics can be quantified to identify different damage stages. One method to achieve this is to obtain the probability distribution of discrete voltage values of the waveform, which is the information entropy. Using AE information entropy analysis, Kahirdeh et al. [106] successfully identified three different stages of damage in composite materials.

The information entropy method has been validated in structural health monitoring of composite materials, metals, and concrete structures [105, 106].

## 2.5 MCF-B method and principles

The MCF-B (Method of Critical Fluctuations-Based) method is an AE signal analysis technique grounded in critical fluctuation theory. It aims to identify the critical state of heterogeneous materials prior to failure. By fitting the nonlinear behavior in the amplitude frequency distribution of AE events, this method extracts two key exponents, $p_2$ (power law decay exponent) and $p_3$ (exponential decay exponent), thereby capturing the critical characteristics of a system before failure.

This section first briefly describes the traditional *b*-value analysis method and its limitations. It then introduces the Method of Critical Fluctuations (MCF) proposed by Contoyiannis and Diakonos [107], describing its main features and the specific approach for calculating its exponents. Subsequently, the new MCF-B method for analyzing AE time series is introduced, and the differences between the traditional power law distribution and the MCF-B method are demonstrated.

### 2.5.1 Traditional *b*-value analysis method and its limitations

In AE and seismology, *b*-value analysis is a classic method based on the G-R power law relationship, used to describe the relationship between earthquake magnitude or event amplitude and frequency ($\log_{10} N = a - bM$, see Eq. 2.20). Here, $N$ is the number of events with magnitude (or logarithm of amplitude in AE analysis) greater

than *M*, a is a constant, and the *b*-value reflects the statistical characteristics of damage evolution within a material. In AE monitoring, a decreasing *b*-value is often regarded as a precursor to impending failure [108].

However, the traditional *b*-value method has the following limitations in practical applications:

1）Deviation from linearity: Actual AE data often deviate from the G-R power law in the high-amplitude or low-amplitude regions. The fitting results become unstable, especially when large events are scarce or small events are incompletely detected [31].

2）Mixing of multiple damage mechanisms: Different damage mechanisms, such as microcracking and fiber fracture, can lead to multiple "clusters" in the amplitude distribution, making a single power law unable to accurately describe the overall behavior [109].

3）Strong dependence on fitting method: The estimated *b*-value is sensitive to the fitting method used (e.g., maximum likelihood estimation, least squares method), resulting in poor robustness [31].

Therefore, a method that can more flexibly describe nonlinear distributions and has physical significance is needed to improve the reliability of failure precursor identification.

### 2.5.2 Theoretical basis of Method of Critical Fluctuations (MCF)

The Method of Critical Fluctuations (MCF) was proposed by Contoyiannis and Diakonos to describe the statistical behavior of systems near the critical point of a continuous phase transition [107]. MCF is based on the analysis of the laminar length distribution, assuming that near the critical point, fluctuations of the system's order parameter exhibit a competition between power law and exponential decay.

In MCF, the probability distribution $P(l)$ of the laminar length $l$ is described by the following function:

$$P(l) = p_1 \cdot l^{-p_2} \cdot e^{-lp_3} \tag{2.30}$$

where $p_1$ is a constant, $p_2$ is called the power law decay exponent (determining the decay rate of the power law term $l^{-p_2}$, and $p_3$ is called the exponential decay exponent (determining the decay rate of the exponential term $e^{-lp_3}$). Under critical conditions, $p_2 \geq 1$ and $p_3 \approx 0$, the distribution exhibits pure power law behavior, indicating that the system has entered a "critical window" [110]. MCF has been successfully applied to the critical identification of complex systems such as seismo electromagnetic signals [111] and electrocardiogram signals [112].

### 2.5.3 Principles and implementation steps of MCF-B

Based on the MCF concept, this thesis adopts a new MCF-B (MCF-Based) method and applies it to the analysis of AE amplitude frequency distributions to overcome the limitations of the traditional *b*-value method. The MCF-B method fits the distribution *N*(A) of AE event amplitudes A as:

$$N(A) = p_1 \cdot A^{-p_2} \cdot e^{-Ap_3} \tag{2.31}$$

where $p_1$ is a constant, $p_2$ is the power law decay exponent, and $p_3$ is the exponential decay exponent. This function contains both a power law term ($A^{-p_2}$) and an exponential decay term ($e^{-Ap_3}$) and can describe the following characteristics:

1）$p_3 > 0$：High-amplitude events are scarce, and the distribution deviates downward from the power law.

2）$p_3 < 0$：High-amplitude events are abundant, and the distribution deviates upward from the power law.

3） $p_3 \approx 0$： The distribution approximates a pure power law, and the system is in a self organized critical state.

Figure 2.11 presents the results of fitting AE amplitude frequency data from an experimental test using Eq. (2.31). It compares the power law distribution (linear fitting of the *b*-value method, blue dashed line) with the MCF-B fitting result (red solid line). The black circles represent the amplitude distribution results of the AE signals. Fig. 2.11(a) and (b) show significant deviations of this new method from the power law, where a positive $p_3$ value indicates a downward exponential tail, while a negative $p_3$ value indicates an upward exponential tail relative to the power law. The MCF-B method captures the scarcity or abundance of larger amplitude events in the distribution. In Fig. 2.11(c), when the distribution is characterized by $p_2 > 1$ and $p_3 = 0$, a strong correlation is observed between the power law distribution and the curve fitted by the MCF-B method.

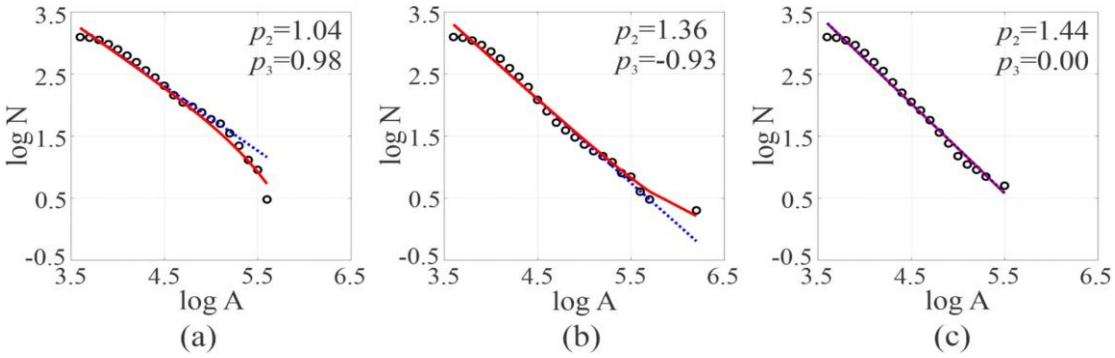


**Figure 2.11** Example of fitting AE signal amplitude distribution using the MCF-B method: (a) $p_2 > 1, p_3 > 0$; (b) $p_2 > 1, p_3 < 0$; (c) $p_2 > 1, p_3 \approx 0$.

The advantage of the MCF-B method is that it is suitable for nonlinear amplitude distributions and can better capture damage evolution. It can also achieve real-time monitoring through sliding event windows or time windows.

The evolution of the fitting parameters $p_2$ and $p_3$ can reveal the system state. When $p_2 > 1$ and $p_3 \approx 0$, the distribution is close to an ideal power law, and the system is in a self organized critical state. When the system approaches instability, a "crossover phenomenon" often occurs, characterized by a decrease in $p_2$ and a monotonic increase in $p_3$. This signals that the system is deviating from the critical state and is about to

become unstable. This crossover behavior is consistent with critical precursors observed in fiber bundle models (FBM) and percolation theory [113].

The MCF-B method follows three main steps:

1）Calculate the AE amplitude histogram for the initial dataset W (window size), starting from event number 1, i.e., consider the time series from event #1 to #W.

2）Plot the obtained distribution $N$(A) on a log-log scale. Fit this distribution using the function proposed in Eq. (2.31) to determine a set of exponents $p_2$ and $p_3$.

3）For each new event in the time series, repeat steps 1 and 2. Specifically, consider events #2 to #W+1, then #3 to #W+2, and so on until the end of the data, sequentially calculating the exponents $p_2$ and $p_3$.

### 2.5.4 Cross-scale application potential of the MCF-B method

The MCF-B method finely captures the deviation of the AE amplitude distribution from an ideal power law through the parameters $p_2$ and $p_3$, providing a new tool for identifying the critical state before material instability. The critical statistical characteristics described by this method have a physical basis for extrapolation from laboratory material fracture to crustal earthquake precursor identification.

An earthquake is the result of macroscopic shear fracture of crustal rocks. Its essence, similar to the brittle fracture of rock or concrete specimens in the laboratory, falls under the category of solid instability problems. Both follow the fundamental laws of fracture mechanics, and both are accompanied by accelerated evolution and clustering of microfractures (AE/microearthquakes) before instability. This homology implies that the physical laws governing the statistical distribution of microfracture events may be universal across scales.

The classic G-R law ($b$-value analysis) in seismology has demonstrated that the power law distribution of seismic moments exhibits widespread scale invariance. The MCF-B method represents a deepening of this concept: $p_2$ can be considered analogous to a dynamic, localized $b$-value, while $p_3$ quantifies the degree to which the system

deviates from this scale invariance. When $p_3 \approx 0$, the system enters a critical self organized state (pure power law). Therefore, the synergistic evolution of $p_2$ and $p_3$ may serve as a cross-scale critical precursor identifier that is more sensitive and physically meaningful than a single *b*-value.

At the laboratory scale, AE data from the entire material fracture process can be acquired with a high signal to noise ratio, allowing for the precise establishment of the relationship between the evolution of MCF-B parameters and the ultimate failure time, thus constructing a typical "critical precursor fingerprint." If a similar MCF-B parameter evolution pattern to the laboratory fingerprint can be found in field crustal microearthquake activity sequences, it could provide a new statistically based, cross-scale validated indicator for imminent earthquake early warning.

This study adopts the MCF-B method as a core analytical tool and applies it sequentially to the following: laboratory concrete fracture tests in Chapter 3, field rock AE data in Chapter 4, and the construction of a deep learning based intelligent identification model in Chapter 5. Through this research path of "a single method applied across multiple scales," the universality and effectiveness of MCF-B characteristics in revealing system criticality are directly tested, thereby circumventing complex direct scale conversion and achieving the integrated driving of physical models and multi-source data.

## 2.6 Chapter Summary

This chapter systematically constructs a theoretical framework from fracture mechanics to AE analysis methods, laying the theoretical foundation for the physics based seismic precursor identification research in this thesis. First, from the perspective of fracture mechanics, it elaborates on the cross-scale evolution law of materials from microscopic damage to macroscopic fracture, clarifying the essence of AE signals as the direct physical response of microfracturing. Subsequently, it introduces the generation mechanism, propagation characteristics, feature parameter extraction, and

source localization methods of AE signals, as well as various signal processing techniques such as *b*-value analysis, NT analysis, and information entropy analysis. Finally, it focuses on the theoretical basis, implementation path, and unique advantages of the MCF-B method in identifying the critical state of systems, providing a physical basis for its cross-scale application. The specific summaries are as follows:

（1）Fracture mechanics theory reveals the cross-scale unity of material failure, indicating that the earthquake preparation process shares physical homology with laboratory material damage. This provides a solid physical foundation for using AE technique to capture seismic precursors and offers a systematic theoretical framework for understanding the complete process from microcrack initiation to macroscopic fracture.

（2）AE technique can effectively monitor internal microfracturing activity in materials. Its waveform parameters (such as energy, amplitude, duration, and RA-AF values) can reflect crack propagation modes and damage levels, while statistical characteristic parameters (such as *b*-value and fractal dimension) can quantify the stage characteristics of damage evolution, providing multi-dimensional indicators for damage assessment.

（3）Although the traditional *b*-value analysis method is widely used in seismology and material failure analysis, its assumption based on a linear power law has obvious shortcomings in describing the fracture process of complex heterogeneous materials. Data deviations are prone to occur especially in the high-amplitude and low-amplitude regions. Moreover, it is sensitive to the fitting method and data selection, and its robustness needs improvement.

（4）By introducing a fitting function that includes a power law term and an exponential decay term, the MCF-B method can more accurately describe the nonlinear characteristics of the AE amplitude distribution. The $p_2$ parameter reflects the underlying power law characteristics of the system, while the $p_3$ parameter characterizes the degree of deviation from an ideal power law distribution. The synergistic evolution of these two parameters provides a more sensitive and physically

meaningful statistical physics criterion for identifying the critical stage before instability in materials or crustal systems.

（5）The critical fluctuation theory on which the MCF-B method is based has universality in statistical physics. The principle of identifying system criticality by quantifying the deviation of the amplitude distribution from an ideal power law is transferable across systems of different scales. This provides theoretical support for extending its application from laboratory material fracture analysis to crustal earthquake precursor identification, making it a unified methodology that runs through subsequent experimental validation, field monitoring analysis, and deep learning models.

# Chapter 3

# 3 Fracture monitoring of concrete structures and validation of MCF-B method

## 3.1 Introduction

Concrete, as a typical quasi brittle heterogeneous material, undergoes a fracture process that is essentially a cross-scale damage evolution process involving the initiation, propagation, and coalescence of internal microdefects under load, ultimately leading to the formation of macroscopic cracks. This process shares profound physical homology with the mechanism of earthquake preparation in crustal rocks under tectonic stress. AE technique, as an effective means of capturing transient stress waves released by internal microfracturing, has been widely used to study damage evolution and fracture precursors in concrete materials. However, existing research has largely focused on the AE characteristics of specimens with specific sizes or single materials under simple loading conditions. Systematic validation of AE response patterns, the universality of cross-scale precursor features, and novel analysis methods for concrete structures under the coupled influence of multiple complex factors, such as specimen size and slenderness ratio, long-term loading history, fiber reinforcement, strengthening and repair, and real structural service environments, remains insufficient.

The MCF-B method, introduced as a novel signal analysis tool based on critical fluctuation theory in Chapter 2, quantifies the degree to which a system deviates from a self organized critical state by fitting the competition between power law and

exponential decay in the AE amplitude distribution (parameters $p_2$ and $p_3$), thereby identifying statistical physics precursors of impending failure. Although this method has demonstrated potential for cross-scale identification of critical states, its effectiveness and robustness in the fracture process of real, complex concrete materials and structures urgently require systematic experimental validation.

Concrete and rock are both quasi brittle heterogeneous materials and share profound physical homology at the level of fracture mechanics. Both follow the cross-scale damage evolution law from microcrack initiation and propagation to macroscopic instability. Compared with natural rock, concrete, as a manufactured material, allows for effective control of its mix proportion, curing conditions, and initial defect distribution through standardized processes. Therefore, it offers advantages in laboratory research such as controllable composition and strong experimental repeatability, making it an ideal laboratory model material for validating precursor identification methods. Based on this, this chapter aims to construct a complete experimental validation system, ranging from intrinsic material fracture behavior to damage evolution in engineering structures, through a series of rigorous and multi-factor fracture monitoring tests on concrete materials and structures. This will provide controllable and repeatable laboratory evidence for the effectiveness of precursor identification methods such as MCF-B in cross-scale systems. The research content of this chapter progresses sequentially. First, through compression tests on steel fiber reinforced concrete (SFRC), the influence of loading rate on damage mode transition and the precursor characteristics of AE parameters is investigated (Section 3.2). Subsequently, by systematically varying specimen size and slenderness ratio, the fractal domain nature of energy emission and the size effect in concrete fracture are revealed (Section 3.3). Next, the research perspective is extended to structural components. Through flexural tests on reinforced concrete beams strengthened with ultra high performance concrete (UHPC) after long-term loading, the AE evolution laws and NT analysis precursors under the influence of existing damage and strengthening interface behavior are explored (Section 3.4). Furthermore, through field measurement of cracks in a steel UHPC composite bridge deck, the capability of AE technique to monitor and

locate the dynamic propagation of real structural cracks under complex environmental noise is validated (Section 3.5). Finally, building on the previous studies, using flexural glass fiber reinforced polymer (GFRP) bar reinforced concrete beams as the object, the superiority of the MCF-B method is systematically compared and validated against traditional *b*-value analysis, NT analysis, and AE information entropy analysis in identifying bond-slip mechanisms and critical failure precursors (Section 3.6).

Through this progressively layered experimental design of "material basic properties, component complex behavior, and structural field monitoring," this chapter not only systematically validates the effectiveness and robustness of the MCF-B method in identifying fracture precursors in concrete but also provides solid experimental evidence and data support for understanding the unified cross-scale precursor laws from laboratory scale material fracture to crustal scale seismic activity.

## 3.2 AE characteristics and fracture precursors of steel fiber reinforced concrete under compression

This section investigates the damage evolution mechanism and fracture precursor characteristics of steel fiber reinforced concrete (SFRC) under compressive failure using AE and digital image correlation (DIC) techniques [114]. The uniaxial compression test was selected for the following main considerations: rock is primarily subjected to compressive stress, making the uniaxial compression state closer to the stress characteristics of crustal rock; this test aims to evaluate the improvement effect of fibers on matrix ductility and to provide a comparison with the uniaxial compression tests on specimens of different sizes in Section 3.3, revealing the mechanical performance characteristics of fiber reinforced concrete from the perspectives of material toughening and size effects, respectively. The study analyzes the mechanical response, AE parameter evolution, and crack mode transition patterns of SFRC under different loading rates (0.4, 0.8, 1.2 mm/min), providing a basis for damage warning of fiber reinforced composites.

### 3.2.1 Experimental setup and mechanical response characteristics

The SFRC material was mainly composed of P.O 42.5 ordinary Portland cement, manufactured sand with a fineness modulus of 3.0, granite crushed stone of 5 30 mm, and a high performance polycarboxylate superplasticizer at a concentration of 10.8%. The specimens were made of C50 SFRC with dimensions of 100 mm × 100 mm × 100 mm. The steel fibers were shear wave shaped, with a length of 28 mm, an aspect ratio of 60, and a volume fraction of 1%. The mix proportion is shown in Table 3.1, and the mechanical properties are shown in Table 3.2.

**Table 3.1** SFRC mix proportion (kg/m$^3$).

| Component | Cement | Sand | Stone | Water | Steel Fibre | Carboxylate Water Reducer |
|---|---|---|---|---|---|---|
| Dosage | 480 | 713 | 1032 | 155 | 75 | 9.6 |

**Table 3.2** SFRC mechanical properties.

| Material | Compression Strength (MPa) | Elastic Modulus (GPa) | Flexural Strength (MPa) | Splitting Strength (MPa) |
|---|---|---|---|---|
| SFRC | 64.8 | 39.0 | 6.8 | 4.6 |

As shown in Fig. 3.1(a), a 200 t electro hydraulic servo system was used to conduct uniaxial compression tests on SFRC specimens. The AE system was the Italian ÆMISSION® device, with sensors having a frequency range of 10 kHz to 1 MHz. The acquisition system featured independent threshold triggering for each channel and automatically extracted AE signal parameters. The AE waves captured by the sensors were amplified with a gain of 60 dB before processing, and the acquisition threshold was set to 2 mV. As shown in Fig. 3.1(b), AE sensors were arranged on the side faces of the specimens. The sensors were coupled and fixed to the specimens using vacuum grease as a coupling agent. During the experiments, Teflon pads were placed on the contact surfaces between the servo system and the two ends of the specimens to

significantly reduce end friction and minimize lateral end constraints. As shown in Fig. 3.1(c) and (d), before testing, the specimen surfaces were coated with matte black paint to form a speckle pattern (with speckle sizes of 5 to 7 pixels). The speckle images were then processed using a DIC image analysis system to obtain the surface displacements and strains of the specimens. Loading was applied under displacement control at rates of 0.4, 0.8, and 1.2 mm/min, and AE and DIC data were acquired in real-time throughout the entire process [114].

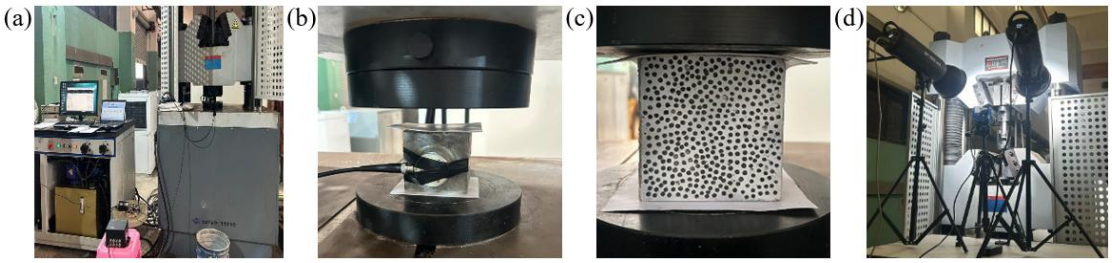


**Figure 3.1** Experimental setup for SFRC compression test: (a) loading system; (b) AE sensor arrangement; (c) DIC speckle pattern; (d) DIC equipment.

As shown in the load-displacement curve in Fig. 3.2(a), the failure process of SFRC can be divided into three stages. Stage I (microcrack initiation and stable propagation period) corresponds to the linear load increase segment. In this stage, the external load is primarily carried by the concrete matrix, and the fibers have not yet been fully mobilized. AE activity is relatively moderate, with a low AE event rate, mainly originating from micro separation at the aggregate mortar interface and the initiation of microcracks in the cement matrix. Stage II (macrocrack formation and propagation period) starts with the initial cracking load $F_{fc}$ and enters the nonlinear deformation stage. Microcracks begin to coalesce into visible macrocracks. Fibers effectively inhibit crack propagation through bridging action, exhibiting a significant toughening effect. In this stage, AE activity increases significantly, with both event rate and energy release rate showing an accelerating growth trend. Stage III (failure and instability period) enters the softening stage after the load reaches the peak load $F_{max}$. The main crack develops rapidly, and fiber slip becomes the dominant deformation mechanism. The load bearing capacity of the specimen continuously decreases, ultimately leading to

failure. AE activity reaches its maximum near the peak load and then gradually attenuates.

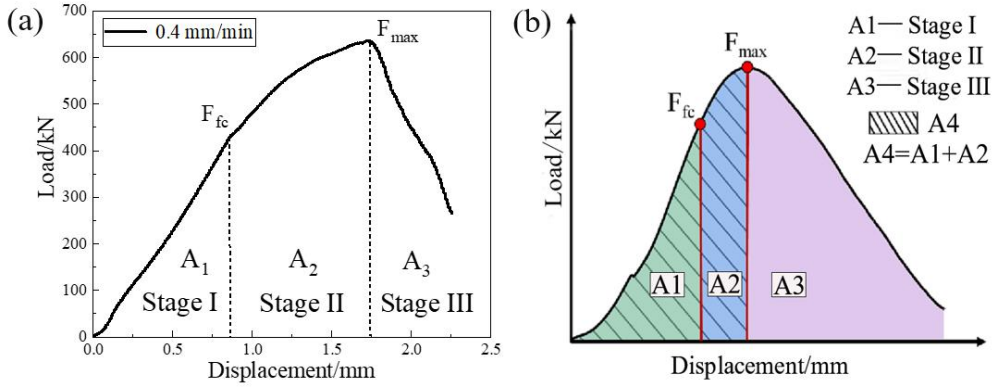


**Figure 3.2** Typical load-displacement curve and damage stage division: (a) three-stage division; (b) CTI calculation.

By calculating the area under the load-displacement curve and referring to the methods proposed by Khan et al. [115] and Qin et al. [116], the compressive toughness of the SFRC specimens can be quantitatively described. As shown in Fig. 3.2(b), the compressive toughness index (CTI) is defined as CTI = A4/A1, where A1 is the energy before initial cracking, and A4 = A1 + A2 is the total energy before the peak load. The CTI reflects the crack resistance of SFRC and quantifies the toughening effect of fibers on concrete [117]. As shown in Table 3.3, as the loading rate increases from 0.4 mm/min to 1.2 mm/min, the CTI decreases from 3.84 to 2.77, indicating that the toughening effect of steel fibers is more significant under low loading rate conditions.

**Table 3.3** Compressive Toughness Index (CTI)

| Loading Rate (mm/min) | A1/(kN·mm) | A2/(kN·mm) | A4/(kN·mm) | CTI (A4/A1) |
|---|---|---|---|---|
| 0.4 | 173 | 492 | 665 | 3.84 |
| 0.8 | 210 | 490 | 700 | 3.33 |
| 1.2 | 275 | 489 | 764 | 2.77 |

## 3.2.2 AE parameter evolution and damage characterization

The temporal scaling exponent $\beta_t$ was calculated using the temporal scaling law described by Eq. (2.24) in Section 2.4.2, and the *b*-value was obtained by fitting the G-

R relationship (Eq. 2.20 in Section 2.4.1). The data were processed using a sliding window of 100 events, and the results are shown in Fig. 3.3. The point at which the *b*-value decreases to its minimum is denoted as t_$b_{min}$, corresponding to the transition from microcracks to macrocracks. Under different loading rates, at time t_$b_{min}$, $b_{min} \approx 1.0$, and $\beta_t > 1$, indicating extensive microcrack accumulation and coalescence. A higher loading rate leads to a faster decrease in the *b*-value, indicating an accelerated damage localization process. The $\beta_t$ curve shows an overall decreasing trend and falls below the $\beta_t = 1$ line. The critical point is marked as t_$\beta_t$. This critical moment corresponds to the occurrence of the unstable fracture process, where all microcracks coalesce into a single main fracture surface. These results confirm that before the critical point t_$\beta_t$, the AE signal sequence exhibits $\beta_t > 1$, indicating unstable crack propagation. After the critical point t_$\beta_t$, the AE sequence exhibits $\beta_t < 1$, indicating that energy dissipation has been exhausted and AE activity remains stable.

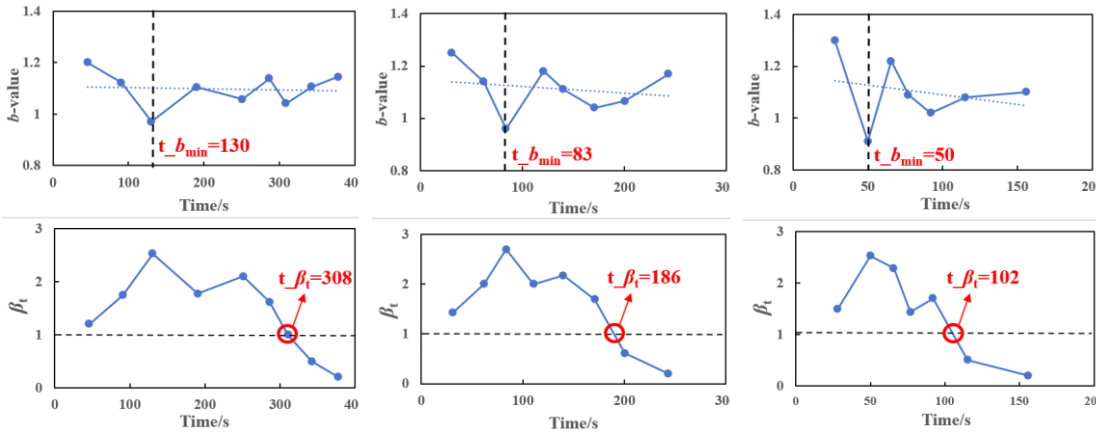


(a) SFRC - 0.4 mm/min (b) SFRC - 0.8 mm/min (c) SFRC - 1.2 mm/min

**Figure 3.3** $\beta_t$ and *b*-values at different loading rates.

Figure 3.4 shows the cumulative AE events and load curves under different loading rates. The values of t_$\beta_t$ and t_$b_{min}$ determined by $\beta_t$ and the *b*-value are also marked in Fig. 3.4. In Stage I, the cumulative AE curve increases linearly. In Stage II, when the concrete matrix first cracks, steel fibers play a bridging role between the crack surfaces. As the load increases, extensive crack propagation occurs in the specimen near the peak load. Entering Stage III, the load bearing capacity of the specimen begins to decrease, and the cumulative AE in this stage gradually diminishes, eventually ceasing entirely.

At lower loading rates, the total number of AE events increases significantly, indicating that a large number of microcracks have initiated within the SFRC. Conversely, as the loading rate increases, SFRC exhibits stronger brittle behavior, leading to sudden crack propagation and an increase in AE events, indicating the formation of wider cracks in the SFRC. The critical moment t_$\beta_t$ marks the occurrence of the unstable fracture process, and the corresponding cumulative AE curve shows a significant inflection point, indicating that the growth rate of AE events begins to decrease. As the loading rate increases, the post-peak softening segment becomes steeper, indicating a transition of material behavior from ductile to relatively brittle.

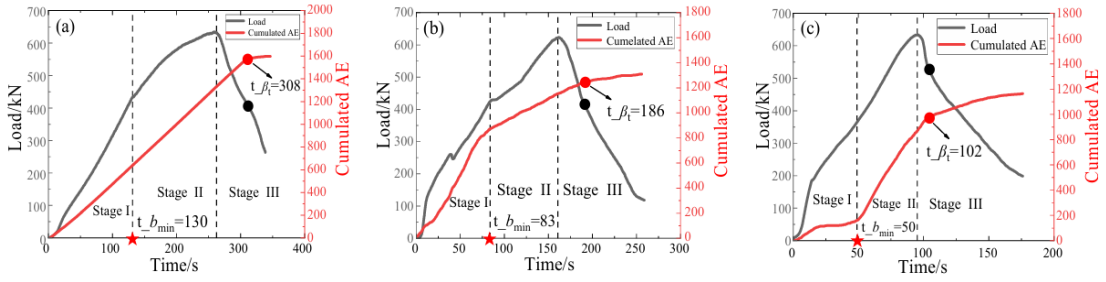


**Figure 3.4** Cumulated AE and loading history at loading rates of (a) 0.4 mm/min, (b) 0.8 mm/min, and (c) 1.2 mm/min.

Figure 3.5 shows the DIC results for SFRC under different loading rates. Under low speed loading (0.4 mm/min), the cracks in SFRC are fine and predominantly tensile. Under high speed loading (1.2 mm/min), the degree of strain localization intensifies, and an obvious shear band appears, indicating that the proportion of shear cracks increases with loading rate. In contrast, normal concrete (NC) under high speed loading exhibits only a single vertical tensile crack on the right side (Fig. 3.5d), displaying typical brittle fracture characteristics, while SFRC (Fig. 3.5c) shows better integrity and ductility.

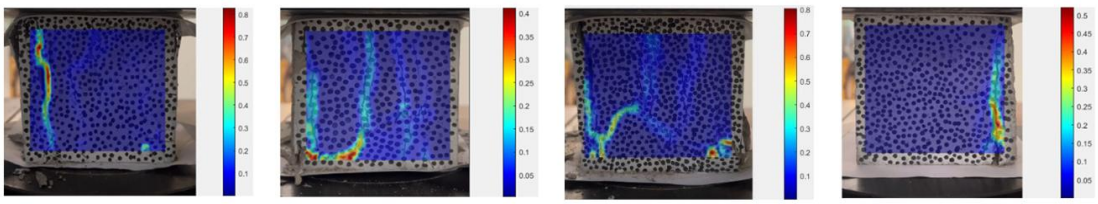

(**a**) SFRC—0.4 mm/min (**b**) SFRC—0.8 mm/min (**c**) SFRC 1.2 mm/min (**d**) NC—1.2 mm/min

**Figure 3.5** DIC strain analysis at fracturing with different loading rates.

The AF and RA values were calculated according to Eq. (2.9) and Eq. (2.10) in Section 2.3.3 to identify the crack modes. The results are shown in Fig. 3.6 and 3.7. The RA-AF analysis results indicate that as loading progresses, the crack type gradually transitions from tensile dominated to shear dominated. In Stage I, newly generated cracks are mainly tensile cracks. For example, at a loading rate of 0.4 mm/min, the ratio of tensile to shear cracks is approximately 7:3, which may correspond to cracking at the aggregate matrix interface. In Stage II, a large number of new cracks appear, and the most significant change is the shift in the ratio of tensile to shear cracks, with the number of shear and tensile cracks approaching 1:1. In Stage III, shear cracks begin to dominate, with the ratio of tensile to shear cracks approximately 1:2.

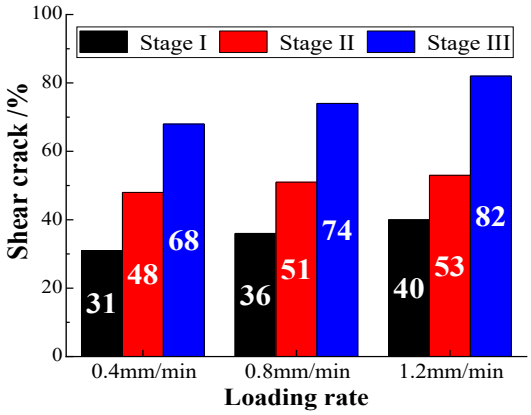


**Figure 3.6** Shear cracks in each damage stage and at different loading rates.

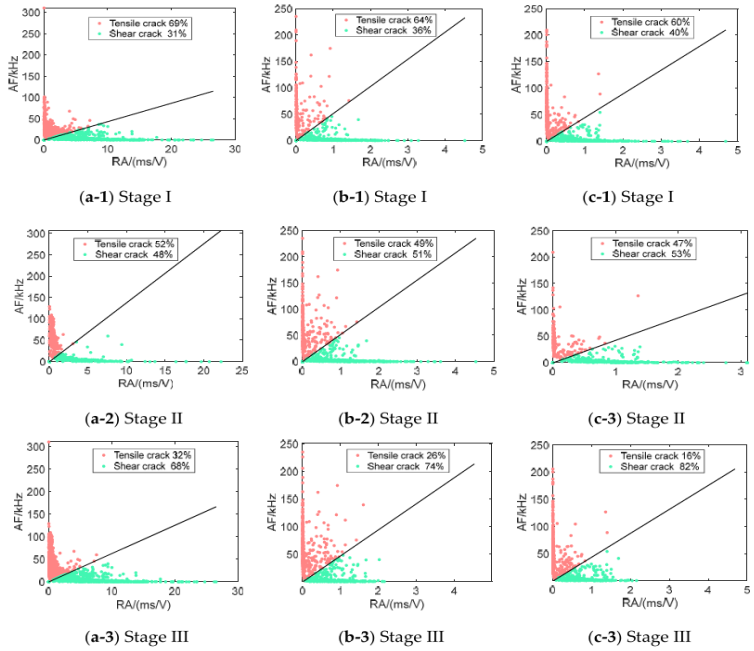


**Figure 3.7** Variation of *RA-AF* with loading rate at different damage stages: (a) SFRC - 0.4 mm/min; (b) SFRC - 0.8 mm/min; (c) SFRC - 1.2 mm/min.

The loading rate has a significant effect on the number of shear cracks. The proportion of shear cracks increases notably at high loading rates (68% at 0.4 mm/min versus 82% at 1.2 mm/min), indicating a decrease in material ductility. Conversely, lower loading rates lead to tensile cracks dominating, allowing the fiber bridging effect to be fully utilized, absorbing more energy and thus enhancing the ductility and toughness of the material. The loading rate effect can be explained from the perspective of fracture mechanics. Under low speed loading, microcracks have sufficient time to initiate and stably propagate in weak regions of the matrix, and the fiber bridging effect is fully exerted, promoting energy dissipation over a larger range. The damage exhibits diffuse characteristics, manifesting macroscopically as tensile crack dominance and enhanced ductility. Under high speed loading, strain energy accumulates rapidly. The propagation speed of microcracks exceeds the response capability of fiber bridging, and stress concentration does not have time to disperse across multiple weak points. This leads to rapid localization of damage to the main crack plane, where interfacial shear slip becomes the dominant mechanism, resulting in an increased proportion of shear cracks and intensified macroscopic brittle behavior.

### 3.2.3 Failure mechanism and AE precursors

As shown in Fig. 3.8, in the early Stage I, initial damage mainly originates from tensile cracks, marking the beginning of matrix cracking. Subsequently, in Stage II, as cracks propagate, fibers inhibit the propagation of tensile cracks through bridging action, and the number of shear cracks gradually increases. Finally, in Stage III, due to the relatively low shear stiffness of the fibers, as the load continues to increase, the matrix fractures along the shear plane, and the number of shear cracks begins to dominate. The failure mechanism analysis indicates that fiber bridging effectively delays crack propagation and promotes the transition of cracks from tensile mode to

shear mode. This transition is the microscopic mechanism for the toughness enhancement of SFRC and also an important characteristic of its failure precursors.

This study employs AE technique to provide reliable precursor indicators for predicting the impending failure of SFRC. Among the AE parameters, the critical value of $\beta_t$, the minimum $b$-value, and the inflection point of the cumulative AE curve can serve as effective fracture precursors. In particular, the sharp increase in the number of shear cracks just before failure can be used as a failure warning signal. Consistent results obtained by applying these AE tools under different loading rates further validate their reliability as failure warning indicators.

This section demonstrates that AE and DIC techniques can effectively reveal the damage evolution and fracture precursor characteristics of SFRC under compressive failure, providing a theoretical basis for structural health monitoring and early warning in engineering applications.

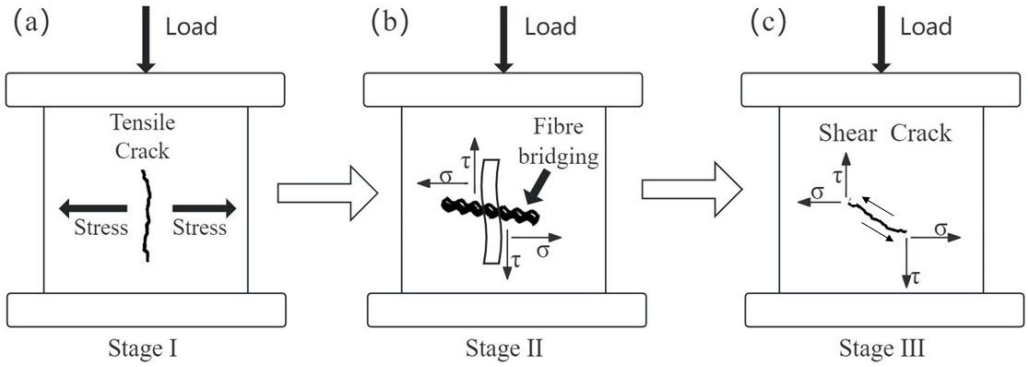


**Figure 3.8** Schematic diagram of the tensile-shear crack transition mechanism: (a) Stage I; (b) Stage II; (c) Stage III.

## 3.3 AE characteristics of specimens with different sizes

As a quasi brittle material, concrete exhibits a significant size effect in its fracture behavior, meaning that the nominal strength, toughness, and failure mode of the material change with the characteristic size of the specimen. Understanding this size dependence is crucial for predicting the failure behavior of large concrete structures [118]. This section aims to systematically investigate the influence of specimen size and slenderness ratio on the energy release characteristics and crack propagation mode

during compressive failure of concrete. By combining AE and DIC techniques, real-time monitoring and analysis of damage evolution were conducted on normal concrete (NC) and ultra high performance concrete (UHPC) specimens under uniaxial compression.

### 3.3.1 Experimental overview

The experiment designed specimen groups with three base dimensions (b = 75, 150, 300 mm) and three slenderness ratios (λ = 0.5, 1.0, 2.0), covering three specimen geometries: "short and thick" (λ = 0.5), "square" (λ = 1.0), and "slender" (λ = 2.0). As shown in Fig. 3.9, there were nine NC specimens. Due to limitations of the loading equipment, only six UHPC specimens were tested. In terms of materials, NC adopted the C25 strength grade with a mix ratio of cement:sand:stone:water = 1:2.24:2.97:0.48. The compressive strength of NC after 28 days of curing was 33.2 MPa, and its mix proportion is shown in Table 3.4. UHPC incorporated steel fibers with a volume fraction of 2% (length 12 mm, diameter 0.2 mm, tensile strength > 3000 MPa), achieving a 28 day compressive strength of 131.1 MPa. Its mix proportion is listed in Table 3.5.

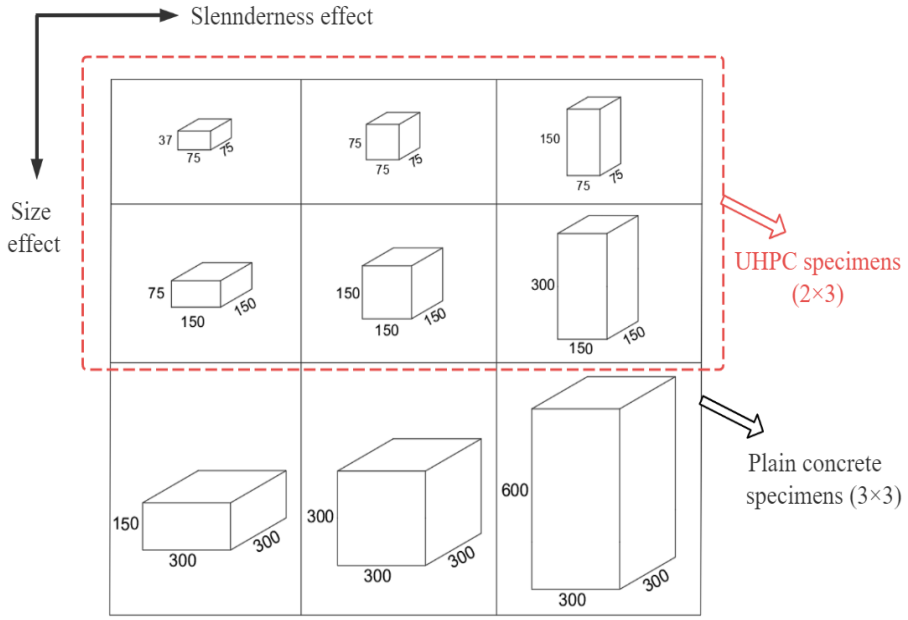


**Figure 3.9** Dimensional layout of specimens for two materials (unit: mm)

**Table 3.4** NC strength and mix ratio

| Concrete grade | Water-binder ratio | Sand rate (%) | Material usage (kg/m$^3$) | | | | | |
|---|---|---|---|---|---|---|---|---|
| | | | Cement | Fly ash | Slag powder | Sand | Stone | Water |
| C25 | 0.48 | 43 | 201 | 100 | 50 | 785 | 1044 | 170 |

**Table 3.5** UHPC mix (kg/m$^3$)

| Component | Cement | Silica ash | Fly ash | Quartz sand | Water | Steel fibre |
|---|---|---|---|---|---|---|
| Dosage | 850 | 137.5 | 112.5 | 1100 | 198 | 234 |

AE monitoring was performed using the Italian ÆMISSION® system, with sensors having a frequency range of 10 kHz to 1 MHz and an acquisition threshold of 2 mV. The sensors were attached to the specimen surface using a coupling agent (see Fig. 3.10a). The test adopted displacement controlled loading at a rate of 0.01 mm/s. To reduce end friction, Teflon pads were placed between the testing machine platens and the specimen ends, as shown in Fig. 3.10(b). DIC technology was used to obtain the full field strain distribution on the specimen surface. Before testing, the specimen surfaces were sprayed with matte black paint to form a speckle pattern.

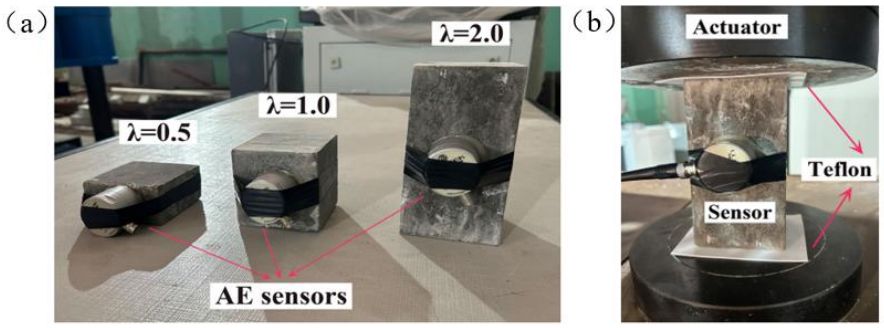


**Figure 3.10** Experimental setup for AE testing: (a) specimens with three slenderness ratios; (b) AE sensor arrangement.

## 3.3.2 Analysis of slenderness ratio and size effect

Taking the NC specimen with a base dimension of 150 mm as an example, the influence of slenderness ratio was analyzed. Figure 3.11 shows the final failure modes

of specimens with different slenderness ratios. As the slenderness ratio increased from 0.5 to 2.0, the failure mode showed a clear transition from "crushing dominated" to "cracking dominated". The stubby specimen ($\lambda = 0.5$) exhibited significant crushing failure, while the slender specimen ($\lambda = 2.0$) exhibited a nearly vertical crack.

The corresponding load-displacement curves and cumulative AE event counts are shown in Fig. 3.12. The stubby specimen ($\lambda = 0.5$) exhibited ductile post-peak softening behavior, with local load drops (snap-back instabilities) in the curve, accompanied by corresponding stepwise increases in the cumulative AE curve. The square specimen ($\lambda = 1.0$) exhibited a single global snap-back instability after the peak load, corresponding to a single increase in the cumulative AE curve. The slender specimen ($\lambda = 2.0$) exhibited completely brittle behavior, with the post-peak curve dropping almost vertically, indicating global instability, accompanied by intense AE energy emission.

Quantitative analysis in Table 3.6 shows that as the slenderness ratio increased from 0.5 to 2.0, the compressive strength decreased by 16.7% (from 36.4 MPa to 30.3 MPa), while the cumulative number of AE events increased by 81.4% (from 982 to 1781). This trend confirms that although slender specimens have lower strength, they release higher energy through AE activity, which is consistent with the transition from ductile crushing to brittle cracking.

Although Teflon pads were placed at the specimen ends to reduce friction, the slenderness ratio effect remained significant. Its physical mechanism can be attributed to the controlling effect of geometry on the damage evolution path. The stubby specimen, constrained by its geometry, does not allow the main crack to easily penetrate the entire specimen, and damage develops diffusely in multiple regions, manifesting as crushing failure. As the slenderness ratio increases, the central region of the specimen moves away from end constraints, the stress distribution becomes more uniform, and cracks can freely propagate vertically. Once a main crack forms, it quickly penetrates, manifesting as brittle cracking failure. This mechanism is consistent with the observation that the number of AE events increases significantly with slenderness ratio, indicating that crack propagation is more fully developed and energy release is more concentrated in slender specimens.

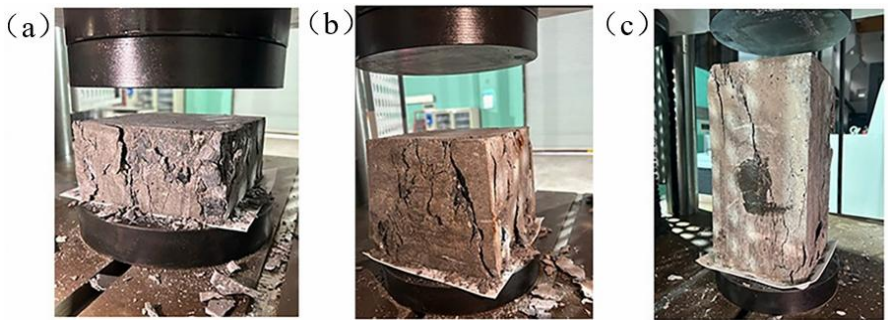


**Figure 3.11** Failure modes of NC specimens with a base dimension of 150 mm under different slenderness ratios: (a) λ = 0.5; (b) λ = 1.0; (c) λ = 2.0.

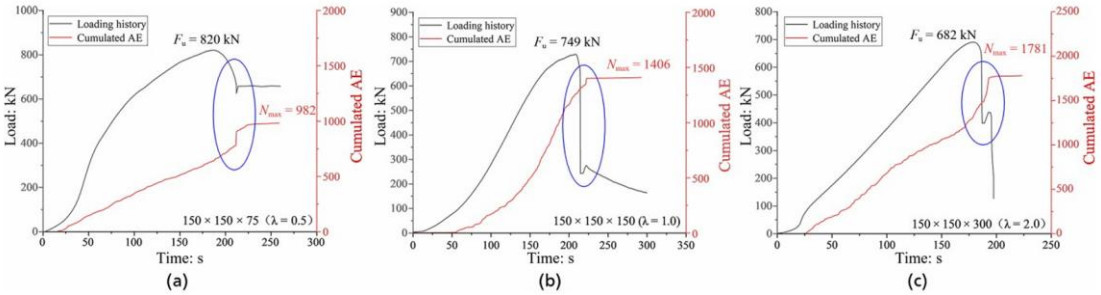


**Figure 3.12** Load history and cumulative AE curves of NC specimens with a base dimension of 150 mm under different slenderness ratios: (a) λ = 0.5; (b) λ = 1.0; (c) λ = 2.0.

**Table 3.6** Compressive strength and AE signals for different slenderness ratios (size = 150 mm)

| Slenderness ratio ($\lambda$) | Compressive strength (MPa) | Strength reduction (%) | AE signals ($N_{max}$) | Failure mode |
|---|---|---|---|---|
| 0.5 | 36.4 | - | 982 | Crushing-dominated |
| 1 | 33.3 | 8.5 | 1406 | Mixed crushing/cracking |
| 2 | 30.3 | 16.7 | 1781 | Cracking-dominated |

To investigate the influence of base dimension, the mechanical behavior of specimens with different base dimensions was analyzed while keeping the slenderness ratio constant (λ = 1.0), as shown in Fig. 3.13. Figure 3.14 shows the load-displacement and cumulative AE curves for NC specimens of different sizes. The smallest specimen (b = 75 mm) exhibited a stable softening response, with the post-peak stage affected only by local snap-back instability. The medium sized specimen (b = 150 mm) exhibited a single global snap-back instability after the peak load. The largest specimen (b = 300

mm) exhibited completely brittle catastrophic instability, with the post-peak curve dropping almost vertically, accompanied by intense bursts of AE energy.

The data in Table 3.7 show that as the specimen size increased from 75 mm to 300 mm (a 64 fold increase in volume), the compressive strength decreased only slightly by 2.7%, but the cumulative number of AE events surged from 264 to 6742, an increase of approximately 25 times. This disproportionate sharp increase in the number of AE events indicates that damage evolution exhibits a significant size effect, and that AE energy emission does not increase linearly with volume.

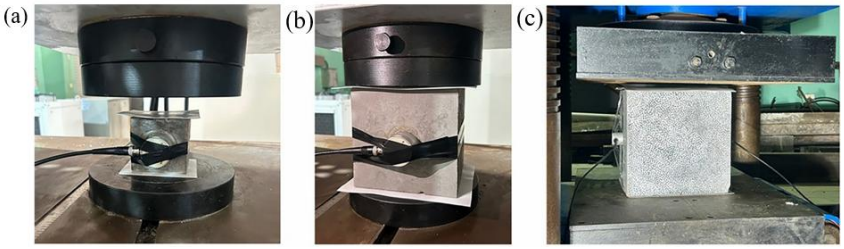


**Figure 3.13** Loading conditions of specimens with different base dimensions at a slenderness ratio of λ = 1.0: (a) b = 75 mm; (b) b = 150 mm; (c) b = 300 mm.

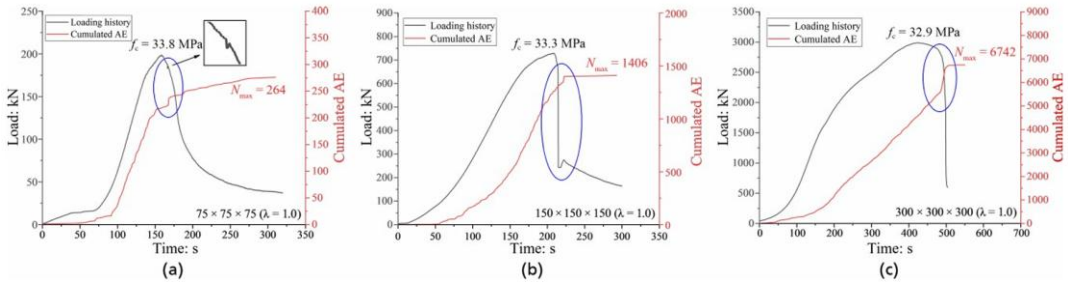


**Figure 3.14** Load history and cumulative AE curves of NC specimens with different dimensions at a slenderness ratio of λ = 1.0: (a) b = 75 mm; (b) b = 150 mm; (c) b = 300 mm

**Table 3.7** Comparison of compressive strength and AE signals for different sizes ($\lambda$ =1)

| Size (mm) | Compressive strength (MPa) | Strength reduction (%) | AE signals ($N_{max}$) | Failure mode |
|---|---|---|---|---|
| 75 | 33.8 | - | 264 | Softening |
| 150 | 33.3 | 1.5 | 1406 | Snap-back instability |
| 300 | 32.9 | 2.7 | 6742 | Catastrophic snap-back |

DIC technology provided intuitive evidence of surface strain evolution during the failure process. Figure 3.15 shows the final DIC strain contours of NC specimens with a base dimension of 300 mm under different slenderness ratios. The short thick

specimen (λ = 0.5) exhibited the initiation and propagation of multiple nearly vertical cracks, with a relatively diffuse strain field distribution, ultimately displaying crushing failure. The slender specimen (λ = 2.0) exhibited highly localized strain concentration, forming a single vertical crack, corresponding to typical brittle fracture. The square specimen (λ = 1.0) fell between the two extremes. These results indicate that as the slenderness ratio increases, the failure mode transitions from a ductile behavior of multi-crack crushing to a brittle behavior of single crack cracking.

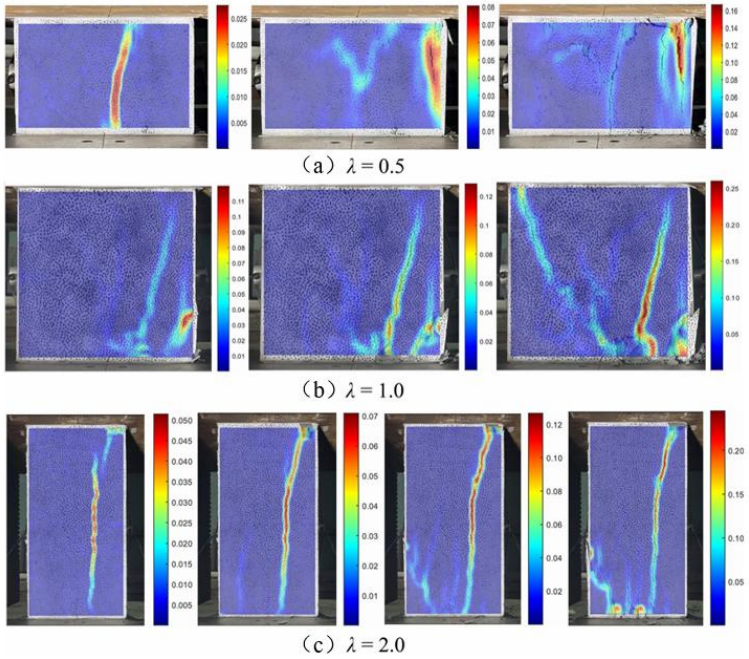


**Figure 3.15** DIC strain contours of NC specimens with a base dimension of 300 mm during failure under different slenderness ratios: (a) λ = 0.5; (b) λ = 1.0; (c) λ = 2.0

### 3.3.3 Fractal domain analysis of energy emission

As described in Section 2.3.5, according to fractal fragmentation theory, the energy $E$ emitted by microcrack propagation is confined to a fractal domain with a dimension $D$ between that of a surface and a volume [77]. Therefore, energy emission follows the size scaling law: $E \propto V^{D/3}$ (Eq. 2.16 in previous text), where $D$ is the fractal dimension ranging between 2.0 and 3.0. If $D$ = 3, damage is uniformly distributed throughout the entire volume; if $D$ = 2, damage is concentrated on a single fracture plane. This leads to the size independent fractal energy density parameter $\Gamma = E / V^{D/3}$

(Eq. 2.17). In AE monitoring, the emitted energy $E$ is proportional to the cumulative number of AE events $N_{max}$. Therefore, the fractal density of AE signals can be defined as $\Gamma_{AE} = \frac{N}{V^{D/3}}$ (Eq. 2.19), where $\Gamma_{AE}$ is also a size independent damage indicator.

Figure 3.16 shows the relationship between the cumulative number of AE events $N_{max}$ and the specimen volume $V$ for NC and UHPC specimens on a log-log scale. By fitting the experimental data, the slope $D/3$, which characterizes the fractal feature of the AE energy emission domain, can be obtained.

The fitted slope for NC specimens was 0.73, corresponding to a fractal dimension $D$ = 2.19 (Fig. 3.16b), while the fitted slope for UHPC specimens was 0.92, corresponding to a fractal dimension $D$ = 2.76 (Fig. 3.16a). Thus, the experimental fractal dimension of NC is closer to 2, indicating that AE energy emission upon failure occurs in a fractal domain close to a two dimensional plane. The fractal dimension of UHPC is significantly closer to 3, indicating that due to the bridging effect of steel fibers, the damage evolution of UHPC occurs in a domain closer to a volume (three dimensional space). This confirms that fiber bridging effectively inhibits damage localization and the formation of macroscopic cracks, allowing the material to withstand more extensive microcrack damage before failure, thereby exhibiting higher toughness and ductility.

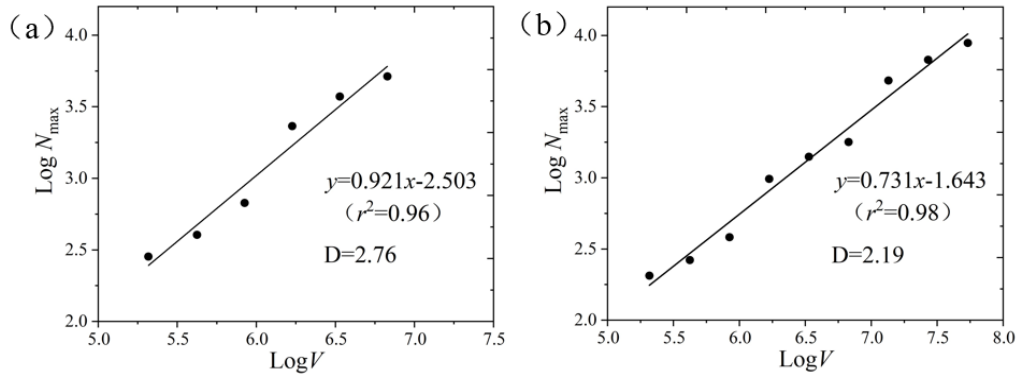


**Figure 3.16** Fractal domain analysis of AE energy emission: (a) UHPC; (b) NC.

From the perspective of statistical physics of energy emission, this study quantitatively elucidates the microscopic mechanisms of size effects and fiber

reinforcement, providing an important basis for size effect analysis and performance optimization design of concrete structures.

## 3.4 AE characteristics of bending failure in long-term loaded concrete beams strengthened with UHPC

Existing concrete structures under long-term loading and environmental actions may experience concrete carbonation, cracking, and steel reinforcement corrosion, leading to a reduction in load bearing capacity and necessitating strengthening to improve their capacity. This section presents the UHPC strengthening of notched reinforced concrete (RC) beams that had been subjected to long-term loading for approximately 24 years. Four point bending tests were conducted, and the flexural failure mechanism of strengthened beams was analyzed using AE technique.

### 3.4.1 Experimental overview

The long-term loaded RC beams were made of C30 concrete and HRB335 steel reinforcement. The concrete mix proportion is shown in Table 3.8. The dimensions and reinforcement details of the RC beam cross section are shown in Fig. 3.17. Two Φ10 steel bars were placed in the tensile zone, two Φ6 steel bars were placed in the compressive zone, and stirrups were arranged along the entire beam at equal spacing of 150 mm. The notch was symmetric about the longitudinal axis of the beam. The longitudinal length of the notch was 900 mm, and the depth was either 60 mm or 90 mm to simulate different existing damage states. Before strengthening, the notch surface was cleaned with high pressure air and a wire brush, and then pre wetted for 24 hours. Subsequently, UHPC was cast. Figure 3.18 shows the UHPC strengthening process of the notched beams. The UHPC strengthened beams were named U60 and U90, where the letter U represents the strengthened beam, and the numbers 60 and 90 indicate the depth of the strengthened notch as 60 mm or 90 mm. UHPC was prepared

using grade 52.5 ordinary Portland cement and incorporated straight round steel fibers with a volume fraction of 2% (length 12 mm, diameter 0.2 mm). The mix proportion and mechanical properties of UHPC are shown in Tables 3.9 and 3.10.

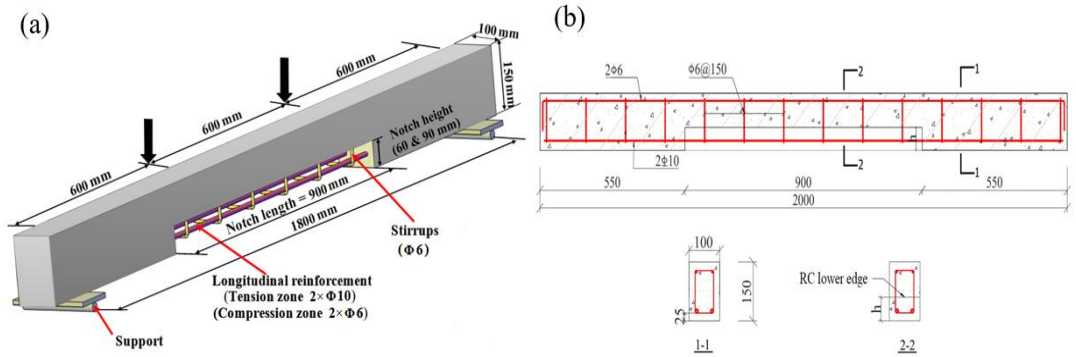


**Figure 3.17** Dimensions of RC notched beams. (a) Schematic diagram; (b) Reinforcement conditions (unit: mm)

**Table 3.8** RC strength and mix design

| Concrete grade | $f_{cu}$ /MPa | Water-cement ratio | Sand ratio | Dosage/(kg/m$^3$) | | | |
|---|---|---|---|---|---|---|---|
| | | | | Cement | Sand | Stone | Water |
| C30 | 28.1 | 0.44 | 38% | 445 | 676 | 1071 | 196 |

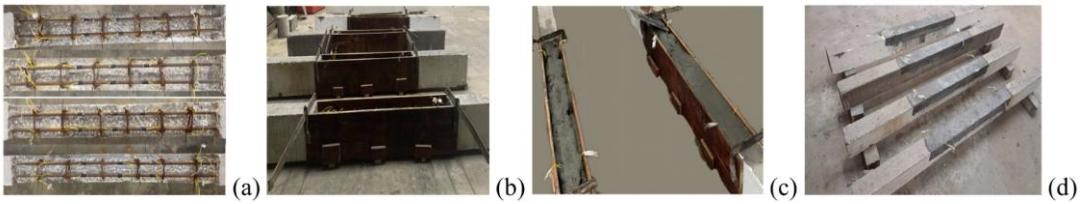


**Figure 3.18** UHPC strengthening process of notched beams: (a) interface treatment; (b) formwork erection; (c) UHPC casting; (d) curing.

**Table 3.9** UHPC mix /(kg/m$^3$)

| Component | Cement | Silica ash | Fly ash | Quartz sand | Water | Steel fibre | Polycarboxylate water reducer |
|---|---|---|---|---|---|---|---|
| Dosage | 850 | 137.5 | 112.5 | 1100 | 198 | 234 | 17.1 |

**Table 3.10** UHPC mechanical properties

| Material | Compression strength (MPa) | Elastic Modulus (GPa) | Flexural strength (MPa) | Uniaxial tensile strength (MPa) | Tensile strain capacity |
|---|---|---|---|---|---|
| UHPC | 131.1 | 44.3 | 10.8 | 8.5 | 0.25% |

As shown in Fig. 3.19, a 50 t MTS actuator was used to perform four point bending loading on the UHPC strengthened beams. A distribution beam ensured uniform loading at the two points. The loading process first adopted force controlled loading, with a load increment of 2.5 ± 0.25 kN per step and a loading rate of 0.1 kN/s. After the steel reinforcement yielded, the test switched to displacement controlled loading at a rate of 0.02 mm/s until the load dropped to 85% of the ultimate load, at which point loading was stopped. The vertical deflection at midspan of the beam was measured using displacement transducers, and concrete and steel reinforcement strains were simultaneously measured using resistance strain gauges. The AE monitoring system was the Italian ÆMISSION® system, with sensors having a frequency range of 10 kHz to 1 MHz. Four sensors (CH1 to CH4) were symmetrically arranged on the same side of the shear bending region at midspan of the beam (Fig. 3.17). The acquisition threshold was set to 2 mV, and the signals were amplified with a gain of 60 dB. Calibration was performed before the test using the pencil lead break test. The sensors were coupled and fixed to the beam using silicone resin.

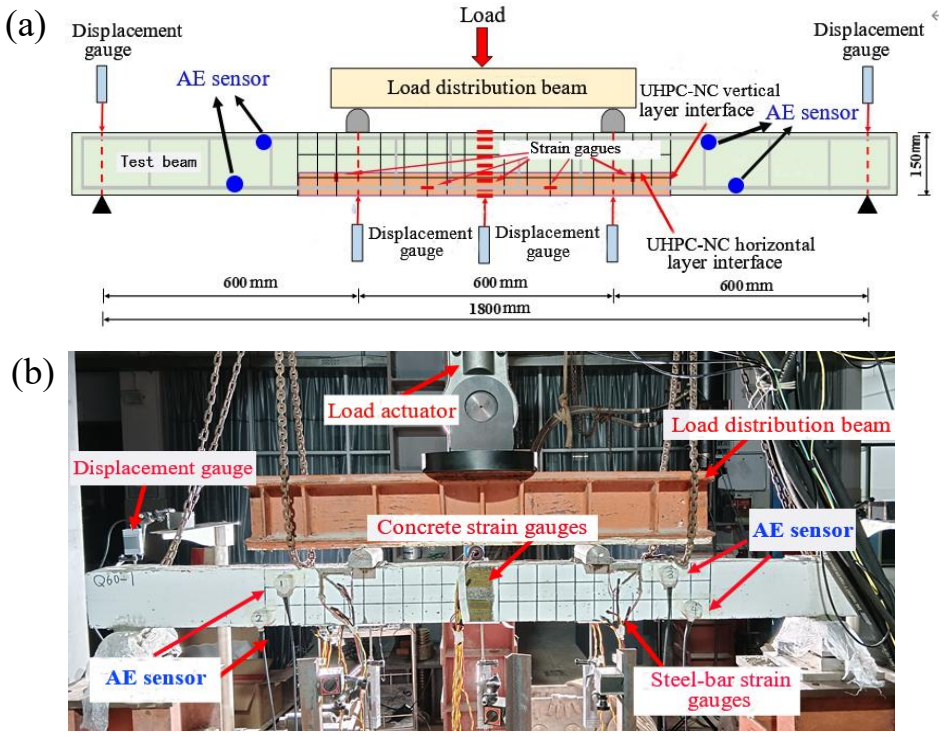


**Figure 3.19** Loading test and AE sensor layout: (a) schematic diagram; (b) loading site.

### 3.4.2 Relationship between damage evolution and AE

Based on crack observations during the flexural process, the load midspan deflection curve of the strengthened beams can be divided into four stages, as shown in Fig. 3.20. Stage I is the elastic stage, where damage within the beam is minor, microcracks are in the initial stage of initiation, and the midspan deflection increases approximately linearly. Stage II is the crack propagation stage. When the load increases to the initial cracking load F_cr, the load deflection curve deviates from linearity, local macroscopic cracks begin to appear until the steel reinforcement yields, corresponding to the stable crack propagation stage. Stage III is the strengthening stage. After the steel reinforcement yields, the fiber bridging effect of UHPC significantly enhances the fracture resistance. As the load increases to the ultimate load $F_u$, the load deflection curve reaches its peak point. Stage IV is the failure stage, where cracks propagate rapidly and the concrete at the top of the beam crushes, corresponding to unstable crack growth and structural failure. As shown in Fig. 3.20, the curve for beam U60 decreases rapidly after the ultimate load, exhibiting low ductility. Beam U90 exhibits a relatively longer plastic plateau, indicating larger plastic deformation and more pronounced ductility characteristics.

The load deflection results in Table 3.11 show that the ductility coefficient of beam U90 is 18% higher than that of beam U60, indicating that deeper UHPC strengthening effectively improves the overall ductility of the strengthened beams. Both beams exhibit a "staircase" phenomenon in the load deflection curves during Stages I and II, indicating that the influence of long-term loading is comprehensive and that local UHPC strengthening cannot completely eliminate the internal changes it induces.

The relationship between load deflection and AE is shown in Fig. 3.20(d) and (e). Peaks in AE rate correspond to yield load $F_y$ and ultimate load $F_u$ on load deflection curves. After reaching the yield point, multiple load drops (snap-back instabilities) are detected in load deflection curves, corresponding to AE energy emissions, indicating local snap-back instabilities caused by sudden increases in crack width.

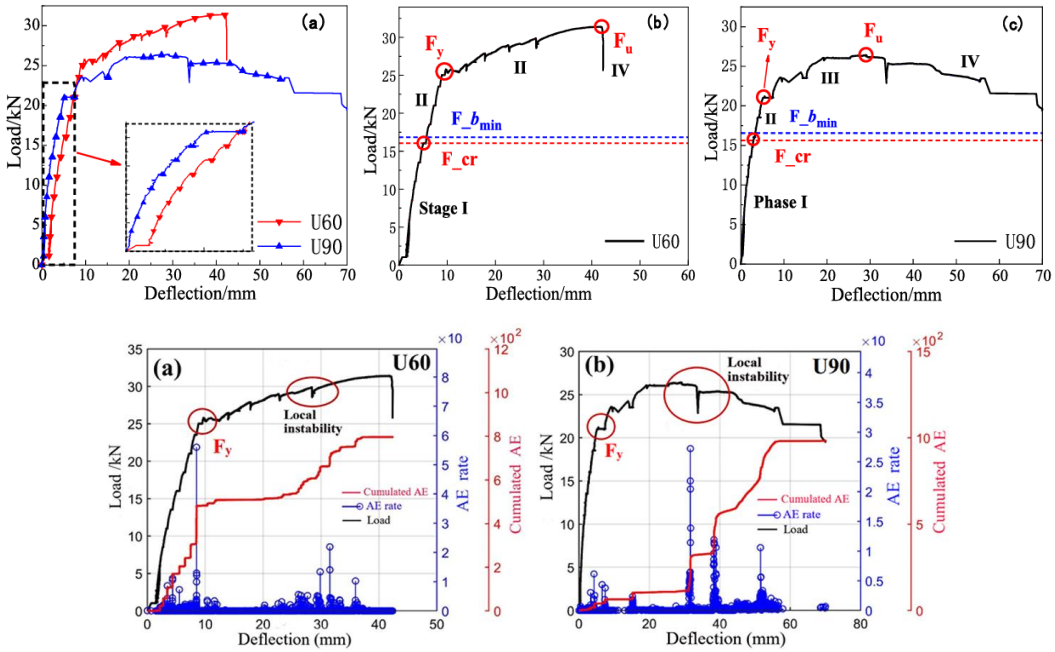


**Figure 3.20** Load-deflection curves (a–c) and AE results (d, e). F_$b_{min}$ denotes the critical load determined by the *b*-value method.

**Table 3.11** Main load-deflection values and ductility

| Beam | First fracturing load F_cr (kN) | Steel-rebar yield load $F_y$ (kN) | Ultimate load $F_u$ (kN) | Deflection at yield load Δy (mm) | Ultimate deflection Δu (mm) | Ductility coefficient μ= Δu / Δy |
|---|---|---|---|---|---|---|
| U60 | 16.4 | 25.4 | 31.4 | 9.6 | 42.1 | 4.4 |
| U90 | 15.9 | 21.2 | 26.4 | 5.6 | 29.2 | 5.2 |

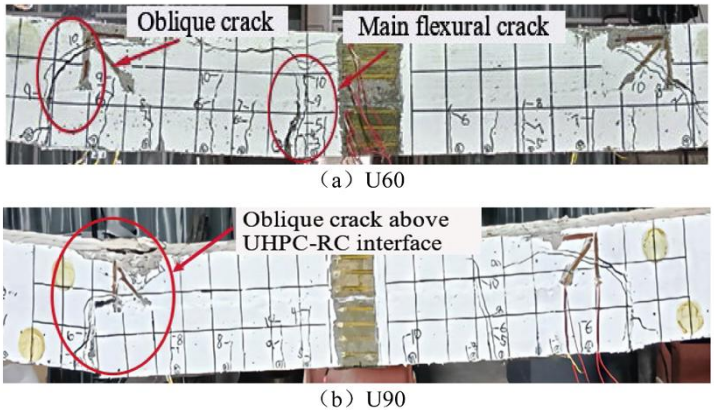


（a）U60

（b）U90

**Figure 3.21** Failure modes of strengthened beams: (a) Beam U60; (b) Beam U90

Figure 3.21 shows the failure modes of the strengthened beams. The analysis indicates that debonding occurred at the UHPC RC notch vertical interface in both beams U60 and U90, while the horizontal interface remained intact. In beam U60, the

main flexural crack penetrated the horizontal interface and propagated into the RC layer. In beam U90, the flexural cracks were mainly confined to the UHPC layer, and the critical failure was dominated by diagonal cracks initiated at the vertical interface. This indicates that the UHPC RC vertical interface is a key meso scale fracture process zone, and its behavior dominates the failure mode.

AE monitoring provided a unique perspective for real-time understanding of damage evolution. Based on the methods in Chapter 2, the AE events detected by the system during the test were grouped into sets of 100 events, and the exponent $\beta_t$ (Eq. 2.24) and the *b*-value (Eq. 2.20) were calculated. Fig. 3.22(a) and (b) show the $\beta_t$ and *b*-value results from AE, with the dashed line representing the *b*-value regression curve. The *b*-value regression curve for beam U60 shows a decreasing trend, declining from 1.5 to 1, revealing unstable crack propagation. In contrast, beam U90 exhibited relatively stable crack propagation, with the *b*-value remaining nearly constant throughout the test.

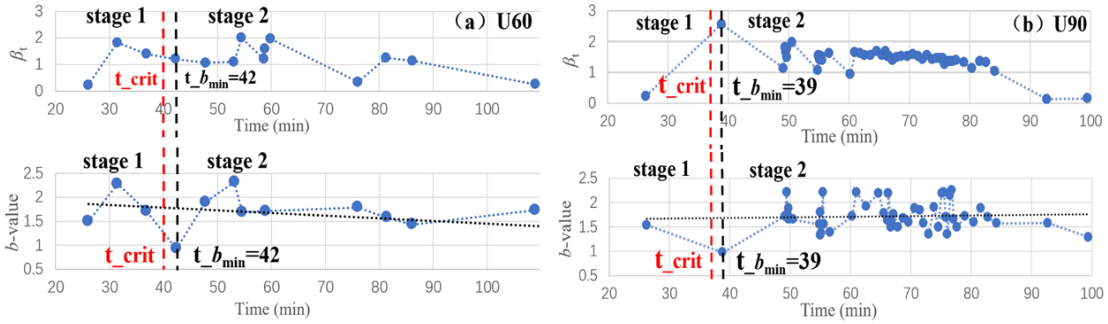


**Figure 3.22** Evolution of $\beta_t$ and *b*-value of AE for strengthened beams: (a) Beam U60; (b) Beam U90. t_crit denotes the critical time determined by NT analysis.

**Table 3.12** Comparison of first fracturing load

| Strengthened beam | Loading history F_cr (kN) | *b*-value F_$b_{min}$ (kN) | Deviation |
|---|---|---|---|
| U60 | 16.4 | 16.7 | 1.8% |
| U90 | 15.9 | 16.1 | 1.3% |

Beam U60 reached the critical condition for macroscopic crack propagation at 42 minutes (t_$b_{min}$, $b_{min}$ = 0.9, $\beta_t$ = 1.2 >1), corresponding to the initiation of the main flexural crack at the bottom of the strengthened zone, as shown in Fig. 3.21(a). The

critical point for beam U90 occurred at 39 minutes (t_$b_{min}$, $b_{min}$ = 1.0, $\beta_t$ = 2.5 >1), corresponding to the cracking of the left UHPC-RC vertical interface, as shown in Fig. 3.21(b). As shown in Table 3.12 and Fig. 3.20, the *b*-value method agreed well with the initial cracking load determined from the load-displacement curve, and t_$b_{min}$ accurately identified the initial cracking point of the beams.

Furthermore, NT analysis (see Section 2.4.3) was further applied, and the evolution of the NT variance $\kappa_1$, entropy $S$, and its time reversed entropy $S_{rev}$ over time was extracted. The results are shown in Fig. 3.23. According to the critical conditions of NT analysis, namely $\kappa_1$ approaching 0.07, and $S$ and $S_{rev}$ falling below the uniform noise entropy $S_u$= 0.0966, the critical time t_crit was determined, as indicated by the vertical dashed line in Fig. 3.23. The results in Fig. 3.22 and 3.23 show that t_crit identified by NT analysis is consistently slightly earlier than $t\_b_{min}$ determined by the *b*-value method, with a deviation within 3% between the two (see Table 3.13). This validates the consistency of the methods and indicates that the critical point of the NT variance can serve as an earlier warning indicator of impending failure.

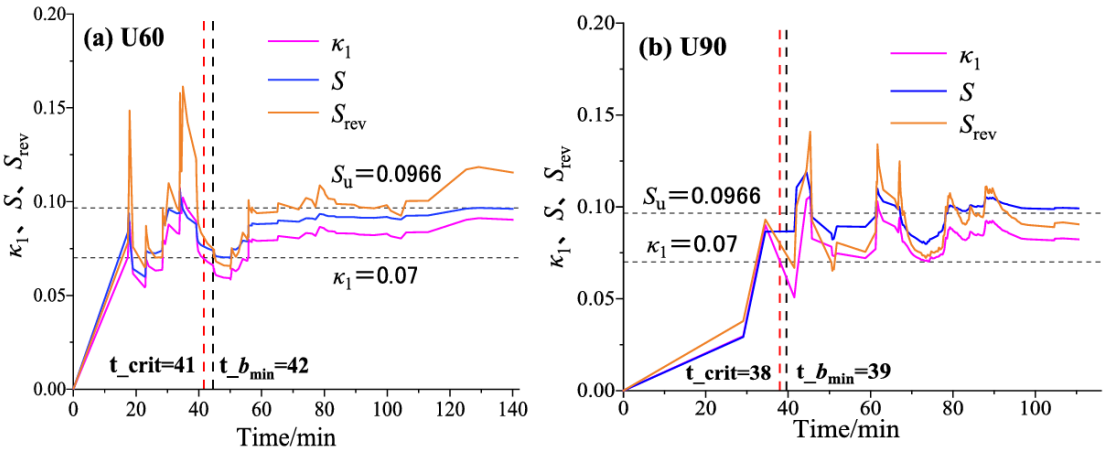


**Figure 3.23** NT analysis results of AE for strengthened beams: (a) Beam U60; (b) Beam U90.

**Table 3.13** Comparison between the natural time and *b*-value

| AE analysis method | Time of first fracturing (minutes) | |
|---|---|---|
| | U60 | U90 |
| *b*-value (t_$b_{min}$) | 42 | 39 |
| Natural time (t_crit) | 41 | 38 |
| Deviation | 2.3% | 2.5% |

### 3.4.3 Damage and fracture mechanisms based on AE

The crack mode analysis based on AE adopted the RA-AF method, as described in Section 2.3.3, Equations (2.9) and (2.10). This method can effectively distinguish between tensile (Mode I) and shear (Mode II) crack modes. The initial cracking point t_$b_{min}$ of the beams was obtained from the *b*-value method as described earlier. Around t_$b_{min}$, cracks transition from global microcracks to local macrocracks. As annotated in Fig. 3.22, the flexural process was divided into two stages. In Stage 1, microcracks diffuse globally within the beam. In Stage 2, macrocracks form and propagate. RA-AF analysis was performed separately for the two stages. Figure 3.24 shows the RA-AF analysis results for beams U60 and U90 at different damage stages.

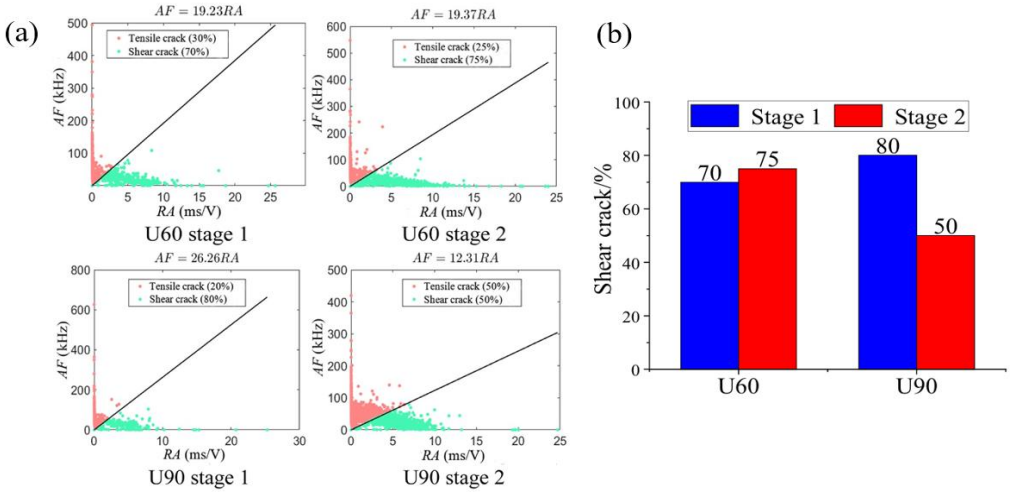


**Figure 3.24** RA-AF analysis of strengthened beams: (a) calculation results at different stages; (b) proportions of crack types.

The analysis indicates that in the initial stage, shear cracks dominate the structural response. However, in Stage 2, for beam U90, tensile cracks gradually become the dominant failure mechanism, highlighting the ductility enhancement achieved through deeper notch UHPC strengthening. This transition of failure mode from shear dominated to flexural dominated is consistent with the post-peak ductile behavior observed in the load-displacement relationship (Fig. 3.20) and aligns with the fundamental transition of the energy dissipation mechanism from Mode II to Mode I fracture. The deeper strengthening layer effectively reduces the overall brittleness of

the structure while decreasing the number of shear cracks. The proportions of crack modes at different stages are shown in Fig. 3.24(b). In the final failure stage, the proportion of tensile cracks in beam U90 increased by approximately 25% compared to beam U60, confirming its transition to a more ductile fracture mode.

Synthesizing the above AE analysis, it is evident that the UHPC layer fundamentally alters the damage evolution process. For beam U90, the stable *b*-value and the transition from shear to tensile cracking mode identified by RA-AF analysis provide quantitative characteristics of its enhanced ductility before its macroscopic manifestation. Conversely, the decreasing *b*-value and the critical point identified by NT analysis for beam U60 provide early warning of its impending brittle failure.

This section demonstrates that AE technique is not merely a passive recording tool for the fracture process but also an active diagnostic tool, under the framework of fracture mechanics, for revealing the entire process from microscopic damage accumulation and meso scale interface debonding to macroscopic structural instability. Through comprehensive analysis of the *b*-value, NT parameters, and RA-AF patterns, it is possible to reliably identify precursors of macroscopic fracture and quantify the transition of cracking modes. This provides profound insights beyond traditional macroscopic measurements for performance evaluation and health monitoring of UHPC strengthened RC components under long-term loading.

## 3.5 Field AE measurement of UHPC crack propagation in a Steel-UHPC composite bridge deck

The orthotropic steel deck (OSD) offers advantages such as light self weight, good load bearing capacity, large span capability, and fast assembly. With the development of UHPC technology, steel UHPC composite bridge decks have been widely used in long span cable stayed bridges. This composite structure can significantly increase the stiffness of the steel deck, reduce local stress effects under wheel loads, and effectively inhibit OSD fatigue cracking. However, due to the low water to binder ratio, the UHPC

deck layer exhibits large drying shrinkage during curing, which can easily induce shrinkage cracks and potentially reduce material durability. This potential issue poses a challenge to the application of UHPC material.

This section presents field AE measurement and data analysis work addressing the drying shrinkage cracking that occurred during the construction of a steel-UHPC composite bridge deck of a long-span cable-stayed bridge. The study aims to reveal the dynamic propagation behavior of cracks in the actual UHPC layer and to validate the applicability and reliability of AE technique for health monitoring of major bridge structures, thereby providing a reference for construction quality control and the avoidance of early cracking in steel-UHPC composite bridge decks.

### 3.5.1 Bridge overview and monitoring system layout

The research object is a twin tower cable stayed bridge located in South China. The bridge elevation layout is shown in Fig. 3.25. The main girder is a plate truss structure combining a steel truss and an OSD, with its cross section shown in Fig. 3.26. The upper deck carries highway traffic, featuring bidirectional three lanes with emergency lanes on both sides. The lower deck accommodates an urban rail transit line. As shown in Fig. 3.27, the steel deck adopts a steel UHPC composite structural system. The specific construction of this system is as follows: short shear studs are welded onto a 16 mm thick steel deck plate, followed by casting a 50 mm thick UHPC structural layer, and finally surfacing with a 40 mm thick SMA 13 asphalt wearing course. Figure 3.28 shows the construction process of the UHPC deck layer. Steam curing can enhance the final strength of the UHPC layer in a short period. At the time of testing, the UHPC deck layer had been cured, but the wearing course was yet to be constructed.

A finite element model of the bridge was established using ANSYS (Fig. 3.25). The model coordinate system was set according to the bridge longitudinal ($x$), transverse ($y$), and vertical ($z$) directions. Beam elements were used to model the steel truss, towers, and piers. Cable elements were used to model the stay cables. Shell elements were used to model the steel deck plate and the UHPC layer. The elastic moduli of steel and

concrete were taken as $2.06 \times 10^5$ MPa and $3.4 \times 10^4$ MPa, respectively, and Poisson's ratios were taken as 0.3 and 0.2, respectively. Soil structure interaction was not considered, and all degrees of freedom of the piers and towers were constrained. Constant load stress analysis indicated that the UHPC deck layer near the midspan was in a tensile state; therefore, this area was selected as the test monitoring zone.

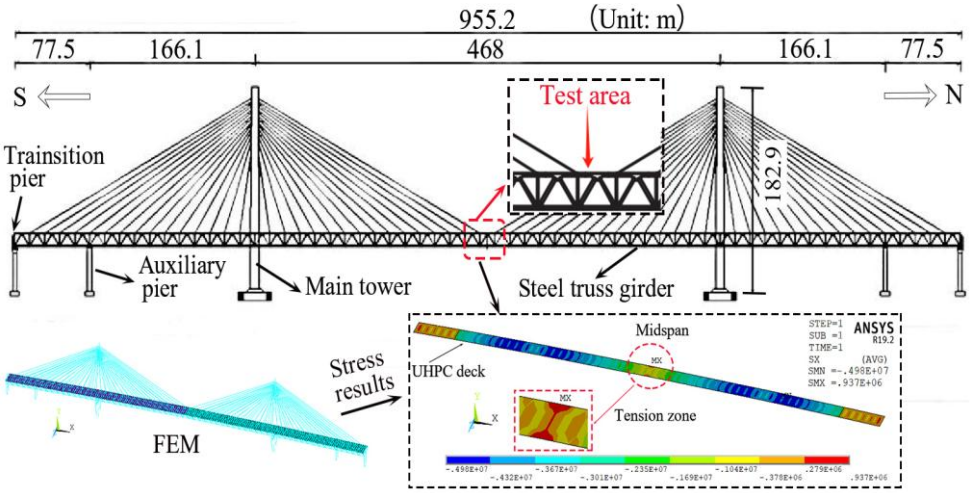


**Figure 3.25** Bridge elevation layout and finite element model.

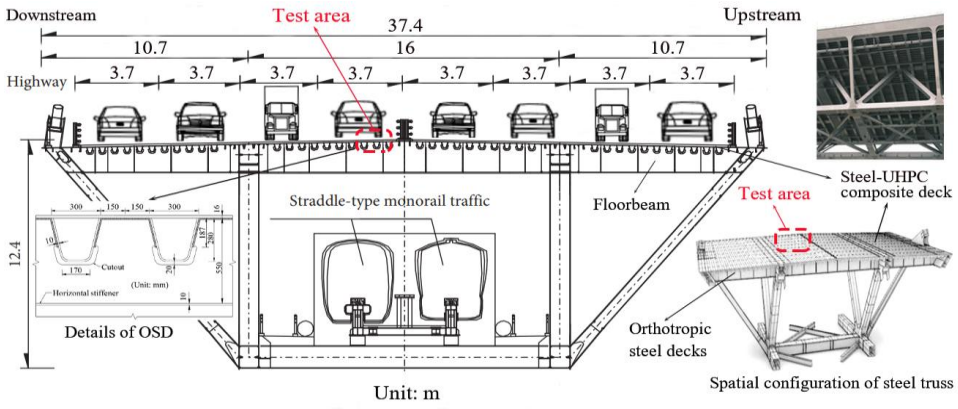


**Figure 3.26** Standard cross-section configuration of the steel truss girder.

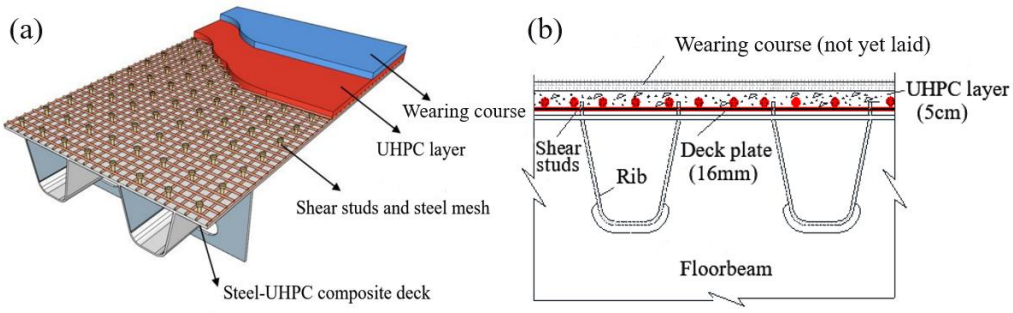


**Figure 3.27** Steel-UHPC composite deck: (a) isometric schematic; (b) cross-section.

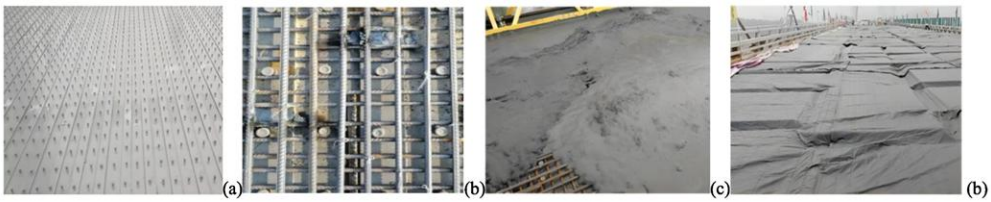


**Figure 3.28** UHPC construction process: welded shear studs (a); steel mesh (b); pouring (c); steam curing (d).

After the construction of the UHPC deck layer was completed, a new transverse crack was found on the south side of the bridge deck at the midspan of the main span, as shown in Fig. 3.29(b). The crack was visible to the naked eye. Field measurements showed that the initial length of the crack was approximately 30 mm, distributed transversely across the bridge deck. It was speculated that the crack was caused by early age drying shrinkage of the UHPC. The monitoring area was selected at the location of the crack, as shown in Fig. 3.29(a) and (c). This area is located between two transverse diaphragms of the main girder and belongs to a stress sensitive region of the deck system. The crack could potentially further propagate due to subsequent construction vehicle traffic and temperature variations.

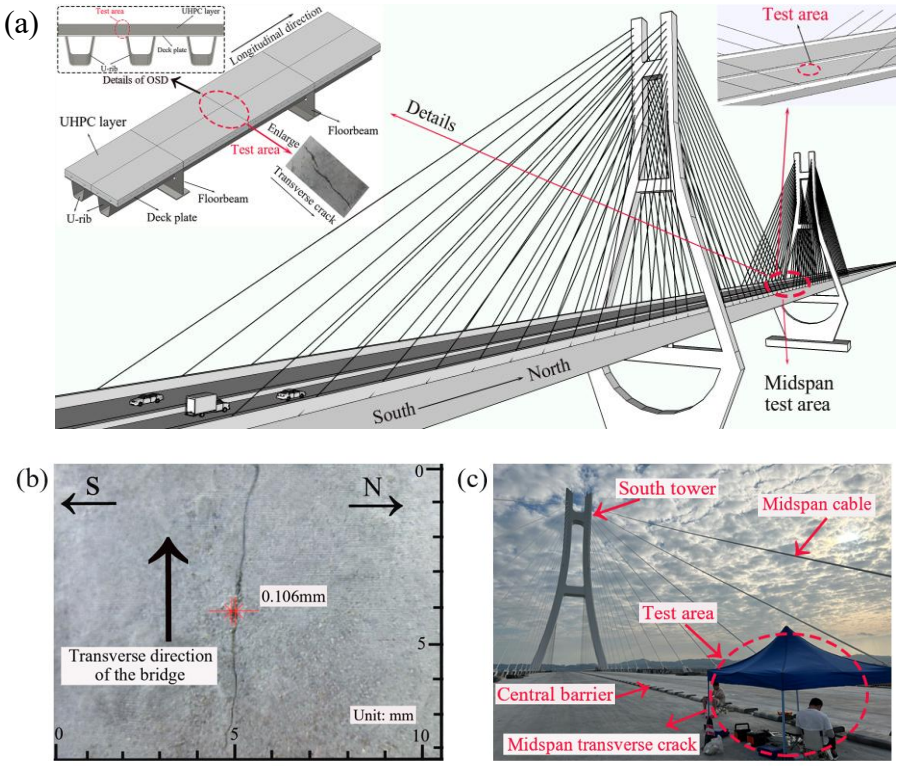


**Figure 3.29** UHPC cracking location and testing area on bridge deck: (a) 3D schematic of main bridge and testing location; (b) local morphology of UHPC crack; (c) monitoring site.

To monitor crack activity, the study employed the ÆMISSION® monitoring system, as shown in Fig. 3.30(a) and (b). This system integrates data acquisition and wireless transmission functions, with sensors having a frequency range of 10 kHz to 1 MHz. In the selected monitoring area, four AE sensors were arranged in a quadrilateral array on the UHPC deck layer (Fig. 3.30c), bonded with silicone resin and fixed with tape to achieve effective spatial localization of the crack source. To effectively extract crack signals from complex field environmental noise, a three hour background noise acquisition and analysis was completed before monitoring began. Statistical analysis showed that the background noise amplitude approximately followed a normal distribution with a mean of 1.2 mV and a standard deviation of 0.3 mV. Based on the 3σ principle, the acquisition threshold was set to 2 mV. Verification showed that this threshold could effectively suppress approximately 99% of the environmental noise, with a signal false alarm rate of only 0.5%. In addition, during post processing, short duration pulse signals (potentially from electromagnetic interference) with a duration of less than 3 μs and low frequency vibration signals (mainly from wind loads and global structural vibration) below 20 kHz were further filtered out to improve the correlation between AE signals and crack activity.

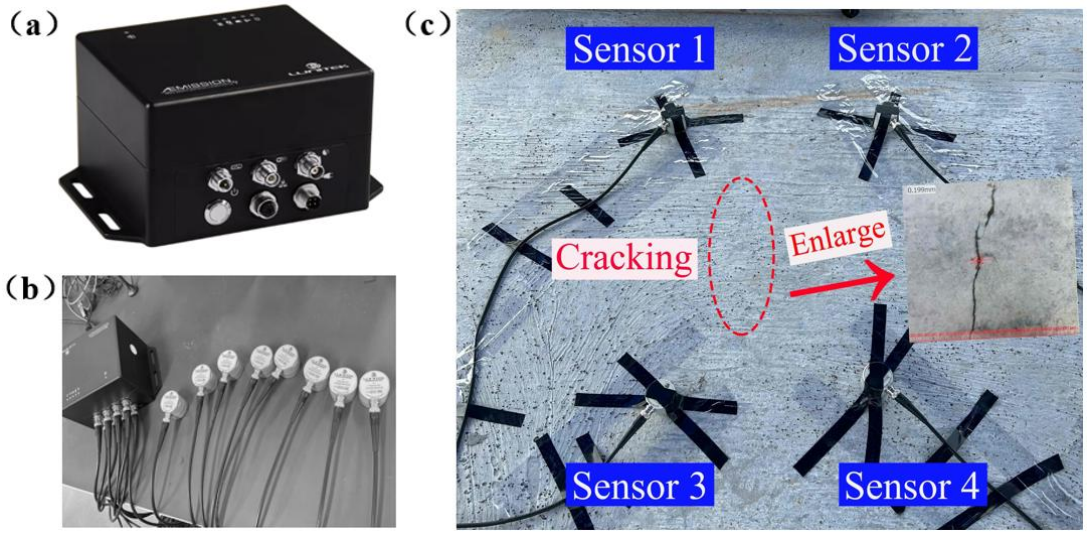


**Figure 3.30** AE monitoring system layout on the UHPC deck layer: (a, b) AE acquisition devices; (c) sensor arrangement on the bridge deck.

### 3.5.2 AE damage evolution analysis and crack source localization

Data recording began at 3:00 PM on October 23, 2023, in the UHPC deck layer test area, with continuous monitoring until 9:00 PM that evening. During the selected time period (3:00 AM to 6:45 AM), crack propagation and arrest in the monitoring area were clearly observed. The evolution curves of the AE event rate (events per minute) and the cumulative number of AE events during the entire monitoring period are shown in Fig. 3.31(a) and (b). It can be seen that around the 73rd and 183rd minutes of monitoring, two significant bursts of AE signals occurred, and the cumulative event curve exhibited stepwise growth, indicating that the crack experienced two major propagation stages.

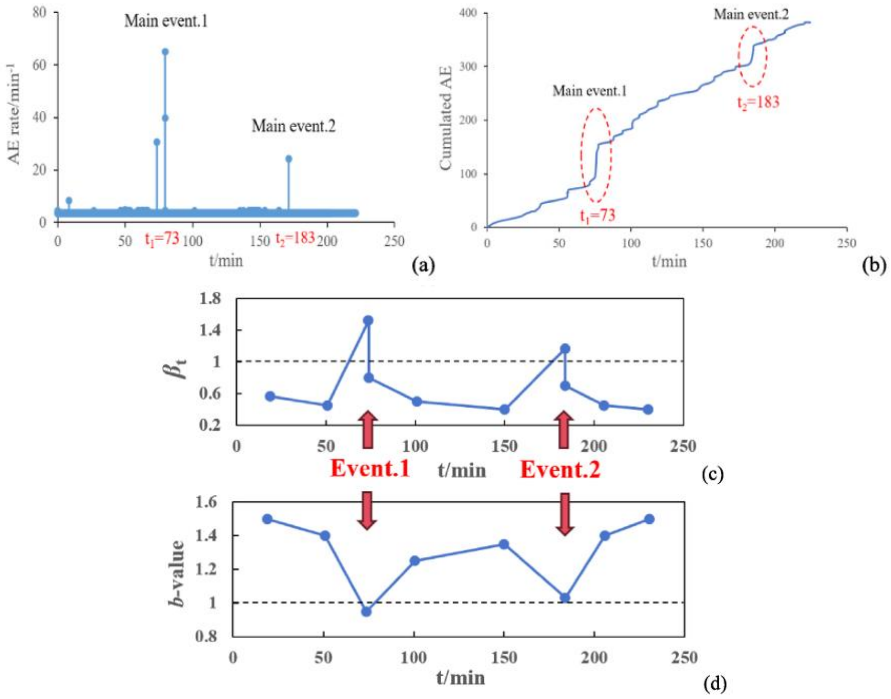


**Figure 3.31** AE time series results: AE signals rate (a); Cumulated AE (b); AE $\beta_t$ coefficient and *b*-value (c), (d).

To quantitatively characterize the damage evolution state, $\beta_t$ and *b*-value analyses were performed on the AE time series using the methods described in Sections 2.4.1 and 2.4.2. The data were processed using a sliding window of 50 events, and the *b*-value and $\beta_t$ exponent were calculated, with the results shown in Fig. 3.31(c) and (d). In the early stage of monitoring (first 50 minutes), the *b*-value remained between 1.4 and 1.5, and the $\beta_t$ value was approximately 0.5. This stage corresponds to a damage

state of microcrack initiation and stable propagation. During the two bursts of AE signals at the 73rd and 183rd minutes, the *b*-value rapidly decreased to around the critical value of 1.0, while the $\beta_t$ value jumped to approximately 1.5. A *b*-value drop to 1.0 typically indicates the coalescence of microcracks into macrocracks, while $\beta_t > 1$ indicates that the damage process is in an unstable accelerating state. The synchronous changes of these two AE parameters confirmed, from a statistical physics perspective, the occurrence of two significant unstable macroscopic crack propagation events during the monitoring period.

To verify the reliability of the AE monitoring results, the width and length of the crack in the monitoring area were also measured periodically (every 20 minutes) using a crack gauge. The results are shown in Fig. 3.32. Comparison shows that the two sudden increases (jumps) in crack width and length measured in the field coincided in time with the two major AE signal bursts detected by the monitoring system. Furthermore, the peak AE event rate showed a positive correlation with the magnitude of the crack jumps, indicating that more intense AE activity corresponds to a larger increase in crack dimensions. This spatiotemporal correlation confirms that the AE signals originate from the crack propagation process and also indicates that AE parameters can sensitively reflect the intensity of crack propagation. The precise temporal correspondence between the two peaks in AE event rate and the two jumps in crack width and length, along with the positive correlation in their magnitudes, demonstrates the reliability of AE activity as a direct acoustic signature of dynamic crack propagation.

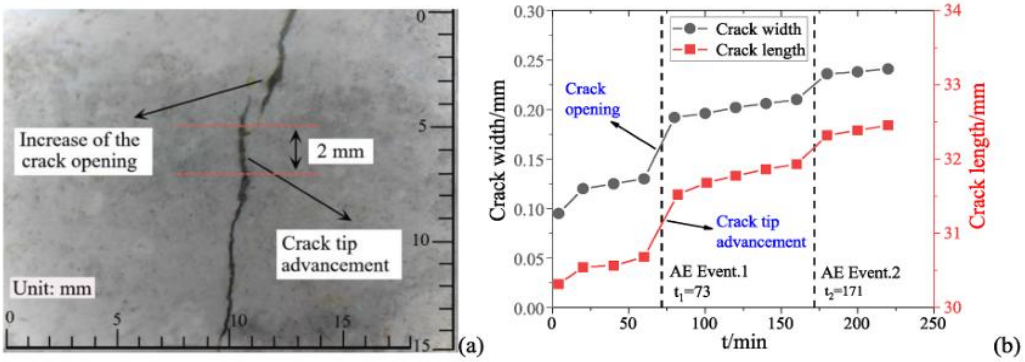


**Figure 3.32** Crack morphology measured in field: (a) crack image; (b) crack growth curve.

Based on the AE source localization principle described in Section 2.3.4, the time differences of arrival of signals received by the four sensors were used to solve the triangulation equations using the least squares method and the Gauss Newton iterative algorithm, inverting the spatial coordinates of each AE source event. The AE source localization results (represented by red dots) are shown in Fig. 3.33.

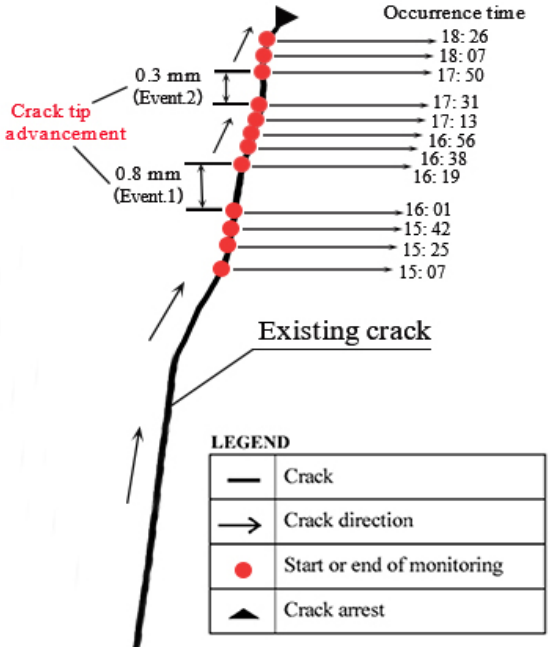


**Figure 3.33** Crack tip propagation trajectory from AE source localization.

The distribution of red dots in Fig. 3.33 clearly outlines the propagation trajectory of the crack tip. The upward movement trend of the red dots indicates that the crack tip propagated progressively. This evidence is consistent with the crack morphology measured in the field (Fig. 3.32). Additionally, the group of AE source points in Fig. 3.33 shows two large spatial gaps, corresponding to the two major AE events at the 73rd and 183rd minutes, respectively. This confirms the two crack tip propagations from a spatial localization perspective. As shown in Fig. 3.33, the crack eventually entered an arrest stage.

The agreement between the AE source localization results and the manually measured crack propagation morphology demonstrates that AE technique possesses the capability to dynamically and accurately track the position of a crack tip.

### 3.5.3 Analysis and discussion of crack propagation triggers

During the monitoring period, the bridge deck had not yet been paved with asphalt, allowing construction vehicles to pass. To investigate the triggers of crack propagation, the cumulative AE event curve was analyzed in correspondence with vehicle records on the bridge during the same period (provided by the bridge management authority). The results are shown in Fig. 3.34(a). The analysis found that the timing of the two major AE event bursts closely corresponded to the periods when traffic volume on the bridge peaked. Furthermore, the cumulative AE curve exhibited a rapid increase immediately after the traffic peaks. This strong correlation indicates that the cyclic bending deformation of the deck structure induced by construction vehicle passage and vehicle bridge coupling vibrations were the main external load sources driving the further propagation of existing drying shrinkage cracks in the UHPC deck layer.

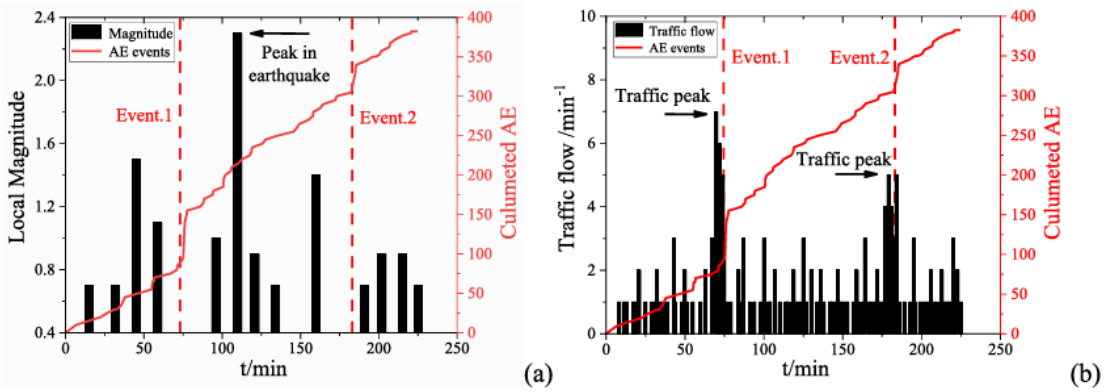


**Figure 3.34** AE and environmental effects: AE and earthquakes (a); AE and vehicle traffic (b).

It should be noted that at 3:20 AM on the monitoring day (October 23, 2023), a magnitude 5.0 earthquake occurred in the sea area several tens of kilometers from the bridge site, and aftershocks were present during the monitoring period. To clarify the influence of the earthquake on crack propagation, the AE activity time series was compared with the earthquake catalog within a 20 km radius of the monitoring point, as shown in Fig. 3.34(b). Statistical analysis showed that there was no clear temporal correlation between the bursts of AE signals and the occurrence of seismic events, and AE activity did not increase after every earthquake. Therefore, during the specific

monitoring period of this case, seismic activity had a negligible influence on the propagation of cracks in the UHPC deck layer, and the cracking was primarily attributed to traffic vehicles.

This field measurement case fully demonstrates the unique advantages of AE technique in structural health monitoring, especially in dynamic crack monitoring: 1) it can capture the initiation of microcracks and internal propagation activities invisible to the naked eye online, enabling early detection; 2) through sensor arrays, it can achieve planar or even spatial localization of damage sources, accurately tracking the crack tip; 3) combined with parameters such as the $b$-value and $\beta_t$, it can quantitatively judge the damage stage and stability. However, challenges also exist in practical applications: field wind, rain, traffic vibrations, etc., generate substantial environmental noise, requiring reasonable threshold settings, filtering techniques, and signal processing algorithms to ensure the signal to noise ratio; the massive amount of AE data requires professional algorithms for interpretation to distinguish structural damage signals from other non damage related signals. This study demonstrates that AE technique is an effective tool for real-time identification, localization, and state assessment of hidden damage in in service bridge structures, providing important technical means and practical references for construction quality control during construction and long-term health monitoring during operation of new bridge systems such as steel UHPC composite structures.

## 3.6 Precursor identification and validation of flexural failure in GFRP bar reinforced concrete beams

This section presents four point bending tests on glass fiber reinforced polymer (GFRP) bar reinforced concrete beams. Combined with AE and DIC techniques, the damage evolution during flexural failure and the bond-slip behavior between the GFRP bars and concrete were investigated. The tests aimed to validate the effectiveness of the MCF-B method proposed in Chapter 2 for identifying critical failure precursors in

structures and to compare its performance with traditional *b*-value analysis, NT analysis, AE entropy analysis, and the DPH index.

### 3.6.1 Experimental overview and mechanical response results

The GFRP bar reinforced concrete beams had a cross section of 200 mm × 200 mm and a total length of 1800 mm. Detailed information is shown in Fig. 3.35. A notch was reserved at midspan of the beam, and the top of the notch was connected by a steel hinge (see Fig. 3.35). Two ribbed sand coated GFRP bars with a diameter of 12 mm were placed at the bottom of the beam as the main tensile reinforcement (morphology shown in Fig. 3.36). Under four point bending, the bottom of the midspan region is the pure bending segment, subjected to the maximum tensile stress. Therefore, the high tensile strength GFRP bars were arranged here to fully utilize their tensile performance. Additionally, two longitudinal bars with a diameter of 10 mm were placed at the top and bottom of the beam, serving as compression reinforcement (top) and mounting bars (bottom), respectively, to ensure the integrity of the beam. The longitudinal bars were fixed by HPB300 stirrups with a diameter of 8 mm spaced at 200 mm, collectively forming the overall reinforcement cage.

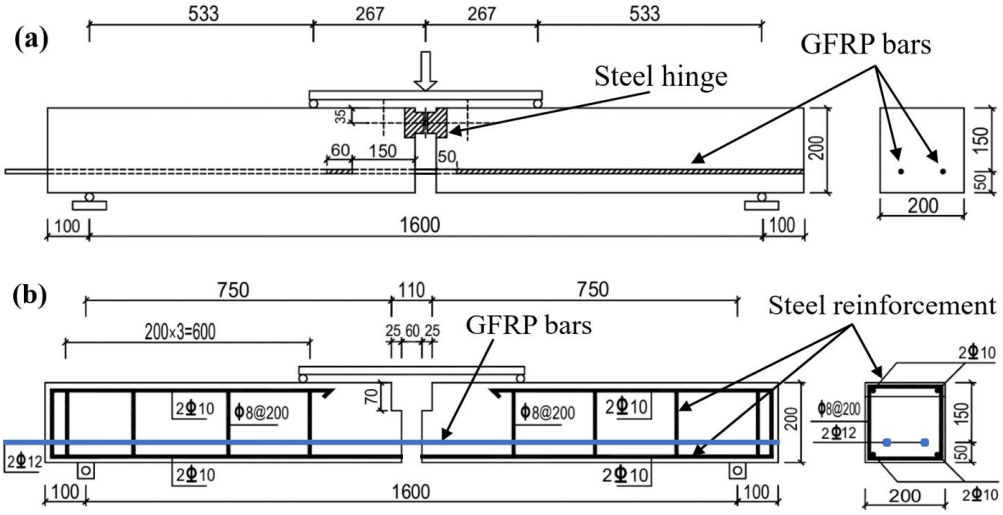


**Figure 3.35** Beam geometry and reinforcement (Unit: mm): (a) GFRP bars; (b)Steel reinforcement.

To induce local damage and study the bond-slip mechanism, a notch was created at the midspan of the beam, as indicated in Fig. 3.35(a). In the pure bending segment on the right side of midspan, the GFRP bar had a 50 mm unbonded segment to prevent premature failure of the concrete at the edge of the compression zone in the pure bending segment. On the left side of midspan, the reinforcement in the pure bending segment had a 150 mm unbonded segment, and the free end was also in an unbonded state. The concrete strength grade was C100, with a mix proportion shown in Table 3.14. The measured 28 day cubic compressive strength was 110.4 MPa, and the elastic modulus was 44.8 GPa. The mechanical properties of the GFRP bars were determined through tensile tests, yielding an average ultimate tensile strength of 1164 MPa and an elastic modulus of 56.4 GPa. Specific characteristics are shown in Table 3.15. The tests monitored the mechanical behavior and crack evolution patterns of three beams.

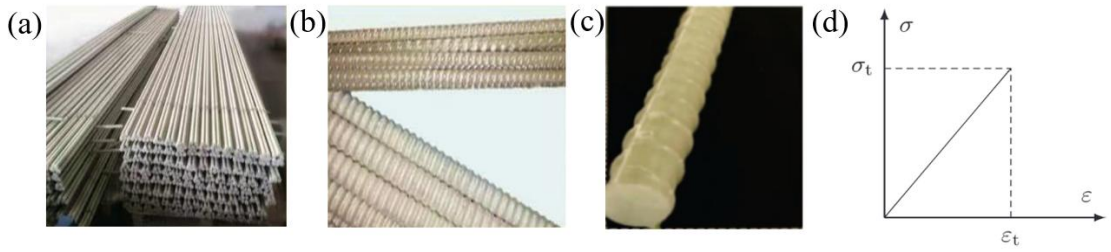


**Figure 3.36** Characterization of the GFRP bars: (a),(b) overall view; (c) close-up view of the sand-coated ribbed surface; (d) representative tensile stress-strain curve.

**Table 3.14** Concrete mix proportion（kg/m³）

| Component | Cement | Silica fume | Fly ash | River sand | Coarse aggregate | Water | Polycarboxylate water reducer |
|---|---|---|---|---|---|---|---|
| Dosage | 1.0 | 0.20 | 0.05 | 1.15 | 1.85 | 0.18 | 0.035 |

**Table 3.15** Mechanical properties of GFRP bars

| Type of bar surface | Cross-section type | Rib spacing (mm) | Bar diameter (mm) | Ultimate strength (MPa) | Elastic modulus (GPa) |
|---|---|---|---|---|---|
| Ribs | Round | 10 | 12 | 1164 | 56.4 |

Four point bending loading was adopted. The short distance of 267 mm between the loading points and supports was designed to create high shear stress conditions,

thereby inducing a bond-slip failure mode at the GFRP bar concrete interface. A crack mouth opening displacement (CMOD) gauge was installed at the notch in the midspan of the beam, and four vertical displacement transducers were arranged along the bottom edge of the beam. Additionally, two AE sensors were placed along the GFRP bar arrangement direction, as shown in Fig. 3.37(a). The AE system was manufactured by Lunitek, Italy, equipped with piezoelectric sensors (frequency range 10 kHz to 1 MHz), which were bonded and fixed to the beam surface using silicone resin (see Fig. 3.37b). The acquisition threshold was set to 2 mV. As shown in Fig. 3.37(c), the strain distribution in the notch region on the front face of the beam was captured and quantified using a DIC system, with the analysis focusing on the strain evolution in the vicinity of the GFRP bars. The test employed a 100 kN MTS loading system controlled by CMOD. The initial loading rate was 0.05 mm/min, which was increased to 0.2 mm/min after the crack opening reached 0.1 mm, until the load dropped to 85% of the peak load, at which point loading was stopped.

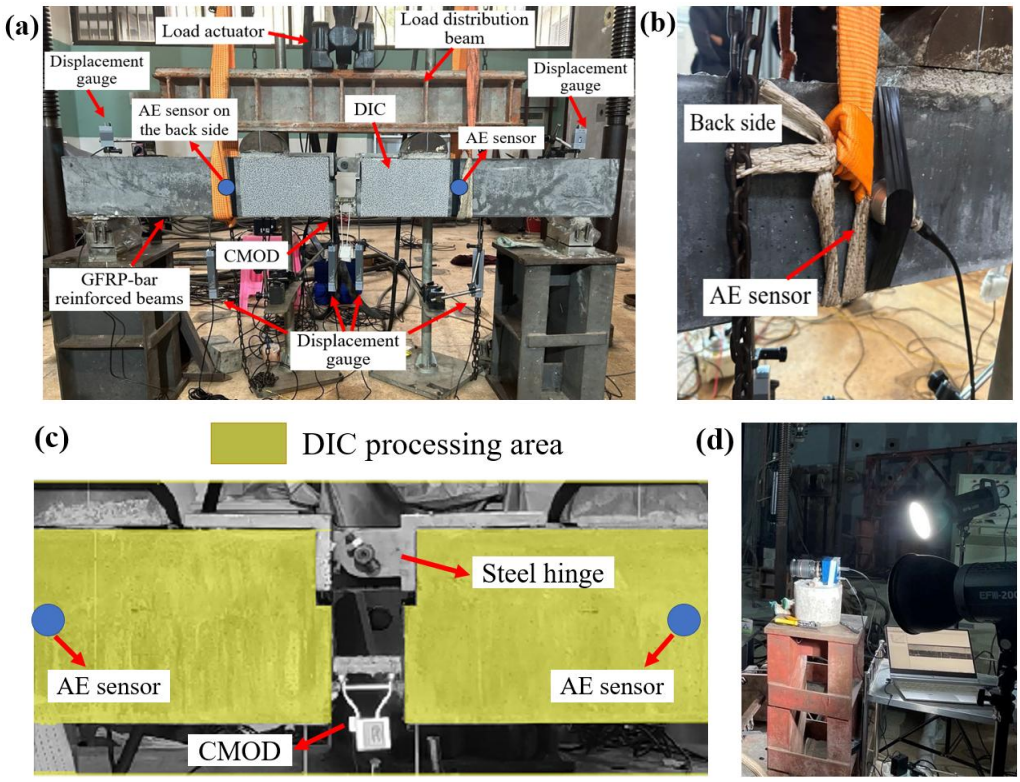


**Figure 3.37** Schematic of experimental setup and instrumentation. (a) Overall testing setup, (b) detail of AE sensor, (c) DIC measurement scheme, and (d) DIC monitoring equipment.

Figure 3.38 shows the load time curves for the three test beams from the same batch, where normalized time 1 corresponds to the peak load. The average peak load of the three beams was 101.4 kN, with little variability in the experimental peak loads (coefficient of variation 2.30%). AE monitoring focused on beam #1, whose peak load was closest to the average value, to conduct an in depth multi-technique fusion analysis of the damage process. The asterisks in Fig. 3.38 mark the time points for DIC image analysis of the three test beams, which will be discussed later.

As shown in Fig. 3.38, all beams exhibited a "saw-tooth" load drop pattern before reaching the peak load, indicating the occurrence of stick-slip behavior between the GFRP bars and the concrete. In the initial stage, the bond force was mainly maintained by the interlocking action and friction provided by the ribbed surface of the GFRP bars. As the load increased, local debonding occurred between the GFRP bars and the concrete, leading to sudden load drops. Each drop corresponded to a slip event, followed by re bonding as the load redistributed. This process was accompanied by shear dominated cracking near the GFRP bar concrete interface.

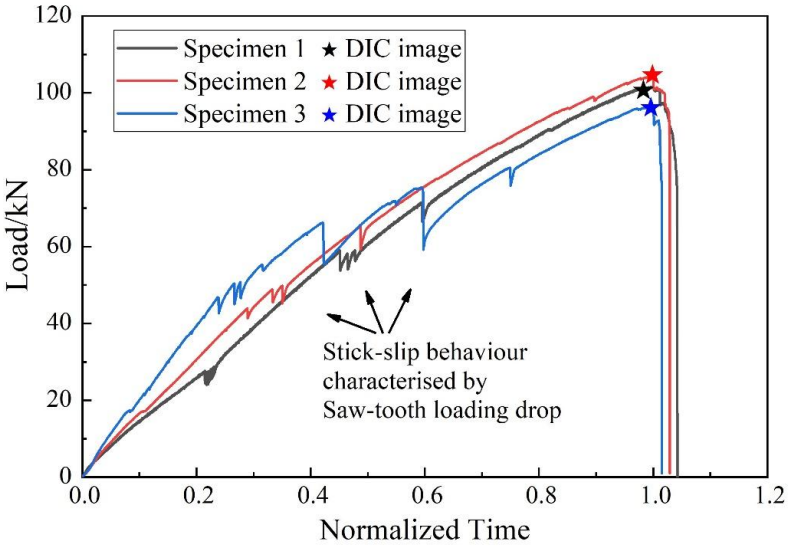


**Figure 3.38** Global behaviours of the test beams.

Figure 3.39 shows the final failure modes of the test beams, characterized by horizontal shear cracks distributed on the beam surface. The beams ultimately failed by GFRP bar pullout. The sand coated layer on the surface of the GFRP bars underwent shear peeling over the entire embedded length, and obvious bond-slip was observed at

the GFRP bar concrete interface. Due to the CMOD controlled loading, the load only reached the conventional compressive strength of the material, and the beams did not completely collapse. Based on this, subsequent analyses focus on the critical failure state of the beams near the peak load. It is worth noting that the failure of all three beams in Fig. 3.39 was caused by horizontal shear cracks near the GFRP bars at the notch, which is consistent with the sharp drop trend after the peak load in Fig. 3.38.

Figure 3.40 shows the DIC results for the three test beams. The crack morphology was predominantly horizontal. Figure 3.40 presents the equivalent strain field and the horizontal strain field. The equivalent strain field results show that cracks were mainly concentrated near the GFRP bars in the notch region. Furthermore, the horizontal strain field results in Fig. 3.40 reveal the morphology of the horizontal cracks, which is consistent with the final failure modes shown in Fig. 3.39.

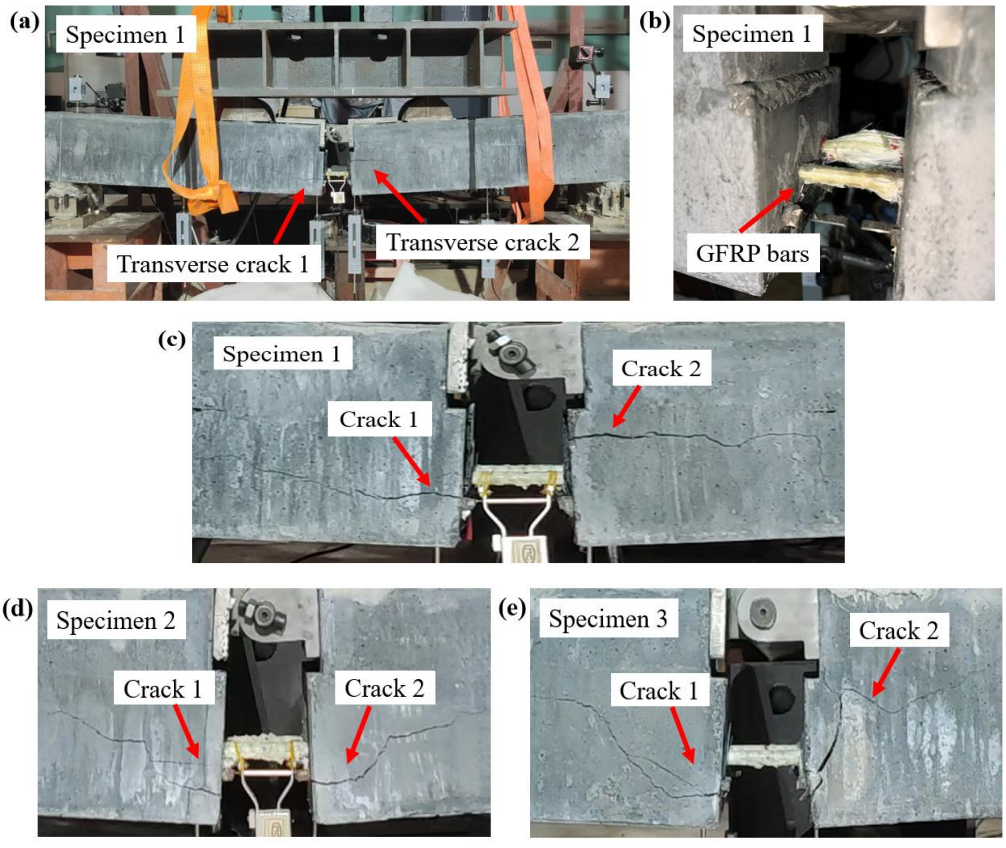


**Figure 3.39** Final failure configuration and details. (a) Final failure of Specimen 1; (b) Failure of the GFRP bars in Specimen 1; (c-e) Details of Specimens.

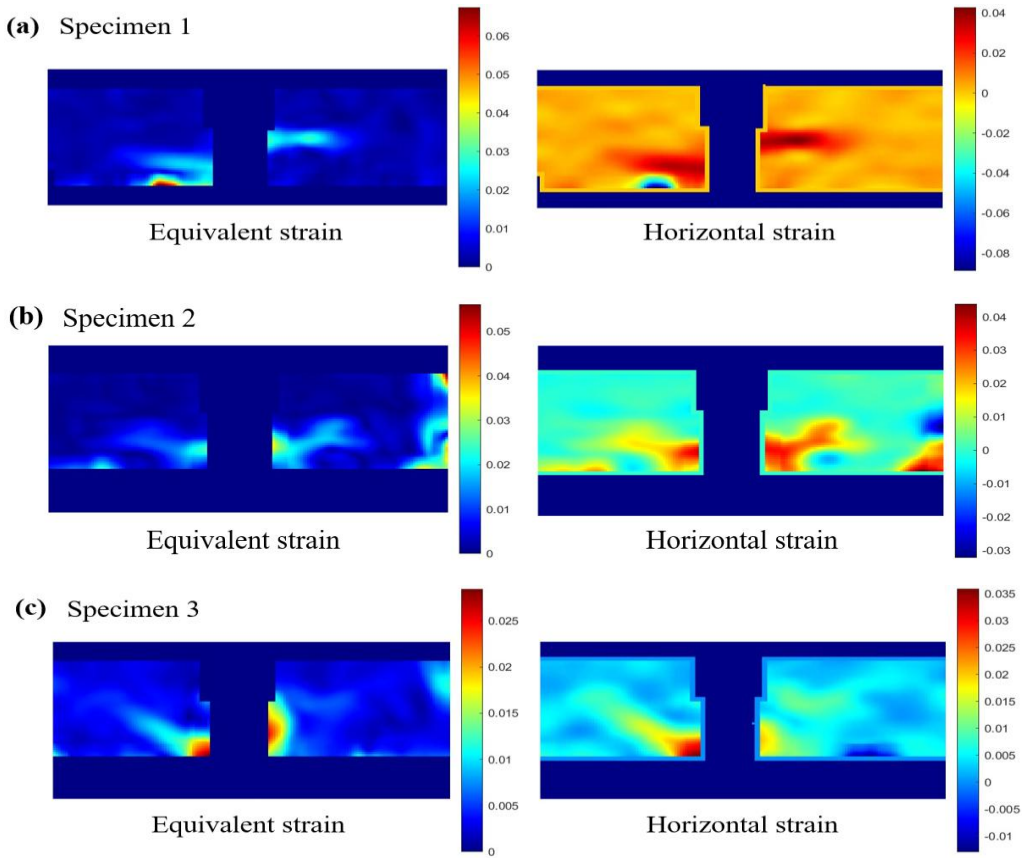


**Figure 3.40** DIC strain field diagram at the final failure of Specimens.

Debski, Pradhan, and Hansen [119] proposed a method for determining failure precursors by calculating the time derivative of the elastic strain energy during system evolution, known as the DPH (Debski Pradhan Hansen) index. Local or global maxima of this index can serve as failure precursors. Figure 3.41 illustrates the relationship between the DPH index and system failure, with the calculation shown in Eq. (3.1). The DPH index is defined as the time derivative of the elastic strain energy E stored in the system. In Fig. 3.41, the external load, elastic strain energy, and DPH index evolution are represented by black, green, and red lines, respectively. The DPH index (red line) is calculated from the numerical derivative of the elastic strain energy (green line). The peak of the DPH index occurs before the peak load and can serve as a precursor to the peak load. The mechanism is as follows: when the rate of energy released by the damage process begins to exceed the rate of energy accumulation, the DPH index, representing the energy change rate, reaches its peak. At this time, the load and elastic strain energy

continue to rise until the structure reaches its ultimate load bearing capacity. Therefore, the peak of the DPH index can serve as an important precursor for identifying the transition of the system from local instability to global failure. In AE testing, the DPH index can serve as complementary information to interpret AE data, thereby enabling a deeper analysis of the damage evolution process [120].

$$\text{DPH Index} = \frac{dE}{dt} \tag{3.1}$$

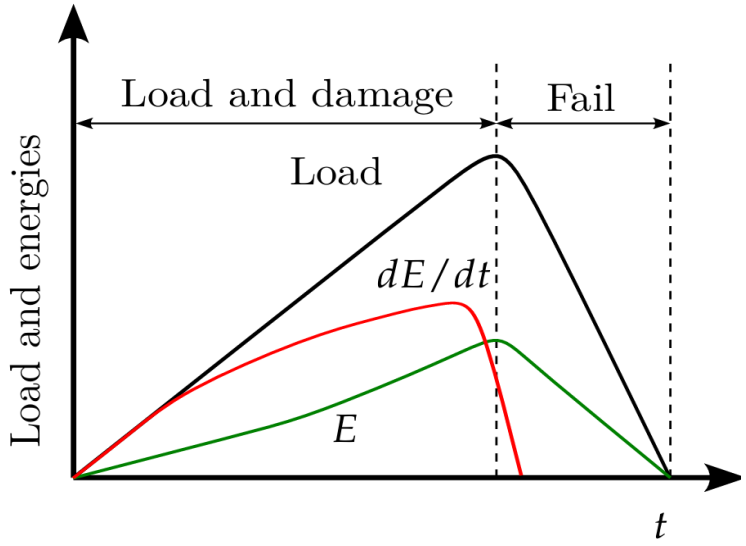


**Figure 3.41** Evolution of the load, elastic energy (E), and the DPH index during the test.

Figure 3.42 shows the evolution curves of the DPH index for the test beams, with the global maximum points of the DPH index marked by red stars. To reduce data fluctuations while preserving the overall evolution trend, a moving average window of 200 data points was used when calculating the DPH index. As described in the literature [121,122], this maximum value can be regarded as an auxiliary precursor to system failure when conducting AE tests. It should be noted that during the experimental loading process, the product of the support reaction and the corresponding displacement is considered as a quantity related to the external work, and the DPH index is calculated based on the time derivative of this product [122]. This method provides a proportional index reflecting the global energy change rate, rather than an absolute measure of the

elastic strain energy inside the specimen. The results in Fig. 3.42 show that the maxima of the DPH index are closely related to local cracking during the test (such as the stick-slip behavior shown in Fig. 3.38). This study employs the DPH index as a characteristic indicator capable of detecting both local and global instabilities. As shown in Fig. 3.42(a c), local maxima of the index (highlighted by yellow areas) have predictive capability for subsequent changes in the mechanical response of the specimen (highlighted by yellow circles). The temporal evolution of this index shows a consistent pattern: after each local maximum, the index value undergoes a transient decrease followed by a substantial increase.

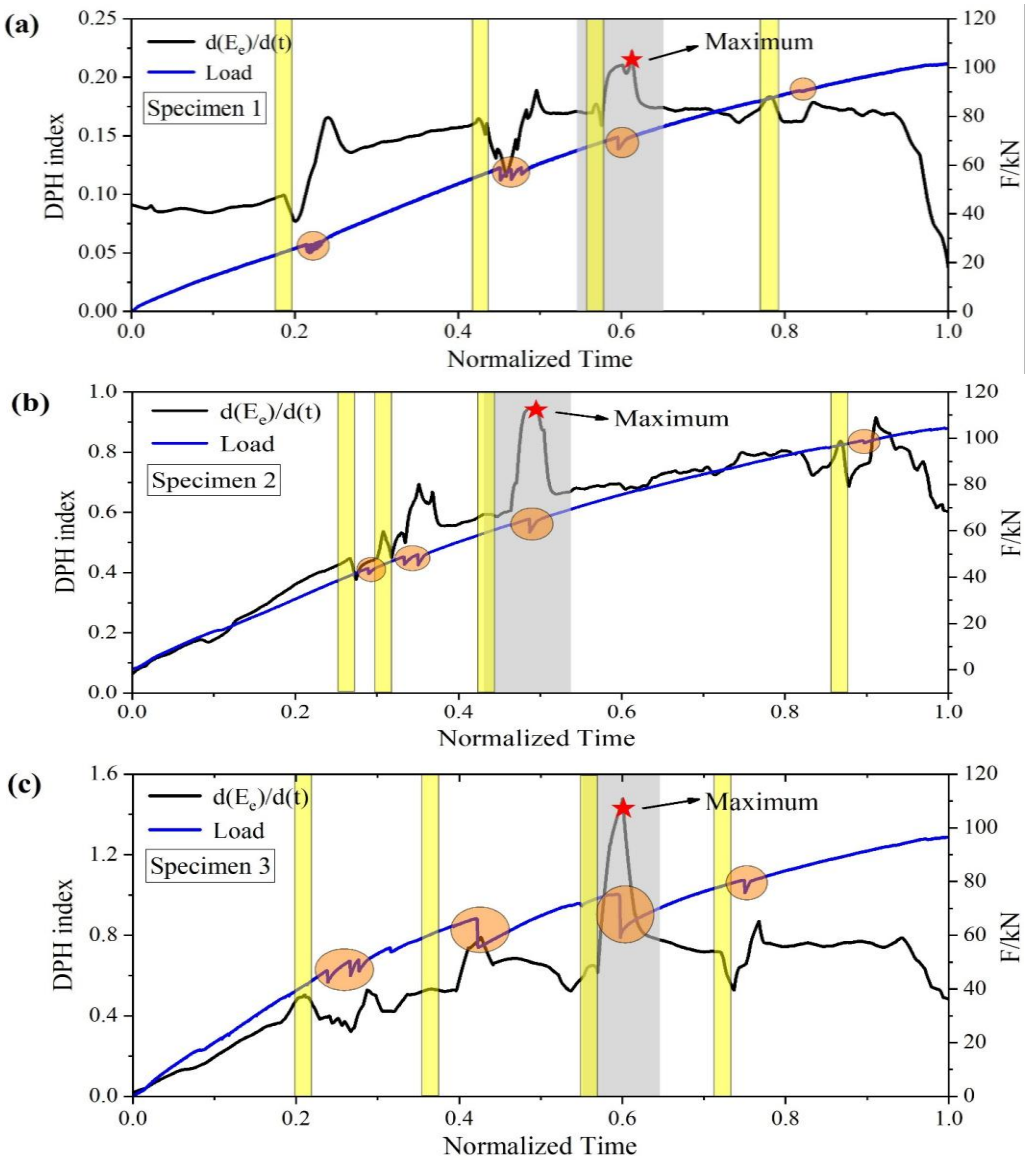


**Figure 3.42** Results for Specimens in terms of DPH index evolution.

### 3.6.2 AE time series analysis and fracture precursor identification

Figure 3.43 shows the evolution of load, cumulative number of AE events, and normalized AE amplitude during the loading of test beam #1. The AE amplitude and number of signals from sensor 1 on the left side were significantly higher than those from sensor 2 on the right side, indicating that AE activity was more intense on the left side and that damage to the beam occurred mainly on the left. The load time curve exhibits "saw-tooth" fluctuations, which are characteristic of the bond-slip behavior between the GFRP bar and the concrete. Notably, each load drop (slip event) corresponds to a peak in AE amplitude, indicating that AE signals are sensitive to local interface instability. The results show that AE signals effectively identify the stick-slip phenomenon between the GFRP bar and concrete, and each amplitude peak signifies elastic energy emission caused by a slip event, generating high-amplitude AE signals.

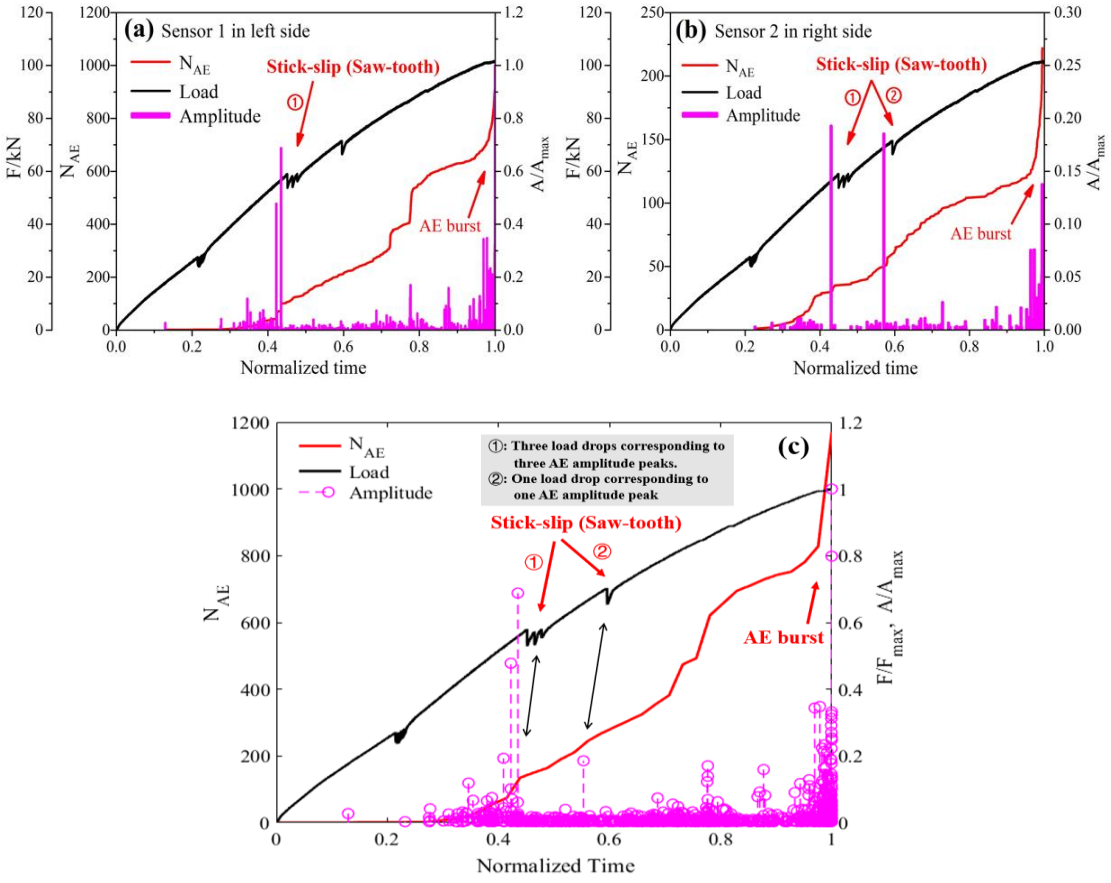


**Figure 3.43** Comparison of AE signals on the left and right sides of the test beam. (a) Sensor 1 on the left side; (b) Sensor 2 on the right side (c) Both Sensors 1 and 2.

The RA-AF method described in Section 2.3.3 was used to analyze the evolution of crack types. As shown in Fig. 3.44, windows with a normalized time span of 0.15 were selected (Stages SS1 and SS2), and RA-AF analysis was performed separately to identify stick-slip behavior. Furthermore, using the stick-slip points as boundaries, the damage process was divided into three stages (TS1, TS2, TS3), and RA-AF analysis was conducted for these three stages.

Figure 3.45 shows the percentage distribution (%) of shear cracks (Mode II) and tensile cracks (Mode I) at different stages. As shown in Fig. 3.45(a), shear cracks dominate in both stick-slip stages, accounting for 62% and 70% of total cracks, respectively, indicating shear dominated cracking behavior in these stages. As shown in Fig. 3.45(b), the damage evolution process divided by the stick-slip points reveals different cracking modes in each stage. In the initial stage TS1, tensile cracks dominate, accounting for approximately 80%. In stage TS2, the proportion of shear cracks increases significantly, and the damage mechanism transitions from tensile dominated to shear dominated. In stage TS3, the proportion of shear cracks reaches approximately 80%, indicating that failure is ultimately dominated by interface shear slip and shear cracking. The results track the gradual evolution from tensile cracking to shear cracking (see Fig. 3.45b), which is highly consistent with the "sawtooth" fluctuations in the load curve and the strain concentration observed by DIC, confirming the effectiveness of AE in identifying changes in damage mechanisms.

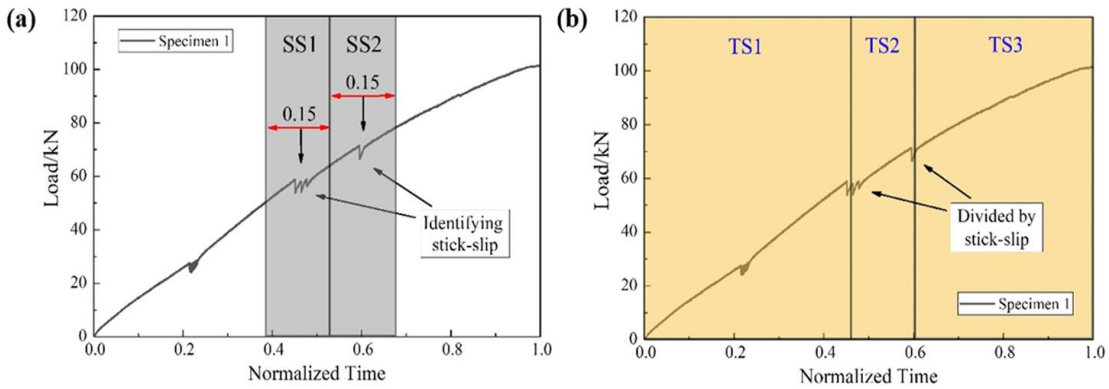


**Figure 3.44** Damage stage divisions for *AF-RA* analysis. (a) Two divisions for identifying the stick-slip and (b) Three divisions for damage process.

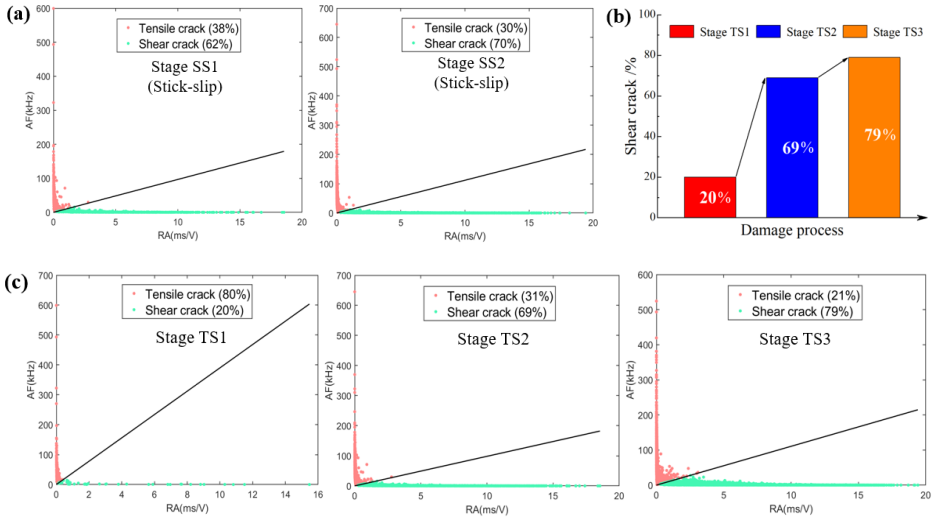


**Figure 3.45** Mode I and Mode II crack openings during the damage process. (a) Results for two stick-slip stages; (b,c) Results for three different damage stages.

To comprehensively capture the failure precursor characteristics during beam loading, NT analysis, AE information entropy analysis, and MCF-B analysis were jointly applied. NT analysis can derive important features related to the damage process, as detailed in Section 2.4.3. The evolution of the NT variance $\kappa_1$, entropy $S$, and its time reversed entropy $S_{rev}$ over time was extracted. The NT analysis used a window size of 100 events, and the NT parameter $Q$ was taken as the AE energy. The results are shown in Fig. 3.46(a). The two horizontal dashed lines represent the critical value for the variance $\kappa_1 = 0.07$ and the critical value for the entropy $S_u = 0.0966$. When $\kappa_1$ approaches 0.07 and the entropy $S$ falls below 0.0966, the system enters a critical state. For the NT analysis results, Figure 3.46(a) shows that a critical region can be identified, highlighted by a grey background, located near a normalized time of 0.65 and appearing before the peak load.

Each AE waveform generated during the damage evolution process has a unique degree of disorder. The probability distribution of the discrete voltage values of the waveform can be quantified as information entropy. By analyzing the evolution curve of AE information entropy, different failure stages of the beam during bending can be identified. The information entropy of the AE time series was calculated using a cumulative window, and the results are shown in Fig. 3.46(b). In the early stage, loading

induces crack propagation, generating local stress concentration and nonlinear mechanical responses. A decrease in AE information entropy reflects that the system is entering a more ordered state, meaning that the structure is approaching the critical point of local or global failure. As shown in the grey background area in Fig. 3.46(b), low entropy (minimum value) indicates that the system is in a more ordered state, representing a critical state just before the structure fails. After this stage, the structure gradually becomes unstable, manifested by local fracture and plastic deformation, leading to a sharp increase in entropy. The AE entropy eventually reaches a peak near 1.2. The increase in entropy reflects a disordered state where the system is far from critical conditions. It is worth noting that the fluctuations in information entropy show a strong temporal correlation with AE activity. The identified critical region (grey background area) is highly consistent with the critical region determined by NT analysis (Fig. 3.46a), where the entropy value must be low to indicate that the system is approaching a critical state.

### 3.6.3 Characteristics of MCF-B critical parameters and comparison with *b*-value method

The MCF-B analysis fits the AE amplitude distribution function N(A) (Eq. 2.31) and identifies criticality through the evolutionary characteristics of the exponents $p_2$ and $p_3$. The analysis was performed using a sliding event window of $W = 50$, advancing incrementally event by event within the normalized time, and the updated fitting results for $p_2$ and $p_3$ are shown in Fig. 3.46(c). The characteristic features for identifying the system entering a critical state using the MCF-B method are as follows: first, an "ideal power law" distribution appears with $p_2 > 1$ and $p_3 \approx 0$; subsequently, $p_2$ begins to decrease while $p_3$ increases monotonically, presenting a "crossover phenomenon". The critical region is shown by the grey background area in Fig. 3.46(c). Figure 3.46(d) shows the fitting of the amplitude distribution at two characteristic points within the critical region. When the distribution satisfies $p_2 > 1$ and $p_3 = 0$, point PL is in an ideal

power law state. In contrast, points $LL_1$ and $LL_2$ exhibit a clear downward tail distribution ($p_3 > 0$), reflecting a deviation of the amplitude event distribution from linearity. The critical region identified by the MCF-B method, spanning normalized times from approximately 0.65 to 0.75, is consistent with the results of NT analysis and AE information entropy analysis. This finding enables the application of the MCF-B method for detecting and analyzing structural failure precursors.

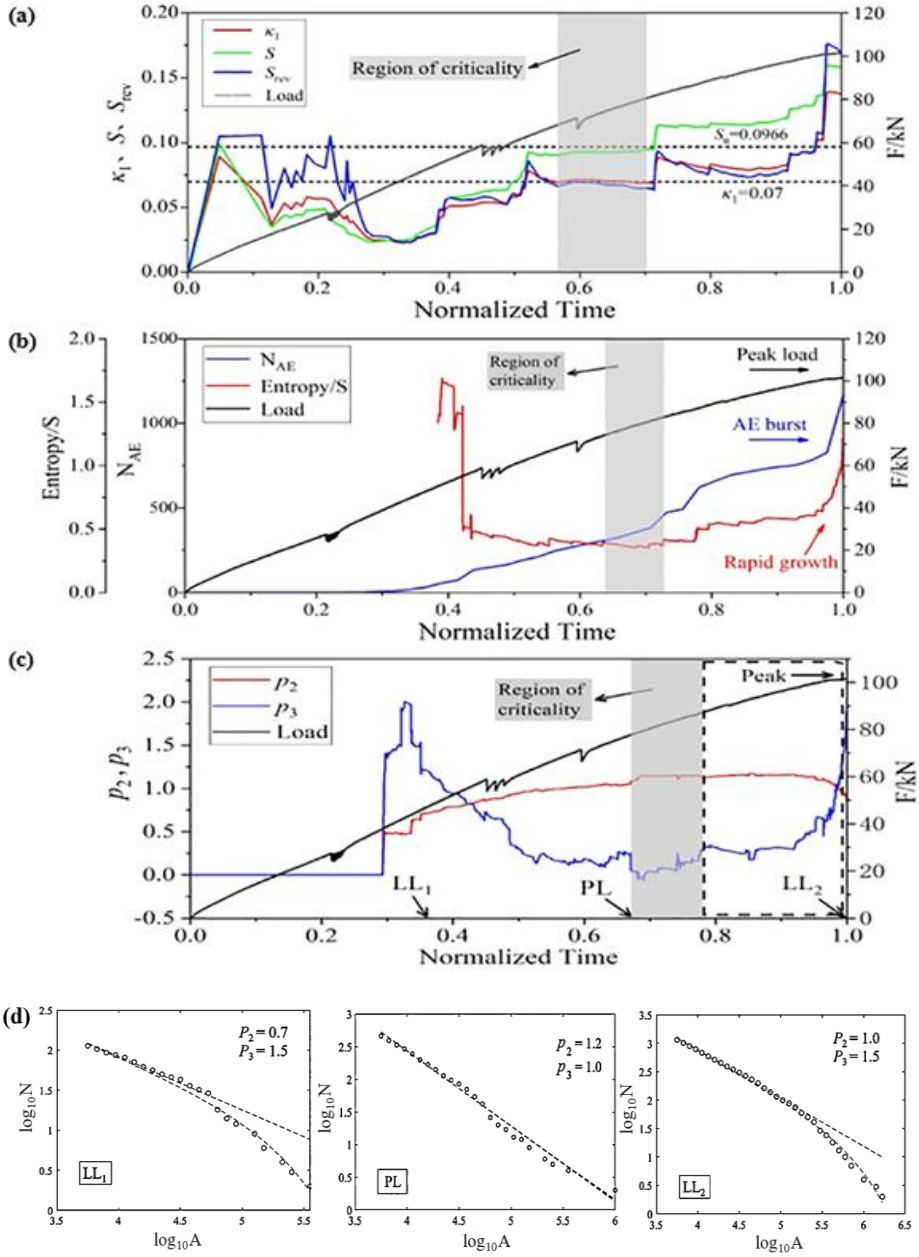


**Figure 3.46** Results of MCF-B, AE Entropy and NTime analysis. (a) NT series and its critical time; (b) AE Entropy Analysis; (c) The exponents $p_2$ and $p_3$ from MCF-B method; (d) The points that satisfy the "perfect" power law distribution labeled as PL and the loss of linearity labelled as $LL_{1\text{-}2}$, see the black arrows in (c).

To highlight the advantages of the MCF-B method, it was compared with traditional *b*-value analysis. Figure 3.47 presents a comparison of the *b*-value and the MCF-B method results over normalized time. A moving event window method was used to estimate the temporal evolution of the *b*-value, with a window size of 100 events and a step size of 50 events. The critical region identified by the MCF-B method is shown as a grey area in Fig. 3.47. Immediately before the MCF-B critical region, a significant decrease in the *b*-value can be observed. Notably, at the end of the MCF-B critical region, the *b*-value reaches its minimum, $b_{min}$. This result indicates consistency between the two methods in identifying the self similar critical state, with the MCF-B precursor characteristics appearing earlier. However, after the critical region, the *b*-value shows a diverging trend of recovery and fluctuation, losing clear precursor indication. In contrast, the MCF-B method maintains its critical characteristics until failure occurs through the systematic crossover behavior of decreasing $p_2$ and monotonically increasing $p_3$. This difference highlights the stronger robustness of the MCF-B method in tracking the ultimate failure process of the system. This robustness is attributed to the dual exponential model adopted by the MCF-B method, which effectively reveals the deviation of the amplitude distribution from an ideal power law, thus overcoming the limitations of the single parameter *b*-value fitting at this stage.

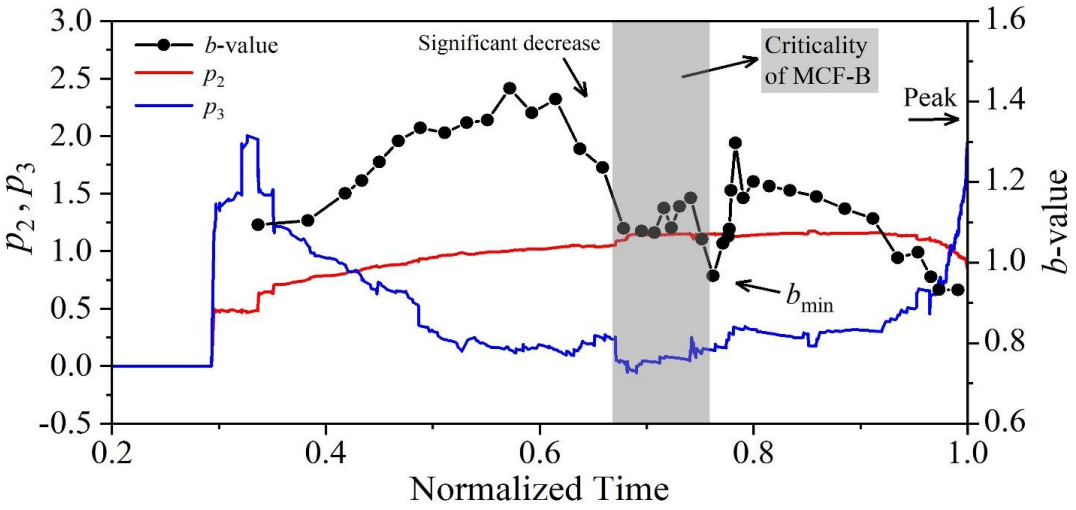


**Figure 3.47** *b*-value and MCF-B versus normalized time.

This comparison demonstrates that by simultaneously capturing the evolution of the power law decay exponent ($p_2$) and the exponential decay tail ($p_3$), the MCF-B method can more robustly describe the deviation from critical behavior of a system before instability, is less susceptible to fitting deviations from a single power law, and exhibits stronger robustness in identifying late stage failure precursors.

Synthesizing the results of this section, the MCF-B method demonstrates good capability for identifying failure precursors in the flexural failure tests of GFRP bar reinforced concrete beams. Its defined critical characteristics (the crossover phenomenon of $p_2$ decrease and $p_3$ increase following an ideal power law) have clear physical meaning and are mutually validated with criteria based on temporal sequence (NT analysis) and waveform disorder (AE information entropy). Compared with the traditional *b*-value method, MCF-B can more persistently and stably track the critical evolution of the system, remaining sensitive even in stages where the amplitude distribution deviates from linearity. The identification of the critical region occurs earlier than the macroscopic peak load, providing an earlier time window for structural failure warning.

Through multi-technique fusion analysis, this experimental study systematically reveals the entire process of GFRP bar reinforced concrete beams from stable damage and bond-slip to critical instability from multiple dimensions, including microscopic damage mechanisms (RA-AF), statistical distribution evolution (MCF-B, *b*-value), temporal organization (NT), and signal complexity (information entropy). It validates the effectiveness of MCF-B as a cross-scale critical precursor identification tool.

## 3.7 Chapter summary

This chapter followed a progressive path from intrinsic material properties (Sections 3.2, 3.3) to component strengthening behavior (Section 3.4), and then to structural field monitoring (Section 3.5), culminating in a comprehensive comparative validation of methods (Section 3.6). By combining AE, DIC, and various advanced

signal analysis methods, it validated the effectiveness and applicability of methods such as MCF-B in revealing damage mechanisms and identifying fracture precursors from multiple dimensions, providing rich experimental evidence for cross-scale precursor research. The main conclusions are as follows:

（1）At the material scale, the damage mechanism exhibits a significant loading rate dependence. SFRC compression tests show that AE parameters ($\beta_t$, *b*-value) and RA-AF analysis can effectively characterize the damage evolution stages and the transition of crack mode from tensile to shear. The loading rate significantly affects the failure mode and AE precursor characteristics. Under low speed loading, the fiber bridging effect is more fully utilized, resulting in better ductility, and the decrease in *b*-value and the appearance of the $\beta_t$ critical point are more gradual. This study provides rate dependent criteria for AE based damage warning.

（2）The size effect and AE energy follow a fractal law. Tests on concrete specimens of different sizes and slenderness ratios confirm that AE energy emission is not uniformly distributed within the volume but is confined to a fractal domain with a fractal dimension *D* between 2 and 3. The *D* value of NC (≈2.19) is closer to 2, indicating that energy emission approaches a plane. Due to the fiber bridging effect, the *D* value of UHPC (≈2.76) is closer to 3, indicating more diffuse damage distribution and higher toughness. This reveals the microscopic physical nature of the size effect and fiber toughening from the perspective of energy statistics.

（3）Flexural tests on long-term loaded concrete beams strengthened with UHPC show that the mechanical behavior of the strengthening interface dominates the failure process and precursor characteristics. AE can effectively monitor UHPC-RC interface debonding and crack propagation. The initial cracking point determined by the *b*-value method is highly consistent with the load curve results, while NT analysis can identify the critical state of the system earlier, validating the potential of NT analysis as an early warning tool. RA-AF analysis further reveals the transition of the failure mode from interface shear dominated to flexural tensile dominated.

（4）AE technique demonstrates reliable dynamic monitoring capability in complex field environments. Field measurements of drying shrinkage cracks in a steel-

UHPC composite bridge deck overcame environmental noise interference and achieved dynamic AE monitoring and precise localization of the crack tip's leapfrog propagation. The simultaneous sharp changes in the *b*-value and $\beta_t$ parameters precisely corresponded to the macroscopic crack jumps, confirming the sensitivity of AE parameters to unstable crack propagation. The case analysis identified vehicle loading as the main cause of crack propagation, demonstrating the practicality of AE technique in structural health monitoring of engineering structures.

（5）The MCF-B method exhibits comprehensive advantages in identifying critical precursors. Using flexural GFRP bar reinforced concrete beams as the object, a systematic comparison was made between MCF-B, the traditional *b*-value, NT analysis, and AE information entropy analysis. The results show that the MCF-B method, through the synergistic evolution (crossover phenomenon) of the parameters $p_2$ (power law decay) and $p_3$ (exponential decay), can clearly and robustly identify the critical region, which is mutually validated with the results of NT analysis and AE entropy analysis. Compared with the fluctuation and divergence of the traditional *b*-value after the critical region, the parameter evolution trend of MCF-B is more distinct and persistent, significantly improving the robustness and reliability of critical precursor identification. Additionally, RA-AF analysis successfully captured the evolution of crack modes from reinforcement bond-slip (shear dominated) to final failure.

In summary, through multi-scale and multi-factor experimental research, this chapter comprehensively reveals the fracture mechanisms and AE response laws of concrete materials and structures under complex conditions. It validates the MCF-B method as a statistical physics tool with clear physical meaning and strong anti interference capability, demonstrating its effectiveness and superiority in identifying critical failure precursors from the laboratory material scale to the engineering structural scale. This lays a solid experimental and methodological foundation for the subsequent research on seismic precursor identification (Chapter 4).

# Chapter 4

# 4 Seismic precursor identification based on field measurement of rock AE

## 4.1 Introduction

The preceding chapters have systematically demonstrated the effectiveness of AE technique for monitoring microfracture activity and identifying system critical precursors from multiple perspectives, including fracture mechanics theory (Chapter 2) and laboratory scale concrete material and component tests (Chapter 3). The research has shown that in fracture tests of concrete specimens and structures with different stress states, sizes, and material compositions, the statistical features embedded in AE signals, such as the *b*-value, NT parameters, and the MCF-B parameters which are the focus of this study, can sensitively capture the critical state of a system transitioning from stable damage accumulation to unstable failure. These studies provide important physical analogies and methodological foundations for understanding the preparation process of macroscopic fracture events at the crustal scale, such as earthquakes.

However, laboratory studies differ significantly from real crustal environments in terms of scale, medium homogeneity, stress state, and boundary conditions. To develop AE technique into a reliable tool for short-term and imminent earthquake precursor identification, it is necessary to bridge the scale gap from "laboratory specimens" to "real crust" and conduct in situ field monitoring based on rock AE. The core objectives of such field tests are to verify whether observable and physically meaningful correlations exist between AE activity and regional earthquake sequences under

complex field geological environments and background noise, to test whether precursor identification methods that perform well in the laboratory remain effective in field monitoring, and to explore the feasibility of using AE signals for seismic precursor identification and earthquake time prediction.

Based on this, this chapter relies on a typical seismically active zone in eastern Guangdong. High sensitivity AE monitoring systems and seismometers were installed in a full granite mountain tunnel at the Shantou Earthquake Monitoring Center. Synchronous continuous observations were conducted for approximately 35 days and 180 days, respectively. This chapter systematically analyzes the field collected rock AE signals and earthquake catalog data, focusing on the following content. First, starting from the physical mechanisms, it elaborates on the relationship between microseismic activity and AE generation, as well as the basis for applying *b*-value statistics in seismic precursor analysis. Then, it introduces the seismic background of the monitoring area, the detailed layout of the field monitoring system, and the data acquisition process. Subsequently, it analyzes the correlation between AE and seismic activity from multiple perspectives, including temporal comparison, multimodal statistical analysis, evolution of AE characteristic parameters, and the performance of methods such as *b*-value and NT analysis in precursor identification. The MCF-B method proposed in this paper is then applied to the field AE data to analyze its advantages and characteristics in identifying real earthquake precursors. Finally, to enhance the reliability of precursor identification, this chapter attempts to introduce electromagnetic emission (EME) monitoring data for multi-precursor cross validation, analyzing the correlation characteristics between AE and EME signals before earthquakes.

This chapter aims to provide direct observational evidence for the proposition that "AE can serve as an earthquake precursor" through rigorous field measurements and multi-method fusion analysis. It also aims to systematically test the analytical methods developed in this paper in real, complex field environments, thereby laying a solid data foundation and providing validation cases for constructing a physics-data synergistic driven seismic precursor identification model.

## 4.2 Seismic activity and physical precursors of AE

Based on fracture mechanics theory, an earthquake is the result of macroscopic fracture of crustal rocks under tectonic stress, and its physical essence is homologous to material fracture. The intensification and evolution of microfracturing activity within the earthquake preparation zone before an earthquake constitute an important physical basis for seismic precursors. This section systematically elaborates the physical basis for applying AE technique to seismic precursor monitoring from the perspectives of microseismic activity mechanisms and statistical physical characterization.

### 4.2.1 Generation mechanisms of microseismic activity and AE signals

Under sustained tectonic stress, pre-existing defects such as microcracks and joints within rocks in the earthquake preparation zone undergo an evolution process from stable propagation to unstable propagation. This process is accompanied by the rapid local release of strain energy and excites elastic stress waves, known as microearthquakes. Microearthquakes are completely isomorphic in physical mechanism to AE monitored on rock or concrete specimens in the laboratory; both are stress wave emissions from microfracturing events within brittle materials. The frequency range of microseismic signals is typically from a few Hz to several hundred Hz, while conventional AE monitoring frequencies are on the order of kHz to MHz. Although there are differences in their frequency spectra, both follow the fundamental laws of fracture mechanics. In near surface rock masses, the higher frequency stress wave components excited by microseismic activity (which can be considered as "macro AE") can be captured by high sensitivity sensors, thus providing a direct observational means for detecting pre earthquake rock fracturing activity.

Studies have found [78] that if AE is used to analyze the relationship between crack propagation and emitted energy, it can be represented by the area corresponding to each

snap-back branch, as shown in Fig. 4.1. The total area under the load-displacement curve represents the total work done by the load W, the grey area represents the dissipated energy D (used to form new crack surfaces), and the red area represents the emitted energy E (emitted in the form of stress waves). From an energy perspective, during a microfracture event, the total work done by the external load W is used, on one hand, to form new crack surfaces, and on the other hand, to release the remaining energy in forms such as AE. The AE signal energy $E_{AE}$ is proportional to the emitted energy E and is a direct reflection of the scale and dynamic process of microfracturing. Therefore, monitoring the spatiotemporal evolution of macro AE activity essentially monitors the intensity and clustering characteristics of microfracturing activity in rocks within the earthquake preparation zone.

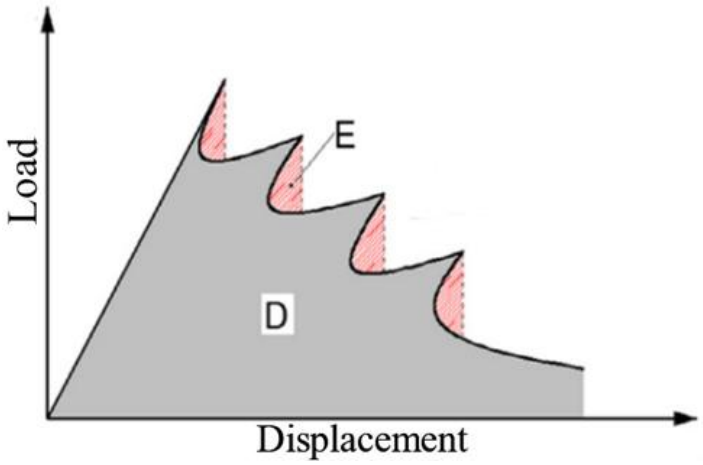


**Figure 4.1** Multiple local instabilities (snap-back) caused by micro-seismic activity.

The earthquake preparation zone is not a static region; its spatial scale r evolves as an earthquake approaches. Dobrovolsky et al. [123] proposed an empirical relationship between the radius *r* of the earthquake preparation zone and the magnitude *M* of a future earthquake: $\log_{10} r = a + bM$ . This implies that precursor anomalies may appear over a large area before a strong earthquake. For example, for a magnitude 5 earthquake on the Richter scale, the radius of the preparation zone could extend for several hundred kilometers. It has also been observed that all earthquake precursors, such as AE activity, may fall within this region. From the perspective of fracture statistical physics, Carpinteri et al. [3] further associated the concept of the preparation zone with the distribution of crack scales and proposed a multi-stage evolution model (Fig. 1.3). Stage

I: Under stress, cracks from nanometer to micrometer scales initiate and stably propagate over a wide area, with the earthquake preparation zone radius at its maximum. Stages II III: As stress concentrates, crack scales grow to the millimeter to meter level, interactions between cracks intensify, the extent of the preparation zone contracts, and damage shows a trend towards localization. Stage IV: Macroscopic cracks coalesce, forming the main rupture surface, and the earthquake occurs. In this model, AE (microseismic) activity reflects the statistical characteristics of crack evolution at each stage. In the early stages, AE events are numerous, have low energy, and exhibit a diffuse spatial distribution. Approaching the earthquake, AE events may show clustering, increased energy, and a tendency towards concentrated spatial distribution. These changes provide a physical basis for identifying critical states based on AE activity.

### 4.2.2 *b*-value statistics and seismic precursors

The magnitude frequency relationship described by the G-R law, $log_{10} N = a - bM$ (Equation 2.20), is a fundamental statistical law of seismic activity. Numerous studies have shown that this power law relationship also applies to the amplitude distribution of AE events during laboratory rock fracture and engineering material damage processes. The parameter *b*-value reflects the proportional relationship between the numbers of events of different sizes.

Furthermore, the energy E released by an earthquake satisfies the relationship $log_{10} E = 1.5M + 11.8$ with the magnitude M. Therefore, the G-R law can be expressed in terms of energy as [124]:

$$log_{10} N = c - \frac{2b}{3} log_{10} E \tag{4.1}$$

where *N* is the number of seismic events with emitted energy greater than or equal to E, and c is a constant.

Interface rupture is a widespread phenomenon in nature, ranging from structural failure due to fracture of heterogeneous materials to earthquakes caused by geological

fault failure. Since interfaces are generally heterogeneous, a large number of rupture events occur during the interface rupture process, leading scholars to study rupture problems based on statistical physics models.

To theoretically explain the G-R law, Hemmer and Hansen [125] modeled the interface as a fiber bundle with rigid clamps at both ends. Through analytical and numerical methods, they demonstrated that the statistical frequency D(Δ) of rupture event sizes Δ during interface rupture follows a power law distribution [126]:

$$D(\Delta) \propto \Delta^{-\xi} \tag{4.2}$$

where $\xi$ is the power law exponent. Taking the logarithm of Eq. (4.2) gives:

$$log_{10} D(\Delta) = a_0 - \xi \, log_{10} \Delta \tag{4.3}$$

where $a_0$ and $\xi$ are coefficients that can be solved using the least squares method. It can be seen that the statistical distribution D(Δ) is very similar to the G-R law. Comparing Eq. (2.20) and Equation (4.3), the logarithm of the rupture event size Δ, $\log_{10}\Delta$, can be analogized to the earthquake magnitude M; the statistical frequency D(Δ) can be analogized to the number of seismic events N; and the coefficient $\xi$ can be analogized to the *b*-value in earthquake statistics. Since the coefficient $\xi$ in the D(Δ) statistics reflects the proportional relationship between the frequencies of rupture events of different sizes, by analogy to earthquakes, the *b*-value represents the proportional relationship between the frequencies of earthquakes of different magnitudes. A larger *b*-value indicates a higher proportion of smaller magnitude earthquakes; conversely, a smaller *b*-value indicates a higher proportion of larger magnitude earthquakes. Therefore, the statistics of interface rupture event sizes D(Δ) can well explain the empirically derived G-R law.

Additionally, during interface rupture, for the high energy segment, the energy of rupture events also follows a power law distribution: $N(\geq E) \propto E^{-\beta}$. Comparing this

with the energy form of the G-R law in Eq. (4.1) yields $\beta = 2b/3$. It is worth noting that rupture is often accompanied by AE signals, and thus the size of rupture events is a physical quantity that can be monitored by AE technique.

It can be seen that there are strong similarities between AE and earthquakes. Although they occur at completely different scales, the former occurring in material fracture and the latter in crustal faults, in both cases, local sources within the medium emit elastic energy, originating from microcracks and earthquake sources, respectively.

Carpinteri [127] used the power law distribution of fracture sizes to establish a theoretical basis for explaining $b = 1$. For Eq. (2.20), by relating the logarithm of AE event amplitude $M$ to the characteristic size $L$, it can be rewritten as:

$$N = cL^{-2b} \tag{4.4}$$

where $N$ is the number of AE events generated by source ruptures with characteristic size $\geq L$, c is a proportionality constant, and D = 2b is the fractal dimension of the damage domain [81]].

Analyzed from the perspective of scaling laws in fracture mechanics, the $b$-value is directly related to the fractal dimension D of the damage domain. When $b \approx 1.5$ ($D \approx 3$), it indicates that microfracture events are uniformly distributed within a three dimensional volume, and the system is in a relatively stable state of damage accumulation. When the $b$-value decreases and approaches the critical value $b \approx 1$ ($D \approx 2$), it indicates intensified damage localization, with fracture events tending to concentrate near a planar fault, and the system tends towards instability. Therefore, the decreasing trend of the $b$-value can serve as a cross-scale statistical precursor indicator for the transition from dispersed damage to localized failure.

In laboratory studies, a systematic decrease in the $b$-value is commonly observed before materials approach failure. Extrapolating this pattern to the crustal scale, the $b$-value of microseismic activity (macro AE) in the earthquake preparation zone may also exhibit a similar anomalous decrease before an impending earthquake, marking the transition of crustal rocks from widespread microfracture activity to damage

localization and acceleration centered on the future source zone. This makes it possible to track the earthquake preparation process by continuously monitoring the *b*-value evolution of macro AE signals in a specific region. Thus, *b*-value statistical analysis can serve as an explanation for earthquake precursors.

It should be pointed out that the physical basis for applying AE technique to seismic precursor monitoring lies in the fact that an earthquake is the endpoint of macroscopic fracture of crustal rocks, and its preparation process is essentially the evolution of microfracture activity in the source zone and surrounding rocks from a statistically uniform distribution to localized clustering. The macro AE activity generated by this process is comparable to the material fracture process in the laboratory in terms of spatiotemporal distribution and statistical laws of energy emission. Therefore, deploying a high sensitivity AE monitoring network in high seismic intensity zones to capture and analyze these microfracture signals holds promise for obtaining direct information reflecting crustal stress accumulation and rock damage evolution, thereby providing a new physics based approach for short-term and imminent seismic precursor identification.

## 4.3 Field measurement at eastern Guangdong seismic monitoring station

### 4.3.1 Mountain tunnel overview and monitoring system layout

This study installed AE and seismic monitoring systems in the dedicated tunnel of the Shantou Earthquake Monitoring Center in eastern Guangdong, China. This center is a backbone station for comprehensive earthquake observation in the eastern region of Guangdong Province, located at 23.41°N latitude and 116.62°E longitude. The location of the monitoring center is shown in Fig. 4.2. The dedicated mountain tunnel within the seismic monitoring station is a full granite tunnel, extending 150 m horizontally into the mountain, and is used for installing seismic observation

instruments. The observation projects at this seismic monitoring station cover three major parameters: seismometry, crustal deformation, and subsurface fluids. It is also networked with the National Regional Digital Seismic Monitoring Network and the Shantou Digital Telemetry Seismic Monitoring Network. All equipment at the seismic monitoring station is digitalized. Because the monitoring point is located in a dedicated tunnel, environmental noises, such as traffic, human activities, and wind effects, have been significantly reduced in their impact on AE activity.

The AE acquisition system used in this study is the Italian ÆMISSION® device, a data processor and recorder specifically designed for AE monitoring. The AE acquisition system is equipped with eight piezoelectric ceramic sensors. The acquisition system features independent threshold triggering for each channel and automatically extracts AE signal parameters, including duration, rise time, energy, amplitude, and ringing count, enabling continuous monitoring of structures as required.

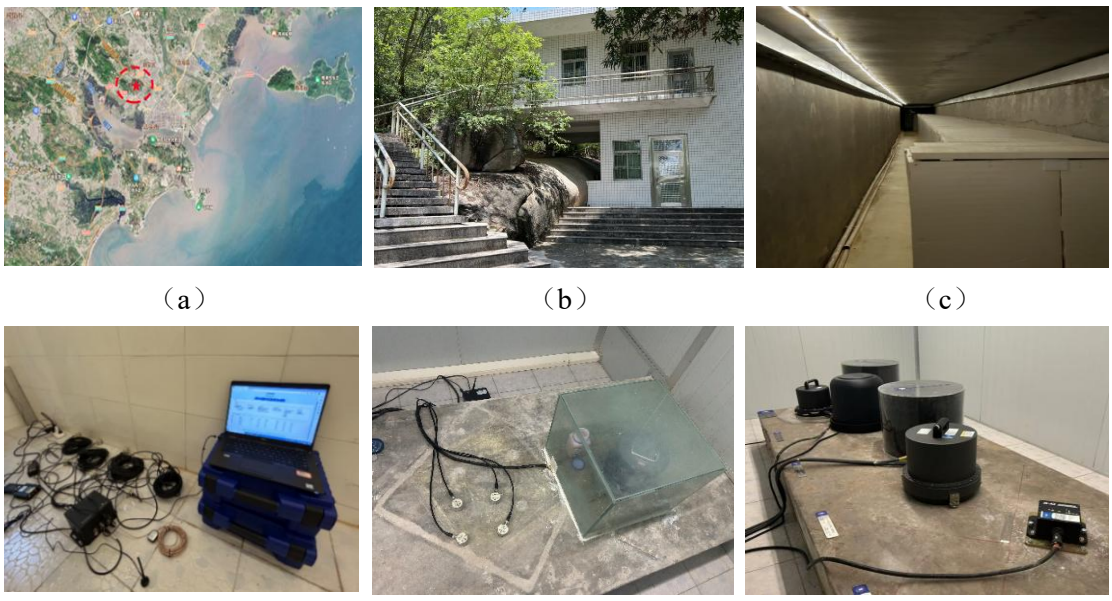


**Figure 4.2** Overview of the AE and seismic monitoring system: (a) monitoring site location; (b) exterior view of the mountain tunnel; (c) interior of the granite tunnel; (d) AE monitoring system; (e) sensor arrangement; (f) seismometer layout.

As shown in Fig. 4.2, four AE sensors were fixed on the floor of the dedicated tunnel, and a seismometer was also installed to monitor seismic activity simultaneously. The acquisition threshold for the AE sensors was set to 1 mV. During post processing, AE

signals with a duration of less than 3 μs and fewer than 3 oscillations within the detection threshold range were discarded to filter out electrical noise spikes. Monitoring began at 12:21 on April 24, 2023, and ended at 11:10 on May 29, 2023, running continuously for approximately 35 days (839 hours). It should be noted that this monitoring campaign was intended to explore the feasibility of using AE for field measurements in the high seismic intensity region of eastern Guangdong, laying the groundwork for subsequent long-term measurements.

### 4.3.2 Regional seismic records of Shantou City

The seismic fortification intensity of Shantou City is VIII, placing it in a strong earthquake zone. Furthermore, the Taiwan Strait to the southeast of Shantou is an area with a high frequency of strong earthquakes. The largest historical earthquake in the Shantou area was the magnitude 7.3 earthquake on Nan'ao Island, Shantou, in 1918. Historical seismic activity in the area surrounding Shantou is shown in Fig. 4.3. Within the regional scope, a total of 51 earthquakes of $M \geq 4.7$ were recorded from 1067 to 2023, including 2 earthquakes of magnitude 7.0 to 7.9, 10 earthquakes of magnitude 6.0 to 6.9, 22 earthquakes of magnitude 5.0 to 5.9, and 17 earthquakes of magnitude 4.7 to 4.9. Since the establishment of the Guangdong Provincial Seismic Network in 1970, one earthquake of $M \geq 4.0$ has been recorded in the near field area (within 25 km of the engineering site), which was the magnitude 4.2 earthquake in Chenghai District, Shantou, on January 16, 2004. Additionally, three distant historical strong earthquakes occurred near the region: the magnitude 7.1 earthquake in Quanzhou, Fujian in 1604, the magnitude 6 earthquake in the sea area of Haifeng, Guangdong in 1911, and the magnitude 7.3 earthquake in the Taiwan Strait in 1994. The active locations of modern small earthquakes within the region are also the sites of historical strong earthquakes, demonstrating the inheritance of seismic activity. As shown in Fig. 4.3, the overall level of seismic activity in this region is relatively high, but its distribution is uneven, exhibiting a regional characteristic of stronger activity in the east and weaker activity

in the west. The majority of destructive earthquakes are distributed along the eastern continental coast.

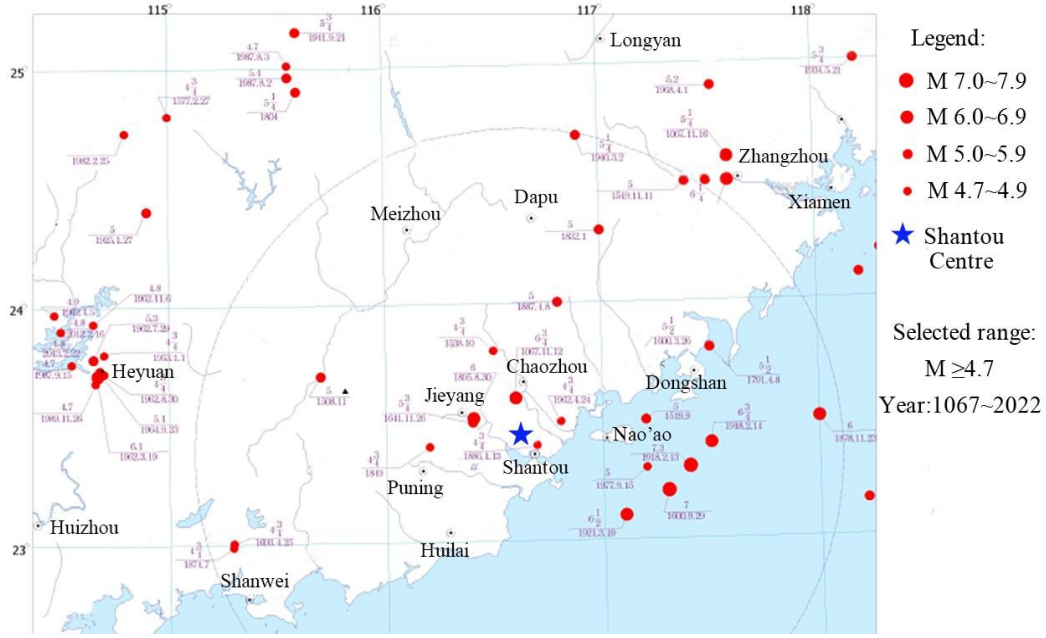


**Figure 4.3** Historical seismic activity in the area surrounding Shantou.

Considering the historical seismic activity in the Shantou area and studies on the scale of the earthquake preparation zone [123] and its temporal evolution [3], earthquakes within 200 km of the monitoring point were selected for analysis. During the monitoring period, small earthquakes occurred frequently in this area. Based on magnitude and epicentral distance, two relatively strong regional earthquakes during the monitoring period were selected: a Richter magnitude 3.2 earthquake in the Taiwan Strait at 23:50 Beijing time on April 30, 2023 (EQ.1), and a Richter magnitude 2.4 earthquake in the sea area of Haifeng, Guangdong at 12:23 on May 17, 2023 (EQ.2). Satellite maps showing the locations of these two earthquakes are presented in Fig. 4.4. EQ.1 (red dot) is the magnitude 3.2 earthquake that occurred in the Taiwan Strait on April 30, with an epicentral distance of 160.1 km from the monitoring point (blue dot). EQ.2 (red dot) is the magnitude 2.4 earthquake that occurred in the sea area of Haifeng, Guangdong on May 17, with an epicentral distance of 132.4 km from the monitoring point (blue dot). The earthquake information is provided in Table 4.1.

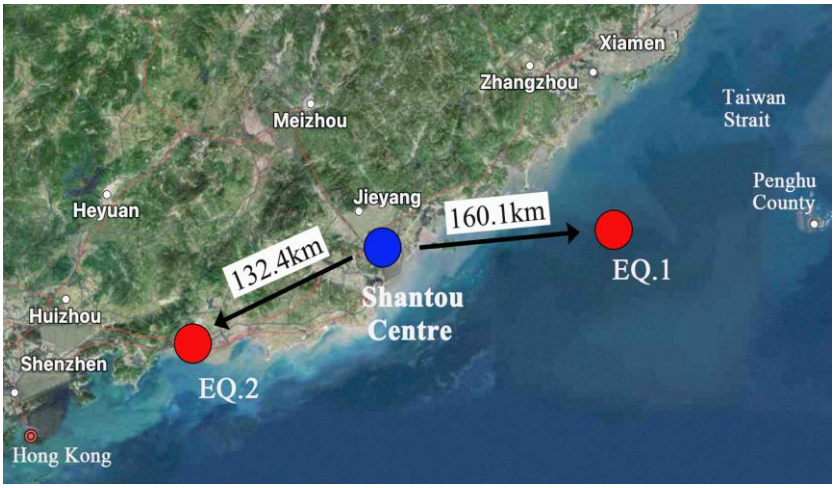


**Figure 4.4** Epicentral locations of the two major earthquakes during the monitoring period.

**Table 4.1** Information about two major earthquakes.

| Local Magnitude ($M_L$) | Date of occurrence | Beijing time | Epicentral distance (km) | Epicentre location | North latitude (°) | East longitude (°) |
|---|---|---|---|---|---|---|
| 3.2 | April 30, 2023 | 23:50 | 160.1 | Taiwan Strait | 23.37 | 118.57 |
| 2.4 | May 17, 2023 | 12:23 | 132.4 | Haifeng Sea Area | 22.83 | 115.24 |

## 4.4 Correlation between AE and seismic activity

### 4.4.1 AE time series and seismic activity

The AE and earthquake sequences during the monitoring period are shown in Fig. 4.5. The AE count represents the cumulative number of AE events during the monitoring period, while the AE count rate represents the number of AE events per unit time. The blue dots in Fig. 4.5 represent the magnitude $M_L$ distribution of the earthquake sequence during the monitoring period. The two marked times, $M_L$ = 3.2 (April 30) and $M_L$ = 2.4 (May 17), indicate the occurrence times of the two major earthquakes.

Throughout the monitoring period, a temporal correlation between AE activity and the earthquake sequence can be observed. Intense bursts of AE, particularly around 142 hours and 566 hours, show significant jumps in the AE count curve and notable peaks

in the AE count rate, which can be considered indicators of a high rate of increase in AE events. It can be seen that seismic events apparently cause an intensification of AE activity, revealing local instability until re-equilibration. Notably, the two intense AE bursts appear closely related to the magnitude 3.2 (EQ.1) and magnitude 2.4 (EQ.2) earthquakes, and the onset of the AE bursts occurred before the seismic events.

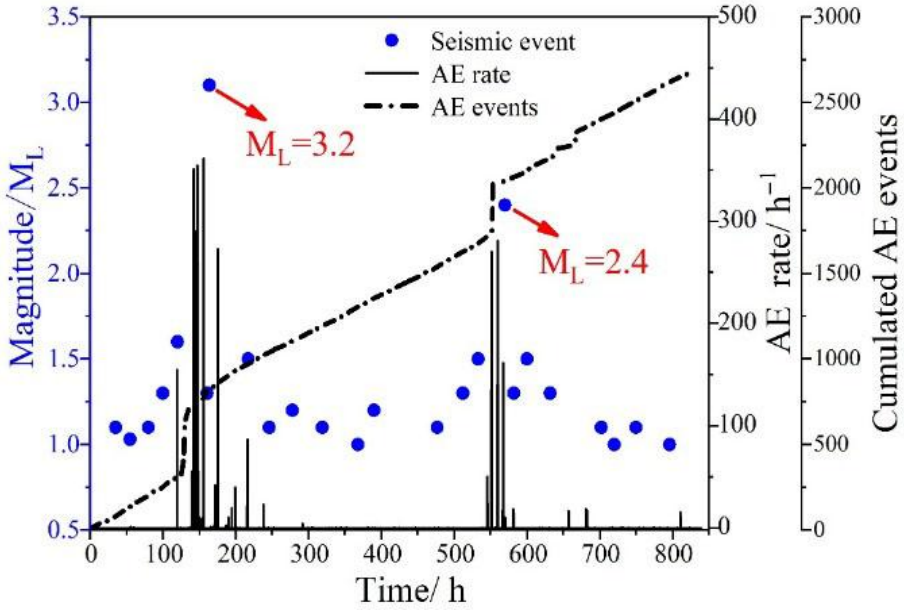


**Figure 4.5** AE time series and earthquake catalog during the monitoring period.

## 4.4.2 Multimodal Statistical Analysis

A multimodal statistical analysis method was applied to process the AE time series and earthquake catalog data. This method can detect different modes or peaks present in the data and determine their positions and quantities. By detecting symmetric or asymmetric curves in the data distribution, the positions corresponding to relative maxima can be located. Subsequently, Gaussian fitting was applied to the detected peaks to obtain the best fit curve describing the characteristics of the data distribution. As shown in Fig. 4.6, starting from the discrete distribution of AE data points, a multimodal curve distribution that best fits the discrete data points is determined through an iterative process involving parameters such as offset $y_0$, center $x_c$, width $w$, and amplitude $A$. Based on the results of multimodal analysis and Gaussian fitting, the

extremum function expression in Eq. (4.5) is the mathematical form extracted from the data, reflecting the extreme values present in the AE and earthquake sequence data during the monitoring period and providing a detailed mathematical description of the data distribution characteristics.

The extremum function can be described by the following analytical expression:

$$y = y_0 + Ae^{(-e^{-z}-z+1)} \tag{4.5}$$

$$z = \frac{x-x_c}{w} \tag{4.6}$$

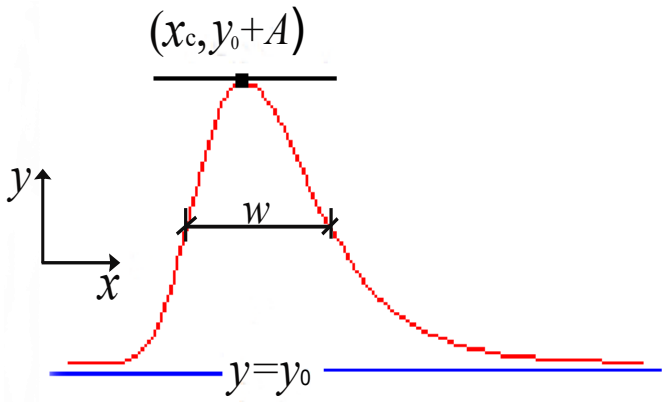


**Figure 4.6** Example curve of the extremum function.

Multimodal statistical analysis was performed on the temporal distributions of earthquakes and AE. Based on the temporal distribution of 24 earthquakes detected during the 35-day monitoring period, two main earthquake clusters were identified. Similarly, for the AE monitoring results, two main AE Gaussian distributions were clearly identified during the monitoring period. The results are shown in Fig. 4.7.

The temporal distributions of earthquakes and AE are shown in Fig. 4.8. The comparison shows that AE has a strong correlation with the earthquake sequences occurring in the nearby area, and the trend of the AE temporal distribution precedes that of the earthquakes, making it a potential earthquake precursor. Figure 4.9 shows the Gaussian distributions of the two seismic events identified by AE. It can be seen that the peaks of the AE distributions identifying subsequent earthquakes exhibit a clear

temporal order, allowing the identification of seismic events regularly about 17 hours in advance.

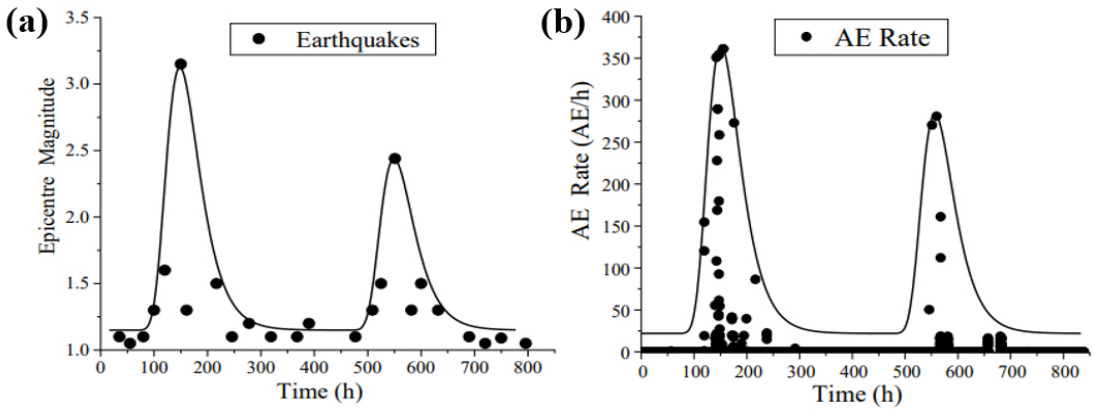


**Figure 4.7** Multimodal Gaussian distribution results during the monitoring period.

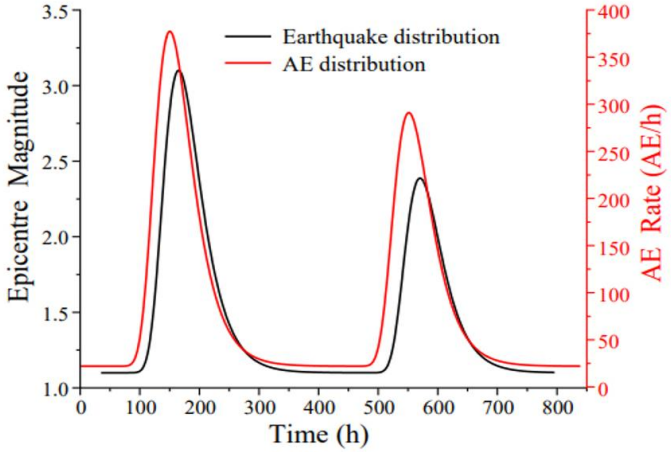


**Figure 4.8** Temporal distribution of earthquakes and AE during the monitoring period.

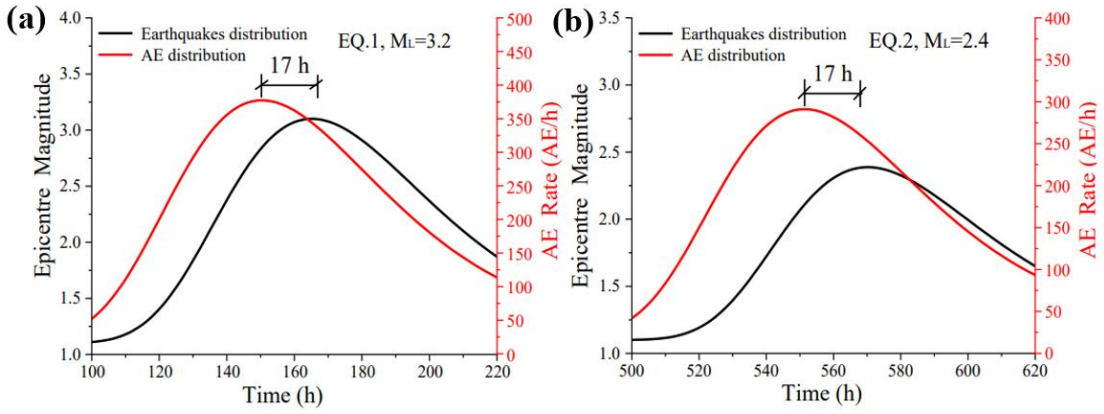


**Figure 4.9** Two major earthquakes identified by AE during the monitoring period.

### 4.4.3 Changes in AE characteristic parameters

To investigate the changes in AE characteristics before the major earthquake (EQ.1), this study focuses on the AE time series and earthquake sequence within the 135 to 155 hour range. The changes in AE time series characteristics and *b*-value during this period are analyzed. AE characteristic parameters were extracted from AE waveforms, as shown in Fig. 2.3.

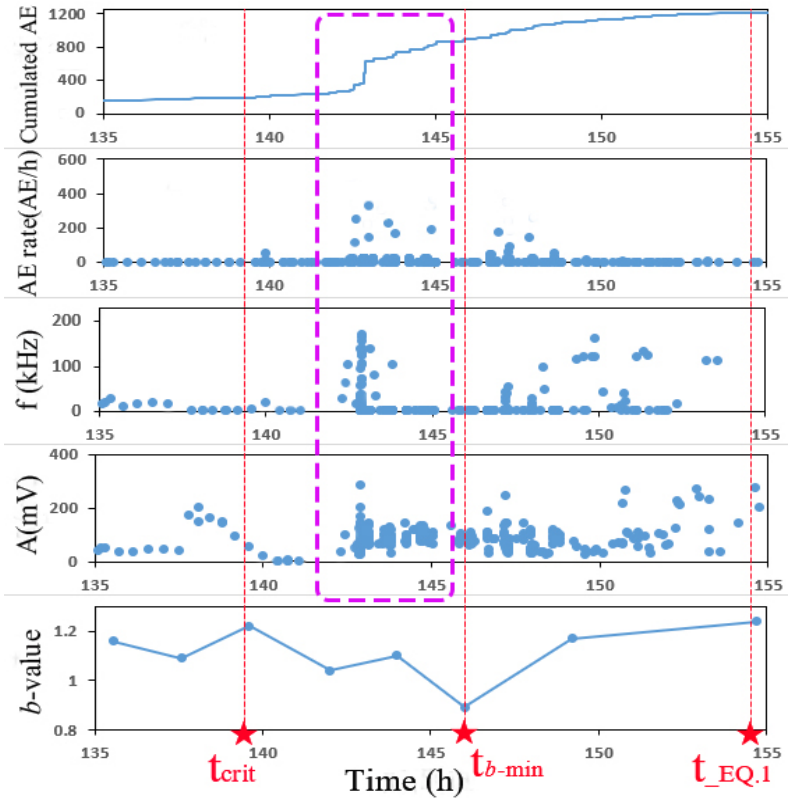


**Figure 4.10** Evolution of AE characteristic parameters and *b*-value before the earthquake: (a) cumulated AE; (b) AE event rate; (c) frequency; (d) amplitude; (e) *b*-value.

Figure 4.10 shows the evolution of AE count, count rate, frequency, amplitude, and *b*-value over time. In the figure, $t\_{EQ.1}$ denotes the occurrence time of earthquake EQ.1, and the dashed box indicates the most intense AE burst characteristics before the earthquake. The AE characteristic changes within the dashed box show the following features: a large jump in AE event count, and significant peaks in AE count rate, frequency, and amplitude. Notably, this intense burst is closely related to the impending magnitude 3.2 earthquake (EQ.1) and occurs approximately 13 hours before it. It can

be seen that significant changes in AE characteristic parameters herald the approach of an earthquake. Furthermore, *b*-value analysis for this time period reveals a continuous decrease in the *b*-value before the earthquake, reaching a minimum (marked as $t_{b\text{-min}}$). This minimum *b*-value occurs approximately 9 hours before the earthquake occurrence time. Thus, the continuous decreasing trend of the *b*-value can serve as an earthquake warning, and changes in the b-value can be used as characteristic indicators for seismic precursor identification.

### 4.4.4 *b*-value evolution and seismic precursors

Considering the evolution of the AE *b*-value over time, the *b*-value and earthquake sequence were analyzed together, with the results shown in Fig. 4.11. The *b*-value was calculated using a sliding window of 200 events. The reference earthquakes were the two relatively strongest regional earthquakes, magnitude 3.2 (EQ.1) and magnitude 2.4 (EQ.2), indicated by vertical dashed lines in Fig. 4.11.

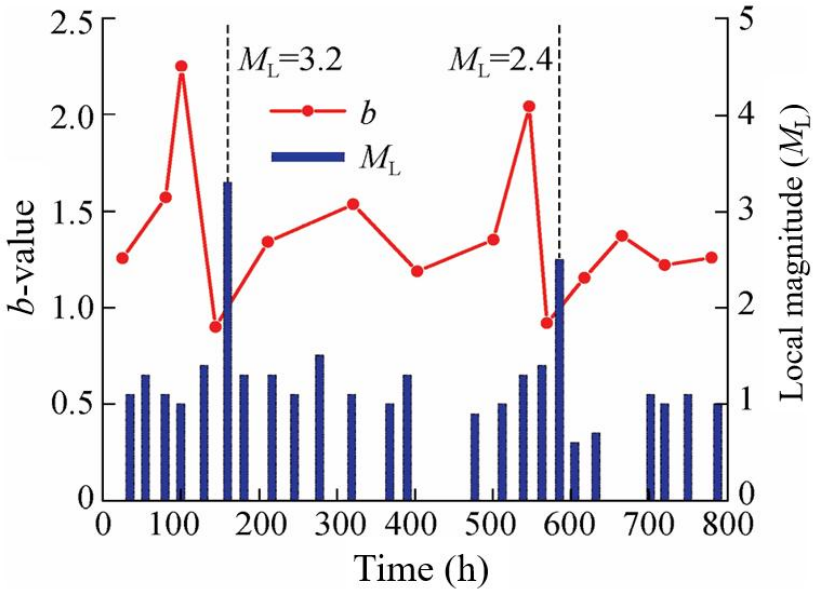


**Figure 4.11** *b*-value evolution and earthquake sequence during the monitoring period.

It can be seen from Fig. 4.11 that changes in the *b*-value have a clear temporal correlation with seismic activity. The occurrence of the two major seismic events led to a significant decrease in the *b*-value, with the minimum *b*-value falling below 1.

Specifically, as the magnitude $M_L$ = 3.2 earthquake approached, the *b*-value decreased from 2.3 to 0.9. Subsequently, as the magnitude $M_L$ = 2.4 earthquake approached, the *b*-value decreased from 2.1 to 0.9. During periods with no major earthquakes recorded, the *b*-value showed a recovery trend. It can be seen that changes in the *b*-value are closely related to seismic events. A substantial decrease in the *b*-value implies the approach of a larger magnitude event, and the minimum *b*-value can serve as a characteristic indicator for seismic precursor identification, useful for imminent precursor identification.

### 4.4.5 NT analysis and seismic precursors

Natural time analysis was performed using a sliding window of 100 events to study the evolution of the NT variance $\kappa_1$, entropy $S$, and time reversed entropy $S_{rev}$. The results are shown in Fig. 4.12. The two horizontal dashed lines represent the variance limit $\kappa_1$ = 0.07 and the entropy limit $S_u$ = 0.0966, respectively. According to the critical conditions, the critical time $t_{crit}$ was obtained, indicated by the red vertical dashed line in Fig. 4.12. The trend of the NT variance shows that before the earthquake occurrence, $\kappa_1$ has a distinct minimum, rapidly decreasing from 0.07 to near 0. It should be noted that $t\_{EQ.1}$ in Fig. 4.12 denotes the occurrence time of the magnitude 3.2 earthquake (EQ.1). Furthermore, $t_{b\text{-min}}$ is the critical time identified by the *b*-value method. A comparison shows that the precursor identifications of the two indicators are generally consistent, with $t_{crit}$ occurring slightly earlier than $t_{b\text{-min}}$.

As shown in Fig. 4.12, taking $M_L$ = 3.2（EQ.1）as an example, $t_{crit}$ (NT critical time), $t_{b\text{-min}}$ (*b*-value critical time), and $t\_{EQ.1}$ (earthquake occurrence time) are marked with dots. Table 4.2 lists the precursor identification results from multiple analyses. The analysis indicates that the NT critical time $t_{crit}$ is 7 hours and 3 hours earlier than the minimum *b*-value and AE characteristic parameters, respectively, and is 16 hours earlier than the seismic event. Therefore, the critical time $t_{crit}$ from NT analysis can serve as another characteristic indicator for seismic precursor identification.

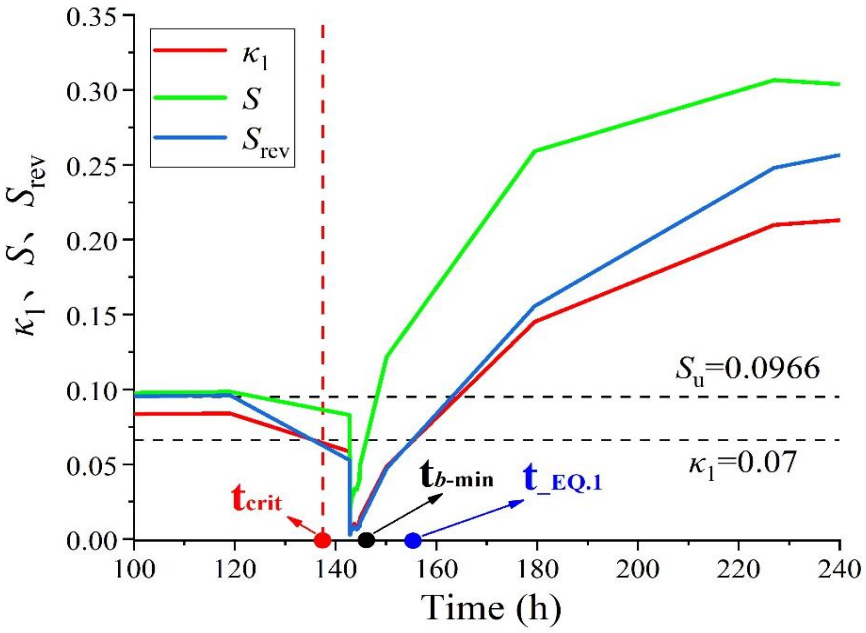


**Figure 4.12** NT series and major seismic events during the monitoring period.

**Table 4.2** Precursor identification results from multiple AE analysis methods.

| Local Magnitude | Multimodal statistical analysis | NT analysis | AE characteristic parameters | *b*-value method |
|---|---|---|---|---|
| $M_L$=3.2 | 17 h in advance | 16 h in advance | 13 h in advance | 9 h in advance |

## 4.5 MCF-B method and seismic precursor identification

### 4.5.1 Evolution of MCF-B parameters in AE time series

This section applies the MCF-B method introduced in Section 2.5 to the rock AE time series collected in the field at the Eastern Guangdong Seismic Monitoring Station, aiming to validate its effectiveness in identifying earthquake precursors in a real environment. The core of the MCF-B method is to quantitatively reveal the deviation of the AE event amplitude distribution from an ideal power law by fitting the AE amplitude distribution function $N(A)$ (Eq. 2.31). The parameter $p_2$ reflects the underlying power law decay characteristics of the distribution, while $p_3$ characterizes the enrichment ($p_3 < 0$) or scarcity ($p_3 > 0$) of high-amplitude events relative to the

power law. When the system is in a self organized critical state, the amplitude distribution approaches a pure power law, i.e., $p_2 > 1$ and $p_3 \approx 0$. When the system deviates from the critical state and is about to become unstable, a "crossover phenomenon" of decreasing $p_2$ and monotonically increasing $p_3$ appears [128].

A sliding window method was used for the recursive analysis of the continuous AE time series. The window size was set to W = 100 events, meaning the initial window consisted of events #1 to #100, from which the first set of ($p_2$, $p_3$) parameters was obtained by fitting. The window was then shifted, calculating parameters for events #2 to #101, #3 to #102, and so on, until the end of the data. All time coordinates were normalized by the total monitoring duration. Figure 4.13 shows the complete evolution curves of the MCF-B parameters $p_2$ and $p_3$ during the monitoring period, with the occurrence times of the two major earthquakes in the catalog marked in the figure.

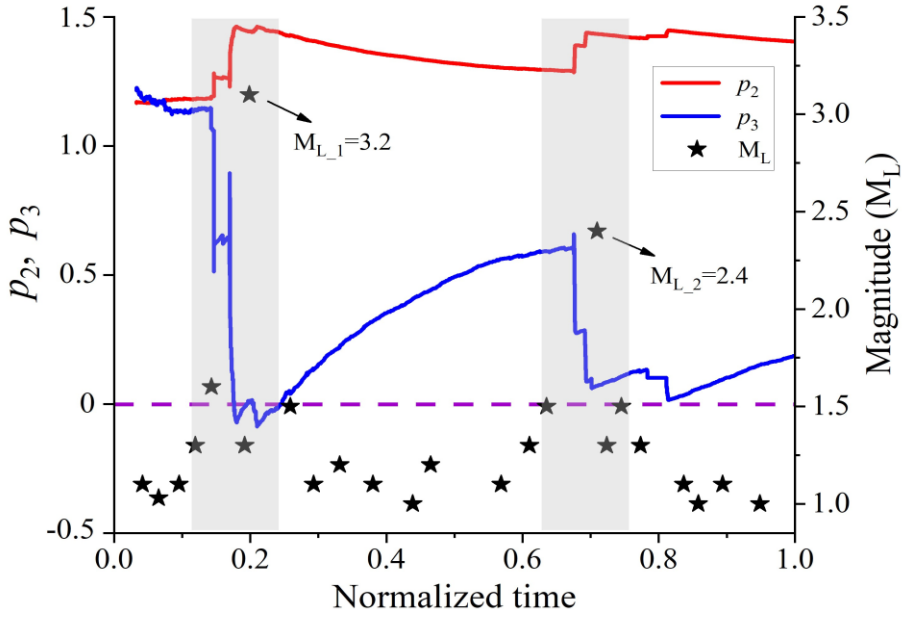


**Figure 4.13** Parameter evolution of the MCF-B method and the earthquake sequence.

It is evident from Fig. 4.13 that the $p_2$ curve remains generally stable, while $p_3$ exhibits significant fluctuations, apparently influenced by the two major earthquakes. The characteristic features for identifying the system entering a critical state (seismic precursor) using the MCF-B method are as follows: first, an

"ideal power law" distribution appears with $p_2 > 1$ and $p_3 \approx 0$; subsequently, $p_2$ begins to decrease while $p_3$ increases monotonically, presenting a "crossover phenomenon". The earliest critical region is shown by the grey background area in Fig. 4.13. It should be noted that following the critical state, two major earthquakes occurred. This indicates that the MCF-B method can be used for seismic precursor identification, and its parameters $p_2$ and $p_3$ can serve as precursor identification parameters.

### 4.5.2 Analysis of precursor characteristics of MCF-B parameters

To reveal the anomalous evolution patterns of MCF-B parameters before earthquakes, the $M_L$=3.2 and $M_L$=2.4 earthquakes were taken as research objects. Based on the results in Fig. 4.13, the typical characteristics of MCF-B parameters before the earthquakes are observed as follows.

First, during the pre earthquake period of the entire monitoring cycle, the $p_2$ value generally fluctuated within the range of 1.2 to 1.5, with an average of approximately 1.32, while the $p_3$ value approached 0. This state corresponds to the exponential decay term $e^{-Ap3} \approx 1$ in Eq. (2.31), indicating that the amplitude distribution approximately follows a pure power law and that the microfracturing activity of the crustal rock is in a self organized critical state. Second, before both earthquakes, the $p_3$ parameter exhibited a pattern of "positive jump followed by peak decline". This pattern coincides temporally with the explosive growth of traditional parameters such as AE count rate and amplitude observed in Section 4.4.3 hours before the earthquakes. However, a significant advantage of the MCF-B method is that its characterization is based on the global statistical features of the amplitude distribution, making it insensitive to random fluctuations of individual event amplitudes. Consequently, its anomaly criteria are more stable and yield a lower false alarm rate. Before both earthquakes, the $p_3$ parameter was observed to exhibit a sustained, monotonic positive deviation ($p_3 > 0$). According to the physical meaning of Eq. (2.31), $p_3 > 0$ indicates a decrease in the proportion of high-

amplitude events relative to the total number of events, i.e., the amplitude distribution exhibits a "downward tail" shape. This phenomenon can be explained by the physical process of earthquake preparation. As the earthquake approaches, stress concentration in the rocks of the preparation zone intensifies, and macroscopic scale cracks begin to initiate and accelerate propagation. The number of such large scale rupture events is limited, but the energy released by each individual event is extremely high, and the corresponding amplitudes should be much higher than those of background microfractures. However, constrained by the dynamic range of the field monitoring system, the frequency response of the sensors, and the strong attenuation of high-frequency signals in the crustal medium, these very few ultra high energy events may not be effectively captured. This leads to a relatively lower proportion of observed high-amplitude events, thus manifesting as a positive shift in $p_3$.

Furthermore, compared with the significant fluctuations of parameter $p_3$, the changes in parameter $p_2$ before and after the two earthquakes were relatively gentle, and a systematic continuous decrease like that observed in the concrete beam failure tests in Section 3.6 did not occur. A continuous decrease in $p_2$ corresponds to the irreversible evolution of damage from a three dimensional volumetric distribution to localization on a two dimensional plane. In laboratory tests with monotonic loading to failure, this process is complete and irreversible. However, during natural earthquake preparation, the crustal stress loading rate is extremely low, the stress path is complex, and the process may be accompanied by stress release, pore pressure adjustment, and other factors, leading to an evolution of $p_2$ characterized by a "slight decrease amidst fluctuations" rather than a "sustained monotonic decline".

Therefore, in practical seismic precursor identification, the $p_3$ parameter, due to its high sensitivity to deviations from criticality, exhibits precursor anomalies that are more easily observable than $p_2$. In seismic precursor identification, priority should be given to monitoring positive shifts in $p_3$, while a sustained decrease in $p_2$ can be used as an auxiliary criterion.

## 4.6 Synchronous cross validation of multiple precursors

When facing complex seismogenic systems, identification methods based on a single physical precursor may struggle to effectively extract critical pre-seismic signals. One feasible path to improve the robustness of precursor identification is to introduce multi-physical precursor cross validation. The core idea of multi-precursor cross validation is that if an earthquake is indeed the physical response of crustal rock fracture, then signals generated by different physical mechanisms should exhibit temporal synergistic anomalies before the earthquake. Electromagnetic emission (EME), as another type of physical signal closely related to rock fracture, has generation mechanisms, propagation characteristics, and pre-seismic anomaly features that are both distinct from and physically related to those of AE. Synergistic analysis of the two holds promise for capturing precursor evidence even when a single signal is drowned out by background noise.

This section relies on the EME monitoring system deployed concurrently at the Eastern Guangdong seismic station. It performs a time domain correlation analysis of AE and EME time series, aiming to reveal the temporal correlation between AE and EME before earthquakes and their precursor identification capabilities, and to explore the application potential of multi-physical precursor fusion in seismic precursor identification.

### 4.6.1 Electromagnetic monitoring system layout and data acquisition

To achieve synchronous monitoring of AE and EME, this study deployed a multi-precursor acquisition platform in the dedicated mountain tunnel of the Shantou Earthquake Monitoring Center. This tunnel features low environmental noise and minimal electromagnetic interference, providing ideal conditions for high sensitivity monitoring. As shown in Fig. 4.16, in addition to the existing AE monitoring system and seismometer, an electromagnetic oscilloscope, an electromagnetic receiving

antenna, and a neutron monitor were newly installed to conduct multi-signal field monitoring simultaneously. It should be noted that the generation of neutron emission signals is related to multiple factors and involves significant uncertainty. Their reliability requires further research and validation; therefore, this thesis does not present results from neutron emission.

The electromagnetic monitoring system employed a combination of a broadband adjustable telescopic antenna and a digital oscilloscope. The telescopic antenna has a maximum extended length of 125 cm and can adjust its resonant length according to the target frequency band. This antenna was used in conjunction with a Lecroy WaveAce 2032 digital oscilloscope. The dual channel oscilloscope has a bandwidth of 300 MHz and a sampling rate of up to 2 GS/s, meeting the requirements for precise capture of high-frequency electromagnetic signals. The WaveAce 2032 digital oscilloscope is equipped with a 7 inch color wide screen display, facilitating real-time observation of waveform characteristics in the field. The device has 32 built in automatic measurement parameters, including amplitude, frequency, and rise time, which can be used for rapid extraction of electromagnetic signal features. Regarding data storage and transmission, the oscilloscope's USB device port supports connection to a computer for remote control. Together with the Lecroy WaveStudio software, it enables communication between the oscilloscope and the computer, allowing real-time transmission of waveform data and measurement results to the computer for subsequent analysis.

Both the AE and EME systems were time synchronized with the seismometer via the NTP protocol. The three sets of data were uniformly stored on the server at the monitoring center, with daily data reports generated. The analysis period for this data was from November 2024 to May 2025, totaling 6 months (180 days) of complete data.

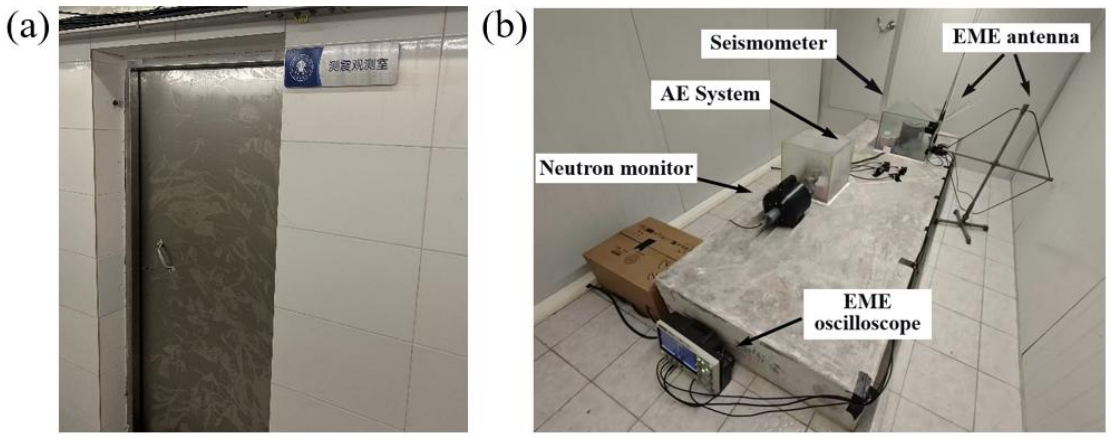


**Figure 4.16** Layout of the multi-precursor observation system in the seismometry room: (a) multi-precursor observation room; (b) arrangement of observation equipment.

## 4.6.2 Earthquake catalog and multimodal statistical analysis

Based on the earthquake catalog collected by the seismometer deployed at the Shantou Earthquake Monitoring Center, seismic events with local magnitude $M_L \geq 1.0$ within a radius of 200 km from the monitoring point were selected. The temporal distribution of earthquakes is shown in Fig. 4.17. During the monitoring period, a total of 102 effective seismic events were recorded, with magnitudes ranging from $M_L$ 1.0–4.0. During this period, small earthquakes occurred frequently in this area, and no earthquake above magnitude 4 occurred within 200 km.

As introduced in Section 5.4.2, the multimodal statistical method can identify the main clustering intervals in the distribution of discrete seismic events and fit them using Gaussian functions, determining the positions of local maxima through iterative optimization.

Based on the temporal distribution of 102 earthquakes detected during the 180-day monitoring period, multimodal statistical analysis was performed. The results show that seismic activity exhibited four significant Gaussian distribution peaks (Fig. 4.17), corresponding to four periods of earthquake clustering. The parameters of each peak are shown in Table 4.3. The largest magnitude occurred on day 68, with $M_L = 3.3$. The identification of four earthquake peaks indicates that regional seismic activity is not

randomly and uniformly distributed but exhibits quasi periodic clustering characteristics. This feature provides a clear temporal benchmark for testing the precursor identification capabilities of AE and EME.

**Table 4.3** Peak parameters of the multimodal distribution of earthquakes

| Peak No. | Peak time (d) | Local magnitude ($M_L$) |
|---|---|---|
| EQ.I | 31 | 2.5 |
| EQ.II | 68 | 3.3 |
| EQ.III | 122 | 2.6 |
| EQ.IV | 151 | 3.0 |

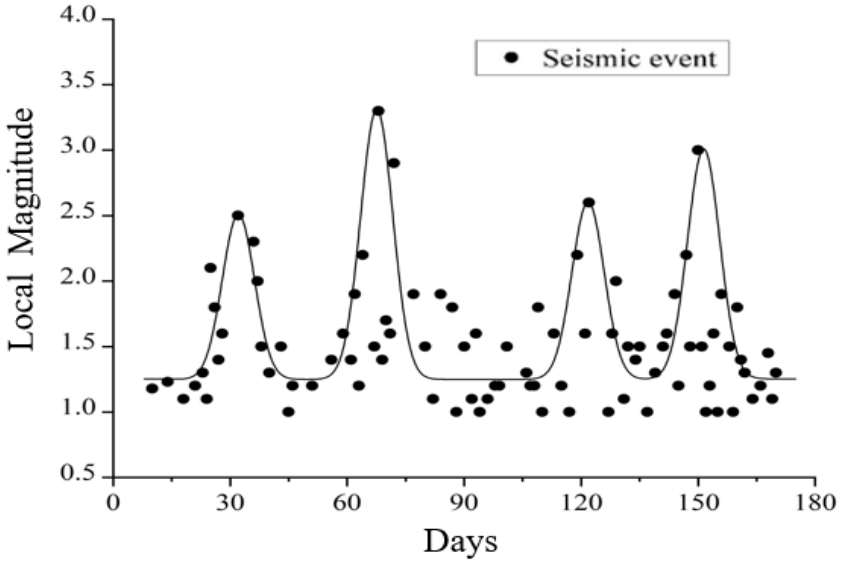


**Figure 4.17** Multimodal Gaussian distribution results of the earthquake sequence during the monitoring period.

## 4.6.3 Synchronous cross validation of EME and AE

Using the identical multimodal analysis method applied to the earthquake distribution, Gaussian fitting was performed on the AE count rate (daily AE event count) and the EME count rate over the 180 days. The multimodal results for the AE and EME distributions are shown in Fig. 4.18(a) and (b). AE and EME each identified four

significant Gaussian peaks, which corresponded exactly in number to the four earthquake peaks.

Furthermore, Fig. 4.18(a) and (b) show the temporal distributions of AE, EME, and earthquakes, respectively. The comparison shows that AE and EME have a strong correlation with the earthquake sequences occurring in the nearby area, and the trends of the AE and EME temporal distributions precede that of the earthquakes, making them potential earthquake precursors.

The temporal comparison between AE and EME is shown in Fig. 4.18(c). It can be intuitively seen from the figure that the trends of the AE and EME distributions are nearly identical. The AE peak time occurs after the EME peak but before the earthquake peak. The EME peak appears first, followed by the AE peak, and finally the earthquake peak. The three exhibit a strict and repeatable temporal order.

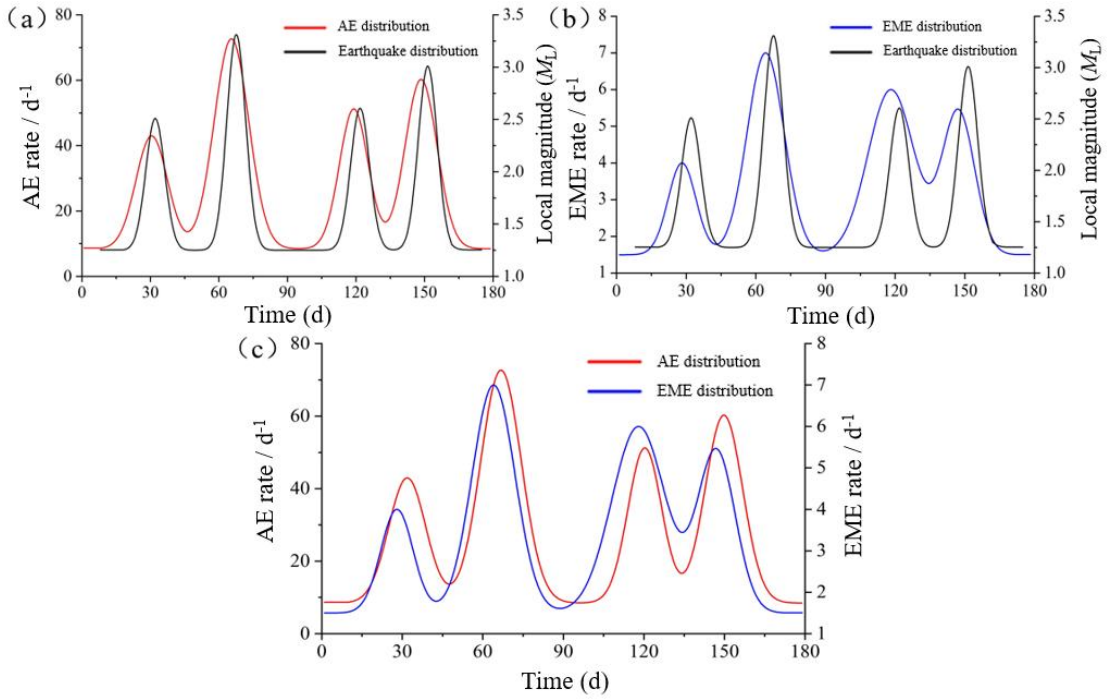


**Figure 4.18** Temporal distribution of earthquakes and AE during the monitoring period: (a) distribution of AE and earthquakes; (b) distribution of EME and earthquakes; (c) distribution of EME and AE.

Taking the $M_L = 3.3$ earthquake on day 68 (EQ.II) as an example, the time range is expanded to ± 25 days to detail the identification effects of AE and EME. The results are shown in Fig. 4.19. The center of the earthquake Gaussian peak is on day 68, the

AE Gaussian peak is on day 67, with AE identifying the seismic event approximately 1 day in advance. The EME Gaussian peak is on day 65, with EME identifying the seismic event approximately 3 days in advance. It can be seen that the peaks of the AE and EME distributions identifying subsequent earthquakes exhibit a clear temporal order. Before the earthquake, EME first shows precursor anomalies 3 days in advance, then AE shows precursor characteristics 1 day in advance, and finally the earthquake occurs. This result validates the effectiveness of AE and EME as earthquake precursors.

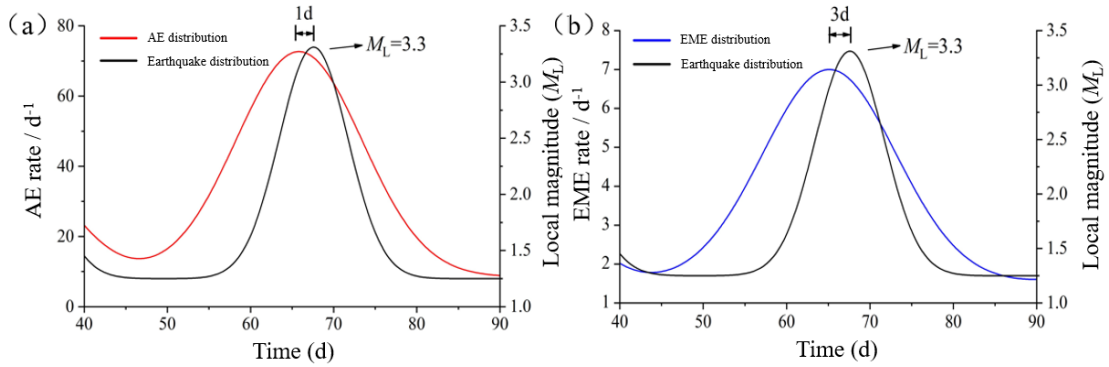


**Figure 4.19** Typical earthquake case identified by AE and EME during the monitoring period: (a) AE identification result; (b) EME identification result

## 4.6.4 Future earthquake identification based on AE and EME signals

Beyond temporal lead time, whether a quantitative relationship exists between the intensity of precursor signals and the magnitude of subsequent earthquakes is a core question in seismic precursor identification research. Based on the four groups of AE peaks and four groups of earthquake peaks identified during the 180-day monitoring period, a linear regression analysis was performed between the peak AE count rate intensity and the maximum magnitude of the corresponding earthquake cluster. The results are shown in Fig. 4.20(a). The analysis indicates a significant positive correlation between AE peak intensity and earthquake magnitude ($R^2 = 0.96$). That is, stronger AE activity corresponds to a larger subsequent earthquake magnitude, confirming a strong correlation between the two. Similarly, a regression analysis was performed on the four groups of EME peak intensities and earthquake magnitudes, with results shown in Fig. 4.20(b). The goodness of fit for EME peak intensity versus

magnitude was 0.61, showing a weaker correlation than for AE signals. This may be due to electromagnetic signals being susceptible to environmental electromagnetic noise during propagation, leading to higher data dispersion. Nevertheless, the trend of EME intensity remains consistent with magnitude and can serve as an auxiliary reference for magnitude identification.

The establishment of the above empirical relationships provides a quantitative basis for identifying earthquake magnitude based on precursor signal intensity. As monitoring continues, more complete data sets of AE and EME peaks corresponding to seismic events will be accumulated in the future, allowing for the gradual development of more statistically significant identification models. In specific applications, by performing sliding window multimodal analysis on AE and EME count rate time series, new anomaly peaks can be identified in real-time and their intensities recorded. The possible magnitude of a subsequent earthquake can then be estimated based on the established intensity magnitude relationship. Furthermore, combined with the previously established relationship between the peak times of AE and EME and the time of earthquake occurrence, the time window of the earthquake can be simultaneously constrained, achieving dual precursor identification of both magnitude and time.

This attempt has preliminarily established a quantitative correlation between precursor signal intensity and earthquake magnitude in this monitoring area, providing a methodological framework for constructing a multi-parameter short-term and imminent warning system based on "identifying magnitude via intensity and identifying the occurrence window via peak time". It should be emphasized that the current conclusions are based on preliminary fitting of six months of data. Their generalizability requires validation with longer time series and more earthquake cases. However, this attempt provides a feasible path for gradually approaching the application requirements of earthquake early warning.

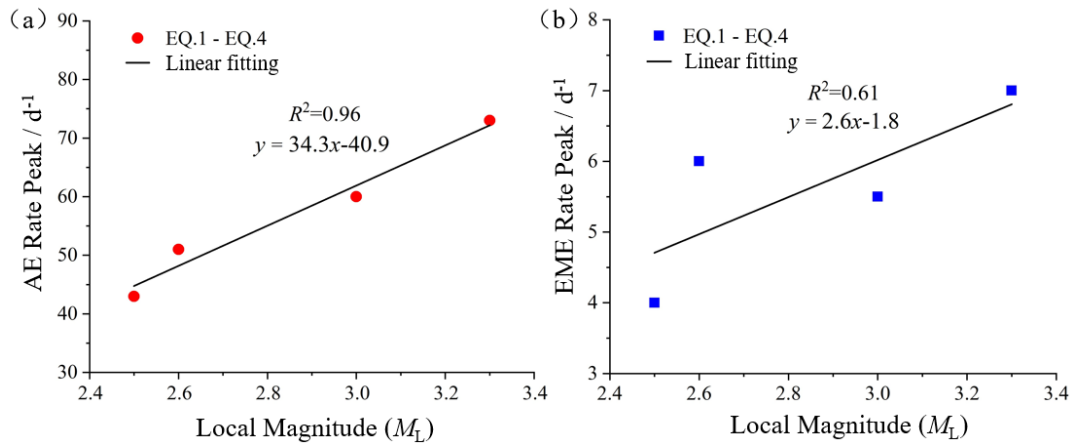


**Figure 4.20** Magnitude identification model based on AE and EME peak intensity: (a) AE fitting results; (b) EME fitting results.

## 4.6.5 Discussion on physical mechanism of multi-precursor synergy

The stable temporal order of "EME first, AE second" before earthquakes has its physical root in the intrinsic relationship between the evolution of microfracture scales in the preparation zone and the frequencies of the excited signals. This corresponds precisely to the "correlation between wavelength scale and frequency" shown in Figure 1.2 and the "evolution model of the earthquake preparation zone" shown in Fig. 1.3 in the introduction of this thesis [3].

According to fracture mechanics theory, the scale of a microfracture event determines the frequency of the stress wave it emits: the smaller the scale of the fracture, the higher the frequency of the excited stress wave; conversely, the larger the scale of the fracture, the lower the frequency. Figure 1.2 clearly shows the multi-scale correspondence between frequency and fracture scale, spanning from nanometer scale (~1 THz) to kilometer scale (~1 Hz).

Applying this principle to the earthquake preparation process and combining it with the earthquake preparation zone evolution model shown in Fig. 1.3, the various stages can be explained as follows. In the days to weeks before an earthquake (corresponding to Stage I or II in Fig. 1.3), the preparation zone is dominated by nano to millimeter scale microfractures. The peak frequency of energy release from these small scale

fractures falls within the MHz or even GHz range. High-frequency stress waves attenuate extremely rapidly when propagating through the crustal medium, but part of their energy can be converted into electromagnetic emissions. Simultaneously, electromagnetic waves attenuate much less in rock than high-frequency stress waves, thus they can propagate over longer distances and be captured by surface antennas, manifesting as EME anomalies. This explains why EME is the earliest appearing precursor signal. As the earthquake preparation process enters the imminent stage (hours to one day before the earthquake, corresponding to Stage III in Fig. 1.3), the scale of microfractures grows to the millimeter to meter level, and the frequency of the excited stress waves drops to the kHz to MHz range, which is the sensitive frequency band for conventional AE monitoring. At this time, large scale fracture activity intensifies significantly, and the AE event rate increases sharply, making AE the most active physical signal. Entering the final stage (Stage IV in Fig. 1.3), macroscopic cracks coalesce, and the earthquake occurs.

This physical mechanism, where fracture scale determines frequency and frequency determines propagation attenuation, creates the universal temporal sequence of "EME (high-frequency signal) first, AE (medium frequency signal) second, earthquake (low frequency signal) last". From the scale frequency relationship in Fig. 1.2, EME and AE can be viewed as observation windows into different frequency bands of the same fracture spectrum. The earthquake preparation zone evolution model in Fig. 1.3 provides a cross-scale dynamic background for this temporal sequence.

Based on above mechanism, EME provides an earlier warning time window, while AE provides more imminent and direct evidence of earthquake precursors. Their synergistic monitoring can construct a multi-level warning system of "EME for medium to long-term warning plus AE for short-term and imminent warning", significantly improving the reliability of precursor identification. The 180-day synchronous monitoring conducted at Eastern Guangdong seismic station has validated the synergistic temporal pattern of AE and EME and its physical mechanism in this region, providing empirical evidence for multi-precursor fusion in earthquake observation.

## 4.7 Chapter summary

This chapter first relied on the seismic monitoring station in the full granite mountain tunnel in eastern Guangdong to carry out 35 days of synchronous AE and earthquake monitoring. It systematically studied the correlation between AE activity and regional seismicity and tested the precursor identification capabilities of the *b*-value method, NT analysis, and the MCF-B method proposed in this thesis at the real crustal scale. Based on this, synchronous EME monitoring was further introduced, and 180 days of synchronous continuous observation and cross validation of AE and EME were conducted. The main conclusions of this chapter can be summarized as follows:

（1）Based on the initial 35 days of synchronous AE and earthquake monitoring in the granite mountain tunnel in eastern Guangdong, a significant temporal correlation was found between intense bursts of AE activity and regional seismic events. Jumps in AE event count, peaks in AE count rate, and anomalous enhancements of characteristic parameters such as frequency and amplitude all occurred before the earthquakes, serving as physical precursors of earthquakes. Multimodal statistical analysis of AE and earthquake distributions showed that the peak of the AE Gaussian distribution could identify seismic events approximately 17 hours in advance.

（2）The AE *b*-value and NT analysis demonstrated good precursor indication capability in field monitoring. Before the two major earthquakes, the AE *b*-value showed a continuous decrease to a minimum, with the minimum *b*-value occurring approximately 9 hours before the earthquake. The critical time identified by NT analysis was earlier than that of the *b*-value method, approximately 16 hours before the earthquake. Before the earthquake, the NT variance $\kappa_1$ rapidly decreased from 0.07 to a minimum near 0, showing its potential as an early warning indicator.

（3）Applying the MCF-B method to field AE monitoring data validated its effectiveness in identifying earthquake precursors in a real geological environment. The seismic precursor characteristics of the MCF-B method are as follows: first, an ideal power law distribution appears with $p_2 > 1$ and $p_3 \approx 0$; subsequently, $p_2$ begins to decrease while $p_3$ increases monotonically, presenting a crossover phenomenon. Before

the earthquake, the parameter $p_3$, which characterizes the shape of the amplitude distribution, begins to show a significant positive jump anomaly, i.e., $p_3$ changes from near zero to positive and continues to increase. This reflects the critical characteristic of relative scarcity of high-amplitude events, constituting a robust statistical physics precursor before earthquakes.

（4）A synergistic earthquake precursor identification model for AE and EME was established. Multimodal statistical analysis based on 180 days of observation data shows that both EME and AE exhibit Gaussian distribution peaks highly correlated with seismic activity before earthquakes, and the three follow a strict temporal order: the EME peak appears first (approximately 3 days in advance), followed by the AE peak (approximately 1 day in advance), and finally the earthquake occurs. This temporal order can be explained by the scaling law relating fracture scale to emission frequency. Furthermore, there is a significant positive correlation between the peak intensities of AE and EME and the magnitude of subsequent earthquakes, providing a quantitative basis for identifying magnitude based on precursor signal intensity.

# Chapter 5

# 5 Deep learning–based intelligent identification of AE seismic precursors

## 5.1 Introduction

The preceding chapters have systematically demonstrated the effectiveness of AE technique for monitoring microfracture activity and identifying system critical precursors from multiple perspectives, including fracture mechanics theory (Chapter 2), laboratory scale concrete structure tests (Chapter 3), and field rock AE measurements (Chapter 4). The research has shown that the statistical features embedded in AE signals, such as MCF-B parameters and NT variance, can sensitively capture the critical state of a system transitioning from stable damage accumulation to unstable failure. This holds true in fracture tests of concrete specimens with different stress states, sizes, and material compositions, as well as in mountain tunnel monitoring under real crustal environmental conditions. Notably, the field measurement work in Chapter 4 verified a significant temporal correlation between AE activity and regional seismic events in the monitoring area of this study and established a seismic precursor identification framework based on AE characteristic parameters.

However, the aforementioned identification methods still face several challenges in practical applications. First, the earthquake preparation process is a highly complex nonlinear evolutionary system, and its precursor signals are often buried in environmental noise and background microseismic activity. Anomalous fluctuations of a single parameter are susceptible to interference, leading to false alarms or missed

detections. Second, when applying the MCF-B method to analyze rock AE data in Section 4.5, it was found that although the method is effective in identifying earthquake precursors, the evolution of its parameters $p_2$ and $p_3$ requires manual interpretation of the "crossover phenomenon", making it difficult to meet the timeliness requirements of real-time early warning.

These limitations indicate that relying solely on physical models or statistical parameter analysis makes it difficult to construct a reliable system that meets the demands of practical earthquake early warning. One feasible path to overcome this difficulty is to introduce AI technology and deeply integrate the precursor knowledge from physical models with the pattern recognition capabilities of data driven methods. Deep learning, with its powerful nonlinear fitting ability, automatic high dimensional feature extraction capability, and end-to-end learning framework, has demonstrated significant advantages in areas such as time series prediction and anomaly detection [51]. Applying deep learning to seismic precursor identification holds promise for achieving the following goals: automatically mining hidden precursor patterns from massive AE data that are difficult to capture with traditional parameters; integrating multi-source features (waveform features, statistical parameter features) to improve identification robustness; and constructing real-time decision models to achieve automatic early warning of seismic events.

Based on this, this chapter relies on the field monitoring data from the Eastern Guangdong seismic station described in Chapter 4 to construct a deep learning based intelligent identification model for AE seismic precursors. First, based on the raw AE data collected in real time by the ÆMISSION® system, four basic features (AE event count, count rate, frequency, and amplitude) are extracted to construct a dataset containing seismic precursor samples and non-earthquake samples (Sections 5.2 5.3). Second, a multi-layer feedforward neural network is designed, network hyperparameters are optimized through cross validation strategies, and the model's identification performance is evaluated on an independent test set (Section 5.4). Subsequently, the trained model is applied to the 180-day long-term time series monitoring data described in Section 4.7 for long-term stability validation and to

evaluate the model's early warning lead time in practical scenarios (Section 5.5). Finally, the integration of physical statistical features such as MCF-B parameters ($p_2$, $p_3$) and NT variance ($\kappa_1$) into the deep learning model as higher order features is explored to construct a "physics-data" hybrid driven collaborative identification framework. The improvement in model performance brought by physical features and their feature importance are analyzed (Section 5.6).

It should be noted that Chapter 4 validated that AE signals can serve as earthquake precursors through physical statistical methods such as MCF-B and NT. However, these methods rely on manual interpretation and cannot meet the early warning demands of real-time massive signal processing. Building on this foundation, this chapter takes the measured data from Chapter 4 as training samples and introduces deep learning models to achieve automatic extraction and real-time identification of precursor features, thereby constructing a technological chain from physical precursors to intelligent early warning. This chapter aims to achieve complementary advantages between physical model knowledge and data driven methods, providing a theoretical basis and technical support for constructing an intelligent earthquake early warning system with physical interpretability and high precision identification capability.

## 5.2 Deep learning-based seismic precursor identification

### 5.2.1 Seismic event identification workflow

Based on real-time monitoring of rock AE data, this thesis proposes a new method for identifying seismic event precursors using AE time series features and deep learning. The overall workflow of this method is shown in Fig. 5.1, where [$x_1$], [$x_2$], …, [$x_m$] represent the extracted AE time series features containing precursor information of seismic events.

The main steps of this method are as follows. First, AE sensors deployed in the rock mass record AE signals generated by rock fracture in real time. Second, feature

extraction and time series analysis are performed on the collected raw AE signals to obtain characteristic parameters that can reflect seismic precursors. Third, the extracted AE features are used as inputs to train a deep learning model, enabling it to learn and classify patterns of seismic precursors. Finally, the trained and optimized model is used to perform binary classification on real-time data, determining whether there is a possibility of an impending earthquake (earthquake or no earthquake), thereby achieving rapid identification of seismic events.

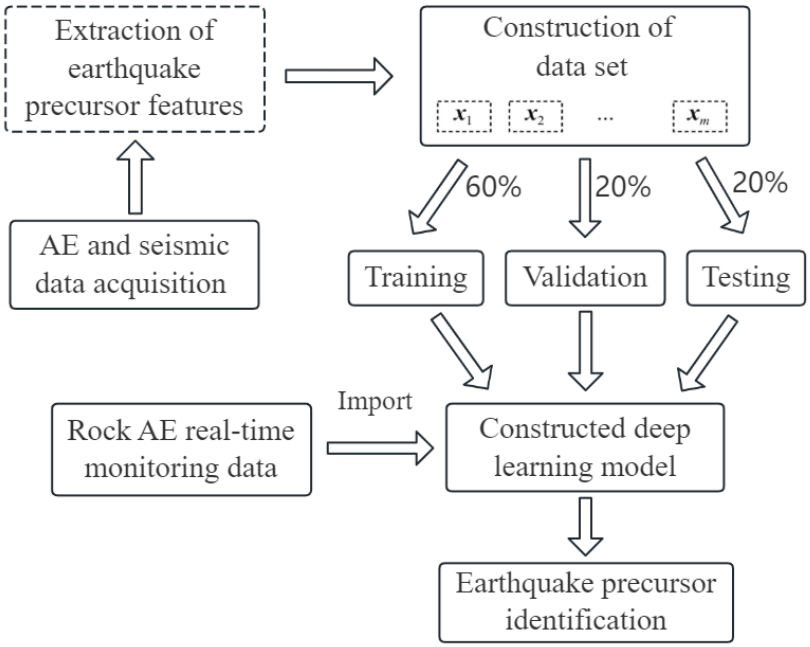


**Figure 5.1** Schematic diagram of the earthquake precursor identification method

It is worth emphasizing that the design of the entire identification workflow follows a closed loop logic of "data acquisition, feature extraction, model training, real-time early warning". In the feature extraction stage, not only the basic parameters automatically output by the AE device are included, but higher order statistical features with physical significance can also be integrated, laying the foundation for the subsequent physics-data hybrid driven model. In the real-time seismic precursor identification stage, the model continuously compares the output prediction probability with a preset threshold. When the prediction probability exceeds the threshold and persists for a certain period, the system automatically triggers a prediction signal, thus

achieving end-to-end automated processing from data to decision. The design of this workflow fully considers the dual requirements of timeliness and robustness in actual earthquake observation scenarios.

### 5.2.2 Deep learning model architecture

The deep neural network adopted in this chapter is a multi-layer feedforward network. Its structure is shown in Fig. 5.2, consisting mainly of an input layer, hidden layers, and an output layer. The hidden layers can contain multiple levels, each composed of multiple neurons. Neurons are connected to neurons in adjacent layers through weights ($w$) and biases ($b$). The network randomly initializes the weights and biases and applies an activation function to compute the predicted output ($\hat{y}$). Subsequently, these parameters are iteratively updated through a backpropagation algorithm to minimize the loss function between the predicted values and the true values. The deep neural network can effectively capture complex nonlinear relationships, enabling it to automatically analyze and extract precursor features from massive AE data [129,130].

The basic unit of a neural network is the neuron, which mimics the behavior of a biological neuron by linearly combining inputs and computing the output $y$, defined as follows:

$$y = \sigma\left(\sum w_i x_i + b\right) \tag{5.1}$$

where $x_i$ and $w_i$ represent the input of the neuron and its corresponding weight, respectively, $b$ is the bias term, and $\sigma(x)$ is the activation function. The activation function used in this chapter is the sigmoid function, expressed as follows:

$$\sigma(x) = \frac{1}{1+e^{-x}} \tag{5.2}$$

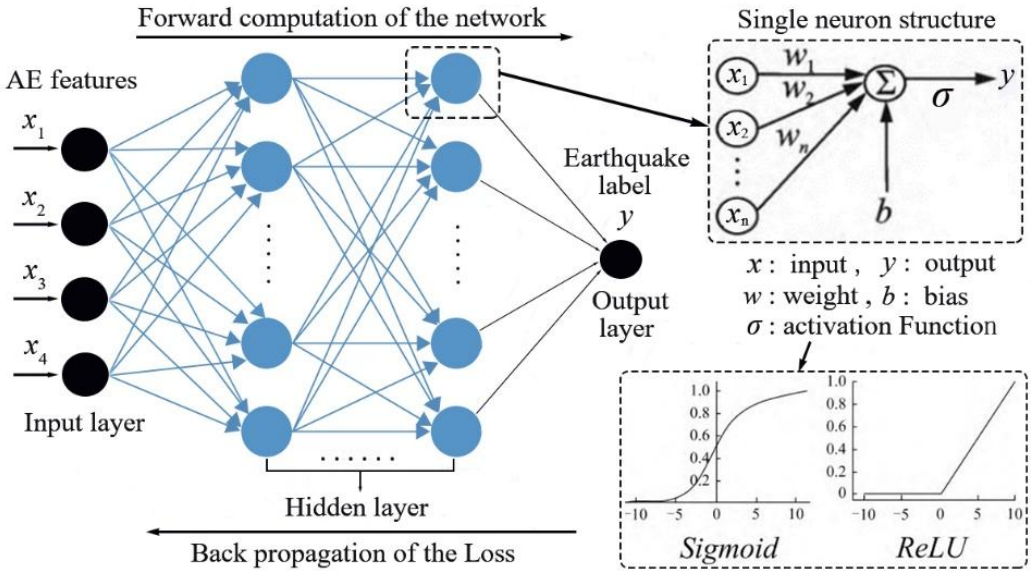


**Figure 5.2** Deep neural network based on the PyTorch framework.

As shown in Fig. 5.2, the input layer of the model constructed in this chapter consists of four extracted AE features ($x_1, x_2, x_3, x_4$), namely AE event count, AE count rate, frequency, and amplitude. The output layer y produces two outcomes: one representing an earthquake (label 1) and the other representing no earthquake (label 0). Therefore, this trained model can be viewed as a multi-dimensional binary classification problem, implemented using the PyTorch framework.

The algorithm model in this chapter is implemented in Python 3.9, and the deep learning framework PyTorch 2.3.1 is used for construction and training. Computations are performed on the Windows operating system, utilizing an AMD Ryzen processor and an Nvidia RTX 8000 GPU for accelerated computing.

## 5.2.3 Training of the deep learning model

The training process of the model includes three main steps: forward computation, backpropagation, and weight update. One complete pass through the entire training set is called an epoch. At the end of each epoch, the loss function is evaluated on the validation set as a measure of model performance. The loss function used in this chapter is the binary cross entropy loss (BCELoss), defined as follows:

$$loss = -\frac{1}{N}\sum_{n=1}^{N} y_n \log_{10} \hat{y}_n + (1 - y_n) \log_{10}(1 - \hat{y}_n) \tag{5.3}$$

where N is the total number of samples, $y_n$ is the true label of the training sample, and $\hat{y}_n$ is the predicted value of the network for the $n$ th sample. The weights are updated using the gradient descent method, calculated by the following formula:

$$w = w - \alpha \frac{\partial loss}{\partial w} \tag{5.4}$$

where $\alpha$ is the learning rate, controlling the step size of parameter updates.

Using the extracted AE features as inputs, this chapter employs a deep learning algorithm to develop a binary classification model for real-time monitoring and identification of seismic events. The dataset containing precursor features is divided into training set (60%), validation set (20%), and test set (20%) in a ratio of 3:1:1. The specific quantitative distribution is shown in Table 5.1. By maintaining a ratio of approximately 1:1 between extracted precursor samples (label 1) and non-earthquake samples (label 0), balanced training of the samples is ensured. The training process of the identification model is shown in Fig. 5.3.

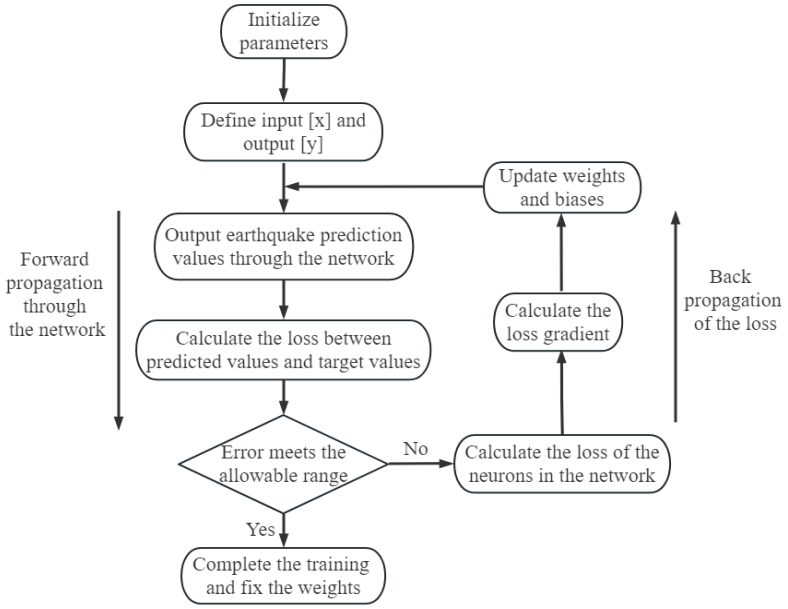


**Figure 5.3** Flowchart of the deep learning model training process

**Table 5.1** Dataset split and sample size distribution.

| Types | Training Set | Validation Set | Test Set |
|---|---|---|---|
| Precursor samples | 1368 | 456 | 456 |
| Non-seismic samples | 1368 | 456 | 456 |
| Total | 2736 | 912 | 912 |

### 5.2.4 Model performance evaluation metrics

The output of a deep learning model is typically treated as a binary classification problem. The evaluation metrics used in this chapter include accuracy, precision, and recall [131]. An earthquake occurrence is considered a positive sample, and no earthquake occurrence is considered a negative sample. The test results can be divided into four categories: true positives ($T_P$), true negatives ($T_N$), false positives ($F_P$), and false negatives ($F_N$), as shown in Table 5.2. Here, $T_P$ and $T_N$ represent the number of correctly predicted positive and negative samples, respectively, while $F_P$ and $F_N$ represent the number of incorrectly predicted positive and negative samples, respectively.

**Table 5.2** Description of the confusion matrix.

| Actual Value | Predicted Value | |
|---|---|---|
| | 1 | 0 |
| 1 | $T_P$ | $F_N$ |
| 0 | $F_P$ | $T_N$ |

Accuracy ($A_{cc}$) is a key evaluation metric, calculated by Eq. (5.5). It represents the proportion of correctly predicted samples to the total number of samples. A higher accuracy indicates better model performance.

$$A_{cc} = \frac{T_p + T_N}{T_p + T_N + F_P + F_N} \tag{5.5}$$

The $F_1$ score is a comprehensive metric, representing the harmonic mean of precision ($P_r$) and recall ($R_e$). It provides a more complete assessment of model performance and is calculated as shown in Eq. (5.6):

$$F_1 = \frac{2P_r R_e}{P_r + R_e} \tag{5.6}$$

where precision ($P_r$) represents the proportion of samples predicted as positive that are actually positive, calculated by Eq. (5.7). Recall ($R_e$) represents the proportion of actual positive samples that are correctly predicted as positive, calculated by Eq. (5.8). Recall is particularly important for evaluating model performance in practical applications.

$$P_r = \frac{T_P}{T_P + F_P} \tag{5.7}$$

$$R_e = \frac{T_P}{T_P + F_N} \tag{5.8}$$

## 5.3 Construction of the AE and seismic dataset

This section elaborates on the process of constructing the dataset used for training the deep learning model. Based on the content of Chapter 4, this section focuses on the processing workflow from raw monitoring data to a model ready dataset, rather than repeating the description of the monitoring system layout and the preliminary analysis of the earthquake catalog.

### 5.3.1 Seismic activity monitoring in the mountain tunnel

The field monitoring experiment of this study was conducted in the dedicated mountain tunnel of the Shantou Earthquake Monitoring Center in Guangdong Province (Chapter 4). To capture signal characteristics related to earthquakes, this study adopted

the ÆMISSION® dedicated AE seismic monitoring device manufactured by Lunitek, Italy. This acquisition system is equipped with eight piezoelectric ceramic sensors with an operating frequency range of 10 kHz to 1 MHz. During the monitoring period, the system operated in continuous acquisition mode with a sampling frequency of 2 MHz, ensuring that the waveform details of AE signals could be fully captured. AE sensors were fixed on the floor of the dedicated tunnel, and a seismometer was simultaneously installed to monitor seismic activity. Detailed information on the monitoring center and the monitoring system layout has been introduced in Section 4.3.1 (Fig. 4.2).

## 5.3.2 AE time series identification method

The Shantou area is located in the Circum Pacific seismic belt with a seismic fortification intensity of VIII degrees, placing it in a strong earthquake zone. The historical seismic activity in the area around the monitoring point has been detailed in Section 4.3.2. During the first 35-day monitoring period, a total of 24 seismic events were recorded, of which two relatively strong earthquakes were selected as the key analysis objects for this study: the local magnitude 3.2 earthquake in the Taiwan Strait on April 30, 2023 (EQ.1) and the local magnitude 2.4 earthquake in the sea area of Haifeng, Guangdong on May 17, 2023 (EQ.2). Their epicentral locations are shown in Fig. 4.4 in Section 4.3.2. To quantitatively analyze the temporal distribution characteristics of seismic activity, Section 4.4.2 applied a multimodal statistical method to process the earthquake catalog. By identifying major seismic events through Gaussian fitting, as shown in Fig. 4.7, two main earthquake clusters, labeled EQ.1 and EQ.2, were clearly identified during the 35-day monitoring period.

The principles of AE signal generation and detection have been detailed in Section 2.3. AE sensors convert the captured stress waves from rock microfractures into electrical signals. After amplification and processing by the AE acquisition system, waveform characteristic parameters are automatically extracted, including event count, frequency, amplitude, duration, and ringing count, as shown in Fig. 2.3. A comparison

of the AE time series and the earthquake catalog during the monitoring period is shown in Fig. 4.5. It can be observed that intense bursts of AE activity (manifested as significant jumps in AE count and peaks in AE count rate) are closely correlated in time with the two major earthquakes (EQ.1 and EQ.2), and the onset of AE bursts occurs before the seismic events. This indicates that an increase in AE activity can be considered a precursor signal of intensified microfracturing activity in the earthquake preparation zone.

Similarly, the multimodal statistical method was applied to analyze the temporal distribution of AE count rate, with results shown in Fig. 4.8. The analysis identified two main Gaussian distribution peaks that correspond highly in time to the two peaks of seismic activity. More importantly, the trend of the AE Gaussian distribution significantly precedes the earthquake distribution, indicating that AE signals can serve as earthquake precursors, providing an early warning for seismic events approximately 17 hours in advance. This content has been discussed in detail in Section 4.4.

### 5.3.3 Feature extraction of AE seismic precursors

To visualize the changes in AE characteristics before a major earthquake, this chapter takes the AE time series before the EQ.1 earthquake as an example and focuses on the evolution of four key features: AE event count, AE count rate, frequency, and amplitude, as shown in Fig. 2.3. AE count represents the cumulative number of events, AE count rate represents the number of events per unit time, frequency is obtained by dividing the ringing count by the duration, and amplitude is the maximum peak value of the signal.

Figure 5.4 shows the raw data results of AE signals before the EQ.1 earthquake, where $t\_{EQ}$ denotes the actual occurrence time of the earthquake. The dashed box highlights the AE precursor characteristics before the earthquake: a significant jump in AE event count and distinct peaks in AE count rate, frequency, and amplitude. The changes in these characteristic parameters clearly indicate the approach of the

magnitude 3.2 earthquake (EQ.1), and these anomalous changes appear approximately 13 hours before the earthquake event. This result demonstrates that raw signal data acquired in real time from the ÆMISSION® device, such as AE event count, count rate, frequency, and amplitude, can effectively capture real-time characteristics of earthquake precursors, providing valuable material for dataset construction.

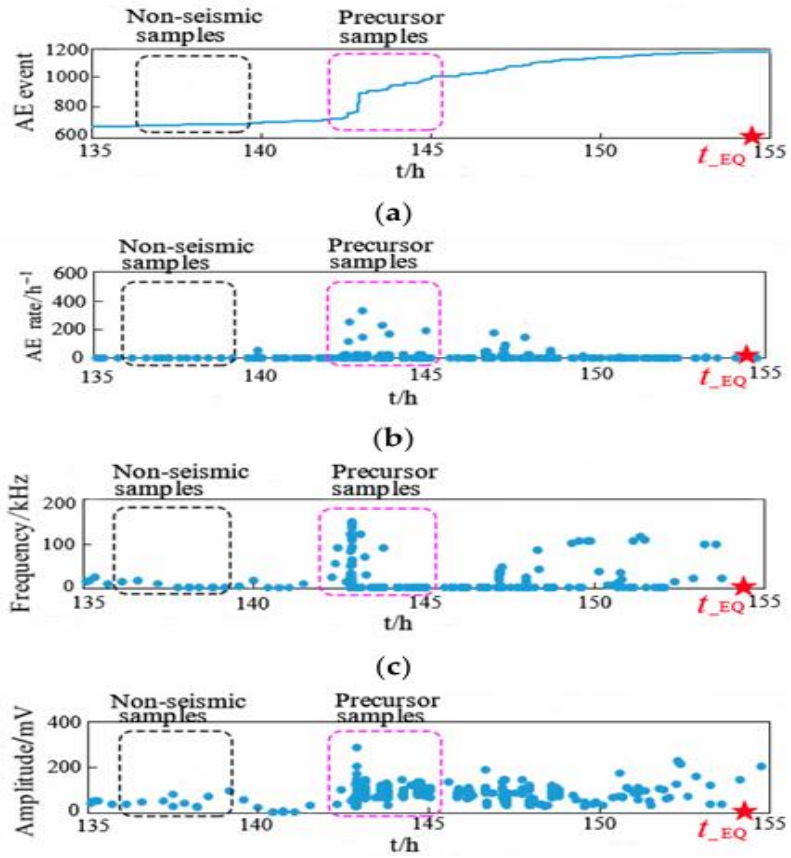


**Figure 5.4** AE feature extraction before the earthquake: (a) AE event (feature $x_1$); (b) AE rate (feature $x_2$); (c) frequency (feature $x_3$); (d) amplitude (feature $x_4$).

## 5.3.4 Dataset construction and labeling

Based on the above analysis, the monitored AE features exhibit clear precursor patterns before earthquakes, making them suitable for training neural network models. Therefore, this chapter constructs a deep learning dataset based on AE features (Fig. 5.4) for seismic precursor identification.

The dataset construction process is shown in Fig. 5.5. Real-time collected AE signals and earthquake catalog data are used for sample construction and label

assignment to create the dataset for model training. The dataset contains two types of samples: seismic precursor samples (labeled 1) and non-earthquake samples (labeled 0). Since earthquake preparation is a continuous process, its precursor signals may persist for a period before the earthquake occurs. Therefore, samples collected within a specific time window before the earthquake can be labeled as having an earthquake (label 1). In this study, AE samples within 24 hours before the earthquake are labeled as positive samples (label 1), while samples from other time periods are labeled as negative samples (label 0). The selection of this window length is based on the statistical results of the anomaly lead times of AE characteristic parameters in Section 4.4, with appropriate relaxation to ensure sample coverage.

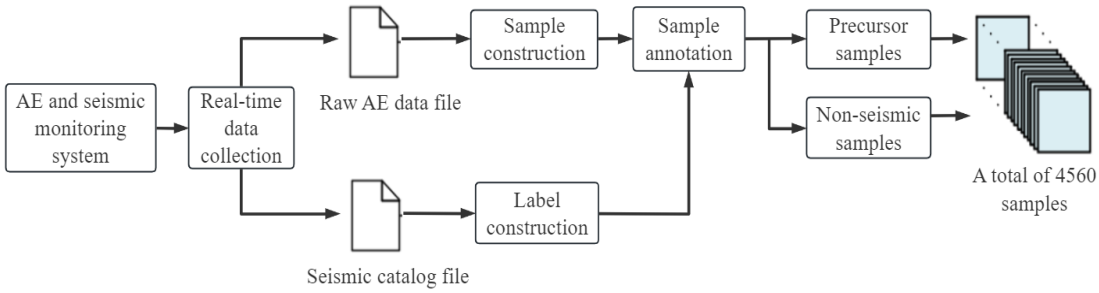


**Figure 5.5** Flowchart of dataset construction.

# 5.4 Experimental analysis of precursor identification models

Based on the constructed dataset, this section trains, validates, and tests the deep learning model, and comprehensively evaluates its performance.

## 5.4.1 Cross validation of the deep learning model

To train and validate the effectiveness of the model architecture and evaluate the performance of each module, this chapter designs a cross validation study. Using the dataset from the two major earthquakes during the 35-day monitoring period, three different deep learning models were developed, as detailed in Table 5.3 and shown in the schematic diagram Fig. 5.6.

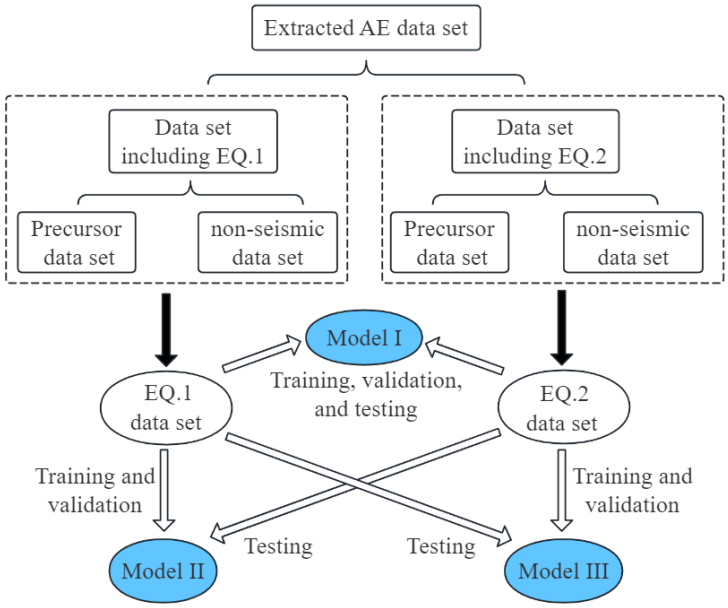


**Figure 5.6** Schematic diagram of cross-validation for the deep learning model.

**Table 5.3** Construction schemes of the three deep learning models.

| Type | Training and Validation | Testing |
|---|---|---|
| Model I | EQ.1 and EQ.2 dataset | EQ.1 and EQ.2 dataset |
| Model II | EQ.1 dataset | EQ.2 dataset |
| Model III | EQ.2 dataset | EQ.1 dataset |

Model I uses combined training and testing on both earthquakes. Model II uses EQ.1 for training and EQ.2 for testing. Model III uses EQ.2 for training and EQ.1 for testing. The purpose of the cross validation design is to evaluate the generalization ability of the model from multiple dimensions. Model I uses all data for training and testing, serving to evaluate the model's comprehensive performance on the overall data distribution as a performance baseline. Models II and III adopt a "cross event validation" strategy, i.e., training with data from one earthquake event and testing with data from the other. This design aims to test whether the model can capture precursor patterns common to different earthquake events, avoiding overfitting to specific noise or features of a single event. It is a rigorous test for evaluating the model's generalization ability. If the performance of Models II and III is similar to that of Model I, it indicates that the features extracted by the model have cross event universality. If

performance drops significantly, it suggests potential overfitting, requiring further optimization of feature selection or network structure.

### 5.4.2 Neural network hyperparameter optimization

To select the optimal model parameters, hyperparameter performance analysis was conducted through pre training experiments. Taking Model I as an example, the sigmoid activation function was selected, mini batch gradient descent was used for data batch loading, the mini batch size was set to 20, and the maximum number of training epochs was set to 1000. Figure 5.7 shows the neural network hyperparameter validation results.

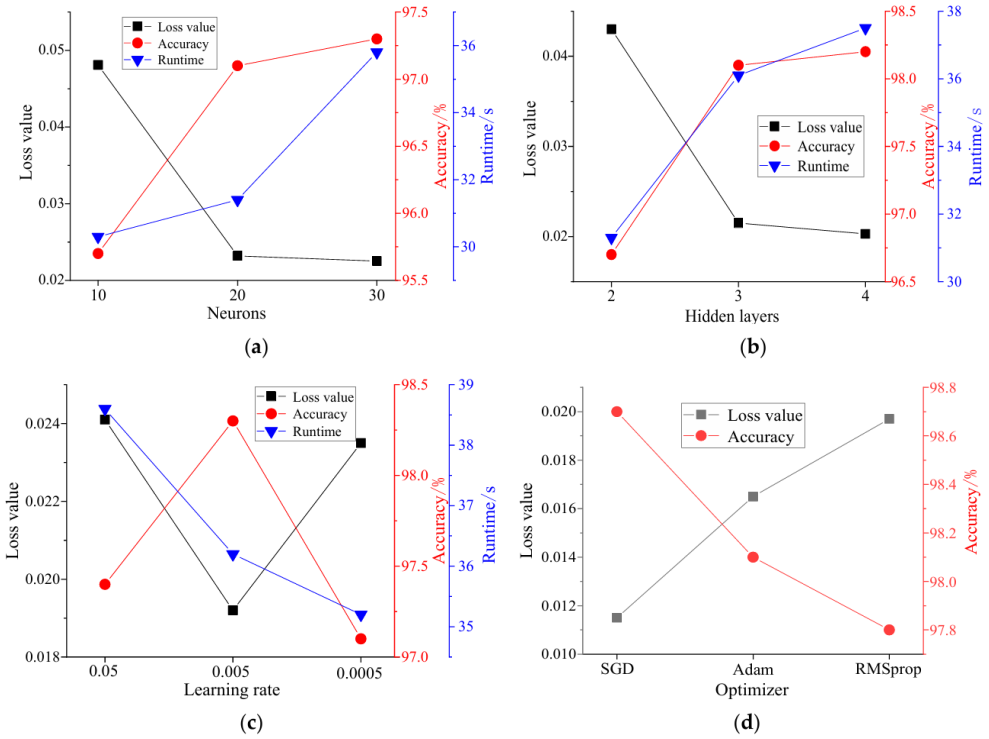


**Figure 5.7** Validation results of different neural network hyperparameters: (a) number of neurons; (b) number of hidden layers; (c) learning rate; (d) optimizer type.

The training results for different numbers of neurons are shown in Fig. 5.7(a). The results indicate that increasing the number of neurons can improve accuracy. When the number of neurons was 20, the loss value decreased to 0.0232. When the number of neurons was increased to 30, the accuracy improved by only about 2%. Therefore,

selecting 20 neurons optimizes computational efficiency while ensuring good training performance.

Keeping 20 neurons, a comparison of different numbers of hidden layers is shown in Fig. 5.7(b). The results indicate that increasing the network depth can reduce the loss value to 0.0207 (with 4 layers). However, compared with the 3 layer model, the improvement in accuracy was negligible, and the risk of overfitting increased. Therefore, 3 hidden layers were selected.

Furthermore, Fig. 5.7(c) and (d) show the comparison results for different learning rates and optimizers, respectively. The optimizers compared included stochastic gradient descent (SGD), adaptive moment estimation (Adam), and root mean square propagation (RMSprop). The results indicated that the model training performed best when the learning rate was 0.005, and when the SGD optimizer was used, the validation set accuracy reached its highest at 98.7%.

Through pre training and validation, appropriate hyperparameters can be selected for subsequent model training, validation, and testing.

### 5.4.3 Model training and validation

After each training epoch, the loss function values for the training set and validation set were obtained using Eq. (5.3). The total number of training epochs was set to 1000. The loss values during the training and validation phases for different epochs are shown in Fig. 5.8 and Table 5.4. The validation set accuracies are shown in Table 5.5.

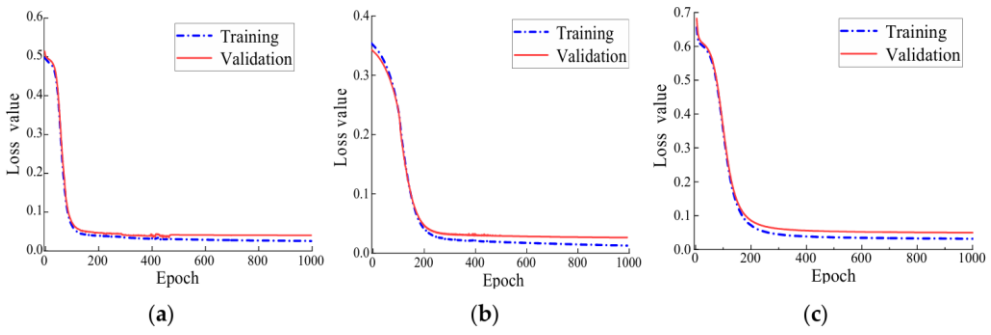


**Figure 5.8** Loss values during the training and validation phases: (a) Model I; (b) Model II; (c) Model III.

**Table 5.4** Loss values at different training epochs.

| Epoch | Model I | | Model II | | Model III | |
|---|---|---|---|---|---|---|
| | Training Set | Validation Set | Training Set | Validation Set | Training Set | Validation Set |
| 600 | 0.0061 | 0.0123 | 0.0071 | 0.0186 | 0.0064 | 0.0133 |
| 800 | 0.0055 | 0.0118 | 0.0065 | 0.0181 | 0.0059 | 0.0127 |
| 1000 | 0.0051 | 0.0115 | 0.0062 | 0.0176 | 0.0056 | 0.0122 |

**Table 5.5** Results after 1000 training epochs.

| Type | Accuracy of Training Set/% | Accuracy of Validation Set/% |
|---|---|---|
| Model I | 99.3 | 98.7 |
| Model II | 98.6 | 97.8 |
| Model III | 99.1 | 98.3 |

From the loss curves in Fig. 5.8, it can be seen that all three models decreased rapidly in the early stage of training (first 200 epochs), subsequently entering a stable convergence phase without obvious overfitting. The convergence speed of Model I was slightly faster than that of Models II and III, which is related to its coverage of more comprehensive feature patterns. Although Models II and III converged slightly slower, their final validation set accuracies remained above 97%, indicating that the models have strong cross event generalization ability. Furthermore, the gap between training set and validation set losses was small, indicating good model goodness of fit without serious overfitting or underfitting issues.

The results show that after 1000 training epochs, the validation set loss values for the three models were 0.0115, 0.0176, and 0.0122, respectively, with corresponding validation set accuracies of 98.7%, 97.8%, and 98.3%. This indicates that after neural network training, all models achieved high accuracy and exhibited strong robustness, fast convergence speed, and effective classification performance.

## 5.4.4 Model testing and evaluation

To evaluate the generalization performance of the models, a test set completely independent of the training and validation sets was selected. For ease of comparative analysis, the identification results of each model on the test set are presented as confusion matrices in Fig. 5.9. Among the 456 test samples, the three models correctly identified 445, 441, and 443 samples, respectively.

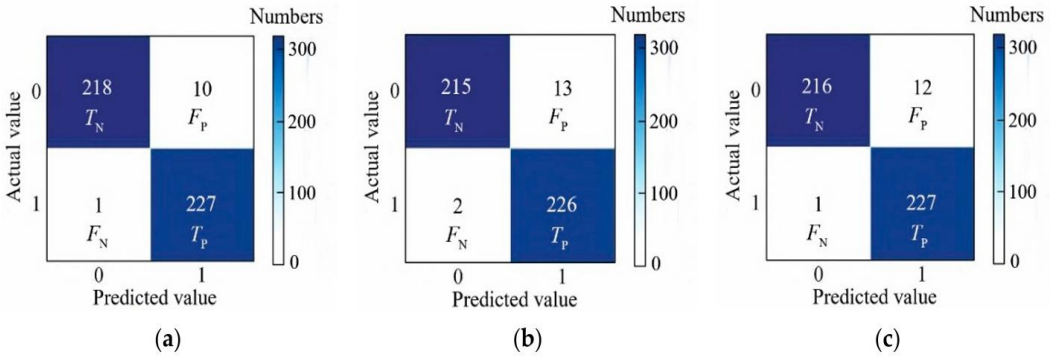


**Figure 5.9** Confusion matrix results on the test set: (a) Model I; (b) Model II; (c) Model III

A comparison of the results of the three models on the test set is shown in Table 5.6. The results indicate that all three models achieved high test accuracy. Among them, Model I achieved an accuracy of 97.6%, a recall of 99.6%, and an $F_1$ score of 0.977, demonstrating the best accuracy and robustness. Therefore, Model I was selected as the best identification model. However, its accuracy was only 0.8% and 0.3% higher than Models II and III, respectively, indicating that all three identification models exhibit good generalization performance. The identification model using AE features as input can effectively identify seismic events, and the trained model is suitable for real-time monitoring of rock AE signals to achieve automatic identification of seismic events.

**Table 5.6** Evaluation metrics of the model based on the confusion matrix.

| Deep Learning Model | Accuracy ($A_{cc}$/%) | Precision ($P_r$/%) | Recall ($R_e$/%) | $F_1$ Score |
|---|---|---|---|---|
| Model I | 97.6 | 95.8 | 99.6 | 0.977 |
| Model II | 96.8 | 94.6 | 99.1 | 0.968 |
| Model III | 97.3 | 95.0 | 99.6 | 0.972 |

### 5.4.5 Real-time seismic event identification results

To evaluate the effectiveness of the model in identifying seismic events in practical applications, cross testing was performed using the collected continuous data. Model II was used to test the data of the EQ.2 earthquake, and Model III was used to test the data of the EQ.1 earthquake. This cross testing strategy aimed to verify the robustness of model performance across different seismic events, rather than being limited to the events on which they were trained.

The identification results of the models are shown in Fig. 5.10. During the selected time period, the model issued two warnings, which accurately corresponded to the two largest earthquake events that occurred during that period. This demonstrates the high identification accuracy of the model for significant seismic events.

From Fig. 5.10, it can be further observed that the prediction signal of the model exhibits a continuous upward trend in probability. Taking EQ.2 as an example, the prediction probability of Model II began to steadily increase approximately 17 hours before the earthquake, gradually rising from a background level of about 0.2 to above 0.8, stably exceeding the decision threshold (0.5). Furthermore, during the quiet period between the two earthquakes, the prediction probability remained at a low level without significant false alarms, indicating that the model has good background noise suppression capability.

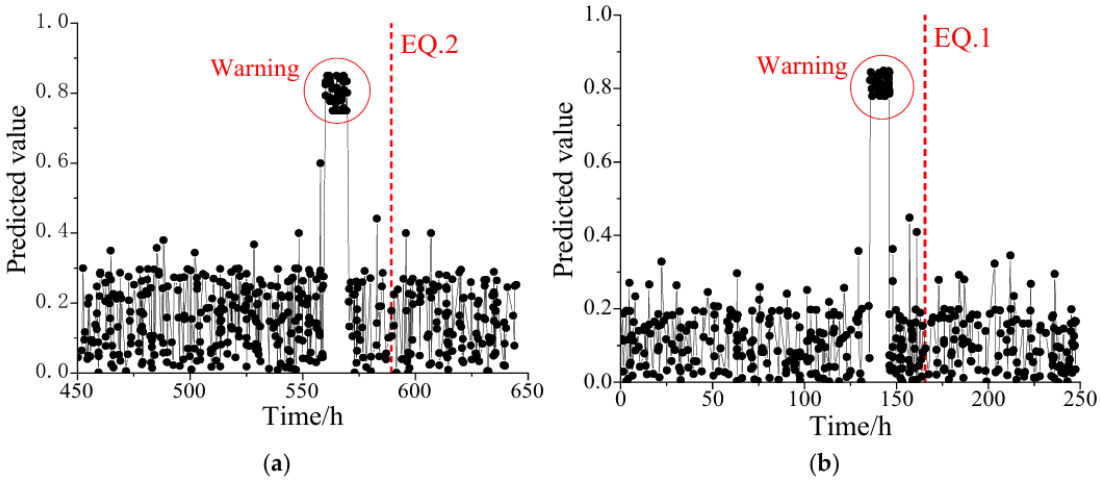


**Figure 5.10** Identification performance of the deep learning model: (a) warning results for EQ.2; (b) warning results for EQ.1.

### 5.4.6 Comparison with machine learning methods

As a comparative study, the proposed deep learning model was experimentally evaluated against traditional machine learning models, including support vector machine (SVM), light gradient boosting machine (LGB), and random forest (RF). SVM is a supervised learning method that performs classification by finding the optimal hyperplane that maximizes the margin between classes. The LGB model is a boosted gradient boosting decision tree algorithm. The RF model is a bagging ensemble algorithm that constructs training subsets through random sampling, trains decision trees, and obtains final predictions through majority voting. Table 5.7 shows the test results of the SVM, LGB, and RF models.

**Table 5.7** Test results of different machine learning models

| Identification Model | Accuracy ($A_{cc}$/%) | Precision ($P_r$/%) | Recall ($R_e$/%) | $F_1$ Score |
|---|---|---|---|---|
| Deep learning | 97.6 | 95.8 | 99.6 | 0.977 |
| SVM | 95.3 | 94.3 | 96.2 | 0.952 |
| LGB | 94.6 | 95.2 | 94.5 | 0.948 |
| RF | 93.2 | 93.4 | 92.7 | 0.930 |

It can be seen from Table 5.7 that the RF model had the lowest accuracy at 93.2%, followed by the LGB model at 94.6% and the SVM model at 95.3%. In contrast, the deep learning model proposed in this chapter achieved higher accuracy, with its F1 score being 2.6%, 3.1%, and 5.1% higher than those of the SVM, LGB, and RF models, respectively. These results highlight the advantages of the deep learning model in extracting hidden features from complex data and enhancing generalization ability through the backpropagation algorithm. For earthquake early warning, the deep learning model using AE features as input demonstrates higher accuracy and robustness in identifying seismic events compared to traditional machine learning algorithms.

Therefore, the trained deep learning model can be used for online monitoring of rock AE signals and automatic early warning of seismic events.

## 5.5 Model stability validation based on long-term data

The previous sections have systematically validated the effectiveness of the deep learning based AE seismic precursor identification model. This section further expands the analysis by applying the trained model to the 180-day long-term time series monitoring data described in Chapter 4, conducting long-term stability validation in practical application scenarios and evaluating the long-term early warning performance of the model. The aim is to provide a theoretical basis and methodological support for constructing a more reliable intelligent earthquake early warning system.

### 5.5.1 Long-term validation and comparison with seismic events

To validate the generalization ability and early warning performance of the trained deep learning model in practical long-term monitoring scenarios, this study performed model stability validation based on the 180 days of continuous monitoring data (November 2024 to May 2025) described in Section 4.7. During this period, a total of 102 seismic events ($M_L \geq 1.0$) were recorded, and the temporal distribution of earthquakes is shown in Fig. 4.17, presenting four significant earthquake clusters (EQ.I to EQ.IV). The best performing model (Model I) determined in Section 5.4.4 was used to perform sliding window prediction on this new data that was not involved in training. The specific method was as follows: using a sliding step of 1 hour, the AE feature sequence (count, count rate, frequency, amplitude) was extracted for each time window and input into the model to obtain the prediction probability of "earthquake" or "no earthquake" for that window. The decision threshold was set to 0.5, meaning a prediction probability ≥ 0.5 was judged as "earthquake" (warning issued), otherwise "no earthquake".

Figure 5.11 shows the comparison results between the model prediction probability and the earthquake catalog during the 180-day validation period. In the figure, the red curve represents the model output prediction probability over time, and the red dashed line is the decision threshold (0.5). The blue vertical lines below represent the actual major earthquake events, with the height of the lines indicating the magnitude (EQ.I to EQ.IV). The grey shaded areas represent periods of correct model warnings (i.e., prediction probability exceeded the threshold and an earthquake occurred within the subsequent 24 hours). The yellow shaded areas represent false alarm periods (prediction probability exceeded the threshold but no earthquake occurred within the subsequent 24 hours). The purple shaded areas represent missed detection periods (prediction probability did not exceed the threshold within 24 hours before an earthquake).

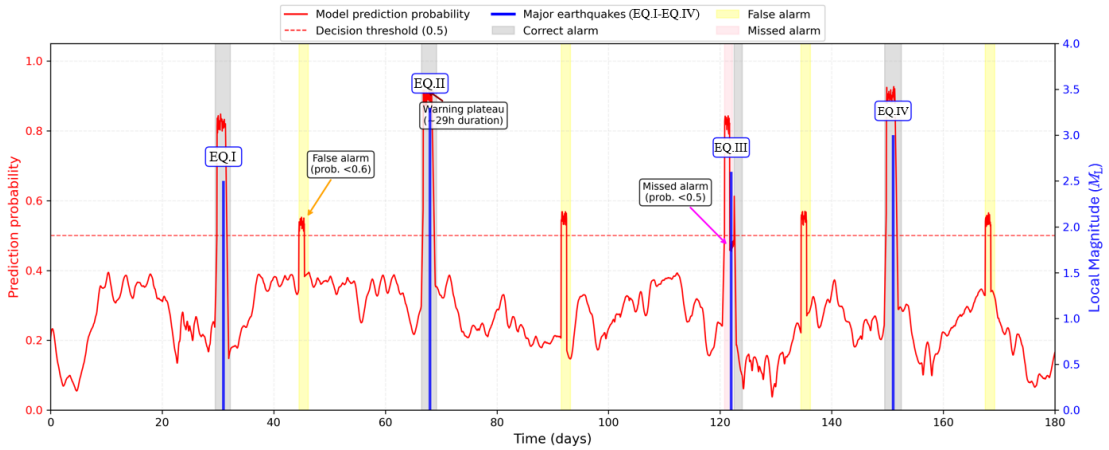


**Figure 5.11** Comparison between model long-term validation results and major seismic events (180 days).

From Fig. 5.11, a strong correlation between model predictions and seismic activity can be observed. The peaks of the model prediction probability are highly consistent with the occurrence periods of seismic events. Before the four major earthquakes (EQ.I to EQ.IV), the model prediction probability showed a significant sustained increase, stably exceeding the decision threshold and issuing warning signals.

During the entire 180-day validation period, false alarms were mainly concentrated in periods with high environmental noise, such as strong winds and rainfall, and the model prediction probability values during false alarm periods were all less than 0.6, which could be eliminated by raising the decision threshold. Missed detections occurred

for events with relatively small magnitudes and distant epicenters, whose precursor signals were relatively weak. It should be noted that the missed detection period was within the warning zone before EQ.III, and the overall warning effect for EQ.III remained significant, so the impact on decision making is negligible. Overall, the model warning time is typically tens of hours before the earthquake occurrence, providing a valuable time window for subsequent emergency response.

## 5.5.2 Statistics of early warning lead time for seismic events

To further quantify the early warning performance of the model, statistical analysis was conducted on the early warning lead times for the four major seismic events (corresponding to EQ.I to EQ.IV in Table 4.3). The results are shown in Table 5.8 and Fig. 5.12.

It can be seen from Table 5.8 that the average early warning lead time of the model for the four major seismic events is 20.5 hours. Among them, the warning lead time for EQ.II ($M_L$=3.3), the largest magnitude event, reached 24 hours, and that for EQ.IV ($M_L$=3.0) reached 22 hours. This result is significantly better than the 13 hour lead time obtained from single AE characteristic parameter analysis in Chapter 4 and the 17 hour lead time from the multimodal statistical method, demonstrating the advantages of the deep learning model in integrating multi-dimensional features, processing massive data, and extracting complex precursor patterns.

**Table 5.8** Statistics of early warning lead time for major seismic events by the model

| Earthquake No. | Time (d) | Magnitude ($M_L$) | Warning time (d) | Lead time (h) | Mean predicted probability | Maximum predicted probability | Plateau duration (h) |
|---|---|---|---|---|---|---|---|
| EQ.I | 31 | 2.5 | 30.2 | 19 | 0.82 | 0.86 | 23 |
| EQ.II | 68 | 3.3 | 67.1 | 24 | 0.92 | 0.95 | 29 |
| EQ.III | 122 | 2.6 | 121.3 | 17 | 0.84 | 0.88 | 21 |
| EQ.IV | 151 | 3.0 | 150.0 | 22 | 0.89 | 0.93 | 28 |
| Mean | - | - | - | 20.5 | 0.87 | 0.91 | 25 |

As shown in Fig. 5.12, the prediction probability correlates with magnitude. Both the average prediction probability and the maximum prediction probability within 24 hours before the earthquake show a positive correlation trend with earthquake magnitude. The maximum prediction probability within 24 hours before EQ.II ($M_L$ = 3.3) reached 0.95, while that for EQ.I ($M_L$ = 2.5) was 0.86. This indicates that the prediction probability output by the model can reflect the intensity information of subsequent earthquakes to some extent.

The average prediction probabilities within 24 hours before the four major earthquakes all stably exceeded the decision threshold of 0.5 ( > 0.8), and the maximum prediction probabilities all exceeded 0.85, indicating that the model has high stability and reliability for early warning of significant seismic events.

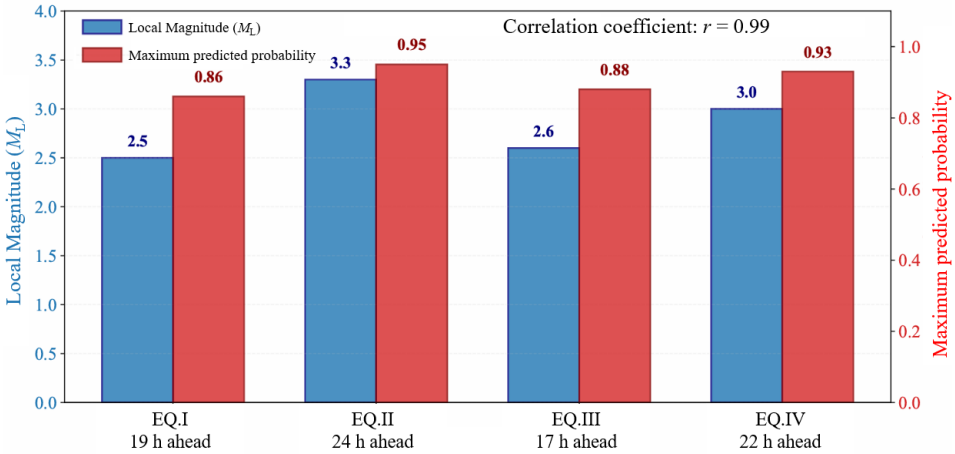


**Figure 5.12** Correlation between earthquake magnitude and early warning characteristics.

## 5.5.3 Model stability evaluation metrics

Based on the 180-day long-term time series data, a total of 4320 prediction windows (1 per hour) were obtained. After comparison with the earthquake catalog, the performance metrics shown in Table 5.9 were calculated. The false alarm rate is the ratio of the number of false alarms to the total number of warnings.

It can be seen from Table 5.9 that the model maintained excellent early warning performance during the 180-day long-term validation. The accuracy reached 97.1%, meaning that out of 4320 prediction windows, the prediction results of 4195 windows

matched the actual earthquake occurrences. The model also maintained a high recall (97.8%) and precision (96.4%), with an $F_1$ score of 0.971, indicating that the model still has good generalization ability and stability in long-term practical applications. The false alarm rate of 1.9% is controlled at a low level, essentially meeting the requirements of practical early warning applications.

**Table 5.9** Long-term stability evaluation metrics of the model.

| Metrics | Accuracy ($A_{cc}$/%) | Precision ($P_r$/%) | Recall ($R_e$/%) | $F_1$ Score | False alarm rate /% |
|---|---|---|---|---|---|
| Values | 97.1 | 96.4 | 97.8 | 0.971 | 1.9 |

Compared with the test set results in Section 5.4.4 (Table 5.6, accuracy 97.6%), the metrics in the long-term validation decreased slightly but remained generally stable. The accuracy decreased by 0.5 percentage points, the precision increased by 0.6 percentage points, and the F1 score decreased by 0.006. This minor fluctuation is within an acceptable range, indicating that after training on 35 days of short-term data, the model maintains good generalization ability when extended to a 180-day long-term monitoring scenario, without significant performance degradation.

Further analysis of performance over different time periods showed that the metrics of the model in the first three months (days 1 to 90) and the last three months (days 91 to 180) were essentially comparable, with accuracies of 97.2% and 97.0%, and recalls of 98.0% and 97.6%, respectively. No performance decline trend was observed with increasing monitoring time. This indicates that the model has good temporal stability and can adapt to slow changes in crustal stress state and seasonal fluctuations in environmental conditions.

Furthermore, targeted analysis of the four major seismic events (EQ.I to EQ.IV) indicates that the model's early warning performance is particularly outstanding before significant seismic events. Taking EQ.II ($M_L$=3.3), the largest magnitude event, as an example, the model's average prediction probability within 24 hours before the earthquake reached 0.92, and the maximum prediction probability reached 0.95,

significantly higher than the decision threshold. This indicates that the model has higher identification sensitivity for significant seismic events with clear precursor characteristics.

In summary, the validation results based on 180 days of long-term data show that the trained deep learning model maintains stable early warning performance in practical long-term monitoring scenarios, with all metrics at high levels, demonstrating its potential for application in practical earthquake early warning systems.

## 5.6 Hybrid driven model with physical feature fusion

Previous sections have shown that the MCF-B method and NT analysis can effectively identify the critical state of a system from a statistical physics perspective, and their output characteristic parameters ($p_2$, $p_3$, $\kappa_1$) have clear physical meanings. This section attempts to integrate these physical statistical features as higher order features into the deep learning model, constructing a "physics-data" hybrid driven collaborative identification framework, and explores the improvement effect of physical features on model performance.

### 5.6.1 Physical feature extraction and hybrid driven model framework

The calculation of physical features is based on the methods described in Chapter 2, extracted from the AE event sequence using a sliding window method with a window size of $W$ = 100 events. For each time window, the following features are calculated. The MCF-B parameter $p_2$ (power law decay exponent) is obtained by nonlinearly fitting the amplitude distribution of AE events within the window using Eq. (2.31); $p_2$ reflects the scale distribution characteristics of microfracture events. The MCF-B parameter $p_3$ (exponential decay exponent) is obtained simultaneously with $p_2$; $p_3$ characterizes the degree of deviation of the system from an ideal power law distribution, with $p_3 \approx 0$ indicating that the system is in a self organized critical state (ideal power law). The NT

variance $\kappa_1$ is calculated using Eq. (2.26) for the AE events within the window; $\kappa_1$ approaching 0.07 indicates that the system has entered a critical state.

The above physical features are concatenated with the basic features extracted in Section 5.3 (count, count rate, frequency, amplitude) to form a new input vector X = [count, count rate, frequency, amplitude, $p_2$, $p_3$, $\kappa_1$] with a dimension of 7.

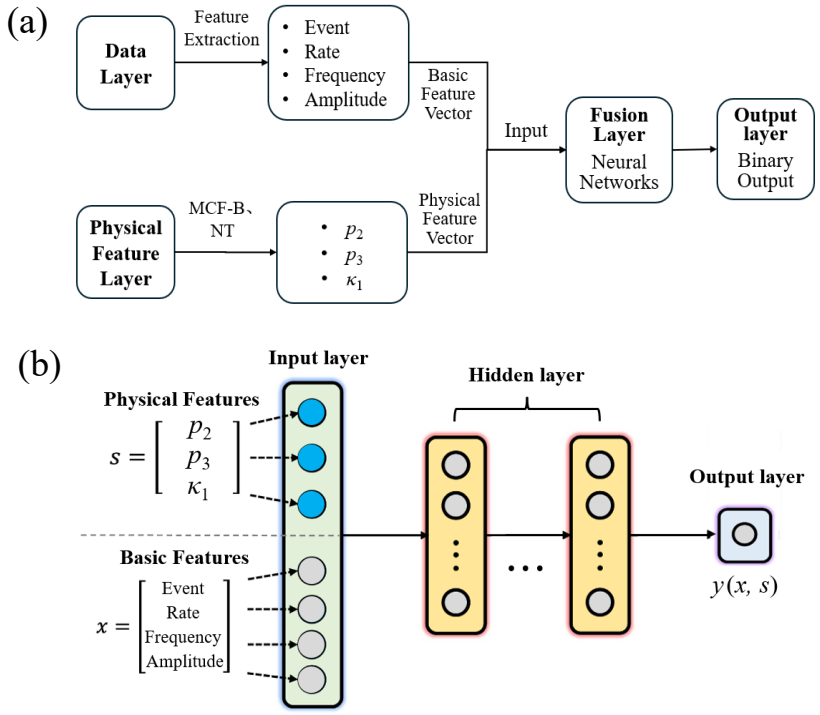


**Figure 5.13** Framework of the physics-data hybrid-driven model: (a) physical feature fusion method; (b) neural network architecture.

Figure 5.13(a) shows the framework of the hybrid driven model with physical feature fusion. This framework is divided into three layers: the data layer, the physical feature layer, and the fusion layer. For the data layer, raw AE waveforms are processed by the ÆMISSION® acquisition system to extract basic features (count, count rate, frequency, amplitude) in real time, forming a basic feature sequence. The physical feature layer performs sliding window analysis on the AE event sequence to calculate physical statistical features such as MCF-B parameters ($p_2$, $p_3$) and NT variance ($\kappa_1$). The function of this layer is to map the raw data into a feature space with clear physical meaning, introducing constraints of physical laws to the model. The fusion layer concatenates the basic features and physical features in the feature dimension and inputs

them into a deep neural network for training and prediction. The structure of the deep neural network is shown in Fig. 5.13(b). The network structure remains consistent with Section 5.2.2 (3 hidden layers, 20 neurons per layer), and the output is the binary classification probability of "earthquake" or "no earthquake".

The core of this framework is that the physical feature layer provides a "physical prior" for the data driven model, guiding the model to focus on anomaly patterns with physical significance. Meanwhile, deep learning leverages its powerful nonlinear fitting capability to automatically learn the higher order interactions between physical features and basic features, thereby achieving synergistic enhancement.

## 5.6.2 Comparative experimental design and result analysis

To evaluate the improvement effect of physical features on model performance, three sets of comparative experiments were designed.

Model I (baseline model): uses only 4 basic features (count, count rate, frequency, amplitude), i.e., Model I trained in Section 5.4.

Model II (physically enhanced model): uses 4 basic features + 3 physical features ($p_2$, $p_3$, $\kappa_1$), retrained using same network structure and training parameters as Model I.

Model III (pure physics model): uses only 3 physical features, with the network structure adjusted to 3 input neurons, while the hidden layer structure and training parameters remain consistent with Model I.

**Table 5.10** Performance comparison of models with different feature combinations.

| Model | Input Features | Accuracy ($A_{cc}$/%) | Precision ($P_r$/%) | Recall ($R_e$/%) | $F_1$ Score | Average warning lead time (h) |
|---|---|---|---|---|---|---|
| Model I | Basic Features | 97.6 | 95.8 | 99.6 | 0.977 | 16.8 |
| Model II | Basic + Physical Features | 98.9 | 98.2 | 99.6 | 0.989 | 21.3 |
| Model III | Physical Features Only | 91.3 | 90.5 | 92.1 | 0.913 | 22.6 |

The three sets of models used the same dataset split (Table 5.1) and training strategy, and their performance was compared on the test set. Table 5.10 shows the performance comparison results of the three sets of models.

From the analysis of Table 5.10, the physically enhanced model (Model II) performs best. Compared with the baseline model, Model II shows an increase in accuracy from 97.6% to 98.9%, an increase in precision from 95.8% to 98.2%, and an increase in $F_1$ score of 0.012. This indicates that the introduction of physical features provides complementary information to the model, helping to identify seismic precursors more accurately and reduce false alarms. The recall remained unchanged (99.6%), indicating that physical features did not reduce the model's sensitivity to positive samples.

Furthermore, the early warning timeliness of Model II is significantly improved. The average early warning lead time of Model II reaches 21.3 hours, which is 4.5 hours more than the baseline model. This is because the MCF-B parameters ($p_2$, $p_3$) are more sensitive to early changes in the system's deviation from the critical state and can capture precursor signals earlier. The convergence behavior of the NT variance $\kappa_1$ also provides supplementary information for early warning. Although Model III has the longest early warning lead time (22.6 hours), its accuracy (91.3%), precision (90.5%), and recall (92.1%) are significantly lower than those of Models I and II. This indicates that although physical features can provide early warning, they are susceptible to noise when used alone, and the amount of information is insufficient to support high precision prediction. They need to work together with basic features to achieve the best effect.

The analysis shows that Model II outperforms Models I and III, validating the effectiveness of the "physics-data" synergistic driven strategy. Physical features provide critical state information of the system, while basic features provide real-time details of microfracture activity. Their fusion achieves complementary advantages.

### 5.6.3 Feature importance analysis

To explore the contribution of each feature to the model's decision making, SHAP (SHapley Additive exPlanations) values were used to perform feature importance analysis on Model II. SHAP value is a feature interpretation method based on game theory that quantifies feature importance by calculating the marginal contribution of each feature to the model output. In binary classification problems, the unit of SHAP value is probability (0 to 1), with positive values indicating a push towards the positive class (earthquake) and negative values indicating a push towards the negative class (no earthquake).

Figure 5.14 shows the SHAP value results. The horizontal axis represents the mean absolute SHAP value, indicating the average contribution of the feature to the model output. The vertical axis lists the feature names, sorted from lowest to highest importance. From Fig. 5.14, the top five features in importance ranking are: AE amplitude, NT variance ($\kappa_1$), MCF-B parameter $p_3$, AE frequency, and MCF-B parameter $p_2$. The sum of the total SHAP values is 1.97. The top 3 features contribute 58.4%, and the top 5 features contribute 84.8%. NT variance ($\kappa_1$) and MCF-B parameter $p_3$ rank second and third, respectively, validating the effectiveness of physical features.

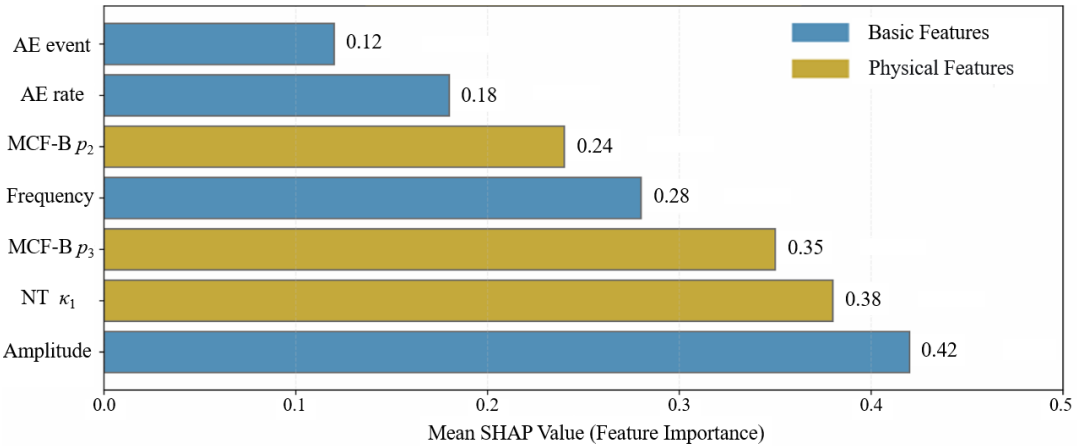


**Figure 5.14** Feature importance ranking based on SHAP values.

From the results, AE amplitude has the highest importance. AE amplitude is a direct measure of AE event intensity. The appearance of high-amplitude events before an

earthquake is a sign of macroscopic crack initiation and propagation in the earthquake preparation zone, consistent with the pre earthquake amplitude anomalies observed in Section 4.4.3. The NT variance $\kappa_1$, as a quantitative indicator of the critical state of the system, ranks second in importance after amplitude, indicating that the model highly relies on this physical feature to identify whether the system has entered a critical state, and the convergence process of $\kappa_1$ provides a key basis for early warning. The MCF-B parameter $p_3$ ranks third; $p_3$ characterizes the deviation of the system from an ideal power law and serves as a key feature for identifying earthquake precursors. The model automatically learns this physical law, validating the effectiveness of introducing physical features. Furthermore, in the importance ranking, basic features (amplitude, frequency, count rate) and physical features ($\kappa_1$, $p_2$, $p_3$) appear alternately, indicating that the information provided by the two is complementary and jointly supports the model's decision making.

The physics-data synergistic driven framework proposed in this section aims to integrate the advantages of physical model methods and data driven methods. Physical features such as MCF-B parameters ($p_2$, $p_3$) and NT variance ($\kappa_1$) essentially encode theoretical knowledge of fracture mechanics and statistical physics into quantifiable features, providing constraints of physical laws for the data driven model. This is equivalent to "pointing the direction" for the model, guiding it to focus on anomaly patterns with physical significance and reducing overfitting to noise. Under the constraints of physical features, the deep learning model still retains the ability to learn autonomously from data. It can capture complex nonlinear relationships not covered by the physical model and continuously optimize feature combinations through the backpropagation algorithm, achieving collaborative correction of theory and experience. The model with fused physical features allows its decision making process to be traced back to specific physical mechanisms, significantly improving the model's interpretability and enhancing the credibility of prediction results.

## 5.7 Chapter summary

Based on the field measurements in Chapter 4, this chapter proposed an intelligent seismic precursor identification method combining AE monitoring and deep learning, and systematically conducted extended research including model construction, training validation, comparative analysis, long-term time series stability validation, and physical feature fusion. By extending AE precursor analysis from traditional statistical physics methods to the field of intelligent identification, it achieved the synergistic fusion of physical models and data driven methods. The main conclusions are as follows.

（1）A deep learning dataset and identification model based on multi-dimensional AE features were constructed. Using four key features (AE count, count rate, frequency, and amplitude) as inputs, a deep neural network model suitable for seismic precursor identification was designed. The model adopted a three hidden layer structure (20 neurons per layer), used sigmoid as the activation function and binary cross entropy as the loss function, and determined the optimal hyperparameter combination through pre training experiments. After 1000 training epochs, the loss value on the validation set dropped to 0.0115, and the accuracy reached 98.7%, demonstrating good convergence speed and fitting performance.

（2）The generalization ability of the model was comprehensively evaluated through cross validation strategies. Three model schemes were designed. The test set results showed that the accuracies of the three models were 97.6%, 96.8%, and 97.3%, respectively, with recalls exceeding 99% and F1 scores above 0.96. Model I (joint training on both earthquakes) had the best overall performance and served as the baseline model for this chapter. Compared with traditional machine learning methods (SVM, LGB, RF), the deep learning model achieved an accuracy 2.3% to 4.4% higher and an F1 score 2.6% to 5.1% higher, highlighting the advantages of deep learning in high dimensional feature extraction and pattern recognition.

（3）Validation based on 180 days of long-term time series data showed that the trained model maintained excellent early warning performance in practical long-term monitoring scenarios. The average early warning lead time of the model for four major

seismic events reached 20.5 hours, significantly better than the 17 hours achieved by the AE based multimodal statistical method alone. Within 24 hours before the earthquakes, the average prediction probability of the model reached 0.87, and the maximum prediction probability reached 0.91, showing a positive correlation trend with magnitude. During the entire validation period, the model achieved an accuracy of 97.1%, a recall of 97.8%, a false alarm rate of only 1.9%, and an $F_1$ score of 0.971, validating the robustness and stability of the model in practical applications.

（4）A "physics-data" hybrid driven collaborative identification framework was proposed. The MCF-B parameters ($p_2$, $p_3$) and NT variance ($\kappa_1$) were integrated into the deep learning model as higher order physical features. Comparative experiments showed that the physically enhanced model improved accuracy from 97.6% to 98.9%, precision from 95.8% to 98.2%, increased the $F_1$ score by 0.012, and extended the average early warning lead time from 16.8 hours to 21.3 hours. Although the pure physics model had the longest early warning lead time (22.6 hours), its accuracy was only 91.3%, indicating that physical features used alone provide limited information and need to work together with basic features to achieve the best effect.

（5）SHAP value feature importance analysis revealed the contribution of each feature to the model's decision making. The top five features in importance ranking were AE amplitude, NT variance ($\kappa_1$), MCF-B parameter $p_3$, AE frequency, and MCF-B parameter $p_2$. The top three features contributed 58.4% of the total SHAP value, and the top five features contributed 84.8%. AE amplitude had the highest importance, reflecting the physical significance of high-amplitude events before an earthquake as a sign of macroscopic crack initiation in the earthquake preparation zone. NT variance and MCF-B parameters, as physical features, ranked second and third, respectively, validating the effectiveness of physical features and their complementarity with basic features.

The research in this chapter shows that the deep learning based intelligent identification method for AE seismic precursors can effectively integrate multi-dimensional feature information to achieve accurate early warning of seismic events. The physics-data hybrid driven model proposed in this chapter integrates physical

statistical features such as MCF-B and NT with deep learning, achieving a unification of physical interpretability and high precision identification, and providing a feasible path for constructing next generation intelligent earthquake early warning systems. It should be noted that the conclusions of this chapter are based on monitoring data from a specific region and time period, and their generalizability requires further validation with more earthquake cases and longer time series data.

# Chapter 6

# 6 Conclusions and future work

## 6.1 Main Research Conclusions

Centered on the core idea of integrating AE physical models with multi-source data, this thesis aimed to identify earthquake precursors. It conducted systematic research ranging from theoretical method innovation and laboratory scale experiments to crustal scale field measurements, and ultimately constructed a deep learning intelligent identification model integrating multi-precursor features. The main conclusions are as follows.

（1）The MCF-B method, as a novel signal analysis tool based on critical fluctuation theory, is more sensitive and robust than traditional methods in identifying precursors of system instability. The MCF-B method proposed in this thesis quantifies the deviation of the event amplitude distribution from an ideal power law through the synergistic evolution (crossover phenomenon) of the parameters $p_2$ (power law decay exponent) and $p_3$ (exponential decay exponent). In both laboratory concrete fracture and field rock AE measurements, this method effectively identified clear critical precursors before system instability. Compared with the traditional *b*-value method, MCF-B maintains a stable evolutionary trend even in the stage where the amplitude distribution deviates from linearity (approaching failure), overcoming the limitation of the *b*-value's fluctuation and divergence at this stage, and demonstrating stronger robustness. Compared with NT analysis, MCF-B is more sensitive to early changes in the system's deviation from the self organized critical state, providing a longer warning

time window, while NT analysis has higher specificity in confirming that the system has entered a "deterministic critical state". The combined use of the two can construct a more reliable multi-level early warning strategy.

（2）The comparison between laboratory scale concrete fracture tests and field AE measurements revealed the applicability and precursor characteristics of the MCF-B method in real complex environments. In the flexural failure tests of concrete beams, the critical precursor of the MCF-B method manifested as the appearance of an ideal power law followed by a clear "crossover phenomenon" of decreasing $p_2$ and increasing $p_3$. In the field AE measurements in eastern Guangdong, in addition to the ideal power law and the crossover phenomenon of decreasing $p_2$ and increasing $p_3$, the earthquake precursor mainly manifested as a "positive jump" anomaly of the $p_3$ parameter, i.e., a critical characteristic of relative scarcity of high-amplitude events. Furthermore, compared with the significant fluctuations of parameter $p_3$, parameter $p_2$ did not exhibit the systematic continuous decrease observed in the concrete beam failure tests. This difference reveals the distinction between laboratory monotonic loading and the complex earthquake preparation process in nature. The former involves a unidirectional and irreversible damage evolution, while the latter may be accompanied by stress perturbations, leading to different manifestations of precursors. Therefore, in practical applications, priority should be given to monitoring anomalous fluctuations of the $p_3$ parameter as a core precursor criterion.

（3）Synchronous cross validation of AE and EME precursors established a precursor identification pattern with a clear temporal order, providing a new approach to improve the reliability of precursor identification. Based on 35 days of preliminary field AE measurements, it was found that intense bursts of AE activity were significantly correlated with regional earthquakes. AE characteristic parameters, *b*-value analysis, NT analysis, and MCF-B analysis all effectively identified pre-seismic anomalies. Multimodal statistical analysis showed that the trend of the AE temporal distribution preceded that of earthquakes, serving as an earthquake precursor capable of identifying seismic events approximately 17 hours in advance. On this basis, to synchronously cross validate the reliability of AE earthquake precursors, EME

monitoring was further introduced. Based on 180 days of synchronous continuous AE and EME observations at the eastern Guangdong station, it was found that both EME and AE activities exhibited Gaussian distribution peaks highly correlated with earthquake clusters before the earthquakes, and the three followed a certain temporal order: the EME precursor peak appeared first (approximately 3 days in advance), followed by the AE precursor peak (approximately 1 day in advance), and finally the earthquake occurred. This pattern can be explained mechanistically by the evolution of microfracture scales in the earthquake preparation zone and the resulting differences in signal frequencies. Furthermore, there was a significant positive correlation between the peak intensities of AE and EME and the magnitude of subsequent earthquakes, providing a quantitative basis for magnitude identification based on precursor signal intensity. This finding highlights the necessity and potential of multi-physical precursor fusion in overcoming the uncertainty of single signal sources.

（4）The synergistic drive of deep learning and physical features offers significant advantages over single methods in achieving high precision and high timeliness intelligent identification of earthquake precursors. A deep neural network model was constructed using AE count, count rate, frequency, and amplitude as basic features. Through cross validation and hyperparameter optimization, the baseline model achieved an accuracy of 97.6% on the test set, significantly outperforming traditional machine learning methods. Stability validation based on 180 days of long-term time series data showed that the model achieved an average early warning lead time of 20.5 hours for four major seismic events, better than the 17 hours achieved by AE based multimodal statistical analysis alone. Furthermore, the model achieved an accuracy of 97.1%, a recall of 97.8%, and a false alarm rate of 1.9%, indicating good generalization ability and stability in long-term time series data applications without significant performance degradation. After integrating physical statistical features such as MCF-B parameters ($p_2$, $p_3$) and NT variance ($\kappa_1$) as higher order inputs together with basic features, the performance of the baseline model was further improved: accuracy increased from 97.6% to 98.9%, and the average early warning lead time was extended to 21.3 hours. Although the pure physics model had the longest early warning lead time

(22.6 hours), its accuracy was only 91.3%, indicating that physical features used alone provide limited information and need to be combined with basic features to achieve the best effect. SHAP value analysis confirmed that the contribution of these physical features to the model's decision making ranked second and third, behind only AE amplitude. This result indicates that the "physics-data" hybrid driven model can effectively integrate the mechanistic understanding of physical models with the data mining capabilities of deep learning, providing a feasible technical path for constructing a high reliability and high timeliness earthquake early warning system.

## 6.2 Main innovations

The main innovations of this thesis are summarized as follows.

（1）An MCF-B analysis method for AE signals based on critical fluctuations was proposed. The critical fluctuation theory from statistical physics was introduced into AE analysis, constructing a precursor identification criterion centered on the synergistic evolution of the power law decay exponent $p_2$ and the exponential decay exponent $p_3$. This method overcomes the limitations of the traditional *b*-value method in handling nonlinear amplitude distributions, providing a more physically meaningful and sensitive analytical tool for cross-scale critical precursor identification from microscopic material fracture to macroscopic earthquake preparation.

（2）A cross-scale, multi-method comparative validation research path spanning "laboratory experiments and field measurements" was constructed. Through fracture tests and field measurements of macro AE and EME in eastern Guangdong, the precursor identification capabilities of various methods such as MCF-B, NT analysis, the *b*-value method, and deep learning were systematically tested. This progressive and mutually validating system not only verified the effectiveness of the new method but also revealed the applicability and complementarity of different methods in identifying critical behavior in complex systems, laying the foundation for establishing multi-level early warning strategies.

（3）The synergistic temporal pattern of earthquake precursors based on AE and EME signals was revealed. Through 180 days of synchronous observation, the temporal characteristic of "EME precursor first, AE precursor second" before earthquakes was discovered and validated in this study area, and an empirical relationship between signal intensity and magnitude was established. This finding provides a basis for multi-source information fusion from the perspective of the physical mechanism of earthquake preparation and opens new avenues for constructing a more reliable framework for short-term and imminent earthquake precursor identification.

（4）A physics-data synergistic driven intelligent identification model for earthquake precursors was established. Physical statistical features with clear physical meanings, such as MCF-B and NT, were integrated as higher order inputs into a deep neural network, constructing a hybrid driven model. This method effectively combines the mechanistic understanding of physical models with the data mining advantages of deep learning. While maintaining a high recall, it further improves prediction accuracy and early warning timeliness, providing a feasible technical paradigm for developing a new generation of intelligent earthquake early warning systems.

## 6.3 Future work outlook

Although this thesis has made progress in cross-scale seismic precursor identification research based on AE, the identification of earthquake precursors remains a challenging scientific problem worldwide. Based on the conclusions and limitations of this study, the following prospects for future work are proposed.

（1）This study preliminarily validated the synergistic potential of AE and EME, but other precursor observations such as neutron emission, ground tilt, and groundwater have not yet been incorporated into the analysis. Future efforts should focus on constructing a multi-parameter, multi-dimensional comprehensive monitoring platform, utilizing more advanced data fusion algorithms to mine correlation patterns and

anomaly features in multi-source data, and building a more robust comprehensive early warning system.

（2）Future work should combine more refined rock mechanics experiments and microscopic observation methods to establish quantitative relationships between the evolution of MCF-B parameters and specific damage mechanisms, further enhancing the persuasiveness of its precursor criteria. At the same time, the application of this method to earthquakes of different tectonic types and magnitudes should be continued to refine its applicability boundaries.

（3）The intelligent identification model in this paper was mainly trained and validated based on data from a specific station in eastern Guangdong. Its generalization ability to different geological backgrounds and regions with different seismic activity levels needs to be tested. In the future, efforts should actively acquire public datasets from other seismically active regions, and conduct model adaptation research based on transfer learning.

（4）Although the intelligent identification model constructed in this study achieved an accuracy of over 98%, it is not 100% perfect and still has a false alarm rate. This is determined by the inherent complexity of seismic precursor identification. Future research should acknowledge this limitation and introduce probabilistic decision mechanisms in the design of early warning systems. For example, multi-level warning thresholds can be set. At the same time, false alarm cases should be incorporated into the model for reverse analysis, and the algorithm should be continuously optimized to further reduce the false alarm rate while maintaining a high recall.

（5）Current research mainly focuses on the identification of precursors for "whether" an earthquake will occur, while the precise identification of the "three elements" (time, location, magnitude) is still insufficient. Future work should integrate precursor information such as AE and EME with physical models such as numerical simulation of crustal stress fields and fault activity analysis to develop dynamic probabilistic identification models based on physical mechanisms.

# References


[1] Mogi K. Seismicity in western Japan and long-term earthquake forecasting. Earthquake prediction: An international review, 1981, 4: 43-51.

[2] Carpinteri A, Borla O. Fracto-emissions as seismic precursors. Engineering Fracture Mechanics, 2017, 177: 239-250.

[3] Carpinteri A, Borla O. Acoustic, electromagnetic, and neutron emissions as seismic precursors: The lunar periodicity of low-magnitude seismic swarms. Engineering Fracture Mechanics, 2019, 210: 29-41.

[4] Russell S, Norvig P, Intelligence A. A modern approach. Artificial Intelligence. Prentice-Hall, Egnlewood Cliffs, 1995, 25(27): 79-80.

[5] LeCun Y, Bengio Y, Hinton G. Deep learning. Nature, 2015, 521(7553): 436-444.

[6] Goodfellow I, Bengio Y, Courville A. Deep Learning. MIT Press, 2016.

[7] Schmidhuber J. Deep learning in neural networks: An overview. Neural Networks, 2015, 61: 85-117.

[8] Reynen A, Audet P. Supervised machine learning on a network scale: Application to seismic event classification and detection. Geophysical Journal International, 2017, 210(3): 1394-1409.

[9] Mousavi S M, Ellsworth W L, Zhu W, et al. Earthquake transformer—an attentive deep-learning model for simultaneous earthquake detection and phase picking . Nature Communications, 2020, 11(1): 3952.

[10] Karniadakis G E, Kevrekidis I G, Lu L, et al. Physics-informed machine learning . Nature Reviews Physics, 2021, 3(6): 422-440.

[11] Bakun W, Lindh A. The parkfield, california, earthquake prediction experiment. Science, 1985, 229 (4714): 619-624.

[12] Padron E, Melián G, Marrero R, et al. Changes on diffuse $CO_2$ emission and relation to seismic activity in and around El Hierro, Canary Islands. Pure and Applied Geophysics, 2008, 165: 95-114.

[13] Immè G, Morelli D. Radon as earthquake precursor. Earthquake Research and Analysis-Statistical Studies, Observations and Planning, 2012.

[14] Hashemi S, Negarestani A, Namvaran M, et al. An analytical algorithm for designing radon monitoring network to predict the location and magnitude of earthquakes. Journal of Radioanalytical and Nuclear Chemistry, 2013, 295(3): 2249-2262.

[15] Chien S, Chi W, Ke C. Precursory and coseismic groundwater temperature perturbation: An example from taiwan. Journal of Hydrology, 2020, 582: 124457.

[16] Singh P, Mukherjee S. Chemical signature detection of groundwater and geothermal waters for evidence of crustal deformation along fault zones. Journal of Hydrology, 2020, 582: 124459.

[17] Li N, Kong X, Lin L. Anomalies in continuous gps data as precursors of 15 large earthquakes in western north america during 2007-2016. Earth Science Informatics, 2020, 13(1): 163-174.

[18] Yusof K, Abdullah M, Hamid N, et al. Correlations between earthquake properties and characteristics of possible ulf geomagnetic precursor over multiple earthquakes. Universe, 2021, 7(1): 20.

[19] Lei X, Ma S. Laboratory acoustic emission study for earthquake generation process. Earthquake Science, 2014, 27(6): 627-646.

[20] Gregori G, Poscolieri M, Paparo G, et al. “Storms of crustal stress” and AE earthquake precursors. Natural Hazards and Earth System Sciences, 2010, 10(2): 319-337.

[21] Carpinteri A, Lacidogna G, Manuello A, et al. A study on the structural stability of the Asinelli Tower in Bologna. Structural Control and Health Monitoring, 2016, 23(4): 659-667.

[22] Lacidogna G, Carpinteri A, Manuello A, et al. Acoustic and electromagnetic emissions as precursor phenomena in failure processes. Strain, 2011, 47(s2): 144-152.

[23] Lei X, Ma S. Laboratory acoustic emission study for earthquake generation process. Earthquake Science, 2014, 27(6): 627-646.

[24] Lukovenkova O, Solodchuk A, Tristanov A, et al. Complex analysis of pre-seismic geoacoustic and electromagnetic emission signals. E3S Web of Conferences, 2019, 03001.

[25] Spivak A, Rybnov Y. Acoustic effects of strong earthquakes. Physics of the Solid Earth, 2021, 57(1): 37-45.

[26] Gregori G, Paparo G, Poscolieri M, et al. Acoustic emission and released seismic energy. Natural Hazards and Earth System Sciences, 2005, 5(6): 777-782.

[27] Carpinteri A, Lacidogna G, Niccolini G. Acoustic emission monitoring of medieval towers considered as sensitive earthquake receptors. Natural Hazards and Earth System Sciences, 2007, 7(2): 251-261.

[28] Lacidogna G, Cutugno P, Niccolini G, et al. Correlation between earthquakes and AE monitoring of historical buildings in seismic areas. Applied Sciences, 2015, 5(4): 1683-1698.

[29] Zimatore G, Garilli G, Poscolieri M, et al. The remarkable coherence between two Italian far away recording stations points to a role of acoustic emissions from crustal rocks for earthquake analysis. Chaos, 2017, 27(4): 043101.

[30] Sammonds P, Meredith P, Main I. Role of pore fluids in the generation of seismic precursors to shear fracture. Nature, 1992, 359: 228-230.

[31] Han Q,Wang L, Xu J, et al. A robust method to estimate the b-value of the magnitude-frequency distribution of earthquakes. Chaos, Solitons & Fractals, 2015, 81: 103-110.

[32] Varotsos P, Sarlis N, Skordas E. On the recent advances in the study of seismic electric signals (VAN method). Physics And Chemistry Earth,Parts A/B/C,2006,31(4/5/6/7/8/9): 189-197.

[33] Sarlis N, Skordas E, Varotsos P, et al. Minimum of the order parameter fluctuations of seismicity before major earthquakes in Japan. Proceedings of the National Academy of Sciences of the United States of America, 2013, 110(34): 13734-13738.

[34] Sarlis N, Skordas E, Christopoulos S, et al. Identifying the occurrence time of the destructive kahramanmaraş-Gazientep earthquake of magnitude m 7.8 in Turkey on 6 february 2023. Applied Sciences, 2024, 14(3): 1215.

[35] Frid V, Rabinovitch A, Bahat D. Earthquake forecast based on nucleation stages and the continuous electromagnetic radiation. PhysicsLetters A, 2020, 384(4): 126102.

[36] Bleier T, Freund F. Impending earthquakes have been sending us warning signals and people are starting to listen. IEEE Spectrum INT, 2005, 3: 3-7.

[37] Ren H, Huang Q, Chen X. Existence of evanescent electromagnetic waves resulting from seismoelectric conversion at a solid-porous interface. Geophysical Journal International, 2016, 204: 147-166.

[38] Gao Y, Zhao G, Chong J, et al. Coseismic electric and magnetic signals observed during 2017 Jiuzhaigou Mw 6.5 earthquake and explained by electrokinetics and magnetometer rotation. Geophysical Journal International, 2020, 223: 1130-1143.

[39] Carpinteri A, Cardone F, Lacidogna G. Energy emissions from failure phenomena: mechanical, electromagnetic, nuclear. Experimental Mechanics, 2010, 50(8): 1235-1243.

[40] Carpinteri A, Lacidogna G, Borla O, et al. Electromagnetic and neutron emissions from brittle rocks failure: Experimental evidence and geological implications. Sadhana, 2012, 37(1): 59-78.

[41] Varotsos P, Sarlis N, Skordas E, et al. Additional evidence on some relationship between seismic electric signals and earthquake source parameters. Acta Geophysica Polonica, 2005, 53(3): 293.

[42] Hayakawa M, Hattori K, Ohta K. Monitoring of ulf (ultra-low-frequency) geomagnetic variations associated with earthquakes. Sensors, 2007, 7(7): 1108-1122.

[43] Eftaxias K, Athanasopoulou L, Balasis G, et al. Unfolding the procedure of characterizing recorded ultra-low frequency, kHZ and MHz electromagnetic anomalies prior to the L'Aquila earthquake as pre-seismic ones - Part 1. Natural Hazards and Earth System Sciences, 2009a, 9: 1953-1971.

[44] Eftaxias K. Footprints of nonextensive Tsallis statistics,selfaffinity and universality in the preparation of the L'Aquila earthquake hidden in a preseismic EM emission. Physica A, 2009b, 389: 133-40.

[45] Potirakis S, Schekotov A, Contoyiannis Y, et al. On possible electromagnetic precursors to a significant earthquake (mw=6.3) occurred in lesvos (greece) on 12 june 2017. Entropy, 2019, 21(3): 241.

[46] Carpinteri A, Cardone F, Lacidogna G. Piezonuclear neutrons from brittle fracture: early results of mechanical compression tests. Strain, 2009, 45(4): 332-339.

[47] Lucia U, Carpinteri A. GeV plasmons and spalling neutrons from crushing of iron-rich natural rocks. Chemical Physics Letters, 2015, 640: 112-114.

[48] Volodichev N, Kuzhevskij B, Nechaev O, et al. Phenomenon of neutron intensity bursts during new and full moons. Cosmic Research, 1997, 31(2): 135-143.

[49] Sobolev G A, Shestopalov I P, Kharin E P. Implications of solar flares for the seismic activity of the Earth. Izvestiya Physics of the Solid Earth, 1998, 34(7): 603-607.

[50] Sigaeva E, Nechaev O, Panasyuk M, et al. Thermal neutrons' observations before the Sumatra earthquake. Geophysical Research Abstracts, 2006, 8: 00435.

[51] Mignan A, Broccardo M. Neural network applications in earthquake prediction (1994-2019): Meta-analytic and statistical insights on their limitations. Seismological Research Letters, 2020, 91(4): 2330-2342.

[52] Maya M, Yu W. Short-term prediction of the earthquake through neural networks and metalearning. 16th International Conference on Electrical Engineering,Computing Science and Automatic Control (CCE), 2019, 1-6.

[53] Berhich A, Belouadha F, Kabbaj M. Lstm-based models for earthquake prediction. Proceedings of the 3rd International Conference on Networking,Information Systems & Security, 2020, 1-7.

[54] Banna A, Ghosh T, Al Nahian M. J, et al. Attention-based bi-directional long-short term memory network for earthquake prediction. IEEE Access, 2021, 9: 56589-56603.

[55] Jozinović D, Lomax A, Štajduhar I, et al. Transfer learning: Improving neural network based prediction of earthquake ground shaking for an area with insufficient training data. Geophysical Journal International, 2022, 229(1): 704-718.

[56] Kail R, Burnaev E, Zaytsev A. Recurrent convolutional neural networks help to predict location of earthquakes. IEEE Geoscience and Remote Sensing Letters, 2021, 19: 1-5.

[57] Fuentes A, Nicolis O, Peralta B, et al. Spatio-temporal seismicity prediction in chile using a multi-column convlstm. IEEE Access, 2022, 10: 107402-107415.

[58] Scholz C H. The mechanics of earthquakes and faulting. Cambridge university press, 2019.

[59] Griffith A A. The phenomena of rupture and flow in solids. Philosophical Transactions of The Royal Society A Mathematical Physical and Engineering Sciences, 1920, 221(4): 163-198.

[60] Irwin G R. Analysis of stresses and strains near the end of a crack traversing a plate. Journal of Applied Mechanics, 1957, 24: 361-364.

[61] Hillerborg A, Modéer M, Petersson P E. Analysis of crack formation and crack growth in concrete by means of fracture mechanics and finite elements. Cement and Concrete Research, 1976, 6(6): 773-781.

[62] Ohtsu M. The history and development of acoustic emission in concrete engineering. Magazine of Concrete Research, 1996, 48(177): 321-330.

[63] Carpinteri A, Lacidogna G, Corrado M, et al. Cracking and crackling in concrete-like materials: a dynamic energy balance . Engineering Fracture Mechanics, 2016, 155: 130–144.

[64] Manuello A, Niccolini G, Carpinteri A. AE monitoring of a concrete arch road tunnel: damage evolution and localization . Engineering Fracture Mechanics, 2019, 210: 279–287.

[65] Niccolini G, Lacidogna G, Carpinteri A. Fracture precursors in a working girder crane: AE natural-time and b-value time series analyses . Engineering Fracture Mechanics, 2019, 210: 393–399.

[66] Zheng Q, Li C, He B, et al. Revealing the effect of silica fume on the flexural behavior of ultra-high-performance fiber-reinforced concrete by acoustic emission technique . Cement and Concrete Composites, 2022, 131: 104563.

[67] Han Q, Yang G, Xu J, et al. Acoustic emission data analyses based on crumb rubber concrete beam bending tests . Engineering Fracture Mechanics, 2019, 210: 189–202.

[68] Zhu Z, Jiang Z, Accornero F, et al. Correlation between seismic activity and acoustic emission on the basis of in situ monitoring. Natural Hazards and Earth System Sciences, 2024, 24(11): 4133-4143.

[69] Carpinteri A, Lacidogna G, Accornero F, et al. Influence of damage in the acoustic emission parameters. Cement and Concrete composites, 2013, 44: 9-16.

[70] JCMS-III, B5706, Monitoring method for active cracks in concrete by acoustic emission, Federation of Construction Materials Industries, JAPAN, 2003.

[71] RECOMMENDATION OF RILEM TC 212-ACD. Acoustic emission and related NDE techniques for crack detection and damage evaluation in concrete: Test method for classification of active cracks in concrete by acoustic emission. Materials and Structures, 2010, 43(9): 1187–1189.

[72] Ohtsu M, Isoda T, Tomoda Y. Acoustic emission techniques standardized for concrete structures. Journal of Acoustic Emission, 2007, 25: 21–32.

[73] Aggelis D G. Classification of cracking mode in concrete by acoustic emission parameters. Mechanics Research Communications, 2011, 38(3): 153-157.

[74] Aggelis D G, Soulioti D V, Sapouridis N, et al. Acoustic emission characterization of the fracture process in fibre reinforced concrete. Construction and Building Materials, 2011, 25(11): 4126-4131.

[75] Soulioti D, Barkoula N M, Paipetis A, et al. Acoustic emission behavior of steel fibre reinforced concrete under bending. Construction and Building Materials, 2009, 23(12): 3532-3536.

[76] Han Q, Xu J, Carpinteri A, et al. Localization of acoustic emission sources in structural health monitoring of masonry bridge. Structural Control and Health Monitoring, 2015, 22(2): 314-329.

[77] Carpinteri A, Corrado M, Lacidogna G. Three different approaches for damage domain characterization in disordered materials: Fractal energy density, b-value statistics, renormalization group theory. Mechanics of Materials, 2012, 53: 15-28.

[78] Lacidogna G, Accornero F, Carpinteri A. Influence of snap-back instabilities on Acoustic Emission damage monitoring. Engineering Fracture Mechanics, 2019, 210: 3-12.

[79] Carpinteri A, Lacidogna G, Manuello A, et al. A study on the structural stability of the Asinelli Tower in Bologna. Structural Control and Health Monitoring, 2016, 23(4): 659-667.

[80] Carpinteri A, Lacidogna G, Pugno N. Structural damage diagnosis and life-time assessment by acoustic emission monitoring. Engineering Fracture Mechanics, 2007, 74(1-2): 273-289.

[81] Rundle J B, Turcotte D L, Shcherbakov R, et al. Statistical physics approach to understanding the multiscale dynamics of earthquake fault systems. Reviews of Geophysics, 2003, 41(4).

[82] Turcotte D L. Fractals and chaos in geology and geophysics. Cambridge University Press, 1997.

[83] Bonnet E, Bour O, Odling N E, et al. Scaling of fracture systems in geological media. Reviews of geophysics, 2001, 39(3): 347-383.

[84] Rojo Tanzi B N, Sobczyk M, Becker T, et al. Damage evolution analysis in a “spaghetti” bridge model using the acoustic emission technique. Applied Sciences, 2021, 11(6): 2718.

[85] Carpinteri A, Lacidogna G, Puzzi S. From criticality to final collapse: Evolution of the “b-value” from 1.5 to 1.0. Chaos, Solitons & Fractals, 2009, 41(2): 843-853.

[86] Carpinteri A. Scaling laws and renormalization groups for strength and toughness of disordered materials. International Journal of solids and structures, 1994, 31(3): 291-302.

[87] Carpinteri A, Lacidogna G. Structural monitoring and integrity assessment of medieval towers. Journal of Structural Engineering, 2006, 132(11): 1681-1690.

[88] Carpinteri A, Lacidogna G. Damage evaluation of three masonry towers by acoustic emission. Engineering Structures, 2007, 29(7): 1569-1579.

[89] Varotsos P A. Spatio-temporal complexity aspects on the interrelation between seismic electric signals and seismicity. Praktika of the Academy of Athens, 2001, 76: 294-321.

[90] Varotsos C A, Tzanis C, Cracknell A P. Precursory signals of the major El Niño Southern Oscillation events. Theoretical and Applied Climatology, 2016, 124(3): 903-912.

[91] Varotsos P A, Sarlis N V, Skordas E S, et al. Seismic Electric Signals: An additional fact showing their physical interconnection with seismicity. Tectonophysics, 2013, 589: 116-125.

[92] Hloupis G, Stavrakas I, Vallianatos F, et al. A preliminary study for prefailure indicators in acoustic emissions using wavelets and natural time analysis. Proceedings of the Institution of Mechanical Engineers, Part L: Journal of Materials: Design and Applications, 2016, 230(3): 780-788.

[93] Loukidis A, Pasiou E D, Sarlis N V, et al. Fracture analysis of typical construction materials in natural time. Physica A: Statistical Mechanics and its Applications, 2020, 547: 123831.

[94] Niccolini G, Manuello A, Marchis E, et al. Signal frequency distribution and natural-time analyses from acoustic emission monitoring of an arched structure in the Castle of Racconigi. Natural Hazards and Earth System Sciences, 2017, 17(7): 1025-1032.

[95] Vallianatos F, Michas G, Benson P, et al. Natural time analysis of critical phenomena: The case of acoustic emissions in triaxially deformed Etna basalt. Physica A: Statistical Mechanics and its Applications, 2013, 392(20): 5172-5178.

[96] Hloupis G, Stavrakas I, Pasiou E D, et al. Natural time analysis of acoustic emissions in Double Edge Notched Tension (DENT) marble specimens. Procedia Engineering, 2015, 109: 248-256.

[97] Loukidis A, Triantis D, Stavrakas I, et al. Detecting criticality by exploring the acoustic activity in terms of the “Natural-Time” concept. Applied Sciences, 2021, 12(1): 231.

[98] Friedrich L F, Tanzi B N R, Colpo A B, et al. Analysis of acoustic emission activity during progressive failure in heterogeneous materials: experimental and numerical investigation. Applied Sciences, 2022, 12(8): 3918.

[99] Triantis D, Stavrakas I, Loukidis A, et al. A Study on the fracture of cementitious materials in terms of the rate of Acoustic Emissions in the Natural Time Domain. Applied Sciences, 2023, 13(10): 6261.

[100] Samal D K, Ray S. Wavelet entropy-based damage characterization and material phase differentiation in concrete using acoustic emissions. Engineering Failure Analysis, 2024, 160: 108144.

[101] Chang X, Wu S, Wang J, et al. Investigating the comprehensive index of acoustic emissions and fractal characteristics of damage of red sandstone based on information entropy. Journal of Nondestructive Evaluation, 2024, 43(2): 36.

[102] Hosseini S M, Azadi M, Ghasemi-Ghalebahman A, et al. Fatigue crack initiation detection in ductile cast iron crankshaft under rotating bending fatigue test using the acoustic emission entropy method. Engineering Failure Analysis, 2023, 144: 106981.

[103] D'Angela D, Ercolino M. Acoustic emission entropy: An innovative approach for structural health monitoring of fracture‐critical metallic components subjected to fatigue loading. Fatigue & fracture of Engineering Materials & Structures, 2021, 44(4): 1041-1058.

[104] Shannon C E. A mathematical theory of communication. The Bell System Technical Journal, 1948, 27(3): 379-423.

[105] Santo F T, Sattar T P, Edwards G. Validation of acoustic emission waveform entropy as a damage identification feature. Applied Sciences, 2019, 9(19): 4070.

[106] Kahirdeh A. Energy dissipation and entropy generation during the fatigue degradation: Application to health monitoring of composites. Louisiana State University and Agricultural & Mechanical College, 2014.

[107] Contoyiannis Y F, Diakonos F K. Criticality and intermittency in the order parameter space. Physics Letters A, 2000, 268(4-6): 286-292.

[108] Colombo I S, Main I G, Forde M C. Assessing damage of reinforced concrete beam using “b-value” analysis of acoustic emission signals. Journal of Materials in Civil Engineering, 2003, 15(3): 280-286.

[109] Birck G, Riera J D, Iturrioz I. Numerical DEM simulation of AE in plate fracture and analogy with the frequency of seismic events in SCRs. Engineering Failure Analysis, 2018, 93: 214-223.

[110] Potirakis S M, Contoyiannis Y, Schekotov A, et al. Evidence of critical dynamics in various electromagnetic precursors. The European Physical Journal Special Topics, 2021, 230(1): 151-177.

[111] Contoyiannis Y F, Potirakis S M, Eftaxias K. The Earth as a living planet: human-type diseases in the earthquake preparation process. Natural Hazards and Earth System Sciences, 2013, 13(1): 125-139.

[112] Contoyiannis Y F, Diakonos F K, Papaefthimiou C, et al. Criticality in the relaxation phase of a spontaneously contracting atria isolated from a frog's heart. Physical Review Letters, 2004, 93(9): 098101.

[113] Pradhan S, Hansen A, Hemmer P C. Crossover behavior in burst avalanches: Signature of imminent failure. Physical Review Letters, 2005, 95(12): 125501.

[114] Jiang Z, Zhu Z, Accornero F. Tensile-to-shear crack transition in the compression failure of steel-fibre-reinforced concrete: insights from acoustic emission monitoring. Buildings, 2024, 14(7): 2039.

[115] Khan M, Ali M. Effectiveness of hair and wave polypropylene fibers for concrete roads . Construction and Building Materials, 2018, 166: 581–591.

[116] Qin Y, Zhang X, Chai J, et al. Experimental study of compressive behavior of polypropylene-fiber-reinforced and polypropylene-fiber-fabric-reinforced concrete . Construction and Building Materials, 2019, 194: 216–225.

[117] Noorsuhada M N. An overview on fatigue damage assessment of reinforced concrete structures with the aid of acoustic emission technique. Construction and Building Materials, 2016, 112: 424-439.

[118] Carpinteri A, Corrado M, Lacidogna G. Heterogeneous materials in compression: Correlations between absorbed, released and acoustic emission energies. Engineering Failure Analysis, 2013, 33: 236-250.

[119] Dębski W, Pradhan S, Hansen A. Criterion for imminent failure during loading—discrete element method analysis. Frontiers in Physics, 2021, 9: 675309.

[120] Jing G, Lacidogna G, Zhao Y, et al. Coal–rock catastrophic collapse: Precursors based on AE and fiber bundle models. International Journal of Geomechanics, 2025, 25(1): 04024314.

[121] Rojo Tanzi B N, Sobczyk M, Iturrioz I, et al. Damage Evolution in Quasi-Brittle Materials: Experimental Analysis by AE and Numerical Simulation. Applied Sciences, 2023, 13(19): 10947.

[122] Almeida W R, Tanzi B N R, Birck G, et al. Analysis of Damage Process in a Pre-Notched Rock Specimen: The Synergy between Experimental Results and Simulations Using a Peridynamic Model. Applied Sciences, 2024, 14(11): 4721.

[123] Dobrovolsky I P, Zubkov S I, Miachkin V I. Estimation of the size of earthquake preparation zones. Pure and Applied Geophysics, 1979, 117(5): 1025-1044.

[124] Hanks T C, Kanamori H. A moment magnitude scale. Journal of Geophysical Research: Solid Earth, 1979, 84(B5): 2348-2350.

[125] Hemmer P C, Hansen A. The distribution of simultaneous fiber failures in fiber bundles. Journal of applied mechanics, 1992, 59(4): 909-914.

[126] Danku Z, Kun F. Fracture process of a fiber bundle with strong disorder. Journal of Statistical Mechanics: Theory and Experiment, 2016, 2016(7): 073211.

[127] Carpinteri A, Lacidogna G, Niccolini G. Critical behaviour in concrete structures and damage localization by acoustic emission. Key Engineering Materials, 2006, 312: 305-310.

[128] Jiang Z, Zhu Z, Friedrich L F, et al. Multi-technical analysis of damage process in GFRP-bar reinforced concrete beam. Engineering Structures, 2026, 348: 121803.

[129] Ahmadzadeh M, Zahrai S M, Bitaraf M. An integrated deep neural network model combining 1D CNN and LSTM for structural health monitoring utilizing multisensor time-series data. Structural Health Monitoring, 2025, 24(1): 447-465.

[130] Dalhat M A. Deep Neural Network modeling and analysis of the laboratory compaction parameter of unbound granular materials. Measurement, 2025, 244: 116488.

[131] Luque A, Carrasco A, Martín A, et al. The impact of class imbalance in classification performance metrics based on the binary confusion matrix. Pattern recognition, 2019, 91: 216-231.